Quenching Heat Treatment Modelling of Thick-Section Parts by CFD Methods with a Semi-mechanistic Boiling Model

By:

Tongyu Wang

A thesis submitted in partial fulfilment of the requirements for the degree of
Doctor of Philosophy

The University of Sheffield
Faculty of Engineering
Department of Material Science and Engineering

December 2024

Abstract

Heat treatment of metallic parts is one of the most important processes to enhance the mechanical properties. Quenching is the key step in a full heat treatment process, and it largely determines the properties of the final product. Successful computer simulations of quenching can significantly improve the production efficiency as well as the research and development progress of industrial manufacturers. However, despite the great efforts that have been made to study simulation of quenching, this complicated process which is involved with multiple physical mechanisms has not been fully understood.

The main goal of this project is to develop robust models which are capable of predicting the temperature evolution of both small- and large-scale samples during a quench cooling process without requiring any experimentally acquired data prior to the simulation. The models are designed to be based on CFD methods and FEM and are constructed and solved by the ANSYS software packages. The heat transfer and boiling effects are mainly solved by a semi-mechanistic model, but an empirical model is also applied to discuss the difference between the performance of these two methods.

The simulated process of this paper is the immersion quench cooling of cylindrical workpieces of different sizes in liquid water at 20 ℃. According to the sample size, the models are divided into two groups: small-scale models and large-scale models. Proper mathematical models are applied to simulate the fluid flow and heat transfer processes in the real world. The influence of multiple parameters on the performance of the prediction is investigated in detail. Finally, the optimal model set-up for both the small- and large-scale models are reported.

Nomenclature

A	Area
a	Coefficient used for pressure interpolation
b	Residual
Bi	Biot number
C	Coefficient
CFL	Global Courant number
C_p	Specific heat
D	Diameter
E	Energy
$\dot{E}$	Energy generation rate
e	Natural logarithm
F	Force
f	Function
g	Gravitational acceleration
H	Latent heat
Hs	Sensible enthalpy
h	Heat transfer coefficient
I	Unit tensor
J	Mass flux
Ja	Jakob number
k	Turbulent kinetic energy
L	Characteristic length
l	Smoothing radius
M	Mach number
$\dot{m}$	Mass transfer rate
N	Number of points
n	Avrami exponent
$\hat{n}$	Unit normal vector
$\vec{n}$	Normal vector

Pe	Peclet number
Pr	Prandtl Number
p	Pressure
q	Heat flux
R	Gas constant
Ra	Rayleigh number
Re	Reynolds number
r	Radius
S	Source term
S°	Entropy
s	Gap size
T	Temperature
t	Time
$\hat{t}$	Unit tangential vector
U	Free stream velocity
u	Velocity magnitude
V	Volume
$\vec{v}$	Velocity vector
W	Kernal function
w	Wetting parameter
x, y, z	Coordinates
α	Volume fraction
β	Thermal expansion coefficient
δ	Interpolation between particles
ε	Turbulent kinetic energy dissipation rate
η	Effectiveness factor
θ	Angle
κ	Von Kármán constant
λ	Thermal conductivity
μ	Dynamic viscosity

ν	Kinematic viscosity
$\hat{\nu}$	Effective ratio of turbulent kinetic energy
ξ	Solid phase mass
$\dot{\xi}$	Solid phase generation rate
ρ	Density
σ	Surface tension
τ	Shear stress
$\bar{\bar{\tau}}$	Stress tensor
ϕ	Scalar
φ	Data value
ω	Solid growth rate
χ	Relative average error

Subscripts

aus	Austenite
B	Boiling
b	Particle
BG	Bubble growth
BW	Bubble wait
CHF	Critical heat flux
Con	Conduction
$Contact$	Contact area
c	Cell
$cond$	Condensation
D	Drag
eff	Effective value
$evap$	Evaporation
$Film$	Film boiling
f	Face
fin	Finish
$freq$	Frequency

I	Interface
i	Index
k	Phase index
l	Liquid phase
MHF	Minimum heat flux
m	Mass
mac	Macroscopic value
mar	Martensite
mic	Microscopic value
mol	Molecular
NC	Natural convection
$n, n+1, n-1$	Time step indices
P	First layer fluid cells from solid wall
Re	Reynolds number
ref	Reference value
s	Solid
sat	Saturation
TB	Transition boiling
t	Turbulence
VM	Virtual mass
v	Vapour phase
vol	Volume
w	Solid wall
x, y, z	Axes

Table of Contents

1 Introduction

Heat treatment plays a vital role in increasing the mechanical properties of an alloy. The result of an entire heat treatment process is determinative of the performance of quenching. Improper heat treatment is often detrimental to the mechanical properties and the structural integrity of the workpiece. Severe defects including segregation, undesired phases or microstructure, significant residual stress, and even cracks can be induced by a heat treatment failure. Therefore, simulation is often carried out prior to industrial production to evaluate possible results and avoid potential failures, particularly if the component is of very high value and hard to recycle. In addition, computer simulation of quenching is also critical for the design and optimization of quenching systems.

During a quenching process, the thermal field, metallurgical field, and mechanical field of the workpiece interact with each other in the way illustrated in Figure 1 and produce the final results as a consequence. The temperature evolution, which is heavily dependent on the fluid flow and the boiling behaviour, is the determining factor of the changes in phase composition and microstructure. On the other hand, the latent heat induced by phase transformation significantly affects the cooling rate of the workpiece. Meanwhile, stress and strain are generated in the workpiece as a result of thermal expansion and volume change caused by phase transformation. Such mechanical property changes in return have an influence on the thermal and metallurgical fields evolution. The influence of mechanical parameters on the phase transformation kinetics is exceptionally significant when the cooling rate is fast and the sample is big [2]. For immersion quenching in water, the change in mechanical field does not have noticeable influence on the cooling rate of the sample [1], but such influence is significant in air cooling process [3]. Nevertheless, thermal and metallurgical fields must be coupled with mechanical field for an accurate prediction on the residual stress, especially for workpieces with complicated geometry [3, 4].

When it comes to predicting the temperature evolution of the sample, evaluation of boiling effects and fluid flow conditions near the solid surface is where the major difficulties lie. Governed by solid surface temperature and heat flux at solid-liquid interface, the quenchant usually goes through several different boiling regimes throughout the whole cooling process.

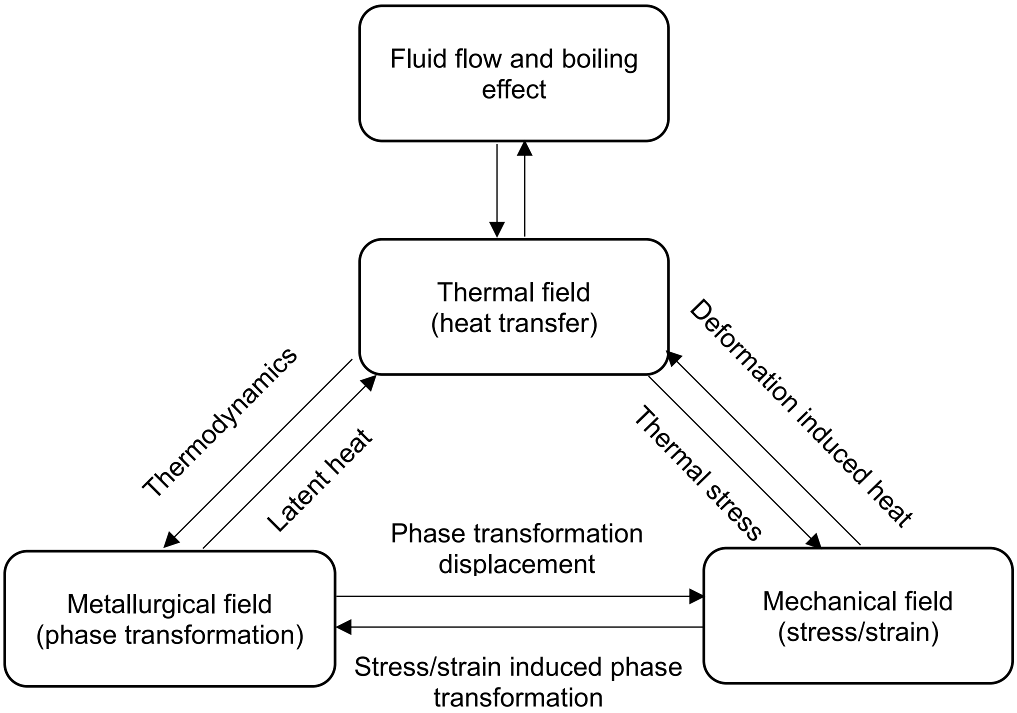

Figure 1 Physical properties involved in a heat treatment process [1].

The relationship between heat flux and wall supersaturation is described by Figure 2. In the initial stage when the solid surface temperature is much higher than the saturation temperature of the quenchant, boiling effect is so intense that the generated gaseous phase forms a layer that completely covers the solid surface, as shown by Figure 3 (a). This specific boiling behaviour is known as film boiling. Cooling rate at this stage is low because heat transfer between solid and vapour phases is much slower than between solid and liquid phases. As solid surface is cooled down to a critical temperature known as the Leidenfrost point [5], the boiling intensity is no longer high enough to sustain the vapour layer, so the layer breaks into multiple big bubbles which partially cover the solid surface. This marks the end of film boiling and the inception of transition boiling. Figure 3 (b) and (c) show the images for both the inception and the ending of transition boiling. During transition boiling, heat transfer is slightly accelerated as the sample is partially in contact with quenchant. After that, when the critical heat flux (CHF) is reached, the boiling mode is converted to nucleate boiling where any gaseous phase generated at the interface forms small bubbles and depart from the solid surface almost immediately. These small bubbles can possibly merge into larger bubbles in the liquid domain, but none of these bubbles covers any part of the solid surface. Since the solid sample is in contact with liquid again, the heat transfer rate at solid surface often reaches its maximum value at this stage. Finally, after the solid surface is cooled down below the evaporation temperature of the quenchant, boiling effect is stopped and heat transfer between solid and liquid relies on conduction and convection.

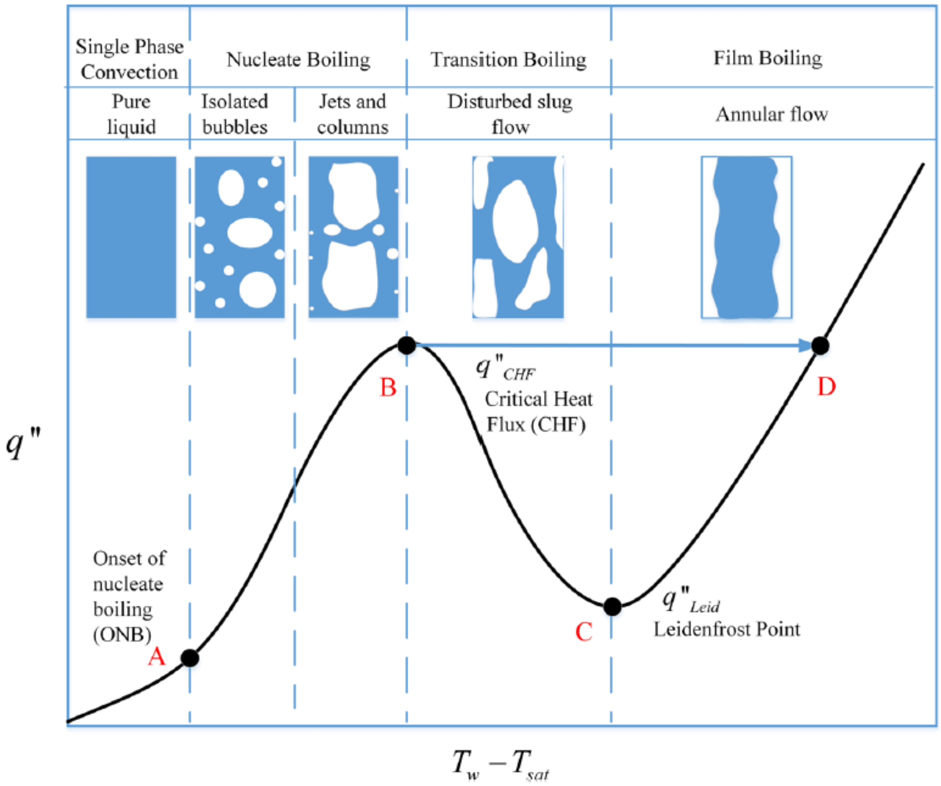

Figure 2 Temperature and heat flux evolution during cooling.

Computational Fluid Dynamics (CFD) is a powerful approach which is often used to obtain insights of various fluid behaviours, including turbulence flow, boiling effect, and heat transfer of multiple mechanisms. There have been numerous studies on complicated fluid flow behaviours and boiling effects carried out with CFD methods, but it is still a relatively new method in terms of simulation of quenching. Compared to conventional lumped heat transfer characteristics, CFD methods have been proven to be a better approach to model quench cooling involved with boiling effects [6]. However, a thorough understanding of the fluid mechanisms involved in quenching has not been established yet due to the randomness of fluid behaviours and lack of knowledge. Generally, three types of models are used to evaluate the overall heat transfer during quenching:

- Equations based on experimental data. These equations refer to the empirical equations developed for various physical mechanisms, including bubble nucleation and departure, as well as boiling heat transfer for each boiling regime. Such equations are usually obtained via regression of experimental cooling results.

- Inverse analysis. Thermal boundary conditions like temperature and heat flux on the solid surface is utterly difficult to measure experimentally. Instead, they can be computed based on the experimentally recorded temperature files at different locations of the sample. High accuracy results can be obtained with low calculating efforts in most cases, but the application of such method is dependent on the availability of experimental results and is restricted to a specific quenching set up.
- Mechanistic and semi-mechanistic models. These models numerically evaluate the physical mechanisms involved in cooling process. Obviously, these models don't require pre-simulation experimental data, but adequate computational power and vast knowledge of fluid dynamics are fundamental. In addition, while dealing with samples with complex geometry, the difficulties of applying such models are increased dramatically.

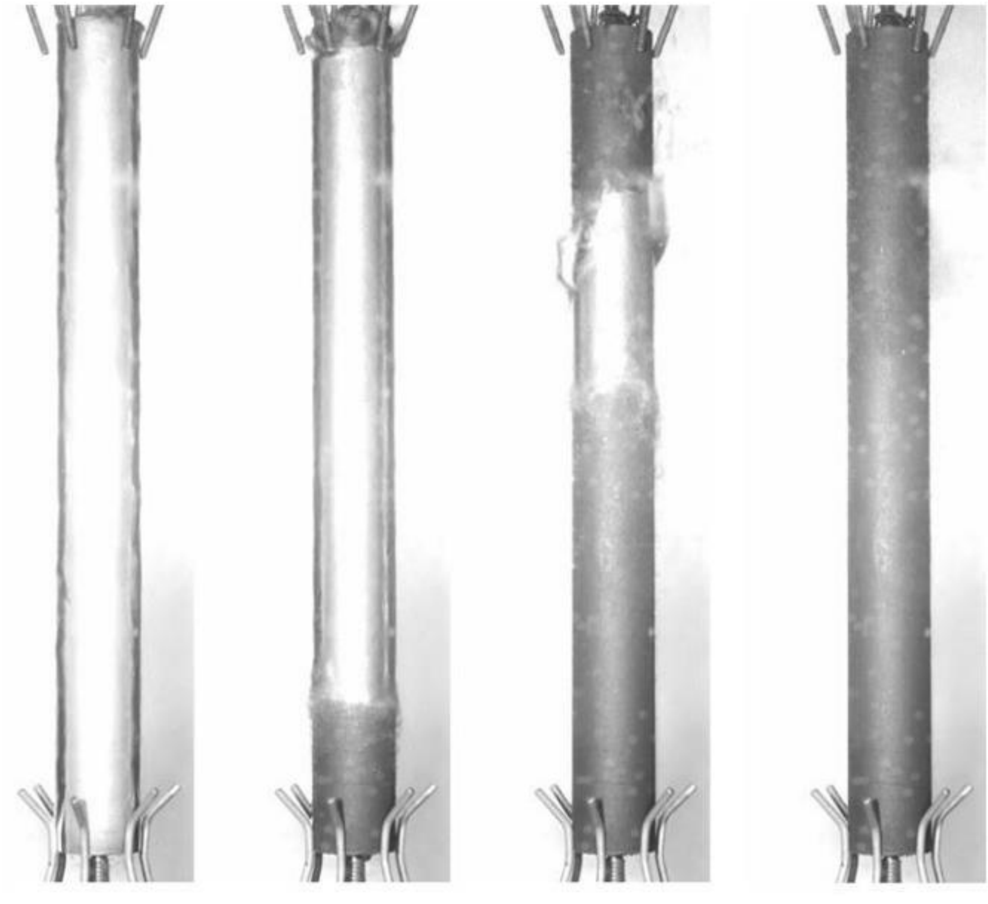

Figure 3 Images of steel rod quenched in water after (a) 1 s, (b) 10 s, (c) 20 s, (d) 24 s [7].

1.1 Project Aim and Novelty

The aim of this project is to predict the temperature evolution of a workpiece during quenching with the application of CFD methods. Semi-mechanistic boiling models are applied to predict the boiling effect. Two particular Ni-based alloys, Inconel 718 and Inconel 600, are studied, and their material properties are generated by JMatPro®. The simulation begins with simulations of small-scale samples and moves on to larger industrial sizes.

Most existing research that uses semi-mechanistic boiling model is focused on the cooling of small-scale samples, i.e., samples with the characteristic length of tens of millimetres. Research studies which analyse the cooling of larger scale samples often rely on empirical models to deal with the heat transfer between sample and quenchant. It is true that for larger workpieces, the heat conduction effect inside the solid domain is a more predominant factor on the cooling rate in bulk material, but correctly predicting the heat transfer rate at interface is crucial, especially for predictions of temperature evolution at locations close to the surface. In the cases where segregation might happen or different phases and microstructures are formed at different depth from the surface, a valid HTC prediction is also essential.

Therefore, this project applies semi-mechanistic CFD models on both small and large samples to obtain the temperature profile for various locations during the whole cooling process. Despite the massive research focused on simulation of quenching, this specific area has been rarely touched upon. The results of this project have great potential to improve the accuracy of modelling quenching processes of workpieces with thick sections.

2 Research Background and Literature Review

Considering the importance of quenching heat treatment, it is not surprising to see the considerable amount of relevant research work. However, only a minority of them are focused on industrial scale workpiece or those with thick sections. For the simulation of workpieces with different sizes, the modelling strategy can be quite different. For a small-scale sample, the whole model has a relatively small volume, and the mesh grids would not contain too many elements and nodes. Thus, the calculation for these kinds of models can be as detailed as desired to achieve high level of accuracy. Especially, with a really fine mesh, a high-resolution temperature map of the sample can be obtained. However, while dealing with large-scale samples, it is no longer possible to obtain such detailed temperature distribution in the solid domain with equivalent calculation resources. Under the consideration of production efficiency, resolution and accuracy are often compromised to avoid extremely heavy calculation burden.

Model arithmetic efficiency, especially the mathematical models of mass and heat transfer, is essential for the overall performance of the model. Meanwhile, the model must avoid being over complicated so that it can be productive and implementable by commercial software packages.

2.1 CFD Basics

As a fundamental part of a CFD analysis, the governing equations are derived from conservation laws of each physical property. In the case of a multi-fluid model, since each fluid phase is considered as a continuous medium, multiple governing equations must be solved for each property of each phase. With the application of a volume fraction parameter and a property exchange term, the governing equations of multiphase model are similar to those of single-phase models.

There are several approaches to discretising the space and investigate the fluid behaviour. We can either create a mesh-based or meshless space, and then track some particular fluid particles or focus on a fixed volume of space. Finite Volume Method (FVM) is one of the most popular methods of achieving this. It partitions the fluid domain into unit cells with certain volume and study the fluid flowing in and out of a cell with fixed volume. It's extensively used in this project as well as most of other CFD related research due to its high computational efficiency and easiness of implementation. Based on the analysis of a controlled volume, the Navier-Stokes equations were developed. The Navier-Stokes equations are a set of spatial difference equations derived from the conservation law of mass and momentum of a Newtonian fluid in a closed volume. The governing equations that are used by almost all CFD codes take the form of Navies-Stokes equations. These governing equations describe the conservation of mass, momentum, and energy of the fluid system. They are impossible to be explicitly solved in most cases, so obtaining approximate solutions is the goal of solution.

In the following sections, some widely used CFD methods are reviewed.

2.1.1 Smoothed Particle Hydrodynamics (SPH)

The SPH method is a Lagrangian meshless CFD method which was initially invented to simulate astrophysics problems. Although it was designed for compressible problems, it is capable of simulating near-incompressible problems by choosing a sound speed which is significantly higher than the flow velocity [8]. Later on, with its satisfying accuracy and ability to model multiphysics flow under complicated conditions, it has drawn great research interests. In addition, it is capable of generating high resolution results [9] and fine animation of fluid flow. An example of this would be the work of Xiong et al. [10] where they simulated the boiling effect on hydrophobic and hydrophilic surfaces. However, its applications in modelling real-life problems are limited by its huge computational cost. Meanwhile, those complex problems with which the great potential of SPH methods really matters are not the most common ones when it comes to industrial scenarios [11]. It is also worth noting that SPH is a fully transient method which can only deal with unsteady state flow problems [12].

In a SPH simulation, the continuous domain is discretized by a number of particles which are disorderly distributed and carry local information like mass, temperature, velocity, etc. For a certain particle, its property is the summation of its interaction with all other particles, represented by Eqn. (1).

$$\phi(\vec{r}) = \int \phi(\overrightarrow{r'}) \cdot \delta(\vec{r} - \overrightarrow{r'}) d\overrightarrow{r'} \tag{1}$$

The right-hand side of this equation is integrated throughout the whole domain to obtain the exact value of a property ϕ of the concerning particle. However, this equation has a critical issue that δ is unable to integrate, because it only has value at one position, and is zero anywhere else in the domain. Therefore, this function is replaced by a continuous kernel function $W\left(\vec{r}-\overrightarrow{r'},l\right)$ which is often chosen that its value falls off rapidly when $\left|\vec{r}-\overrightarrow{r'}\right| > l$. The integral is calculated on all particles, resulting in Eqn. (2).

$$\phi(\vec{r}) = \sum_{b} \frac{m_b}{\rho_b} \phi\left(\overrightarrow{r'}\right) W\left(\vec{r}-\overrightarrow{r'},l\right) \tag{2}$$

Thus, the gradient of a property is obtained by Eqn. (3).

$$\nabla\phi(\vec{r}) = \sum_{b} \frac{m_b}{\rho_b} \phi\left(\overrightarrow{r'}\right) \nabla W\left(\vec{r}-\overrightarrow{r'},l\right) \tag{3}$$

The performance of the simulation depends heavily on the selection of the kernel function [11]. With a Gaussian kernel function which is one of the most used ones, it is most likely to have a physical interpretation of the SPH equation [13]. It was reported that a splines-based kernel makes the calculation more efficient [14]. Sigolatti [15] applied an adaptive kernel function which adjusts according to the particle distribution, resulting in enhanced stability and accuracy.

SPH method can also be coupled with other simulation methods. To model wet industrial banana screens, Fernandez [16] used Discrete Element Method (DEM) to characterize large solid particles which are much less mobile. The small particles which flow through the large particles are modeled by the SPH method. Potakov et al. [17] have also coupled DEM with SPH method to model a similar problem which is macroscopic particles flowing in a viscous fluid. Such coupling is accomplished through no-slip boundary conditions on solid-liquid interface. Barcarolo et al. [18] combined FVM with SPH method to take the advantage of the accuracy of FVM and the ability to model the free surface. In their work, the fluid domain is divided into two sections, and one of them is treated by FVM while the other is modeled by SPH method [18].

2.1.2 Lattice Boltzmann Method (LBM)

LBM is based on microscale and mesoscale characterization of the fluid domain [19]. The fluid is analyzed according to the distribution function of particles. This method is capable of solving multiphase and multi-physical problems as well as both compressible and incompressible fluids. It is gaining popularity because it's easy to implement and is efficient for computation as well as its great parallelization performance [20]. Especially, LBM shows great performance while dealing with complex geometries and physics involved with low Knudsen number and Mach number [21].

The Lattice Boltzmann Equation is shown in Eqn. (4).

$$f_i(\vec{x}+\vec{v_i}\delta_t, t+\delta_t) = f_i(\vec{x},t) - \frac{1}{t'}\left[f_i(\vec{x},t) - f_i^{eq}(\vec{x},t)\right] \tag{4}$$

In this equation, the second term on the right-hand side is the collision term, which represents the interaction between particles. t' is a dimensionless relaxation time which is the ratio of the time needed to reach equilibrium to the time step size. This represents the Bhatnagar-Gross-Krook (BGK) relaxation model, which is a single relaxation that relies only on t'. The results of Eqn. (4) can be considered equivalent to the solution of Navies-Stokes equations as long as it takes the viscosity term into account properly. This is achieved by the speed of sound factor which appears in the expression of $f_i^{eq}(\vec{x},t)$.

One of the most used LBM is the two-dimensional nine directions method, also known as the D2Q9 method. In a 2-D space, at a certain node, the collision is evaluated along nine different directions in a single time step. During this process, conservation of mass, momentum and energy is maintained. After all the collision effects are figured out, the advancement in time is completed. For 3-D cases, a common method is D3Q18 which allows for the velocity in 18 directions.

Even though the BGK collision model is one of the earliest developed and most used models, it is slightly oversimplified so that its stability is not the best (especially with low viscosity values[22]) and the Prandl number is limited to unity while dealing with thermal fluids [23]. In order to overcome this issue, Lallemand and Luo [23] developed a multi-relaxation-time (MRT) collision model described by Eqn. (5).

$$f_i(\vec{x}+\vec{v_i}\delta_t, t+\delta_t) = f_i(\vec{x},t) - \boldsymbol{M}^{-1}\boldsymbol{C}\boldsymbol{M}\left[f_j(\vec{x},t) - f_j^{eq}(\vec{x},t)\right] \tag{5}$$

In this equation, $\boldsymbol{M}$ is a transformation matrix which transforms a vector in the velocity space into the moment space, $\boldsymbol{C}$ is a diagonal matrix which stores the relaxation time in each direction. This model is more stable compared to the BGK collision model, but the transformation between the discrete velocity space and moment space makes it slightly more computational expensive. Zhang et al. [24] applied this MRT model in their study on the influence of temperature dependent wettability on boiling heat transfer and found out that when the wall superheat is low, heat transfer is faster on hydrophobic surfaces, whereas in high wall superheat region, heat flux is higher on hydrophilic surfaces. Li et al. [25] solved for the boiling curve with a combination of MRT and an improved pseudopotential approach, and successfully reproduced the three boiling stages with their model.

Gong et al. [26] derived a source term which incorporates phase change (liquid-vapour phase change) and plugged it into the temperature distribution function. This reduces the computational cost by eliminating the time derivative of density term. Subsequently, they numerically investigated bubble nucleation, growth and departure under different heating conditions during pool boiling [27]. Sun et al. [28] carried out simulations on a similar problem but during flow boiling, and numerically related bubble departure diameter and frequency to the flowing velocity of the fluid.

2.1.3 Finite Element Method (FEM)

As one of the most popular approaches of numerical simulation, FEM can also be used to solve some of the fluid mechanics problems. It shows great performance in solving fluid flow and heat transfer problems, even with complex geometries. However, it struggles when solving nonlinear partial differential equations, such as the Navier-Stokes equations, thus instability and divergence problems can arise as a result.

The basic mechanism of FEM can be summarized as follows:

1. The given domain is discretized into small and simple domains called finite elements. Thus, the geometrical complexity of the domain and the difficulty of evaluating the variation inside the domain are mitigated.
2. Each element is analyzed, and functions containing variables are derived. These functions are often in the form of algebraic equations. Apart from the geometry, number of nodes is also a determining factor of these approximation functions [29].
3. The elements are assembled and functions that can represent the original domain is obtained.

For years, FEM and FVM have been two popular numerical methods for CFD simulations. Thus, the comparison between the performance of these two methods drew big research interests. Jeong et al. [30] solved a 3-D incompressible laminar flow problems with FEM and FVM commercial codes, respectively, and found out that the FEM codes are more sensitive to the mesh type and quality, whereas the FVM codes had much shorter computational time. However, in the work of Gohil et al. [31], they claimed that the FEM they used is 20 times faster than the FVM on unstructured meshes. A possible reason would be that the mass and momentum equations were coupled in FEM, whereas in FVM, a decoupled pressure correction strategy was applied. An earlier study from Ahmad et al. [32] on macrosegregation indicates that both methods show great performance but suffer from instabilities in different zones.

A relatively new FEM approach called Particle Finite Element Method (PFEM) was developed two decades ago [33, 34]. This method combines the mesh-based and particle-based techniques. In PFEM, the mesh is generated based on the distribution of particles, so each node represents a particle. After solving the governing equations with the current mesh in a typical FE style, the position of each mesh node is changed according to the motion equation. Subsequently, remeshing is carried out with the updated positions of the nodes. Due to such Lagrangian description of motion, the convective term is avoided in the PFEM governing equations and material derivatives are reduced to time derivatives, making PFEM quite suitable for situations where the history behaviours of a material matter a lot [35]. Benefitting from both mesh-based and particle-based features, PFEM has great accuracy and robustness, as well as the ability to track free surfaces. However, its performance can be severely affected if the discretized domain undergoes large deformation. Aubry et al. [36] solved heat convection problems with incompressible flows with PFEM. Bravo et al. [37] solved transport problems of sediment which are multiphysics with solid-fluid interaction with PFEM.

In recent years, FEM is more and more used in combination with CFD methods to solve problems with structure-fluid interaction [38-40] and solid particles in fluid [41]. In this case, the domain is partitioned into solid and fluid domains, and these two types of domains are simulated by FEM and CFD methods, respectively. Finally, the interactions are evaluated by a coupling method (either one-way or two-way) to obtain a final simulation result.

2.2 Simulation Process in General

2.2.1 Simulation concepts and procedure

Like other computer modelling processes, the simulation of quenching numerically analyses a physical process and predicts its results by solving equations established based on the understanding of the physical process. Figure 4 shows a diagram of the phases involved in a general computational modelling or simulation process proposed by Obrkampf et al. [42]. In this diagram, the solid lines indicate using the results of the current step as the input of the next step, and the dash lines indicate making adjustments to the previous step according to the results of the current step. Model verification depicts the process of checking whether the programmed model is in good correspondence with the conceptual model, i.e., whether the unknown properties in the conceptual model will be solved by proper equations and solution methods. Model validation refers to comparing simulation results with experimentally measured values to check the accuracy and performance of the computational model.

However, the procedure described by Figure 4 is only valid for the analysis of an isolated or a simple process. As mentioned previously, a typical quenching process is involved with multiple physical fields and the complicated interactions between each two of them. Therefore, in the case of simulation of quenching, the procedures in Figure 4 need to be implemented once for each physical property of interest, then the interactions between each two of them are evaluated based on the results. Finally, a thorough and reliable prediction coupling all the factors can be made.

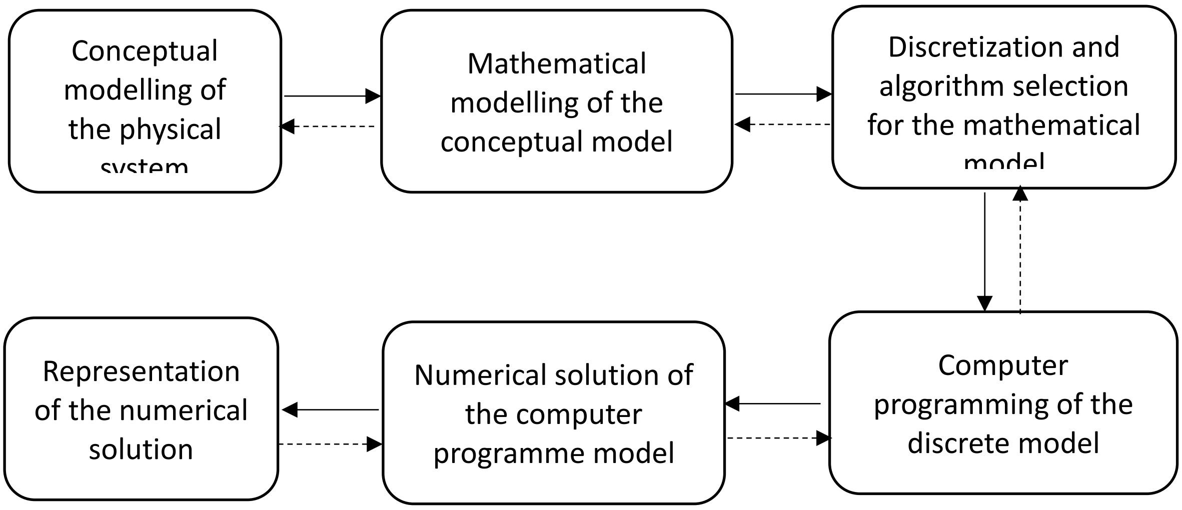

Figure 4 Proposed phases for computational modelling and simulation [42].

2.2.2 Error Analysis and visualisation

During the model validation process, it is important to evaluate the error of the model by numerically evaluating the difference between simulation results and experimental data. The error can be reflected by relative average error which is calculated by Equation (6).

$$\chi = \frac{\sum_{i=1}^{N} \frac{\left|\varphi_{sim} - \varphi_{exp}\right|}{\varphi_{exp}}}{N} \tag{6}$$

Different types of error could be introduced to the model from different sources, and they affect the accuracy of the results in multiple ways. Generally, the sources of error are two types of uncertainties, aleatory and epistemic uncertainty. Aleatory uncertainty refers to the natural stochasticity of the analysed physical system or environment, and it's irreducible due to its nature [42]. Typically, it's evaluated by cumulative distribution functions (CDFs) or complementary CDFs (CCDFs) [43]. Epistemic uncertainty is a reducible uncertainty which originates from a lack of knowledge possibly involved with any phase or activity mentioned in Figure 4 [42, 43]. The evaluation of epistemic uncertainty is much more complicated than aleatory uncertainty. Most applicable mathematical methods, including interval analysis, possibility theory, evidence theory, and probability theory, require a group of CDFs and CCDFs which are derived from the uncertainty [43].

2.2.3 Simulation of Industrial Quenching

Even though a lot of research studies have reported successful predictions on the temperature evolution of quench cooling of laboratory-scale samples, reports on analysis of industrial scale samples cooling are much rarer [44]. Numerical simulation of the quenching process of an industrial-size sample can be extremely time consuming, due to the difficulties in determining estimations and assumptions of numerical parameters in the model [44], as well as a huge increase in the number of elements and nodes of mesh grids. Even with available quenchant data and solid material properties, numerical simulation of industrial workpiece quenching takes great efforts and time [44].

Workpieces for industrial quenching normally have significantly larger size than samples for laboratory quenching. Consequently, the Biot Number of samples for industrial quenching is much larger than laboratory quenching, according to Equation (7). This indicates that heat conduction process in bulk material plays a more important role in the whole cooling process and the temperature gradient induced by the resistance to thermal conduction is no longer negligible. The spatial difference in temperature from surface to centroid of solid leads to different cooling rate and subsequently different microstructure [45]. Such spatial difference in temperature is also the foundation of evaluating the hardenability of a material [46].

$$Bi = \frac{h}{\lambda} L \tag{7}$$

Therefore, in practice, most industrial scale simulations of quenching assume the HTC at solid boundary is constant, and it would not be detrimental to the cooling rate predicted [4]. The reasons of using a constant HTC are:

1. The influence of heat transfer between solid and liquid on the cooling rate of the sample is not profound.
2. The long lasting and intense boiling effect is hard to deal with, and it creates great calculation burden.
3. The fluid flow conditions in the quench tank becomes extremely complicated because of boiling effects.

However, there has not been any report on a proper critical size of the sample beyond which it is acceptable for the researcher to assume a constant HTC. Most of such decisions are made based on the researcher's experience.

Nevertheless, there is no doubt that analysing the fluid flow conditions in the quench tank has great potential in improving the design of quenching parameters and the geometry of a quench tank. The full-scale analysis on the whole fluid domain is usually avoided because of the huge calculation power and memory storage required. In some cases, experimentally measured data is added to the model as supplementary information to simplify the analysis [47].

Efforts have been made to mitigate the huge calculation power burden of large-scale models. One of the feasible methods is to partition the full domain into subdomains which don't have strong interaction with each other. By analysing each subdomain and combining the results, the accuracy is comparable with that of analysing the full domain, but the time and calculation power can be largely saved [47]. Another reported approach is the superposition method used by Jiang et al. [48], where representative elements from each zone of the model are analysed separately, and the resulting data map is propagated to the elements in the same zone via FEM. The final temperature evolution of a certain node is obtained by calculating the summation of the effects of all the elements [48]. The more representative elements analysed, the more accurate is the final prediction [48].

2.3 Heat Transfer Mechanisms

Though the cooling processes for samples of different sizes involve the same physical mechanisms, the predominant mechanism of the cooling rate inside the sample shifts from heat transfer at the solid-liquid interface to a combination of thermal conduction inside the solid domain and the heat transfer at the interface as the size of the workpiece increases. This could be reflected by the increasing the Biot Number as a result of increasing sample size, as previously mentioned.

Bi increases with the size of the workpiece if all other thermal conditions are kept the same. As this number increases, the spatial difference of the temperature inside the solid domain increases accordingly. Therefore, if the sample is large, a high temperature gradient is very likely to form inside the solid domain, resulting in a delayed cooling effect for the centre part of the sample than the near-surface area. The thicker the sample is, the more delayed is the cooling at centroid.

The influence of macro convection and transient heat conduction is dependent on boiling conditions and the geometry of the quench tank [49].

2.3.1 Convection

Convection refers to the mechanism where heat is transferred by the flowing behaviour of the fluid phase. This mechanism is predominant in quenching of small-scale workpieces, because the temperature inside solid reaches homogeneity in a very short time period due to the small thickness of the sample. Thus, thermal conduction heat flux is close to zero because of the absence of a temperature gradient, and convection heat transfer is the rate limiting factor. Nevertheless, as an important boundary condition, convection also plays an important role in the cooling of large-scale workpieces, especially for the positions that are close to solid surface.

Since the solid wall temperature is much higher than the saturation temperature of water before immersion, intense boiling behaviour happens immediately at the interface when the solid is in contact with water. This yields complicated fluid behaviours in a near surface thin film of liquid, which makes the HTC extremely hard to precisely predict. Reynolds number is the key factor in determining the boundary of this thin liquid film. It is calculated by Equation (8). If boiling happens at the same time, vapour Reynolds Number also has a great influence on convective heat transfer, though such influence is often overlooked [50].

$$Re = \frac{\rho \vec{v} L}{\mu} \tag{8}$$

2.3.2 Radiation

Even though the radiative heat flux is a function of solid surface temperature, the radiative heat transfer only makes up a trivial part of the overall heat transfer during quenching. However, in some cases, radiation heat transfer makes a significant part of the overall heat transfer. When the workpiece is transferred from a furnace to a quench tank, the predominant heat transfer mechanism during this process is radiation, because the heat conduction from solid to air is really slow. Therefore, if the sample is kept in the air for a while, its surface is very likely to be cooled via radiation and an initial temperature gradient inside the sample may form. Radiation heat transfer rate is also one of the most predominant factors for solid cooling during film boiling stage [1].

2.3.3 Conduction

Conduction denotes heat transfer that happens at the solid-liquid interface as well as within the solid domain. Transient heat conduction within solid wall and liquid thermal boundary layer is the mechanism that mainly determines the heat transfer rate at solid-liquid interface [49].

At the interface, the heat transfer rate between solid and liquid is dependent on HTC and the temperature difference between the solid wall and fluid adjacent to it. The calculation of HTC is most important in the evaluation of conduction heat transfer rate at interface. Several factors must be taken into account, including the composition and thermal properties of the fluid phase, boiling effect, and the solid surface properties (like hydrophilicity, surface roughness, etc).

The conduction heat transfer rate inside solid domain is highly dependent on the thermal conductivity and the temperature gradient of the solid material. The heat flux due to thermal conduction is calculated by Fourier's Law described in Equation (9).

$$q = -\lambda \frac{\partial T}{\partial x} \tag{9}$$

For simulation of quenching, transient heat conduction problem must be studied because of the time dependency of the solid temperature. Meanwhile, the latent heat released by phase transformation during cooling has a profound influence on the temperature evolution and is usually considered as well [1]. Thus, the three dimensional and time dependent form of Equation (9) is applied to evaluate conduction heat transfer in solid, and it's shown by Equation (10).

$$\rho_s C_{p,s} \frac{\partial T}{\partial t} = \lambda_s \left(\frac{\partial T}{\partial x} + \frac{\partial T}{\partial y} + \frac{\partial T}{\partial z} \right) + S \tag{10}$$

In Equation (10), S is the internal heat source, and is defined as the latent heat of solid phase transformation in most cases. As indicated by Equation (10), the temperature gradient, which is frequently observed in large workpieces, is the predominant factor of determining the cooling rate in solid domain, but the influence of phase transformation latent heat must be considered to obtain an accurate prediction [51].

2.3.4 Conjugate Heat Transfer Study

Conjugate heat transfer is a concept that combines the heat transfer in a solid domain and in a fluid domain at the interface. With simultaneous analysis of both the thermal conduction effect of the solid and the convection effect of the fluid, conjugate heat transfer studies have become the most effective method to solve heat transfer problems between a solid and liquid [52].

In conventional methods, the heat transfer process in either a solid or liquid domain is usually studied separately with simplified thermal boundary conditions, i.e., constant or simple temperature and heat flux input at the interface. On the other hand, in a conjugate heat transfer study, the thermal boundary conditions are derived from the heat transfer mechanisms of the solid and liquid phases in the vicinity of interface. That yields much more accurate thermal boundary conditions, which in turn contribute to better predictions of heat transfer rate between solid and liquid phases.

Conjugate heat transfer problems are solved either by analytical methods or numerical methods. Analytical methods solve the problem based on understanding of a certain heat transfer problem and require complicated mathematical calculations derived on basis of simplifications and assumptions of a real case [52]. Numerical methods are relatively easier to deal with [52], but the calculation results must be carefully ensured to be able to reflect physical reality [53].

Conjugate heat transfer analysis can also be coupled with radiation heat transfer in cases where radiation makes up a remarkable part of total heat transfer. Errera et al. [54] numerically coupled conjugate heat transfer with radiation for a quenching process implemented in transparent medium and grey walls. As shown in Figure 5, there is noticeable difference between the temperature profiles with and without considering the effect of radiation. Though not universally applicable, this model shows the potential to improve the accuracy of conjugate heat transfer analysis by taking radiation heat transfer into account.

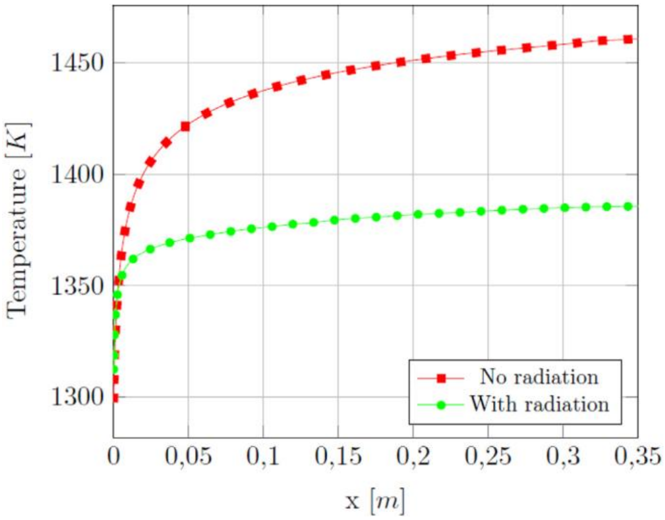

Figure 5 Temperature profiles along the solid-liquid interface [54].

2.4 Boiling Effect

Boiling refers to the phase change of fluid that forms vapour bubbles either on a heated surface or in the liquid where the temperature is above its saturation point [55]. The difficulties of numerical simulation of boiling heat transfer can be attributed to several factors, including solid surface structure, effect of surface tension, discontinuity of fluid properties due to boiling mass transfer, and complicated phase interface dynamics [56].

According to the flow conditions of liquid, boiling can be categorized into two types: pool boiling and flow boiling. Pool boiling refers to boiling that happens under natural convection, whereas flow boiling happens in forced fluid flow adjacent to the heated surface [55]. Flow boiling can be further divided into external flow boiling where the boiling fluid flows over an open surface and internal flow boiling, also known as channel boiling, which is the boiling that occurs inside a channel with flowing fluid [55]. Although the basic physical mechanism is the same for both types, the confinement state of the boiling fluid largely influences the boiling HTC. For example, for flow boiling happens between two heated plates, with a gap size range of 0.6 mm to 5 mm, boiling HTC decreases with an increasing gap size [57].

In the case of an immersion quenching process in water, different boiling behaviours may happen throughout the whole cooling period. Shortly after the sample is fully immersed, the temperature of the solid wall is high enough to favour intense and continuous bubble formation at the interface. These highly concentrated bubbles coalesce and form a vapour blanket that fully covers the solid surface [58]. Condensation also happens continuously at the same time, along with high intensity evaporation [59]. The vapour blanket prevents the contact between the solid and liquid, and it significantly slows down the cooling rate with its low heat transfer coefficient with the solid, resulting in a nearly linear relationship between the solid wall temperature and time [60]. This stage is referred to as film boiling. The temperature distribution close to the solid surface is profoundly influenced by preceding heating as well [61]. As the solid temperature decreases, it gradually falls below the Leidenfrost temperature, then the vapour film becomes discrete and the solid surface is partially in contact with liquid again, known as the re-wetting process. During the re-wetting process, the change in heat transfer coefficient is continuous, and the re-wetting temperature lies between the temperature corresponding to the CHF and the Leidenfrost point [59]. As a result of vapour film breaking up, HTC increases and so does interfacial heat flux. When the heat flux reaches the CHF, bubbles no longer cover the solid surface, and they depart immediately after nucleating at the solid surface. This is known as nucleate boiling, which is the last boiling regime before the wall temperature is cooled below liquid saturation temperature.

To analytically predict boiling heat transfer, the boiling behaviours must be explicitly understood. Mass transfer mechanism is a key factor in determining boiling heat transfer rate. These micro phenomena are important in evaluating the macro heat and mass transfer caused by boiling effects [49, 62]. The predominant microscopic factors are intermolecular adsorption forces, capillary forces, interfacial phase change resistance, and change of phase equilibrium[49].

An early study on the micro mechanisms of subcooled nucleate boiling carried out by Snyder and Robin [63] established fundamental knowledge on bubble formation and growth during nucleate boiling in a microscopic view, as shown in Figure 6. In this study, they stated that the cooling effect in solid material is a result of intense evaporation of the thin fluid layer between bubbles and solid surfaces, and heat is transferred by vapour phase from bottom to the top surface of the bubble and then carried away by turbulent flow through vapour condensation on the top surface of bubble [63].

Two macroscopic parameters that control boiling behaviours are heat flux and temperature. As the critical factor of determining the transition of boiling behaviour, Leidenfrost Temperature is extensively studied. Hsu et al. [58] reported an absence of film boiling during quenching tests for 304 stainless steel and 702 zircaloy spheres in natural sea water. After observing the process with a high-speed camera and comparing the discoveries with quenching in de-ionized water, they conclude the reason is that bubble coalescence is inhibited by dissolved salt in sea water [58]. Though the specific mechanism behind this phenomenon is not clearly stated, they believe that the zeta potential of electrical double layer (EDL) at solid-liquid interface under ultra-high temperature is a major cause [58]. A similar phenomenon was also reported by Firouzi et al. [64], and they attributed it to multiple factors, including colloidal forces, gas solubility, Gibbs-Marangoni effect, surface rheology, and ion-specific effect. Furthermore, they have developed a linear relationship between the transition salt concentration (a critical salt concentration above which 95% of bubble coalescence will be inhibited) and the reciprocal of the square root of bubble size [64]. This correlation is in good agreement with the conclusion of Abdalrahman [65] that Leidenfrost Temperature, HTC and maximum heat flux all increase with increasing electrical conductivity which reflects the salinity of the solution. In addition, the influence of salt mixture is more significant than a single species of salt [65].

Though the higher cooling rate of a salt solution is often desired in industrial production, the corrosion problems significantly limit its application. Apart from salinity, film boiling behaviour is also strongly influenced by the wettability of solid surface according to Vakarelski et al. [66]. It is deemed that hydrophilic surfaces tend to accelerate cooling with a higher Leidenfrost Temperature and consequently a shorter film boiling period, whereas in the case of super hydrophobic surface, film boiling is very likely to be maintained throughout the whole cooling process [66].

2.4.1 Empirical Correlations

Though many developed empirical correlations have been proved to be valid in some cases, significant fluctuations can be observed in their results [67]. Despite the efforts made by many researchers to take other factors like relative humidity into consideration for improved accuracy, the performance of empirical correlations is hardly changed.

In most early studies of empirical correlations, the calculation methods for different boiling regimes are not highly distinguished. Instead, a lot of factors are considered, and complicated correlations are generated. For example, the model developed by Chen [68] combined effects of microscopic and macroscopic boiling heat transfer mechanisms. The evaluation methods for microscopic and macroscopic heat transfer coefficients are described by Equation (11) and (12) , respectively, and the overall heat transfer coefficient is the sum of microscopic and macroscopic heat transfer coefficients [68].

$$h_{mic} = 0.00122\left(\frac{\lambda_l^{0.79} C_{p,l}^{0.45} \rho_l^{0.49} g^{0.25}}{\sigma^{0.5} \mu_L^{0.29} H^{0.24} \rho_v^{0.24}}\right)(\Delta T)^{0.24}(\Delta p)^{0.75} f_{BG} \tag{11}$$

$$h_{mac} = 0.023(Re_l)^{0.8}(Pr_l)^{0.4}\left(\frac{\lambda_l}{D}\right) f_{Re} \tag{12}$$

In Equation (11), f_{bg} is a bubble growth suppression function empirically calculated as a function of the two-phase Reynolds number as described by Equation (13) [68]. In Equation (12), f_{Re} is a Reynolds number factor based on the Martinelli parameter of the boiling effects and is calculated as the ratio of Reynolds number to the Reynolds number of liquid, as shown in Equation (14) [68].

$$f_{BG} = \left(\frac{\Delta T_{eff}}{\Delta T}\right)^{0.24} \left(\frac{\Delta p_{eff}}{\Delta p}\right)^{0.75} \tag{13}$$

$$f_{Re} = \left(\frac{Re}{Re_l}\right)^{0.8} = \left(Re \times \frac{\mu_l}{DJ_z}\right)^{0.8} \tag{14}$$

It should be noted that Equations (11)-(14) are developed in English units.

The predicted coefficients of this model show good agreement with those measured experimentally, and the model is applicable to a decent number of problems. Though the derivation procedure is rather complicated, the actual calculation process is simple and straightforward if the developed correlations are followed. There is no doubt that the development of this model provides valuable insights into contributions of various factors, whether microscopic or macroscopic, on overall boiling HTCs.

Kiyomura et al. [69] developed a rather comprehensive regression model which takes up to 12 parameters into account. Described by Equation (15), this model is reported to generate results within the ±30% error range when compared to experimental data [69].

$$\frac{hL_b}{\lambda_l} = 154\left[\left(\frac{C_{p,l}T_{sat}}{H}\right)^{1.72} \left(\frac{C_{p,l}u_{ref,l}}{k_l}\right)^{-0.34} \left(\frac{D_b q}{\mu_l H}\right)^{0.62} \left(\frac{s}{L_b}\right)^{-0.05}\right] \tag{15}$$

Apart from these properties that appear in Equation (15), other parameters, including gravity acceleration, surface tension and densities of liquid and vapour phases, are also considered at the first place of model development.

Another early method to increase the accuracy of an empirical model is to include as many experimental data points as possible in the regression calculation. For example, Stephan and Abdelsalam [70] created a regression model based on over 5,000 experimental data points and managed to evaluate boiling heat transfer under natural convection conditions. Based on calculation of Nusselts number, the average deviation between predictions of this model and experimental data can be reduced to 11.3% if enough data points are included [70].

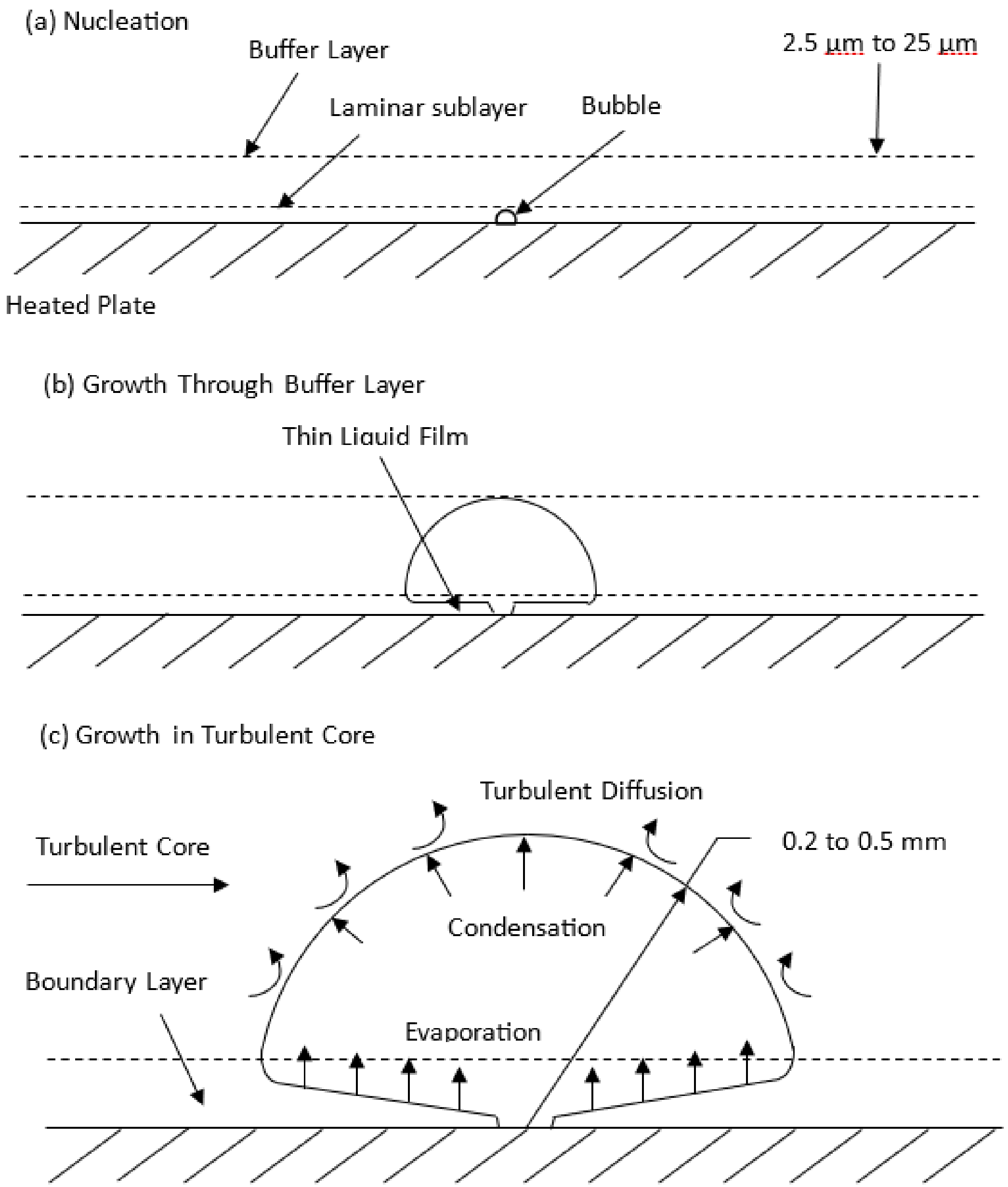

Figure 6 Bubble nucleation and growth [63].

Some correlations are developed focusing on one specific boiling mode. Based on Nusselt's method, Bromley [71] proposed Equation (16) to calculate HTCs for film boiling. Radiation is not considered in this model because of its minor effect on the heat transfer rate.

$$h_{film} = 0.62\left[\frac{\lambda_v^3\rho_v(\rho_l-\rho_v)g\left(H+0.4C_{p,v}\Delta T\right)}{L_b\mu_v\Delta T}\right]^{\frac{1}{4}} \tag{16}$$

In terms of transition boiling, the uncertainty of re-wetting mechanism makes it difficult to directly evaluate heat transfer rate. Therefore, Srinivasan et al. [72] proposed a model that calculates the transition boiling HTC by Newton's cooling law based on the evaluation of heat flux, described by Equation (17).

$$h_{TB} = \frac{q_{TB}}{T_w - T_{sat}} \tag{17}$$

The evaluation of q_{TB} starts from analysing the steady state transition boiling under CHF. The CHF is calculated via Equation (18) according to Zuber's work [73].

$$q_{CHF,sat} = 0.131\rho_v H\left[\frac{\sigma g(\rho_l-\rho_v)}{\rho_v^2}\right]^{1/4} \tag{18}$$

Furthermore, according to Hua et al.[74], in the case of subcooled liquid, the CHF is different due to the fact that bubbles generated by transition boiling effect tend to condensate quickly after formation and consequently generate extra heat flux near the interface. This relationship is described by Equation (19) [74].

$$q_{CHF,subcool} = C_{CHF}q_{CHF,sat}\left(1+0.345Ja/Pe^{1/4}\right) \tag{19}$$

In Equation (19), C_{CHF} is a coefficient ranging from 0.5 to 4.0 that describes the fluctuation of the transient heat flux [75].

Jeschar et al.'s [76] developed Equation (20) to calculate minimum heat flux which is the starting heat flux of transition boiling during cooling.

$$q_{MHF} = C_{MHF}\cdot 0.09\rho_v H\left[\frac{g(\rho_l-\rho_v)}{\rho_l+\rho_v}\right]^{1/2}\left[\frac{\sigma}{g(\rho_l-\rho_v)}\right]^{1/4} \tag{20}$$

In this equation, C_{MHF} is another coefficient of fluctuation ranged from 1 to 10 [75].

Based on the calculation of these heat flux values, overall heat flux of transition boiling is calculated by Equation (21) [75].

$$q_{TB} = q_{CHF} f_{contact} + q_{MHF}(1 - f_{contact}) \tag{21}$$

In this equation, $f_{contact}$ describes the fraction of solid-liquid contact area, and is evaluated by Equation (22) [75].

$$f_{contact} = \mathrm{w} \frac{T_{CHF}}{T_w - T_{CHF}} \tag{22}$$

In most cases, nucleate boiling becomes a predominant heat transfer mechanism when the solid wall temperature is 30-40 K above the saturation temperature [76]. Nevertheless, with proper solid surface configuration and quench medium species, it can start at a higher solid wall temperature and potentially generate high an HTC due to the full contact between the solid and liquid phases. For example, according to Ribatski and Jabardo's research, the boiling heat transfer coefficient becomes higher if a high pressure cooling medium is used [77].

The predominant factors during nucleate boiling are evaporation latent heat, transient conduction happens at solid liquid interface, and convection in liquid domain. A model developed by Chu and Yu [78] predicts the overall heat flux of nucleate boiling based on nucleation site density on solid surface while incorporating the three factors mentioned above, and the calculation method is shown by Equation (23).

$$q = C_{freq}(q_B \cdot t_{BG} + q_{CON} \cdot t_{BW}) + q_{NC} \tag{23}$$

This model has great performance with a relatively low heat flux and contains less empirical constants than other models [78].

2.4.2 Inverse Heat Conduction Problems

Thermal boundary conditions like temperature, heat flux and HTC are usually difficult to measure[79]. Instead, such properties at the surface are usually calculated from the measured temperature at other positions, especially positions that are close to the surface. This is referred to as inverse heat conduction problems (IHCP). By means of FEM, temperature and heat flux at solid surface can be derived from temperature profiles recorded at other positions. A lot of calculation methods are applied in inverse analysis, including sequential function specification, FEM, advance-retreat and golden section method.

Archambault et al. [80] studied the IHCP of quenched steel and aluminium alloy and developed a model that calculates surface temperature and heat flux using the experimentally measured internal solid temperature. In their model, latent heat of phase transformation is also taken into account to reduce error. Later on, in reference [81] they studied the case of one-dimensional heat conduction problem with the same model and discussed the model sensitivity to time step and space. Their analysis show that the accuracy of predicted values is determined by space step whereas oscillation in results is significantly dependent on time step. A two-dimensional inverse heat transfer formulation was developed by Kim and Oh [82] and reported to be capable of calculating HTC at different time and location at the surface. Compared to one-dimensional models, this two-dimensional model provides more details on non-uniform cooling effects [82].

Li et al. [83] carried out a research on IHCP in combination with other calculation methods that evaluates HTC during quenching. In their work, the phase transformation kinetics was determined using FEM, and the spatial discretization method was improved by means of advance-retreat and golden section methods [83].

Modern computer science has also found its applications in simulation of quenching. A method that evaluates boiling heat transfer with imaging information of boiling behaviours was developed by Hobold et al. [84]. This method relies on the application of a neural network to analyse the boiling behaviours and is totally irrelevant with solution of any governing equation. According to Hobold et al. [84], the boiling heat flux is predicted based on bubble morphology, and error of the predicted result is less than 10%.

A study by Bouissa et al. [85] showed another great example of combining artificial neural network (ANN) with simulation of quenching. The study proposed an iterative ANN model that is capable of predicting temperature and HTC profiles by means of FEM. In this model, the initial HTC data used by ANN model is taken from literature, and the corresponding temperature profile is calculated by FEM. The ANN model predicts HTC based on the initial data, then the result is compared with available literature and a mean absolute percentage error (MAPE) value is calculated. If the MAPE does not meet the standard (less than 5% in [85]), the result is fed back into the ANN model as supplementary training data and the model is iterated once again. The corresponding temperature profile of each set of predicted HTCs is calculated via FEM and validated by experimental data. The two curve plots in Figure 7 show the HTCs predicted by ANN model and the corresponding temperature profiles, respectively.

In both figures, the index numbers after ANN indicates the number of iterations. Obviously, the predicted HTC data tend to vary less with an increasing iteration number starting from the third iteration, and the last three sets of data show a highly converging trend. Similar trend is also observed in Figure 8, where the calculated temperature by FEM gets closer to the experimental data as the number of iterations increases. Both figures indicate that this model is quite successful in predicting HTC and temperature profiles of quench cooling. The authors claim that the MAPE of the best prediction of HTC is less than 3.0% [85]. This model illustrates the great potential of applying ANN in simulation of quenching, but still cannot get rid of the dependence on experimentally measured data. However, it is possible that with a sufficient and open database of HTCs measured by other researchers, most cases can be solved without doing extra experiment.

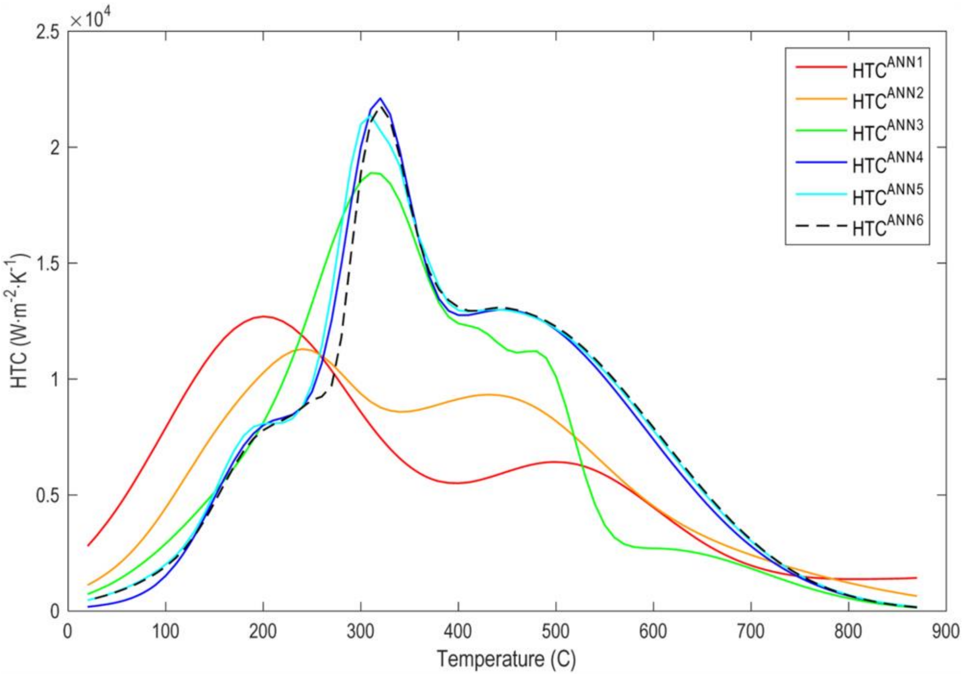

Figure 7 HTCs predicted by ANN [85].

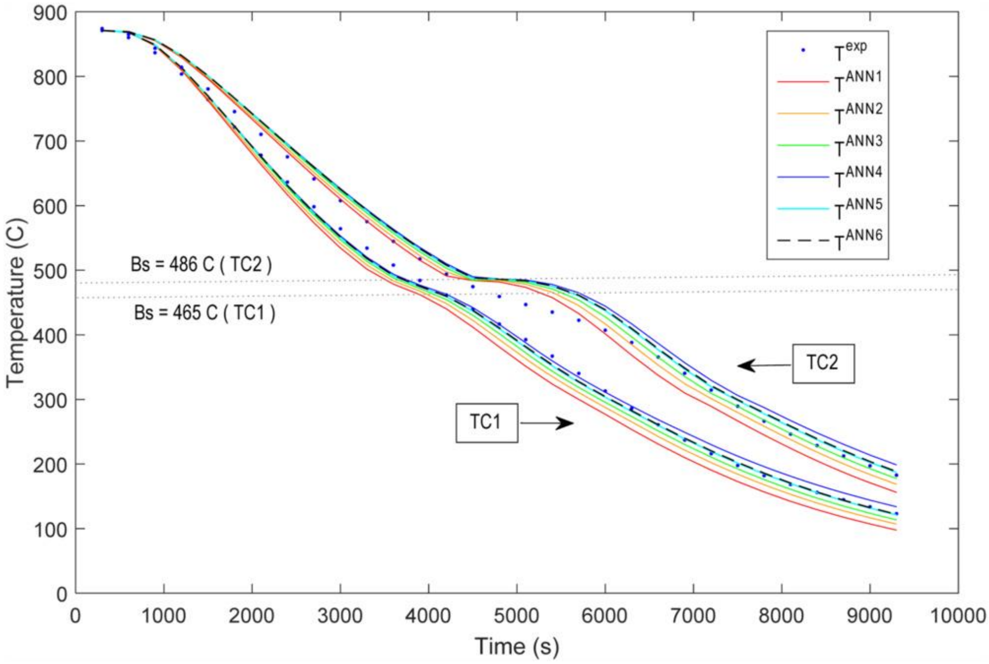

Figure 8 FEM of cooling curves using predicted HTCs [85].

Combined with optimization tools, simulation results can also be used to provide insights for design improvements. For example, De Kock et al. [86] studied a simple two-dimensional continuous quenching process and combined CFD tools with the DYNAMIC-Q optimization method for better operating parameters of a manufacturing process in the design phase. Such optimization is capable of reducing production cost of the process [86].

2.4.3 Mechanistic and Semi-mechanistic Models

The most widely used boiling phase transfer model is the model developed by Lee et al.[87]. It is described by Equation (24).

$$\dot{m}_k = C\alpha_k\rho_k\left(\frac{T - T_{sat}}{T_{sat}}\right) \tag{24}$$

In this equation, C is an empirical coefficient normally set as 0.1 [88-90]. According to this model, if the local temperature of fluid T is greater than saturation temperature T_{sat}, the mass transfer rate to vapour is proportional to supersaturation.

Even though this equation is usually acceptable, the accuracy of this model is not excellent. Among the intensive research carried out, Sun et al. [91] evaluated a heat flux jump phenomenon at interface and determined mass transfer flux accordingly based on Fourier's Law. Equations (25) and (26) calculate the heat flux jump and mass transfer flux, respectively.

$$\Delta q_I = \left[\left(-\lambda_l \frac{\partial T}{\partial n}\right)_l - \left(-\lambda_v \frac{\partial T}{\partial n}\right)_v\right]\vec{n} \tag{25}$$

$$\dot{m}_l = -\dot{m}_v = \frac{(\Delta q_I \cdot \vec{n}) A_{I,\mathrm{c}}}{H V_c} \tag{26}$$

In these equations, the direction of the normal vector $\vec{n}$ is towards the liquid phase. By precisely calculating heat fluxes on both sides of interface, boiling heat transfer is numerically analysed. However, this model has a poor compatibility with most CFD commercial software packages because the boundary of liquid-vapour interface is hard to identify and Equation (25) is consequently difficult to implement. Therefore, a simplified model with improved compatibility is derived from Equation (25) and (26) by Ganapathy et al. [92], as described by Equation (27).

$$\dot{m}_l = -\dot{m}_v = \frac{(\alpha_v \lambda_v + \alpha_l \lambda_l)(\nabla \alpha_l \cdot \nabla T)}{H} \tag{27}$$

However, the accuracy of this mass transfer model is compromised. According to Equation (27) , bubble growth rate has a clear dependency on vapour thermal conductivity κ_v, whereas these two properties are supposed to be irrelevant in reality [91]. Sun et al [93] made modifications on Equation (27) while assuming that thermal conductivity remains the same for both liquid and vapour phases, and proposed Equation (28).

$$\dot{m}_l = -\dot{m}_v = \frac{2\lambda_l (\nabla \alpha_l \cdot \nabla T)}{H} \tag{28}$$

The disadvantage of this model is that the gradient factors indicate that mass transfer happens in a finite thickness region near interface, whereas in real case it only happens at interface. Nevertheless, for engineering applications, this problem isn’t critical, and the model is productive enough.

In addition, Wang et al. [94] assumed that boiling mass transfer rate is proportional to heat transfer rate and developed a correlation accordingly which is described by Equation (29).

$$\dot{m}_v = C_I \cdot C_B \cdot h_B \cdot \frac{A_I (T_w - T_{sat})}{H} \tag{29}$$

In Equation (29), C_B is a boiling correction coefficient and varies with boiling mode, C_m is a closure coefficient which corrects the interfacial area density. For different boiling modes, h_B is also calculated in different ways. This model is capable of modelling different boiling behaviours with only one equation via changing some of the coefficients but is strictly limited to implicit solution methods because the boiling heat transfer coefficient h_b is included in the calculation process.

In 2014, Tanguy et al. [95] developed a two-dimensional model using Level Set/Ghost Fluid methodology which has been proved to be capable of accurately simulating bubble growth controlled by thermal conditions. They also reported that moving bubbles in both spherical and deformed shapes could be successfully simulated [95]. Based on this method, Sahut et al. [96] extended the application to unstructured grids in both two- and three-dimensional problems. With the ability to locate liquid-vapour interface, this method is outstanding in dealing with problems involved with moving interface in unstructured grids as well as complicated geometry, and mass transfer rate is calculated based on surface heat flux [96].

As a critical factor of determining boiling mode, surface heat flux has been studied since decades ago. Das and Punekar [97] succeeded in solving a subcooled boiling flow inside a hot channel with the application of Chen's [68] derivation in a semi-mechanistic model. Another research focused on studying heat flux was carried out by Kobasko et al. [98], where they discovered that initial heat flux density during quenching is much less than critical heat flux density, and the comparison between these two values helps determine the boiling modes. As an important initial condition, initial heat flux determines the boiling mode of the inceptive period, whereas critical heat flux determines the transition from initial boiling mode to film boiling. Therefore, with sufficient critical heat flux, it is possible to avoid film boiling [98]. Another model that evaluates the CHF by analysing the lift-off mechanism, i.e., the mechanism where liquid in contact with heating surface is lifted from surface by a momentum flux of vapour phase, was proposed by Guan et al. [99] as described by Equation (30). Through validation with experimental data, the model is claimed to be able to capture the influence of an increasing pressure on the CHF [99].

$$q_{CHF} = 0.2445\rho_v H \left[\frac{\sigma(\rho_l - \rho_v)g}{\rho_v^2}\right]^{1/4} \left(1 + \frac{\rho_v}{\rho_l}\right)^{1/4} \left(\frac{\rho_v}{\rho_l}\right)^{1/10} \tag{30}$$

A two-phase model which directly evaluates streaming and collision effects of fluid particles instead of solving the Navier-Stokes equations was developed by Tentner et al. [100]. In this model, fluid behaviour is directly analysed considering streaming and collision effects of fluid particles and the corresponding heat transfer mechanism is evaluated based on lattice Boltzmann method [100]. Similarly, Stephan and Hammer [62] predicted nucleate boiling heat transfer based on the micro fluid behaviour caused by bubble generation and bubble departure processes. The input parameters for this model are bubble site density, departure diameters, and thermophysical properties of fluid. With these properties, the influence of bubble curvature, adhesion forces, and thermodynamic equilibrium at liquid-vapour interface are considered [62]. This model undoubtedly emphasizes the importance of micro processes in calculation of macro heat transfer and draws great research interests on micro phenomena that happen during quench cooling. Later, a model proposed by Chien et al. [101] predicts the HTC for pool boiling of various coolant based on the analysis of meniscus thickness, bubble departure diameter, and bubble growth kinetics and the results had a mean square deviation of less than 20%.

A more detailed study on forces applied on a bubble was carried out by Colombo et al. [102], and their analysis is shown in Figure 9. In this figure, F_{st} is surface tension, F_b is buoyancy force, F_{qsd} is quasi-steady drag force, F_{sl} is shear lift force, F_{du} is the unsteady drag force induced by asymmetrical bubble growth, F_p is hydrodynamic force, F_{cp} is contact pressure force [102]. The hydrodynamic force balance consists of the forces mentioned above, together with gravity acceleration and fluid flow acceleration. In the proposed model, the total heat flux at interface is partitioned into four parts: heat flux caused by evaporation, solid surface re-wetting caused by bubble departure, pure convection of liquid phase in regions not affected by boiling, and convection heat transfer between solid and vapour phases where bubble is generated and in contact with solid surface [102]. Though the evaluation of each factor is derived from empirical relations [102], the analysis of hydrodynamic force balance of a bubble helps improve the accuracy and reliability of the evaluation of the contribution of each factor.

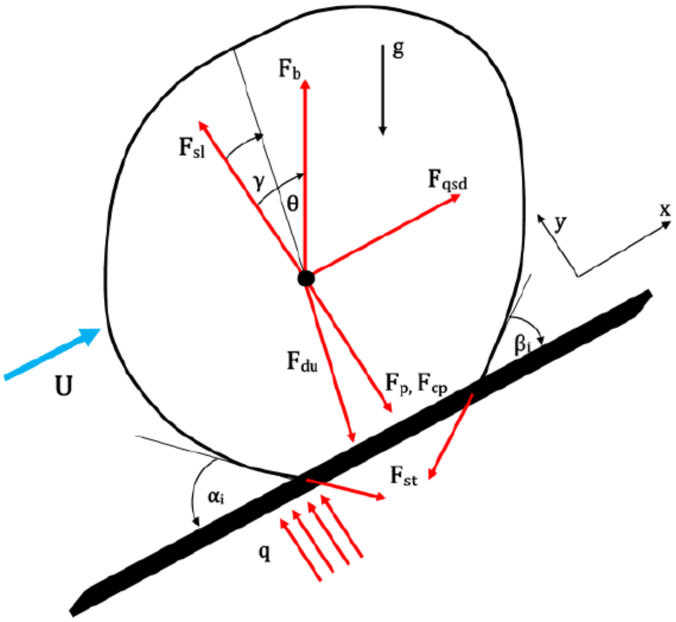

Figure 9 forces acting on a bubble at the nucleation site [102].

2.4.4 Factors Influencing Boiling Effect

Apart from sample geometry and physical properties of fluid, boiling behaviour can also be influenced by solid properties, especially solid surface properties. Marto and Rohsenow [103] review work of other researchers and stated that some solid surface properties, including surface material, surface roughness and contact angle, have profound influence on bubble nucleation. Regarding the critical heat flux which is one of the determining factors of boiling, the effect of heater wall thickness was reported by Tachibana et al. [104]. This statement is supported by Guglielmini and Nannei [105] who have also established a relationship between solid surface thermal diffusivity and the critical thickness below which CHF is influenced by wall thickness. In addition, Paz et al. [106] argue that models which take both solid surface roughness and solid thermal diffusivity into account have improved prediction of heat flux as a function of wall temperature.

Despite the amount of research done to study the influence of solid properties on boiling effects, strong quantitative correlation has not been reported. One of the main reasons would be the fact that solid surface properties can significantly evolve during boiling because of surface oxidation, ageing, and strain. Nevertheless, high roughness arguably increases the bubble nucleation rate and consequently leads to more intense boiling effect.

In a microscopic view, boiling behaviour is heavily dependent on the physical systems around bubbles and the thin liquid layer at solid-liquid interface. Kern and Stephan [107] analysed the pressure balance of a bubble near solid liquid interface, as shown in Figure 10 and stated that external forces can cause shift in saturation temperature of fluid.

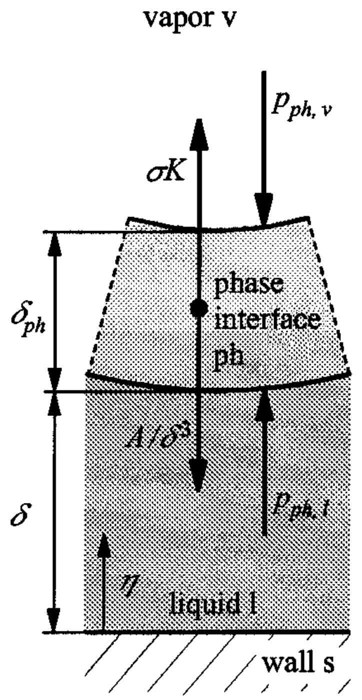

Figure 10 Microscopic pressure balance of a bubble near solid liquid interface [107].

Over the last three decades, the use of nanofluids in cooling systems has been introduced for better cooling performance, and a number of studies have been carried out. According to Kamatchi and Venkatachalapathy [108], using nanofluid for quenching can promote boiling CHF due to the deposition of nanoparticles on the heating surface. The particle species and its volume fraction mainly dominate the cooling process [109, 110], but other factors such as preparation methods and thermal transport properties of nanofluids also have an influence on boiling CHF [108]. For better cooling performance, smaller size nanoparticles are often preferred.

When a sample is quenched in nanofluids, the nanoparticles deposit on the solid surface form a porous layer which increases solid surface roughness and reduces the contact angle between solid and liquid [109, 111]. This is also the reason why film boiling is very likely to be avoided if a sample is repetitively quenched in a nanofluid [109, 110]. If not avoided, film boiling heat transfer in nanofluids is almost the same as that in pure water [110]. Liquid subcooling is a key factor of destabilization of vapour blanket caused by particle deposition for quenching in nanofluids [110].

Kim et al. [111] claimed that optimum CHF is often achieved at low nanoparticle concentrations (<0.1% by volume) which is in good agreement with the conclusions of [108]. They have also experimentally characterized the quantitative relationship between solid surface contact angle and CHF, and the results are shown in Figure 11 [111]. In this figure, DNB stands for Departure from Nucleate Boiling, which marks the existence of CHF. As the contact angle decreases from π/2 to π/8, the CHF increases by almost 100%, and the cooling performance is significantly improved. Therefore, specifying the correct contact angles for solid surfaces in a CFD model is very important in getting more accurate cooling predictions [6]. However, nucleate boiling heat transfer is hardly influenced by nanofluid [109].

Similarly, surface modifications that increase the surface roughness could also improve cooling performance. Such modification methods are not limited to pre-quenching artificial modifications, but also include surface evolution caused by quenching itself. Lee et al. [112] characterized the surface morphology of copper specimens under three different states:

a) as-received
b) being quenched for 15 times as received
c) being oxidized for two hours at 500 ℃ and then quenched for 15 times

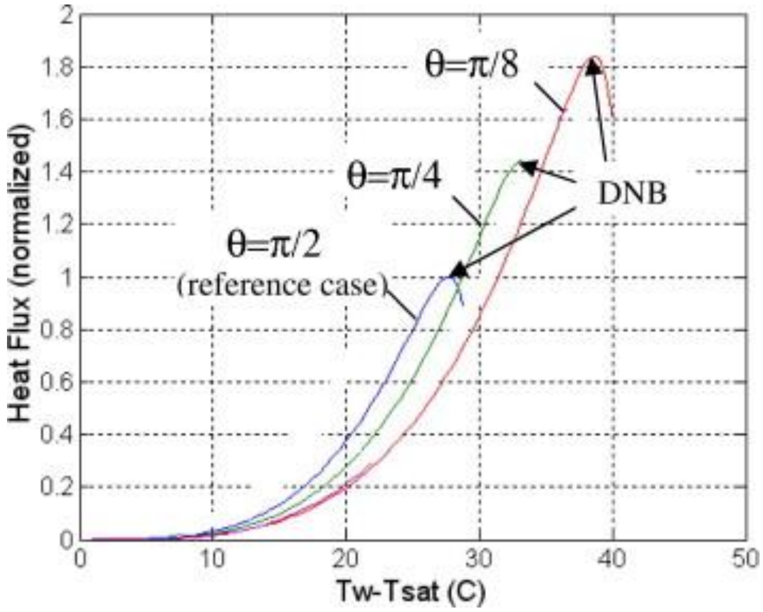

Figure 11 Heat flux vs. temperature curves for different contact angles [111].

The results are shown in Figure 12. It can be clearly seen from the figures that the surface morphology of the as-received sample has changed dramatically after 15 times of quenching and large pits are formed at the surface [112]. The average size of the pits is significantly increased if the specimen is oxidized prior to quenching.

Due to the effect of convective heat transfer, the HTC and CHF on a structured surface is significantly higher than on a smooth surface [113]. With increasing pore radius and density, the CHF and Leidenfrost temperature increase significantly [114]. According to Krause et al. [115], Leidenfrost temperature can shift as much as 175 ℃ on a micro/nano-structured surface comparing to a smooth surface. However, surface roughness and porosity do not have noticeable effect on film boiling heat transfer [114]. Moreover, the influence of surface roughness on boiling heat transfer becomes much less significant when surface roughness exceeds a critical value, according to the evaluation carried out by Kim et al. [113] based on capillary wicking effect. In addition, with different species of cooling medium, the influence of pressure, surface material and roughness on nucleate boiling heat transfer varies [77].

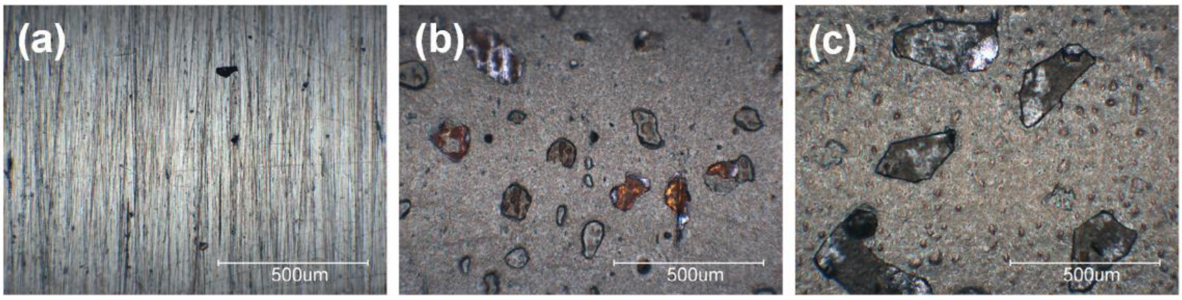

Figure 12 Oxidation Surface morphology of copper specimens: (a) as-received, (b) after 15 quenching using as-received one, (c) after 15 quenching using two hour oxidized one [112].

Apart from water-based quenchants, oil coolants are also commonly used in industrial quenching. It is well acknowledged that cooling rates of oil quenchants are less than that of aqueous quenchants. Even though aqueous solutions have a larger contact angles than oil, the influence of much greater viscosity of oil is the predominant factor in determining cooling rate [116]. Different types of oil, including various mineral oils and vegetable oils, have different HTCs and heat fluxes during cooling, but the difference is much smaller comparing to the difference between oil and water [116].

In terms of other polymer coolants, Bertsch et al. [117] analysed the performance of R-134a and R-245a by experimentally measuring their HTCs during cooling. It is found that the difference in heat flux and vapour volume fraction contribute most to the HTC difference, whereas saturation temperature and mass flux only have trivial influence in the case of microchannel boiling [117].

Mainly under the effects of gravity, the orientation of quenched surface also has a profound influence on boiling heat transfer rate. Such effect is predominant in low heat flux region, whereas in high heat flux region, it becomes almost negligible [118]. Nishikawa et al. [118] attributed such phenomenon to two mechanisms:

1. Rising bubbles break the thermal fluid layer and force the heat transfer between solid and liquid to happen.
2. Heat is transported by evaporation latent heat of the thin liquid film between rising bubbles and solid surface.

Different temperatures of quench mediums can also result in different cooling rate, especially if the quenched part has relatively thick sections. Zhu et al. [119] carried out a series of simulations for cooling of Al7055 thick plates in water with temperature ranged from 20 ℃ to 80 ℃, and the results are shown in Figure 13 and Table 1. It could be clearly observed from Figure 13 that in both cases the final temperature of the workpiece is uniform and equal to the quench medium temperature after 70 seconds.

However, after 6 seconds of cooling, there is huge difference between the solid temperatures for both cases, and the spatial temperature difference inside the plate is also increased if the quench medium temperature is higher. This could be attributed to the heat transfer coefficient difference shown in Table 1. The HTC of cooling in 20 ℃ water is more than two times of that of cooling in 80 ℃ water. This induces the big difference in the solid temperature between the two cases at 6 seconds. Analysing the spatial difference of temperature inside solid material is essential for predicting the distribution of residual stress after cooling, and is critical in evaluating the subsequent machining distortion, especially for thin-walled parts [119].

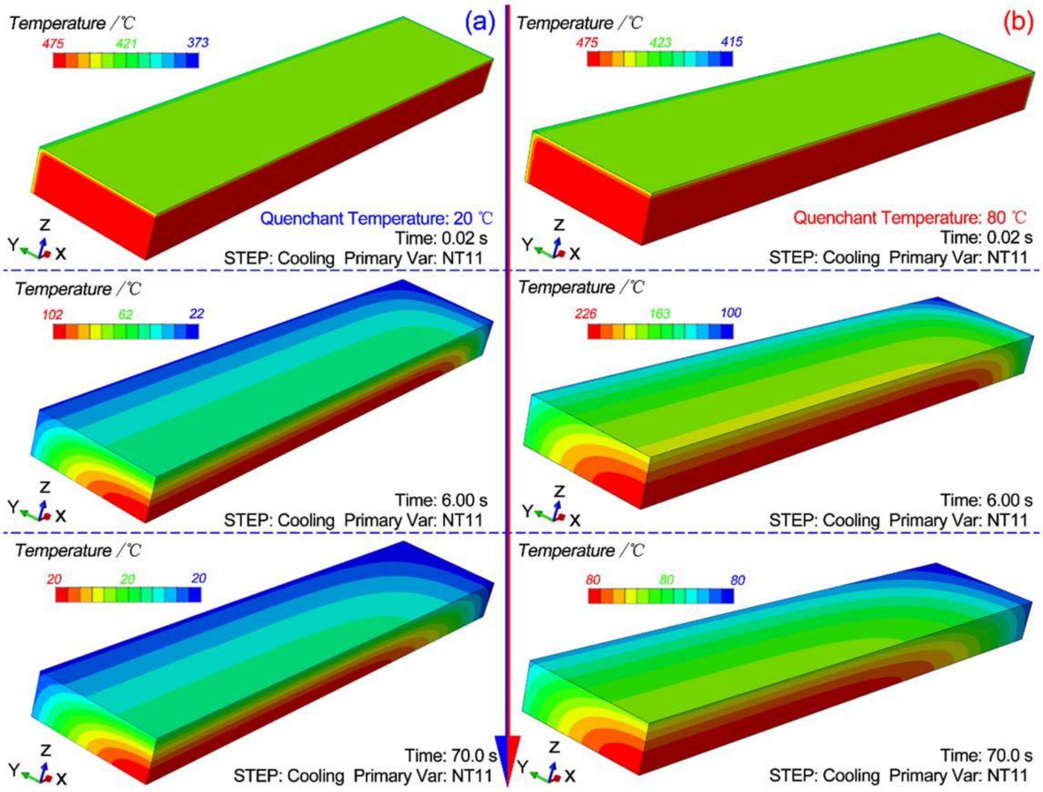

Figure 13 Temperature fields evolution in the quenching process of thick plates at different medium temperatures of (a) 20 °Cand (b) 80 °C [119].

Table 1 The average heat transfer coefficients corresponding to different quenching medium (water) temperatures [119].

Temperature (℃)	20	40	60	80
Heat Transfer Coefficient (W·m-2·℃-2)	26000	20500	17500	9500

However, for oil quenchant, the influence of the quenchant temperature on the cooling rate can be right the opposite. As shown in Figure 14, for both types of oils, the HTCs increase with increased quenchant temperature [120]. Such effect is most obvious around the HTC peak during cooling, whereas it’s almost negligible at very low and high temperature ranges. For oil coolants, the cooling performance also changes after a long time of using [120]. According to Figure 15, the HTC of oil A is increased after 2 years of utilization, but for oil B, the HTC is decreased. Such phenomenon has not been clearly explained yet. However, considering the highly random nature of HTC during quenching, attributing such performance difference to material properties is not convincing enough. Whether it's a result of random error or not, further investigation is needed.

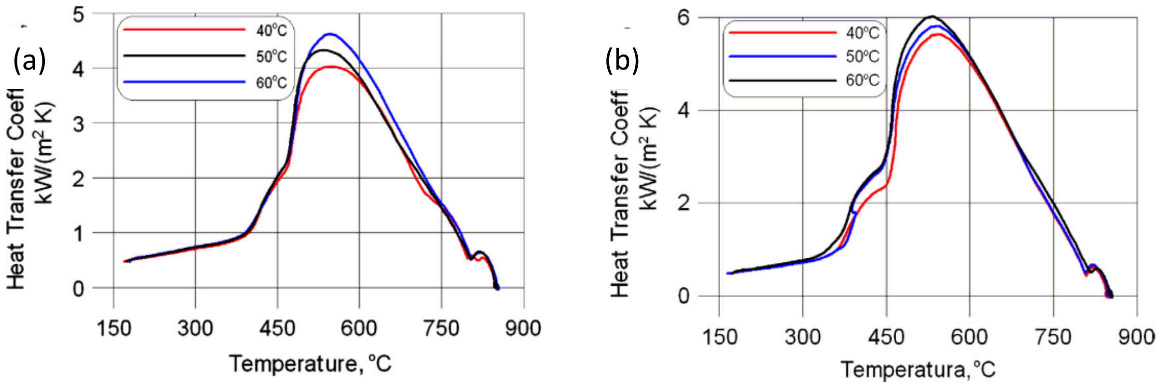

Figure 14 HTC as a function of wall temperature for different quenchant subcooling (a) Oil A, (b) Oil B [120].

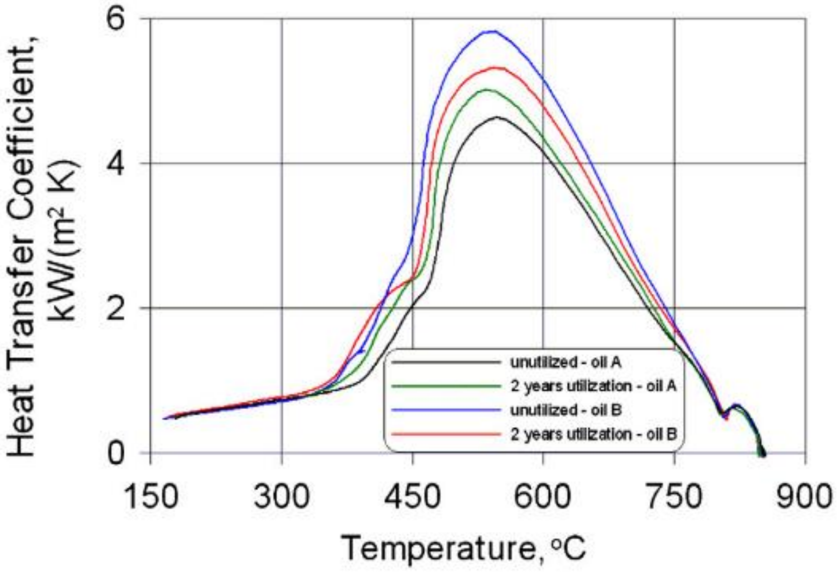

Figure 15 HTC vs. wall temperature for aged and non-aged quenchants [120].

2.5 Solid Phase Transformation

In the energy governing equation, the internal heat source term is defined as the latent heat released by phase transformation that occurs during quenching process. Estimation of phase transformation latent heat is of vital importance in correctly predicting the temperature evolution of a quenched part. Latent heat of phase transformation is calculated by Equation (31).

$$\dot{E} = H_s \frac{\Delta \xi_k}{\Delta t} \tag{31}$$

Equation (31) needs to be integrated over time and the total amount of a new phase k is required. However, clearly specifying the eventual phase composition is another major challenge for simulation of quenching, mainly due to the strong interaction among the physical mechanisms, insufficiency of knowledge with respect to materials physics, and unsatisfactory quantitative model.

One of the most basic and widely used methods of predicting solid phase and microstructure evolution is based on the inverse application of Scheil's additivity rule. Isothermal parameters of a material could be obtained from a continuous cooling transformation (CCT) diagram or a time temperature transformation (TTT) diagram. The parameters obtained from CCT diagrams are believed to be superior to TTT diagrams because of their lower sensitivity to overlapping transformations [1]. Meanwhile, since the isothermal transformation mechanisms described by TTT diagrams are not practical in industrial production, CCT diagrams are more commonly used in practice. Nevertheless, predictions based on CCT diagram are still far from reality because of the cooling rate variation in practice. It has been reported by Leblond et al. [121] that two cooling processes with the same cooling period, initial temperature and final temperature but different temperature evolution would have the same amount of phase transformed, which is in contradiction with CCT diagrams.

Prediction of final harness distribution in the sample is usually made based on predicting final phase composition while considering the influence of alloy elements [45, 122]. Parameters of subsequent heat treatment also play an important role in such evaluation process [45]. It is reported that after a very short period of isothermal holding, the average grain size is proportional to $t^{1/2}$ [122].

To precisely evaluate phase transformation results, quantitative models must be applied depending on the phase transformation mechanism. Preceding heat treatments like heating and holding also need to be considered if it has strong influence on the phase transformation happens during subsequent quench cooing process. In the case of steel quenching, simulation of austenite formation based on nucleation and growth kinetics during heating and holding processes can contribute to a better prediction of the final phase distribution [51, 123].

2.5.1 Diffusional Transformation

Diffusional transformation is also known as reconstructive transformation and refers to the transformation that forms a new phase which is different in composition. This process relies on long-distance atomic transportation in solid domain. The basic principle for most models studying diffusional transformation is the Avrami relationship described in Equation (32).

$$\xi_k = 1 - \exp\left(-\omega_k t^{n_k}\right) \tag{32}$$

This equation is applied in combination with Scheil's additivity rule. For each time step, parameters are extracted from the CCT or TTT diagram and the amount of transformed phase is calculated accordingly. However, in this way, anisothermal processes like industrial quenching are evaluated by the parameters of isothermal process, which is a source of error.

Starink [124] eliminated the time dependency of ξ_k while calculating transient phase transformation rate $\dot{\xi_k}$ by Equation (33) by means of Taylor expansion. This model is based on modifications of the Avrami equation and deals with phase transformation of a mixture of phases without reaching saturation [124].

$$\dot{\xi_k} \approx \omega n \left(\frac{\xi_{k,eq} - \xi_k}{\xi_{k,eq} - \xi_{k,0}}\right)^{1+\frac{r-1}{n}} \left(\frac{\xi_k - \xi_{k,eq}}{\xi_{k,eq} - \xi_{k,0}}\right)^{1-\frac{1}{n}} \tag{33}$$

2.5.2 Non-diffusional Transformation

Instead of composition, non-diffusional transformation (a.k.a. displacive transformation) only changes the crystal structure of the parent phase. In the case of steel making and quenching, the martensitic transformation is the most important and the most concerned one. It is an athermal process and happens nearly at the speed of sound and releases a huge amount of latent heat and induces significant transformational strain. Equation (34) derived by Koistinen and Margurber [125] is most widely accepted and used in calculating the extent of austenite-martensite transformation.

$$\xi_{mar} = \xi_{aus}\{1 - exp[-C_{mar}(T_{mar} - T)]\} \tag{34}$$

In this equation, C_{mar} is 0.011 K^{-1} for most steels and is independent of composition.

Some factors that potentially affects the martensitic transformation kinetics are summarized by Fernandes et al. [2] as followings:

1. Pre-cooling nucleation that happens at high temperatures
2. Austenite grain size
3. Stress state of the sample
4. Plastic deformation during cooling process

These factors are not numerically reflected in Equation (34), but can be taken into account when necessary [2].

3 Modelling Methods

The modelling and calculation processes of all the models involved in this paper are carried out by the ANSYS software package (v2020 R2, aka v20.2). ANSYS is a well-developed and powerful simulation tool package for a number of engineering problems, including CFD, mechanical analysis, acoustics, electricity, etc. Currently, ANSYS has already been widely used by quite a few industrial manufacturers and engineering consulting companies. However, because the source codes of ANSYS are not fully open to the public, the detailed algorithms of the software can only be obtained via the theory guide published by the company, or from the users' own experience.

In this paper, the geometries of the models are constructed by ANSYS DesignModeler, then the mesh grids are generated accordingly by the ANSYS meshing tool based on the preference of Fluent solver. The material properties, initial and boundary conditions, equations, and other model parameters are specified in Fluent and then the model is solved transiently. Finally, the generated results are visualized and analyzed by CFD-Post.

3.1 Solid Materials Properties

The physical properties of the solid materials are generated by JMatPro according to the averaged composition of the alloys selected. The densities of the materials are assumed to be constant, whereas the specific heat and thermal conductivity are expressed as functions of temperature. The cooling performance of samples made from Inconel 600 and Inconel 718 are studied in this research. Table 2 and Table 3 show the nominal composition of these two nickel-based superalloys, which are also the input of the calculation of JMatPro.

Table 2 Chemical Composition of Inconel 600 [126].

Element	Ni	Cr	Fe	C	Mn	S	Si	Cu
wt%	≥ 72.0	14-17	6-10	≤ 0.15	≤ 1.0	≤ 0.015	≤ 0.5	≤ 0.5

Table 3 Chemical Composition of Inconel 718 [127].

Element	Ni	Cr	Fe	Nb	Mo	Co	Ti	Mn
wt%	50-55	17-21	17	4.75-5.5	2.8-3.3	≤ 1	0.65-1.15	≤ 0.35

Element	S	P	C	Al	B	Si	Cu	Ta
wt%	≤ 0.015	≤ 0.015	≤ 0.08	0.2-0.8	≤ 0.006	≤ 0.35	≤ 0.3	≤ 0.05

The thermal properties of both alloys are calculated as a function of temperature in a range from 298.15 K to 1273.15 K (25 ℃ to 1000 ℃), and polynomial regression is taken for the purpose of inputting the properties into the CFD solver. Equations (35) and (36) are the regression equations of the specific heat and thermal conductivity of Inconel 600, respectively, and Equations (37) and (38) are the expression of the specific heat and thermal conductivity of Inconel 718, respectively. The regression results of the thermal properties of both alloys are plotted and shown by Figure 16 and Figure 17, where R evaluates the overall percent deviation between the regression results and the values derived by JMatPro, calculated as the root mean square error divided by the average of the according property.

$$C_{p,Inconel\ 600} = 1.41 \times 10^{-7} T^3 - 2.54 \times 10^{-4} T^2 + 0.32T + 360.82 \tag{35}$$

$$k_{Inconel\ 600} = -8.06 \times 10^{-10} T^3 - 1.31 \times 10^{-6} T^2 + 0.02T + 8.51 \tag{36}$$

$$C_{p,Inconel\ 718} = 8.05 \times 10^{-6} T^2 + 0.16T + 394.22 \tag{37}$$

$$k_{Inconel\ 718} = -4.28 \times 10^{-8} T^2 + 0.017T + 6.53 \tag{38}$$

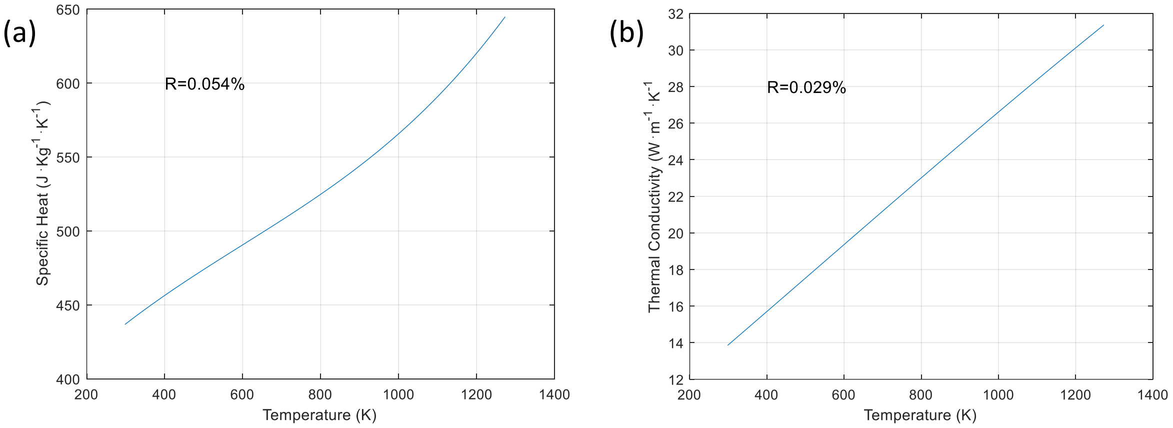

Figure 16 Thermal Properties Regression of Inconel 600 (a) Specific Heat, (b) Thermal Conductivity.

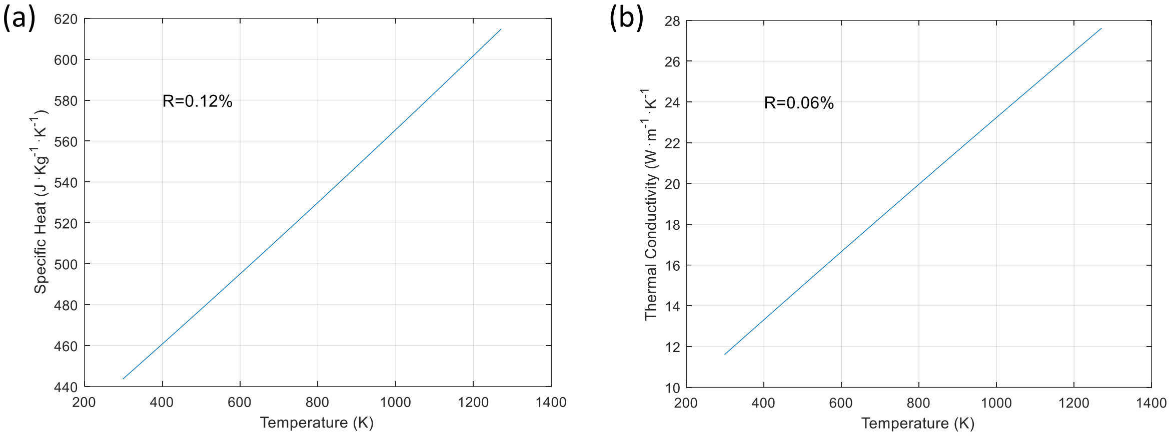

Figure 17 Thermal Properties Regression of Inconel 718 (a) Specific Heat, (b) Thermal Conductivity.

3.2 Single Phase Model

The mathematical logic behind the basic single-phase model reflects the framework of the calculation process of ANSYS Fluent. Meanwhile, in this paper, a model is solved in a single-phase case to illustrate the necessity of taking into account the effect of boiling mass and heat transfer.

3.2.1 Mass Conservation Equation

Equation (39) is a general form of mass conservation equation and it's valid for both incompressible and compressible flows. It is also called a continuity equation.

$$\frac{\partial \rho}{\partial t} + \nabla \cdot (\rho \vec{v}) = S_m \tag{39}$$

3.2.2 Momentum Conservation Equation

Equation (40) is the momentum conservation equation, where p is static pressure, $\rho\vec{g}$ and $\vec{F}$ are the gravitational body force and external body forces, respectively.

$$\frac{\partial}{\partial t}(\rho \vec{v}) + \nabla \cdot (\rho \vec{v}\vec{v}) = -\nabla p + \nabla \cdot (\bar{\bar{\tau}}) + \rho \vec{g} + \vec{F} \tag{40}$$

In this equation, the stress tensor $\bar{\bar{\tau}}$ is defined by Equation (41).

$$\bar{\bar{\tau}} = \mu_{mol}\left[(\nabla\vec{v} + (\nabla\vec{v})^T) - \frac{2}{3}\nabla\cdot\vec{v}I\right] \tag{41}$$

3.2.3 Energy Equations in Fluid Regions

The generic form of the energy equation solved by the solver is shown as Equation (42).

$$\frac{\partial}{\partial t}(\rho E) + \nabla\cdot\big(\vec{v}(\rho E + p)\big) = \nabla\cdot\left[\lambda_{eff}\nabla T - \sum_{k} Hs_k\vec{J}_k + \big(\bar{\bar{\tau}}_{eff}\cdot\vec{v}\big)\right] + S_E \tag{42}$$

In this equation, λ_{eff} is calculated as the summation of the liquid thermal conductivity and the turbulent thermal conductivity, and it depends on the turbulence model in use. The three terms in the bracket on the right-hand side of the equation represent the influence of thermal conduction, species diffusion, and viscous dissipation, respectively. Since the models in this project only deal water quenching problem, the term of species diffusion is negligible. S_E is the volumetric heat source term. More specifically, it represents evaporation latent heat in this project. E is calculated by Equation (43), where T_{ref} is 25 ℃ (298.15 K).

$$E = \int_{T_{ref}}^{T} C_{p,k}\, dT + \frac{v^2}{2} \tag{43}$$

3.2.4 Energy Equations in Solid Regions

Equation (44) is the generic form of energy equation solved for solid regions.

$$\frac{\partial}{\partial t}(\rho\cdot Hs) + \nabla\cdot(\vec{v}\rho\cdot Hs) = \nabla\cdot(\lambda\nabla T) + S_E \tag{44}$$

The second term on the left-hand side of this equation is the energy transfer due to rotational or translational movement of solid. In this study, it is zero because all solids are fixed. The thermal conductivity λ in the first term on the right-hand side of this equation can optionally be specified as a matrix if the pressure-based solver is in use. This provides great potential of studying the quenching of anisotropic solid samples.

3.3 Multiphase Model

To properly simulate the influence of the boiling mass and heat transfer, both the liquid water and the vapour phases have to be considered simultaneously in a multiphase model. One of the Euler-Euler multiphase models, the Volume of Fluid (VOF) model, is applied in the models that consider boiling effects. In the VOF model, both phases are considered to be able to interpenetrate with each other, but the volume of one phase cannot be occupied by the other. Thus, the phase composition of a control volume is described by the volume fraction of each phase, and the volume fractions of both phases must add up to unity.

Various interaction mechanisms between liquid water and vapour phases are also considered in a multiphase model. The interactions include mass transfer (mainly due to boiling), surface tension at the liquid-gas interface, flowing interactions, buoyancy effect, etc. These mechanisms must be taken into account to ensure an accurate prediction of multiphase flow behaviours, and the modelling methods are introduced in the following sections.

The VOF model is good at tracking the interface between different fluid phases. Such tracking is achieved by solving a modified continuity equation based on Equation (39) for the volume fraction of each phase. For the vapour phase, the modified continuity equation is given by Equation (45).

$$\frac{\partial}{\partial t}(\alpha_v \rho_v) + \nabla \cdot (\alpha_v \rho_v \overrightarrow{v_v}) = S_{\alpha_v} + (\dot{m}_v - \dot{m}_l) \tag{45}$$

Equation (45) is only solved for vapour phase which is the secondary phase in the models. The volume fraction of the primary phase, the liquid phase, is calculated by subtracting the volume fraction of the vapour phase from unity. For control volumes that contain both phases, the overall fluid property is determined by a volume fraction average, described by Equation (46).

$$\phi = \alpha_v \phi_v + (1 - \alpha_v)\phi_l \tag{46}$$

However, in terms of turbulence properties (including turbulent kinetic energy and turbulent kinetic energy dissipation rate), the scalar value is obtained by solving a single set of transport equations and the solution is shared for all the phases. When the VOF model is specified, the solver has to be pressure-based, and the second order implicit time-stepping is not available. In addition, since the volume fractions of all phases in each control volume must add up to one, void cells which do not contain any phase is not allowed. The mesh grids and model set up must be carefully checked to avoid any void cell that may cause the solver to crash.

3.3.1 The Implicit Formulation Scheme

If the time discretization is carried out in an implicit scheme, the time advancement of Equation (45) is described by Equation (47).

$$\frac{\alpha_{v,n+1}\rho_{v,n+1}-\alpha_v\rho_v}{\Delta t}+\sum_f\left(\alpha_{f,n+1}\rho_{v,n+1}U_{f,n+1}\right)=\left[S_{\alpha_v}+(\dot{m}_v-\dot{m}_l)\right]V \tag{47}$$

The face values required by this equation are obtained via the spatial discretization scheme determined by the model, which are introduced in section §3.8 .

3.3.2 Momentum Equation

A single momentum equation is solved throughout the whole domain, and the resulted velocity is irrelevant to the phase species. As shown by Equation (48), the momentum equation of the VOF model is almost the same as the single-phase equation. However, some properties used in this equation, $\bar{\rho}$ and $\bar{\mu}$, are the volume fraction average values calculated by Equation (46).

$$\frac{\partial}{\partial t}(\bar{\rho}\vec{v})+\nabla\cdot(\bar{\rho}\vec{v}\vec{v})=-\nabla p+\nabla\cdot\left[\bar{\mu}(\nabla\vec{v}+(\nabla\vec{v})^T)\right]+\bar{\rho}\vec{g}+\vec{F} \tag{48}$$

3.3.3 Drag Force

As part of the force balance of a bubble, a drag force is applied when the bubble moves in the liquid phase. The differential form of the bubble force balance is given by Equation (49).

$$\frac{du_b}{dt}=F_D(u-u_b)+\frac{g_x(\rho_v-\bar{\rho})}{\rho_v}+F_x \tag{49}$$

In this equation, F_x is a term of additional acceleration caused by body force, $F_D(u-u_b)$ is the term for drag force given by Equation (50).

$$F_D=\frac{3C_D}{4D_b}|u_b-u| \tag{50}$$

3.3.4 Virtual Mass Force

The virtual mass force is a part of the force balance of a bubble and is reflected by the F_x term in Equation (49). Since the density of the primary phase (liquid water) is much larger than that of vapour bubble, the effect of this force is important. It is expressed by Equation (51).

$$F_{VM} = \frac{1}{2}\frac{\bar{\rho}}{\rho_v}\frac{d}{dt}(u - u_b) \tag{51}$$

The virtual mass force is generated by the phenomenon that the fluid phase is accelerated to occupy the vacancy left behind by a moving bubble. An additional force is generated due to the acceleration of the fluid phase as a result of the virtual mass force, and its calculation is described by Equation (52).

$$F_p = \frac{\bar{\rho}}{\rho_v} u_{b,i} \frac{\partial u}{\partial x_i} \tag{52}$$

3.3.5 Energy Equation

The energy equation solved for the VOF model is almost the same as Equation (42). The only difference is that it doesn't contain the species diffusion and viscous dissipation terms, as shown by Equation (53).

$$\frac{\partial}{\partial t}\left(\bar{\rho}E_{vof}\right) + \nabla \cdot \left(\vec{v}\left(\bar{\rho}E_{vof} + \bar{p}\right)\right) = \nabla \cdot \left(k_{eff}\nabla T\right) + S_E \tag{53}$$

In addition, the energy E in the equation is treated as a mass average of both phases, described by Equation (54).

$$E_{vof} = \frac{\alpha_v \rho_v E_v + \alpha_l \rho_l E_l}{\alpha_v \rho_v + \alpha_l \rho_l} \tag{54}$$

The energy terms of a single phase (E_v and E_l) are still defined by Equation (43).

3.3.6 Surface Tension

The surface tension is modelled by the continuum surface force model which is proposed by Brackbill et al. [128], and the result is added to the momentum equation as a source term. The pressure drop across the interface depends on both the surface tension coefficient and the surface curvature which is measured by two radii in two orthogonal directions. The characterization of pressure drop is shown by Equation (55).

$$p_2 - p_1 = \sigma\left(\frac{1}{r_1} + \frac{1}{r_2}\right) \tag{55}$$

Thus, with proper representation of the curvature term, Equation (56) is derived.

$$F_{vol} = \sigma_{lv}\frac{\bar{\rho}K_v\nabla\alpha_v}{\frac{1}{2}(p_v + p_l)} \tag{56}$$

In this equation, σ_{lv} is the surface tension coefficient, K_v represents the divergence of the unified volume fraction gradient of the vapour phase, which is defined by Equation (57) [128].

$$K_v = \nabla\hat{n} = \nabla\cdot\frac{\nabla\alpha_v}{|\nabla\alpha_v|} \tag{57}$$

The calculation of the surface tension is more accurate on quadrilateral and hexahedral mesh grids than on triangular and tetrahedral meshes. Therefore, all the models involved in this paper are aimed at having structured mesh grids for the fluid domain, especially in the regions where boiling behaviours are expected to happen.

3.3.7 Contact Angle

The contact angle between the liquid phase and the solid wall is an additional parameter when the modelling of surface tension is enabled. This parameter is used to adjust the surface normal of cells near the solid wall, and subsequently the curvature of these cells. The adjustment method is described by Equation (58) [128].

$$\hat{n} = \hat{n}_w\cos\theta_w + \hat{t}_w\sin\theta_w \tag{58}$$

By combining the Equation (58) with Equations (56) and (57), this adjustment incorporates the influence of contact angle on the surface tension while calculating the surface tension of the surfaces near the solid wall (usually within one or several cells).

3.4 Inclusion of Natural Convection and Buoyancy-Driven Forces

The influence of natural convection is characterized by the value of Rayleigh number, which is calculated by Equation (59). If Rayleigh number is less than 10^8, laminar flow is induced by buoyancy effect. The transition from laminar flow to turbulence occurs when the Rayleigh number is in the range from 10^8 to 10^{10}.

$$\mathrm{Ra} = \frac{g\beta\left(T_w - T_{ref}\right)L^3\rho}{\alpha\mu} \tag{59}$$

In this equation, β is the volumetric thermal expansion coefficient which is generically calculated by Equation (60), and the approximated β value of liquid water is 2.1e-4 1/℃ [129].

$$\beta = -\frac{1}{\rho}\left(\frac{\partial\rho}{\partial T}\right)_p \tag{60}$$

3.5 Boiling Mass Transfer Model

Boiling mass transfer model is applied in the models to evaluate the mass transfer rate from liquid water to the vapour phase and the subsequent bubble growth and departure dynamics. These behaviours occur within a short distance from the solid surface and have significant influence on the local fluid flow conditions.

3.5.1 Evaporation Condensation Model

The evaporation condensation model is a mechanistic model and is one of the most widely used models for engineering applications. This model is originally proposed by Lee [130]. When the fluid temperature is above its saturation temperature, the mass transfer rate from the liquid phase to the vapour phase is described by Equation (61). If the temperature is below saturation temperature, the vapour phase is transferred to the liquid phase at the rate calculated by Equation (62).

$$\dot{m}_v = C_{evap}\frac{\alpha_l\rho_l(T - T_{sat})}{T_{sat}} \tag{61}$$

$$\dot{m}_l = C_{cond}\frac{\alpha_v\rho_v(T - T_{sat})}{T_{sat}} \tag{62}$$

In these equations, the two coefficients C_{evap} and C_{cond} are tuned according to experimental data in a lot of research, but theoretical calculation is also feasible.

The relationship between pressure and temperature under saturation conditions can be described by the Clapeyron-Clausius relationship given by Equation (63).

$$\frac{dT}{dp}=\frac{L}{T\left(\frac{1}{\rho_v}-\frac{1}{\rho_l}\right)} \tag{63}$$

Based on this equation, the variation of temperature and pressure close to the saturation condition is given by Equation (64).

$$p^{*}-p_{sat}=\frac{L}{T(\nu_v-\nu_l)}(T^{*}-T_{sat}) \tag{64}$$

In this equation, p^{*} is the vapour partial pressure at the interface on the vapour side. Meanwhile, the mass transfer flux on an interface based on its kinetic theory is given by the Herts Knudsen formula, as shown by Equation (65).

$$F=C_a\sqrt{\frac{M}{2\pi RT_{sat}}}(p^{*}-p_{sat}) \tag{65}$$

In equation (65), C_a is the accommodation coefficient which describes the portion of vapour molecules that are adsorbed by the interface and is close to 1 at near equilibrium conditions. Combining Equations (64) and (65), the following Equation (66) is obtained.

$$F=C_a\sqrt{\frac{M}{2\pi RT_{sat}}}L\frac{\rho_v\rho_l}{\rho_l-\rho_v}\frac{T^{*}-T_{sat}}{T_{sat}} \tag{66}$$

If it is assumed that all the vapour bubbles have the same or very close diameters, then the interfacial area density can be expressed as Equation (67).

$$\frac{A_I}{V_{cell}}=\frac{6\alpha_v}{D} \tag{67}$$

Therefore, the three-dimensional mass transfer rate can be obtained by combining Equations (66) and (67), as shown by Equation (68).

$$F\frac{A_I}{V_{cell}}=\frac{6}{D}C_a\sqrt{\frac{M}{2\pi RT_{sat}}}L\frac{\rho_l}{\rho_l-\rho_v}\left(\rho_v\alpha_v\frac{T^{*}-T_{sat}}{T_{sat}}\right) \tag{68}$$

Comparing Equations (61) and (68), the expression of the evaporation coefficient can be determined as the form shown in Equation (69).

$$C_{evap} = \frac{6}{D} C_a \sqrt{\frac{M}{2\pi R T_{sat}}} L \frac{\rho_l}{\rho_l - \rho_v} \tag{69}$$

The condensation coefficient can be derived in a similar manner, but the vapour phase, instead of the liquid phase, should be treated as the primary phase in this case. Difference in the accommodation coefficient C_a should also be taken into account. Therefore, the theoretical value of the coefficients of evaporation and condensation are not the same in real case.

It is worth mentioning that the derivation of evaporation coefficient is based on these assumptions:

1) The interface between liquid and vapour phases is flat.
2) Bubbles (secondary phase) are dispersed and have the same diameter.
3) The accommodation coefficient C_a is known.

3.5.2 Other Applied Mass Transfer Models

In this paper, the boiling phase transfer model proposed by Sun et al. [93] is applied via the usage of a user-defined function (UDF). The calculation method of the mass transfer rate is described by Equation (28).

Since this evaluation is based on the gradient of the temperature and the vapour phase volume fraction, three methods of determining the gradient of a scalar value are tested. The methods of determining the gradients are illustrated in §3.10 .

3.6 Turbulence Model

During a quenching process, turbulent flows are generated as a result of immersion of the solid sample and causes varying temperature and velocity of fluid near the solid surface, which has a profound influence on bubble nucleation and departure. The fast-fluctuating velocity field of turbulent flows make it extremely computationally expensive to directly calculate the instantaneous properties from a practical engineering perspective. Therefore, a set of modified equations that are based on time average, ensemble average, or other manipulations are solved to mitigate the heavy calculation burden. However, such modifications can induce additional unknown variables, and a turbulence model is applied to evaluate these variables according to known properties.

In this paper, the Renormalization-group (RNG) k-ε model is used. This model is derived from instantaneous Navier-Stokes equations with a method called Renormalization Group [131]. It is very similar to the standard k-ε model but includes some additional terms and algorithms to analyse a wider range of flows.

In this model, two variables, turbulent kinetic energy k and turbulent kinetic energy dissipation rate ε, are simulated. The turbulent viscosity is calculated by the integration of Equation (70).

$$d\left(\frac{\rho^2 k}{\sqrt{\varepsilon\mu}}\right) = 1.72\frac{\hat{v}}{\sqrt{\hat{v}^3 - 1 + 100}}d\hat{v} \tag{70}$$

The integration of Equation (70) reflects the relationship between the effective turbulent transport and the effective Reynolds number for low-Reynolds-number and near-wall flows. If the Reynolds number is high, the integration yields Equation (71).

$$\mu_t = 0.0845\rho\frac{k^2}{\varepsilon} \tag{71}$$

The turbulent kinetic energy k and its dissipation rate ε are obtained from Equations (72) and (73).

$$\frac{\partial}{\partial t}(\rho k) + \frac{\partial}{\partial x_i}(\rho k u_i) = \frac{\partial}{\partial x_i}\left(C_k \mu_{eff}\frac{\partial k}{\partial x_j}\right) + G_k + G_{buo} - \rho\varepsilon + S_k \tag{72}$$

$$\begin{aligned}\frac{\partial}{\partial t}(\rho\varepsilon) + \frac{\partial}{\partial x_i}(\rho\varepsilon u_i)& \\ &= \frac{\partial}{\partial x_i}\left(C_\varepsilon \mu_{eff}\frac{\partial\varepsilon}{\partial x_j}\right) + 1.42\frac{\varepsilon}{k}(G_k + C_G G_{buo}) - 1.68\rho\frac{\varepsilon^2}{k} \\ &- G_\varepsilon + S_\varepsilon\end{aligned} \tag{73}$$

In these equations, G_k is the evaluation of turbulent kinetic energy generation due to mean velocity gradients and is calculated by Equation (74).

$$G_k = -\rho\overline{u_i' u_j'}\frac{\partial u_j}{\partial x_i} \tag{74}$$

G_{buo} is the evaluation of the generation of turbulent kinetic energy due to buoyancy and is calculated by Equation (75). The influence of G_{buo} on turbulent kinetic energy dissipation rate is evaluated by a coefficient C_{ε} in Equation (73) which is calculated by Equation (76) where $u_{\parallel}$ and $u_{\perp}$ are components of the flow velocity magnitudes that are parallel and perpendicular to the gravitational direction, respectively.

$$G_{buo} = \beta g \mu_t C \frac{\partial T}{\partial x_i} \tag{75}$$

$$C_G = \tanh\left(\left|\frac{u_{\parallel}}{u_{\perp}}\right|\right) \tag{76}$$

In Equations (72) and (73), C_k and C_{ε} are the inverse effective Prandtl numbers which are computed analytically by Equation (77). C_0 is 1.0 for the calculation of C_k and C_{ε}, but the C used in Equation (75) takes the value of $\frac{k}{\mu C_p}$.

$$\left|\frac{C - 1.3929}{C_0 - 1.3929}\right|^{0.6321} \left|\frac{C + 2.3929}{C_0 + 2.3929}\right|^{0.3679} = \frac{\mu_{mol}}{\mu_{eff}} \tag{77}$$

In Equation (73), R_{ε} is a distinctive term of RNG k-ε model which is calculated by Equation (78), where η is an effectiveness factor defined as $\eta \equiv S^{\circ} k/\varepsilon$. This term reflects the influence of the local strain rate of fluid on the turbulent kinetic energy dissipation rate.

$$G_{\varepsilon} = \frac{0.00845 \rho \eta^3 (1 - \eta/4.38)}{(1 + 0.012\eta^3)} \frac{\varepsilon^2}{k} \tag{78}$$

By combining Equation (78) and Equation (73) and merging the terms, the following Equation (79) can be obtained.

$$\begin{aligned} &\frac{\partial}{\partial t}(\rho \varepsilon) + \frac{\partial}{\partial x_i}(\rho \varepsilon u_i) \\ &\quad = \frac{\partial}{\partial x_i}\left(C_{\varepsilon} \mu_{eff} \frac{\partial \varepsilon}{\partial x_j}\right) + 1.42 \frac{\varepsilon}{k}(G_k + C_G G_b) - C_{\varepsilon}^* \rho \frac{\varepsilon^2}{k} + S_{\varepsilon} \end{aligned} \tag{79}$$

C_{ε}^* is defined by Equation (80).

$$C_{\varepsilon}^* \equiv 1.68 + \frac{0.00845 \rho \eta^3 (1 - \eta/4.38)}{(1 + 0.012\eta^3)} \tag{80}$$

If $\eta < 4.38$, C_ε^* becomes larger than 1.68. When the value of η is close to 4.38, the whole term is very close to that of standard k-ε model. In regions where $\eta > 4.38$, R_ε has a positive contribution to the term of $\frac{\varepsilon^2}{k}$, resulting in a higher ε, smaller k, and eventually a reduced effective viscosity. Thus, with the inclusion of the R_ε term in the turbulent kinetic dissipation rate equation, the RNG k-ε model has a better performance while analysing the near-wall rapid flow caused by heated liquid and bubble movement than the standard k-ε model.

3.7 Near-Wall Treatment

Due to the no-slip condition on the solid wall, high fluid velocity gradients related to the distance from the solid wall are often observed in the near-wall fluid regions. As a result, additional turbulent kinetic energy is generated, contributing of higher intensity turbulence. However, it is worth noting that the turbulence generated due to the existence of a solid wall is different from the swirling flows discussed in section §3.6 , so the above-mentioned methods of modelling turbulence is not suitable in the near-wall fluid region. Thus, special treatments for the near-wall regions are developed, and the selections of these treatment as well as the turbulence models are essential for an accurate prediction of the fluid regions influenced by the wall [132]. In this paper, the near-wall treatment is standard wall function which is proposed by Launder and Spalding [133].

To characterize the effective thickness of the near-wall fluid region, a dimensionless distance y^* is applied by the ANSYS Fluent solver. It is calculated by Equation (81).

$$y^* \equiv \frac{\rho C_\mu^{1/4} k_P^{1/2} y_P}{\mu} \tag{81}$$

According to the law of the wall, the dimensionless velocity u^* is in logarithmic relationship with y^*, as described by Equation (82).

$$u^* = \frac{1}{\kappa}\ln(E y^*) \tag{82}$$

This relationship yields the best results in the range of 30 < y^* < 300. Specifically, when y^* is less than 11.225 in the cells adjacent to the wall, the relationship can be further simplified as Equation (83).

$$u^* = y^* \tag{83}$$

The near-wall fluid region is divided in a similar fashion to analyse its energy conditions, i.e., the whole region is divided into two sublayers according to the y^* value and these two sublayers are applied with the linear relationship similar to Equation (83) and the logarithmic relationship similar to Equation (82). In the sublayer that's closer to the solid wall, the predominant heat transfer mechanism is conduction, and the linear law is applied to solve for the energy properties, whereas for a relatively larger distance, high intensity turbulence flow is generated as a result of the large fluid velocity gradient, so the heat conditions are mostly determined by the turbulence properties and the logarithmic law is applied. However, even though the energy properties can be closely related to the velocity field, the critical y^* values that mark the transition between the linear relationship and the logarithmic relationship are different.

The overall expression of the temperature of the near-wall fluid is described by Equation (84).

$$T^* \equiv \frac{(T_w - T_P)\rho c_P k_P^{1/2}}{q} = \begin{cases} Pr \cdot y^* & (y^* < y_T^*) \\ Pr_t \left[\frac{1}{\kappa}\ln(Ey^*) + C_{T^*}\right] & (y^* > y_T^*) \end{cases} \tag{84}$$

In this equation, y_T^* is a critical value of y^* calculated as the interception of the linear law and the logarithmic law. According to the formula developed by Jayatilleke [134], the extra term C_{T^*} is calculated by Equation (85).

$$C_{T^*} = 9.24\left[\left(\frac{Pr}{Pr_t}\right)^{3/4} - 1\right]\left(1 + 0.28e^{-0.007Pr/Pr_t}\right) \tag{85}$$

In terms of the turbulence properties, the overall turbulence model is solved in the near-wall fluid regions with a boundary condition at the wall which is described by Equation (86).

$$\frac{\partial k}{\partial y} = 0 \tag{86}$$

As a result of this boundary condition, the production of turbulent kinetic energy G_k and turbulent kinetic dissipation rate ε are assumed to be equal in the cells adjacent to the wall. These two variables are calculated by Equations (87) and (88), respectively.

$$G_k \approx \tau_w \frac{\partial U}{\partial y} = \tau_w \frac{\tau_w}{\kappa \rho k_P^{1/2} y_P} \tag{87}$$

$$\varepsilon_P = \frac{C_\mu^{3/4} k_P^{3/4}}{\kappa y_P} \tag{88}$$

It must be noted that for the first layer of fluid cells at the solid surface, the turbulent kinetic energy dissipation rate is calculated by Equation (88) instead of Equation (79).

For the best performance of the Standard Wall Function, the following conditions must be satisfied:

a) The turbulent kinetic energy production and dissipation rate are in equilibrium state in the cells adjacent to the wall.

b) The shear conditions do not vary in the region, i.e., the pressure gradient is negligible.

3.8 Spatial Discretization Methods

By default, the scalar values are stored at the cell centroids by the solver, so in order to calculate the transport of a scalar value from a solved cell to an adjacent unsolved cell and to calculate the facial flux of a desired scalar, the face value of the scalar is needed. Such process of determining the face value based on the cell centre value is known as spatial discretization and is accomplished by either First Order Upwind or Second Order Upwind in this paper.

3.8.1 First Order Upwind

In the First Order Upwind Scheme, it is assumed that the value of a variable at a cell centre is the cell-average value, and it’s homogeneous in the entire cell. Thus, the face value of a given variable is equal to the value at the centre of the upstream cell.

When the solver returns unrealistically high value of a variable, such as temperature and turbulent kinetic energy, the First Order Upwind Scheme can be applied to the abnormal variable to avoid instability. However, the variables discretized by this scheme can only reach first order accuracy. In many of models with initial inlet flows, First Order Upwind method is selected as the spatial discretization scheme of momentum.

3.8.2 Second Order Upwind

When higher order of accuracy is desired, the face value of a variable is calculated by a linear reconstruction approach proposed by Barth and Jespersen [135] given by Equation (89).

$$\phi_f = \phi_c + \nabla\phi \cdot \vec{r} \tag{89}$$

In this equation, $\nabla\phi$ is the gradient of the variable at cell centroid of the upstream cell, $\vec{r}$ is the displacement vector from the cell centroid of the upstream cell to the face centroid. This calculation process is known as the Second Order Upwind discretization scheme and is slightly more complicated than First Order Upwind because it requires the gradient of the discretized variable at the upstream cell centroid.

With Second Order Upwind scheme, second order of accuracy can be achieved for the face values of the discretized variable. Since temperature is the most concerned property, this discretization method is the preferred method for temperature discretization in all the models.

3.9 Temporal Discretization

Since the simulations carried out in this paper are transient simulations, the governing equations must be discretized in time as well. Since all the models of this paper apply pressure-based solver, the only temporal discretization method is the Implicit Time Integration, where the temporal variation of a property is evaluated based on the values of the next time step. In this case, the temporal discretization of first order accuracy can be described by Equation (90).

$$\frac{\phi_{n+1} - \phi_n}{\Delta t} = f(\phi_{n+1}) \tag{90}$$

Here, $f(\phi_{n+1})$ incorporates both spatial and temporal difference. Similarly, the second order accuracy form of temporal discretization is described by Equation (91).

$$\frac{3\phi_{n+1} - 4\phi_n + \phi_{n-1}}{\Delta t} = f(\phi_{n+1}) \tag{91}$$

3.10 Evaluation of Gradients

The calculation of gradients of various parameters are needed for not only computing the face values of the scalars, but also for the determination of velocity derivatives and other non-steady transport effects. In this section, three different methods of gradient evaluation are introduced, and their performances are analysed by different models in later chapters.

3.10.1 Green-Gauss Cell-based

According to the Green-Gauss theorem, the gradient of a scalar is calculated by Equation (92). The summation is made over all the faces that enclose the calculated cell.

$$\nabla \phi_c = \sum_f \overline{\phi_f}\, \hat{n}_f \tag{92}$$

In the cell-based method, the face value of a variable is determined by Equation (93).

$$\overline{\phi_f} = \frac{\phi_1 + \phi_2}{2} \tag{93}$$

In this equation, ϕ_1 and ϕ_2 are the values of the scalar at the centroid of the two cells that are adjacent to the face analysed.

3.10.2 Green-Gauss Node-based

The only difference between Green-Gauss Cell-based and Green-Gauss Node-based methods is the approach of determining the face value of a scalar. In the node-based method, it is calculated as the average of the values at all the nodes that are on the face, as described by Equation (94).

$$\overline{\phi_f} = \frac{1}{N_f} \sum_n^{N_f} \bar{\phi}_{node} \tag{94}$$

In this equation, $\bar{\phi}_{node}$ is the value of the scalar at a node on the analysed face and is calculated as a weight average of the values of all the cells that contains the node.

The node-based method is originally proposed by Holmes and Connel [136] and Rauch et al. [137] and known to be more accurate than the cell-based method, and better at dealing with irregular and unstructured mesh. However, it is involved with much heavier calculation as well.

3.10.3 Least Squares Cell-based

In this method, the gradient of a scalar is assumed to be the same between each two neighbouring cell centroids. For example, in Figure 18, based on the gradient of cell c_0, the scalar variation from cell c_0 to c_i can be expressed by Equation (95).

$$\nabla\phi_{c0}\cdot\vec{r_i}=\phi_{ci}-\phi_{c0} \tag{95}$$

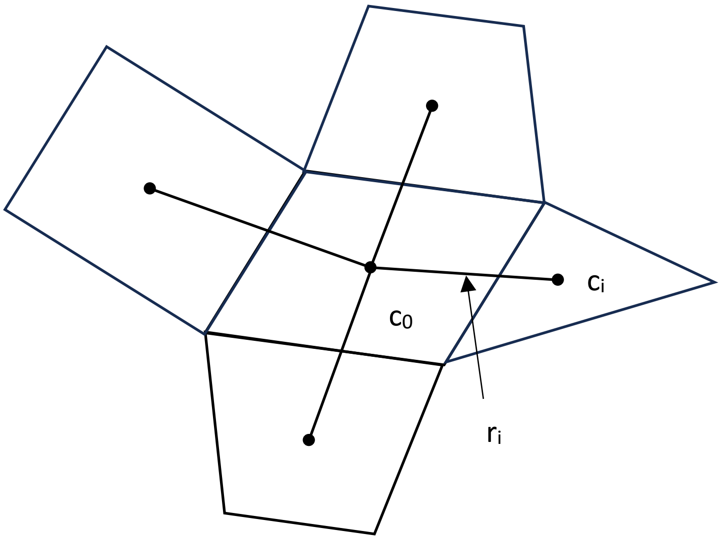

Figure 18 Illustration of Least Squares Cell-based Method.

A group of equations similar to Equation (95) can be derived for all the cells surrounding c_0 in Figure 18. These equations can be combined and written in a matrix form, as shown by Equation (96).

$$[R]\cdot\nabla\phi_{c0}=\overrightarrow{\Delta\phi} \tag{96}$$

In this equation, $[R]$ is a matrix containing all the displacement vectors, so it's determined purely by geometry, and $\overrightarrow{\Delta\phi}$ is a vector consists of all the scalar differences. The gradient can be obtained by solving this over-determined group of equations. The Gram-Schmidt process [138] is applied here to decompose the coefficient matrix $[R]$, and it yields a matrix of weights (W_i^x, W_i^y, W_i^z) of each surrounding cell. Therefore, the three components of the gradient at cell centroid of c_0 can be computed by Equations (97)-(99).

$$\nabla\phi_{c_0,x} = \sum_{i=1}^{n} W_{i,x} \cdot (\phi_{ci} - \phi_{c0}) \tag{97}$$

$$\nabla\phi_{c_0,y} = \sum_{i=1}^{n} W_{i,x} \cdot (\phi_{ci} - \phi_{c0}) \tag{98}$$

$$\nabla\phi_{c_0,z} = \sum_{i=1}^{n} W_{i,x} \cdot (\phi_{ci} - \phi_{c0}) \tag{99}$$

The accuracy of Least Squares Cell-based method is comparable to that of Green-Gauss Node-based method while dealing with distorted and unstructured mesh grids, and both are much better than Green-Gauss Cell-based method. However, the calculation needed for Least Squares method is much less than Green-Gauss Node-based method.

3.11 Initial Conditions

The initial conditions define the initial values needed for the iterative solution process. These conditions are determined based on the parameters of the simulated cooling process and can potentially incorporate the influence of any prior processing.

3.11.1 Immersion Process of the Solid Sample

The solid sample is immersed into water as the beginning of a quench cooling process. Such motion creates swirling flows around the solid sample, and these flow behaviours are important for an accurate prediction of the initial heat transfer rate between the solid and liquid phases. However, the simulation of moving the solid sample into stationery water is difficult to accomplish and require huge calculation power because the movement of mesh grids have to be considered, and the mesh grids have to be updated for each time step until the motion of the solid sample completely terminates. For samples of larger sizes, the immersion process is very likely to take far longer than smaller scale samples and could take up to several seconds, which may contain thousands of time steps.

To avoid such huge effort, the solid sample is assumed to be stationery and the water level rises from the bottom surface of the solid sample to the top surface of the water tank. In this way, the solid sample is relatively immersed into water, and the fluid behaviours caused by the immersion process can be properly simulated. The detailed configuration of velocity inlet conditions is introduced in § 3.12.3

3.11.2 Cell Zone Conditions

The cell zones of the models are basically divided into two areas, the solid sample and the water tank. The material of the solid sample is selected between Inconel 718 and Inconel 600 according to the material used in the corresponding experiment for validation. If an initial solid temperature gradient is not in existence, the temperature distribution in the samples is homogeneous and is equal to the starting temperature of the corresponding cooling process. For some of the models, an initial solid temperature gradient is assumed to be presented as an initial condition to study its influence on the solid sample cooling rate in the initial stage. The temperature gradient conditions of such cases are introduced in detail in § 3.11.3 .

In terms of the water tank, its phase is liquid water for the single-phase models and is mixture for the multiphase models. For all the models, the initial temperature of the fluid in the water tank is 25 ℃ (298.15 K), regardless of whether the gas phase exists or not. In the models that include the initial velocity inlet, the initial fluid phase below the bottom surface of the solid sample is liquid, and the rest areas in the water tank is gas.

3.11.3 Initial Solid Temperature Gradient

In some cases where it takes too long to transfer the solid sample from the heating furnace to the water tank, the influence of prior cooling in air may not be negligible anymore. As a result, there is already spatial difference in the temperature inside the solid sample before the quench cooling starts, and the effect is considered by setting up corresponding initial conditions.

Since the initial temperature distribution inside the solid domain is not measurable, it is assumed to be in a linear relationship with the distance from the solid sample centroid (or the position where the temperature is recorded experimentally). This relationship can be shown by Equation (100).

$$T_0 = -2833.33\sqrt{x^2 + y^2 + z^2} + 1128.15 \tag{100}$$

In the equation, the coordinates are in the unit of m, and the coordinates of the solid sample centroid is specified as (0,0,0).

3.12 Boundary Conditions

The boundary conditions are specified to define the conditions on the interfaces and walls in the models, including thermal, velocity, and pressure conditions. In this section, the basic boundary condition settings related to this project are introduced.

3.12.1 Coupled Solid-liquid Interface

The solid-liquid interface is characterized as a coupled wall. In ANSYS Fluent, a coupled solid-liquid interface is treated as a two-sided wall. A shadowed wall which does not exist in reality is created at the solid-liquid interface when the mesh is read, so that each side of the wall belongs to only one domain and the material of each side of the wall can be clearly specified without confliction. For a coupled wall, no extra thermal condition is needed because the solver calculates the heat transfer rate based on the solution of the energy equation of the adjacent cells.

3.12.2 Heat Flux

The heat flux boundary condition is implemented as an alternative thermal BC on the solid-liquid interface. When such BC is applied, the model no longer contains any fluid domain, because this BC is applied on the solid surface, and there will be no interaction between the solid and liquid domains without a coupled thermal BC. The heat flux expression used in this project is an empirical correlation provided by Babu et al. [139].

Typically, during a quench process, as the solid surface temperature decreases from its initial temperature, the surface heat flux firstly increases and subsequently decreases after reaching a peak value. When the heat flux peak value is reached, the peak heat flux q_{peak} and the corresponding wall temperature T_{peak} are calculated based on the soak temperature of the sample T_{soak} by Equations (101) and (102), respectively.

$$q_{peak} = 0.089386T_{soak}^3 - 203.74T_{soak}^2 + 158374.52T_{soak} - 38817398.6 \quad (101)$$

$$T_{peak} = 1.929 \times 10^{-5}T_{soak}^3 - 9.52701T_{soak}^2 + 47.74T_{soak} - 13874.59 \quad (102)$$

The unit of q_{peak} is W/m^2, and the unit of T_{peak} is ℃.

The heat flux under a certain surface temperature of the solid wall is calculated as the product of the peak heat flux q_{peak} and a dimensionless heat flux factor q_{norm}. This normalized heat flux factor q_{norm} is evaluated based on a dimensionless temperature T_{norm}, and has a range of 0-1. The whole temperature range is divided into two parts by T_{peak}, and the calculation methods of q_{norm} and T_{norm} are different for the two temperature ranges.

When the wall temperature is greater than T_{peak}, the dimensionless temperature is given by Equation (103).

$$T_{norm,1} = \frac{T_w - T_l}{T_{soak} - T_l} \tag{103}$$

Subsequently, the normalized heat flux factor is calculated by Equation (104).

$$\begin{aligned} q_{norm,1} = -236.277T_{norm,1}^5 + 939.959T_{norm,1}^4 - 1468.072T_{norm,1}^3 \\ + 1121.514T_{norm,1}^2 - 419.969T_{norm,1} + 62.864 \end{aligned} \tag{104}$$

If the wall temperature is smaller than T_{peak}, the dimensionless temperature is calculated by Equation (105) instead.

$$T_{norm,2} = \frac{T_w}{T_{peak}} \tag{105}$$

Similarly, q_{norm} is also calculated by a different equation given by Equation (106).

$$\begin{aligned} q_{norm,2} = -13.752T_{norm,2}^5 + 51.469T_{norm,2}^4 - 73.201T_{norm,2}^3 \\ + 47.338T_{norm,2}^2 - 11.876T_{norm,2} + 1.0302 \end{aligned} \tag{106}$$

3.12.3 Velocity Inlet

The surface of velocity inlet is the bottom face of the water tank. The magnitude of velocity inlet takes the form of the sigmoid function because the discontinuous velocity can cause severe instability to the model. The expression of the velocity magnitude is shown by Equation (107). A positive velocity value indicates that its direction is the normal direction of the inlet face pointing towards the inner domain of the water tank. An example of the velocity magnitude curve is given by Figure 19.

$$u_0 = C_{vol} \frac{1}{1 + exp[C_{u_0}(t - t_0)]} \tag{107}$$

In this equation, C_{u_0} is a coefficient that adjusts the slope of the curve, t_0 is a time shift, C_{vol} is the coefficient that ensures the overall inlet volume is close to the initial vacant volume in the water tank. The time needed for the whole immersion process t_{fin} is calculated based on t_0 and C_{u_0} as shown by Equation (108). The curve becomes steeper with an increasing C_{u_0}, and is shifted to the right with an increasing t_0.

$$t_{fin} = t_0 + \frac{6}{C_{u_0}} \tag{108}$$

The facial mass flux is the product of the velocity inlet face area and the velocity inlet magnitude, and the overall inlet volume is obtained by integrating the facial mass flux over time.

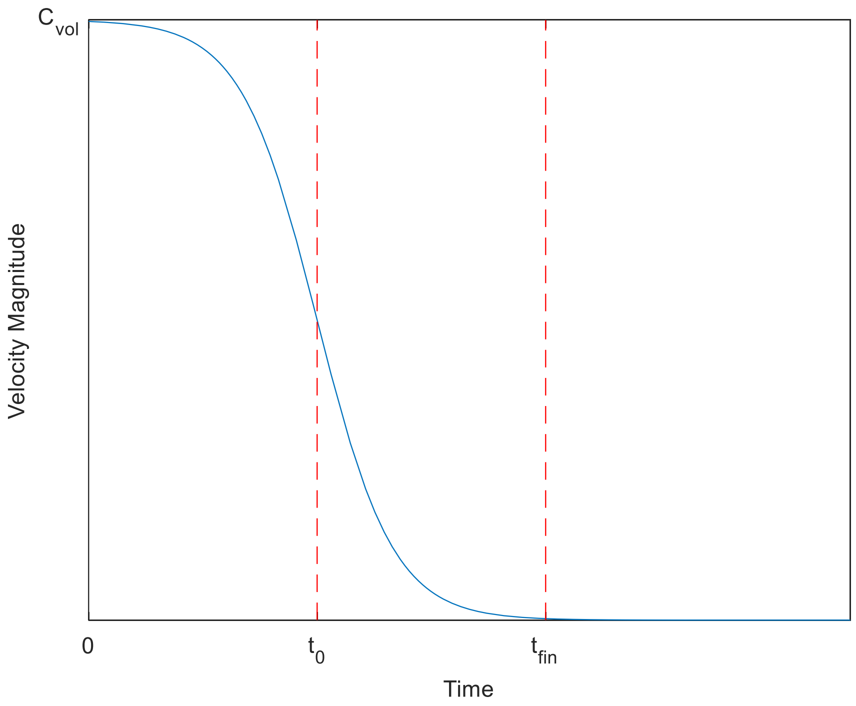

Figure 19 Velocity Inlet Magnitude Curve.

3.12.4 Pressure Outlet

In most of the models, the top surface of the water tank is selected as the pressure outlet to allow any potential fluid exchange between the water tank and the environment. Since all the simulated processes are performed under ambient conditions, the backflow pressure is 1 atm, the backflow temperature is 25 ℃ (298.15 K), and the backflow phase is 100% vapour. This indicates that whenever the gas pressure in the water tank is less than 1 atm, vapour mass flux with a temperature of 25 ℃ flows into the water tank via the pressure outlet surface. At the same time, fluid can freely exit the water tank under the effect of fluid motion or pressure difference.

3.12.5 Tank Wall

The faces of the water tank (excluding the velocity inlet and pressure outlet surfaces) are assumed to be adiabatic walls. Though this is not the case in reality, the water temperature near the water tank wall is hardly changed throughout the whole cooling process. Therefore, ignoring the heat transfer through the tank wall only have minimum influence on the overall temperature distribution inside the water tank.

3.13 Pressure-based Solver

In all the models of this paper, the fluid of concern is water, which is incompressible, so the pressure-based solver is applied. The steady-state continuity and momentum equations in integral forms are given by Equations (109) and (110).

$$\oint \rho\vec{v}\cdot d\vec{A} = 0 \tag{109}$$

$$\oint \rho\vec{v}\vec{v}\cdot d\vec{A} = -\oint pI\cdot d\vec{A} + \oint \bar{\bar{\tau}}\cdot d\vec{A} + \int \vec{F}dV \tag{110}$$

3.13.1 Discretization of Momentum Equation

From Equation (110), a discretized momentum transport equation along a single axis is derived as Equation (111).

$$a_p u = \sum_{nb} a_{nb}u_{nb} + \sum p_f\vec{A} + S \tag{111}$$

The solution of this equation leads to a velocity field, but the pressure value at the interface between two neighbouring cells p_f is required. Since the solver stores values at cell centroids, an interpolation scheme which is different from those mentioned in §3.8 is applied here to obtain face values of pressure. Take cells c_0 and c_i in Figure 18 as an example, the p_f at the interface between them is calculated by Equation (112) [140].

$$p_f = \frac{\frac{p_{c0}}{a_{p,c0}} + \frac{p_{ci}}{a_{p,ci}}}{\frac{1}{a_{p,c0}} + \frac{1}{a_{p,ci}}} \tag{112}$$

This interpolation method performs the best when pressure variation is smooth between neighbouring cells. However, for flows with huge body forces and strong swirling behaviour, significant errors can be induced. This problem could be solved by having refined mesh grids in the regions that may cause such problems. Therefore, in the models of this paper, finest meshes are always preferred for near-wall fluid regions where high temperature change and bubble movement can cause rapid fluid flow and swirls.

3.13.2 Discretization of Continuity Equation

By integrating Equation (109) over a certain cell, Equation (113) can be obtained.

$$\sum_{f}^{N_f} J_f A_f = 0 \tag{113}$$

This is a discretized continuity equation, where J_f represents the mass flux through a face f, defined by Equation (114).

$$J_f = \rho \vec{v} \tag{114}$$

By default, the solver stores velocity values at the cell centroids similarly to pressure values. Therefore, in Equation (114), the face value of fluid velocity must be derived according to velocity values at cell centroids. Instead of linear interpolation, the face value of velocity is calculated based on a momentum-weighted average. The weight factors are based on the a_p coefficient from Equation (111). Thus, J_f can be re-written as Equation (115).

$$\begin{aligned} J_f = p_f \frac{a_{p,c0} \cdot \vec{v}_{c0} + a_{p,ci} \cdot \vec{v}_{ci}}{a_{p,c0} + a_{p,ci}} \\ + f_p[(p_{c0} + (\nabla p)_{c0} \cdot \vec{r_0}) - (p_{ci} + (\nabla p)_{ci} \cdot \vec{r_i})] \\ = \hat{J}_f + D_f(p_{c0} - p_{ci}) \end{aligned} \tag{115}$$

In this equation, p_{c0}, p_{ci} and $\vec{v}_{c0}$, $\vec{v}_{ci}$ are the pressures and velocities on the side of c_0 and c_i

of the face, respectively, $\hat{J}_f$ contains the influence of velocities in these cells, f_p is a function of the average of the coefficients a_p of cells c_0 and c_i.

3.14 Coupled Algorithm

In terms of pressure-velocity coupling, the pressure-based coupled algorithm is selected over the segregated algorithm. In the coupled algorithm, the solution process of momentum and continuity equations are implicitly coupled. However, equations of other properties, like energy, species, turbulence, and other scalars, are solved separately like in the segregated algorithm.

The procedures of the pressure-based coupled algorithm are described in Figure 20. The steps of each iteration can be summarized below:

1. Update fluid properties (e.g., density, viscosity, specific heat) and turbulent viscosity (diffusivity) based on the current solution.
2. Solve a coupled system of equations comprising the momentum equations and the pressure-based continuity equation.
3. Correct face mass fluxes, pressure, and the velocity field using the pressure correction obtained from Step 2.
4. Solve the equations for additional scalars, if any, such as turbulent quantities, energy, species, and radiation intensity using the current values of the solution variables.
5. Update the source terms arising from the interactions among different phases (e.g., source term for the carrier phase due to discrete particles).
6. Check for the convergence of the equations. If the solutions cannot meet convergence, they are used as updated properties and the process starts again from step 1.

The coupling between the momentum and continuity equations is achieved by discretizing the pressure gradient term in Equation (111) and the face mass flux in Equation (115). In Equation (111), the pressure gradient along a certain axis k can be written as Equation (116).

$$\sum p_f \vec{A}_k = -\sum_j a_{u_k,p} p_j \tag{116}$$

$a_{u_k,p}$ is a coefficient derived by Divergence Theorem and the pressure interpolation scheme described by Equation (112). Therefore, for a given cell c_j, Equation (111) can be re-written considering the velocity component along axis k, as described by Equation (117).

$$\sum_j a_{ij,u_k,u_k} u_{k,j} + \sum_j a_{ij,u_k,p} p_j = b_{i,u_k} \tag{117}$$

Meanwhile, Equation (115) can be discretized in a similar manner, resulting in Equation (118).

$$\sum_k \sum_j a_{ij,p,u_k} u_{k,j} + \sum_j a_{ij,p,p} p_j = b_{i,p} \tag{118}$$

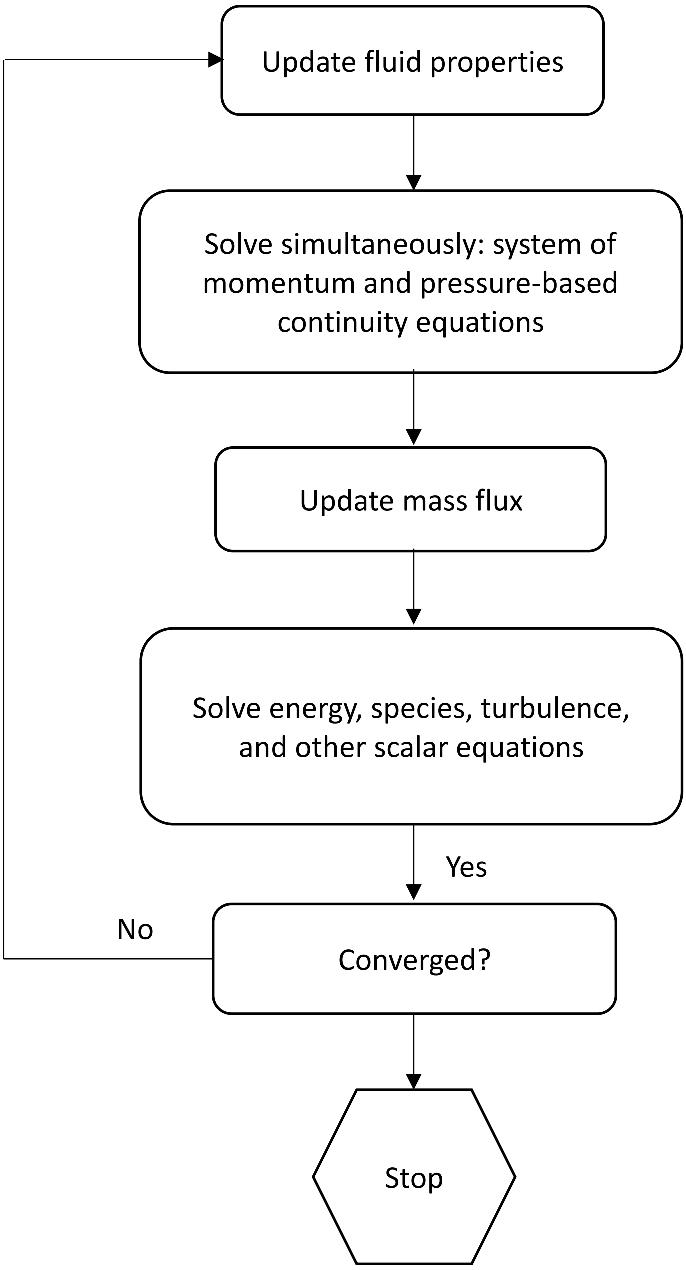

Figure 20 Flow chart of Pressure-based coupled solver.

Thus, by considering all the components, the overall system of Equations (117) and (118) can be written in the form of Equation (119).

$$\sum_j [A]_{ij}\vec{X}_j = \vec{B}_i \tag{119}$$

In this equation, $[A]_{ij}$ is the influence of a cell c_i on a cell c_j and is described by Equation (120), $\overrightarrow{X_j}$ contains the unknowns as shown by Equation (121), and $\overrightarrow{B_i}$ is the vector of residuals given by Equation (122).

$$[A]_{ij} = \begin{bmatrix} a_{ij,p,p} & a_{ij,p,u} & a_{ij,p,v} & a_{ij,p,w} \\ a_{ij,u,p} & a_{ij,u,u} & a_{ij,u,v} & a_{ij,u,w} \\ a_{ij,v,p} & a_{ij,v,u} & a_{ij,v,v} & a_{ij,v,w} \\ a_{ij,w,p} & a_{ij,w,u} & a_{ij,w,v} & a_{ij,w,w} \end{bmatrix} \tag{120}$$

$$\vec{X}_j = \begin{bmatrix} p'_i \\ u'_i \\ v'_i \\ w'_i \end{bmatrix} \tag{121}$$

$$\vec{B}_i = \begin{bmatrix} -r_{i,p} \\ -r_{i,u} \\ -r_{i,v} \\ -r_{i,w} \end{bmatrix} \tag{122}$$

While dealing with transient flows, the pressure-based coupled algorithm is much more compatible with coarse mesh and large time steps comparing to the segregated algorithms, including SIMPLE, SIMPLEC, PISO, etc. However, it can use as much as two times of memory than the segregated algorithms.

3.15 Algebraic Multigrid

This scheme is applied as a solution method of the Pressure-based Coupling Algorithm and mainly solves Equation (119). To start with, a new matrix $[M]$ is created as an approximation of the matrix $[A]$ in the equation. $[M]$ should be close to $[A]$ and calculation of $[M]^{-1}$ should not be over-complicated. M is obtained via Incomplete Lower Upper (ILU) factorization of $[A]$ as shown by Equation (123).

$$[M] = ([D] + [L]_A)[D]^{-1}([D] + [U]_A) \tag{123}$$

In this equation, $[L]_A$ and $[U]_A$ are the lower tridiagonal and upper tridiagonal parts of $[A]$, and $[D]$ is a diagonal matrix which is very close to the diagonals of both $[M]$ and $[A]$. The elements of the diagonal matrix $[D]$ are calculated by Equation (124).

$$d_{ii} = a_{ii} - \sum_{j<i} \frac{a_{ij} a_{ji}}{d_{jj}} \tag{124}$$

The relationship between $[M]$ and $[A]$ is expressed by Equation (125).

$$[M]\left(\vec{X}_{k+1} - \vec{X}_k\right) = \vec{B} - [A]\vec{X}_k \tag{125}$$

Subsequently, the calculation of $\overrightarrow{X_{k+1}}$ is carried out by two symmetric recursive sweeps on the elements in the matrices and vectors, which are described by Equations (126) and (127).

$$x_{k+\frac{1}{2}} = \frac{1}{a_{ii}}\left(b_i - \sum_{j<i} a_{ij} x_{j,k+\frac{1}{2}} - \sum_{j>i} a_{ij} x_{j,k}\right) \tag{126}$$

$$x_{k+1} = \frac{1}{a_{ii}}\left(b_i - \sum_{j<i} a_{ij} x_{j,k+\frac{1}{2}} - \sum_{j>i} a_{ij} x_{j,k+1}\right) \tag{127}$$

In these equations, i iterates from 1 to the total number of unknowns. The iterative calculation of $\overrightarrow{X_{k+1}}$ continues until convergence is reached, or when the residuals are below a group of pre-set values. This calculation process is also known as the Gauss Seidel method.

3.16 Time Advancement Algorithm

For transient flows, the generic scalar transport equation which is implicitly discretized in time is given by Equation (128).

$$\int \frac{\partial \rho \phi}{\partial t} dV + \oint \rho_{n+1} \phi_{n+1} \vec{v}_{n+1} \cdot d\vec{A} = \oint \Gamma_{\phi,n+1} \nabla \phi_{n+1} \cdot d\vec{A} + \int S_{\phi,n+1} dV \tag{128}$$

In this equation, $\vec{v}$ is the velocity vector, Γ is the diffusion coefficient, $\vec{A}$ is surface area, S is a volumetric source term.

In this paper, the iterative time advancement scheme is selected. At a certain time step, all the equations are solved iteratively until convergence is achieved. Even though the process of solving the equations one by one can induce splitting error, such splitting error is very likely to be eliminated by the iterative solution process, because non-linearity of the individual equations and inter-equation couplings are well considered. The schematic illustration of the iterative time advancement is shown by Figure 21.

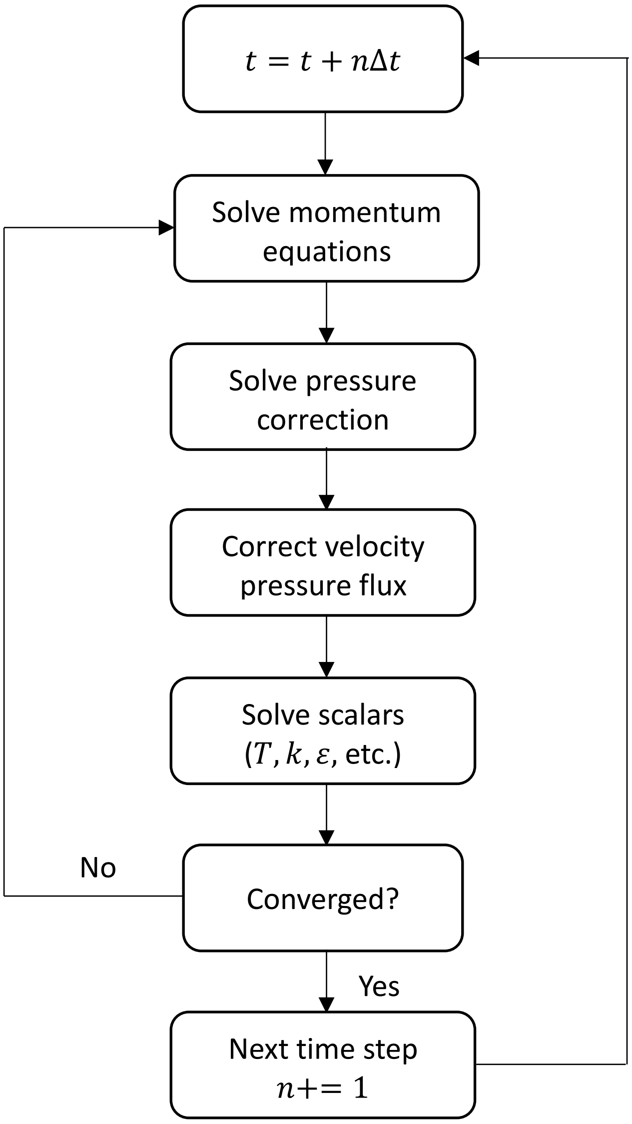

Figure 21 Procedures of iterative time advancement.

3.17 Model Verification

The model is verified by a classical 1-D Stefan problem. As shown in Figure 22, a 1-D mesh grid is generated along z axis, and all the elements are identical and have a length of 1×10^{-5} m. The surface temperature at z=0 is 10 K higher than the saturation temperature of the liquid phase, and the domain is filled with saturated liquid before the simulation starts. The initial phase of the first cell at the bottom is vapour phase.

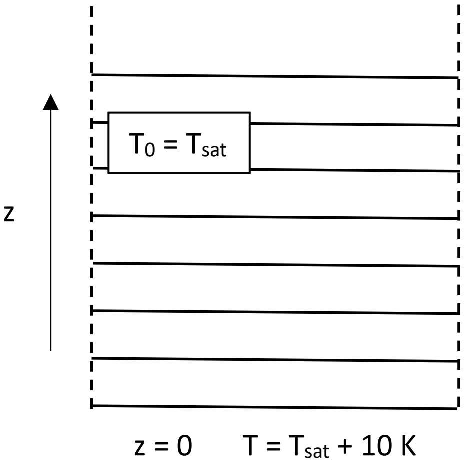

Figure 22 1-D Stefan Problem Model Illustration.

The analytical solution of the interface position as a function of time is given by Eqn. (129) and Eqn. (130).

$$z(t) = 2C_\lambda \sqrt{\frac{\lambda}{\rho C_{p,v}} t} \tag{129}$$

$$C_\lambda H = \frac{C_{p,v}(T_W - T_{sat})}{\sqrt{\pi} exp\left(C_\lambda^2\right) erf(C_\lambda)} \tag{130}$$

The position where both the volume fractions of liquid and gas phases are equally 0.5 is recorded as the interface position of simulation data. Liquid and vapour water are the fluid phases used in this verification process.

Figure 23 shows the interface position vs. time curves for both analytical solution and simulation result. According to Eqn. (6), the average error between these two curves is 17.3%. Overall, the model predicts a faster phase transformation from liquid to vapour phase. This reflects the fact that this model treats the vapourization process in a phenomenological manner which over predicts the rate of interface movement. Even though the velocity divergence term is present in the continuity equation (Eqn. (39)), which claims to be valid for the whole fluid domain for both incompressible and compressible solver, the continuity equation is simplified by setting $\nabla \cdot \vec{v} = 0$, i.e., incompressible assumption. As a result, the correct physics at the interface is not accurately modelled and errors are introduced with the liquid-vapour interface tracking, and the predicted volume of vapour bubble would be higher than reality. The compressibility at the interface is not taken into account by the model as well.

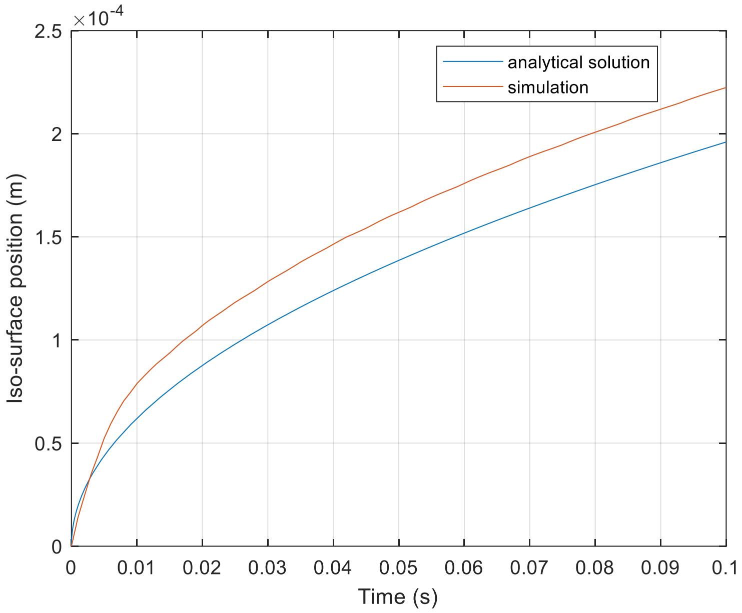

Figure 23 Simulated Result and Analytical Solution for 1-D Stefan Problem.

In order to correct this error, von Neumann boundary condition at the emerged vapour bubble surfaces must be implemented. At the liquid-vapour boundary, the divergence of velocity should be defined as the volumetric net mass generation rate. Such process relies on the use of UDF for ANSYS Fluent. As mentioned by Flint et al. [141], this condition needs to be manually defined in other software packages as well. However, there is no doubt that with intense boiling effect going on, implementing this condition on the boundaries of a large number of bubbles requires considerable calculation power and significantly induces instability to the solution process. Therefore, this condition is not implemented in the models of this thesis. As a result, the models will predict higher overall volume of vapour phase, but smaller and less bubbles. This is because the interfacial compressibility physically represents the hydrostatic force on the bubble surface from the surrounding liquid. Without this force, the surface tension cannot be correctly calculated, and the bubble is much less stable than the real case. In terms of the boiling behaviours associated with quenching, the gaseous layer that covers the whole solid surface during film boiling stage is much less possible to form. This is likely to accelerate the cooling rate of the solid sample through enabling more direct contact between the solid surface and liquid phase.

In terms of energy calculation, the vapourization latent heat is incorporated in the source term in Eqn. (53). It is expressed by the product of the volumetric mass transfer rate from one phase to another and the latent heat. With a larger volume of vapour phase generated, the volumetric mass transfer rate is reduced, and the heat extraction due to vapourization is spread in a wider area. Therefore, the predicted vapourization latent heat is less than the true value, and the fluid temperature would be higher than the experiment.

3.18 Scaling Performance with CPUs

Considering the amount of calculation power needed for the simulation, multiple CPUs are often needed. The multi-core performance of the software package is investigated. The calculation power is represented by the number of iterations calculated during a certain amount of time, and the numbers of cores used are 1, 2, 4, 8, 16, 32. Due to the limitation of the High Performance Computer (HPC) clusters, the number of CPU cores used for a single task cannot exceed 32.

Figure 24 shows the scaling performance with multiple cores. A near-linear relationship between the calculation power and the number of CPU cores used can be observed. Therefore, for the best calculation efficiency and rate, using the most possible number of CPU cores is desired.

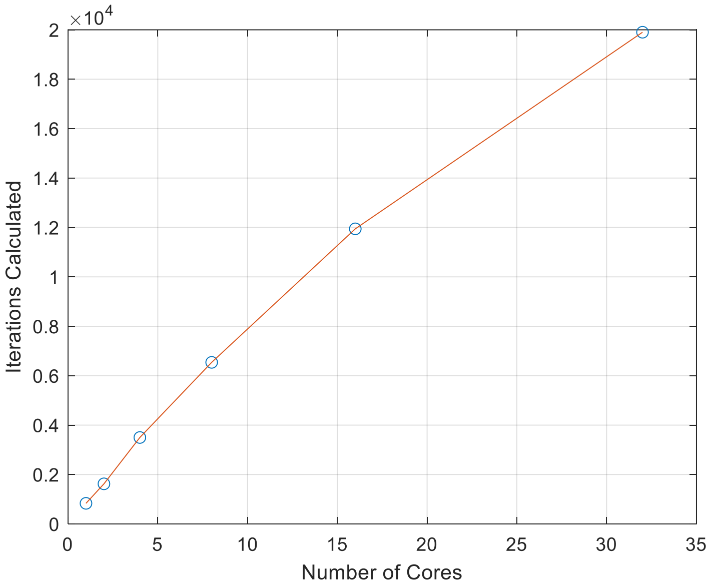

Figure 24 Scaling Performance with Multiple Cores.

4 Small-Scale Cylindrical Sample

In this chapter, the modelling results of a quench cooling test of a small-scale sample are visualized and discussed. The experiment was carried out by Howson et al. [142], and the experimental data is used to validate the modelling results. To have a better understanding of the influence of the model parameters on the predicted cooling behaviour, comparisons are made between each two sets of simulation results that differ in only one model parameter. The difference in the simulation results is then discussed based on the understanding of the model algorithms and the physics of quench cooling processes.

4.1 Experiment and Model Information

The facilities used for this quench cooling test are shown in Figure 25. Figure 25 (a) is a 12.5 mm diameter probe with a thermocouple at its centre to record the temperature profile. The first 60 mm from the tip of the probe is heated in the furnace and then quenched in the left part of the quench tank without agitation. Since the glass plate in the middle of the quench

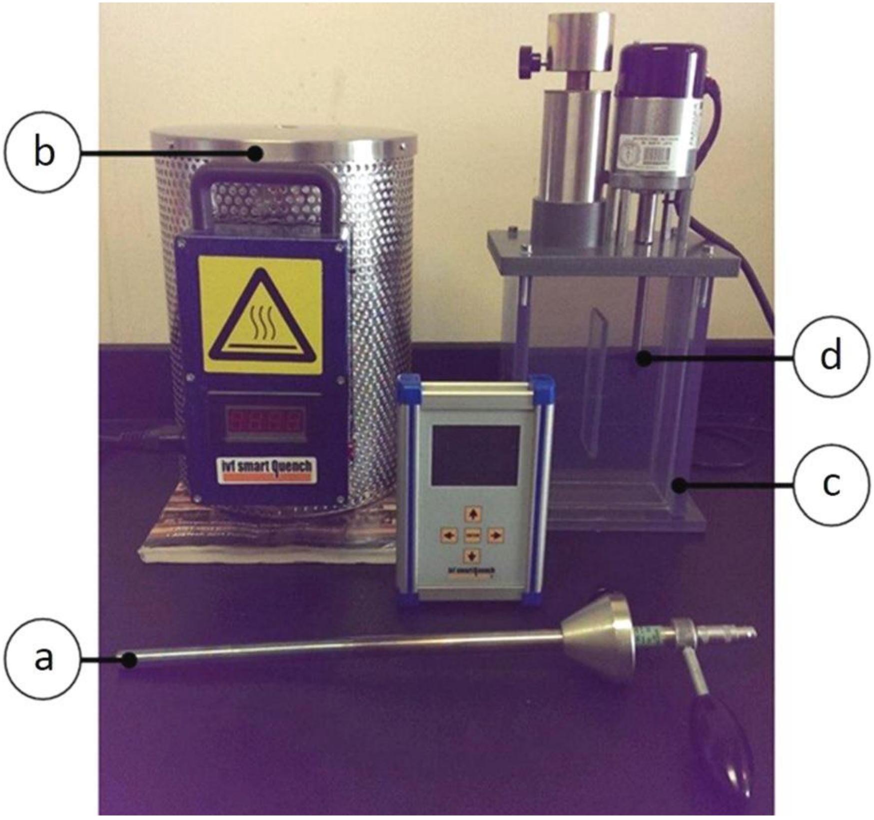

Figure 25 Facilities Used to Perform the Quench Test: (a) the Inconel 600 probe with a k-type thermocouple, (b) furnace, (c) quench tank (d) agitator [142].

tank largely inhibits the convection and heat exchange between the two parts of the water tank, the actual effective quenching area is only the left half of the quench tank. Therefore, this case is simplified as the quench cooling of a 60 mm long cylinder sample in a cuboid quench tank that has a width of approximately half of Figure 25 (c).

The quench cooling tests have been performed for three times, generating three groups of temperature data. For the purpose of validation, the algebraic average of the three groups of data is taken to reduce potential random error.

Figure 26 shows the geometry of the conceptual model constructed based on the experimental quench cooling process. The solid sample has a cylindrical shape, with a diameter of 12.5 mm and a height of 60 mm, and the water tank is a cuboid with a dimension of 100 mm by 100 mm by 180 mm. In this figure, the pressure outlet is only enabled when the

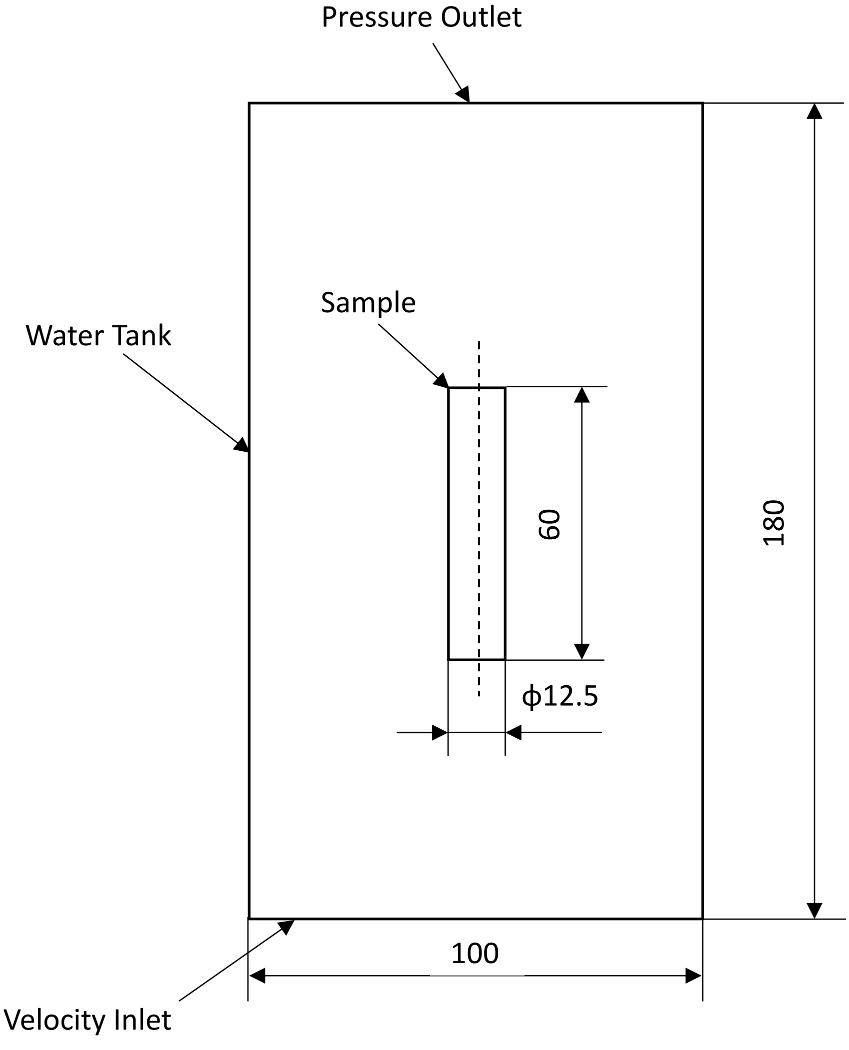

Figure 26 Geometry of a Small-Scale Cylindrical Sample Model.

multiphase model is specified, and the velocity inlet is enabled when the immersion process of the solid sample is simulated. The solid material used in this model is Inconel 600, and the initial temperature is 855 ℃ (1128.15 K).

It is worth mentioning that even though the solid sample is planned to be heated to 855 ℃, the experimentally recorded initial temperature is slightly lower than this temperature (about 10 ℃).

4.2 Meshing Properties

All the mesh elements are hexahedral and structured mesh is constructed for the model. The mesh size of the solid sample is refined to obtain more detailed predictions of thermal conduction rate and temperature distribution. In the quench tank, since the fluid near the solid surface is of the most concerns, the corresponding mesh sizes are the finest. Meanwhile, the thickness of the first layer of fluid cells from the solid-liquid interface is small enough to ensure proper y^* values that yield the best performance of the standard wall treatment. From this area to the boundary of the quench tank, the mesh size is gradually increased to reduce the required calculation power. Thus, the meshing properties of the regions close to the quench tank boundary are relatively poor, but this is not detrimental to the simulation results because the changes in the temperature and velocity of the fluid phase in these regions are considered trivial.

At the solid-liquid interface, the mesh grids on both sides are made conformal, i.e., all the nodes on the interface are shared by the elements from both sides of the interface. As a result, the heat flux calculation would not be disturbed by any non-matching faces and nodes on the interface. The cylinder block which represents the solid sample is properly partitioned to obtain structured mesh that matches with the quench tank.

Based on the number of divisions on each edge, five mesh grids are generated. From level 1 to level 5, the number of divisions on each edge is proportionally increased. A basic model is simulated on each mesh grid, and the results are shown in Figure 27. Obviously, the results of level 1 and 2 are far from realistic, and after the refinement level reaches 3, the results start to converge. The number of nodes and elements for each mesh level is shown in Table 4.

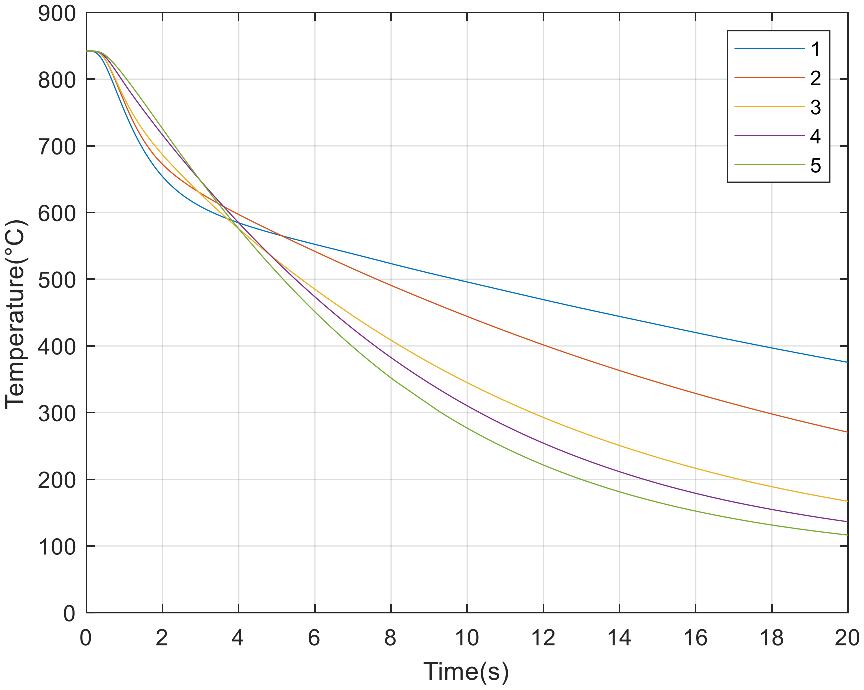

Figure 27 Solid Cooling Curves of Different Mesh Level.

Based on the consideration of both simulation efficiency and model accuracy, the level 3 is chosen as the mesh for all small-scale models (including the small-scale probe shaped models). Nevertheless, it must be noted that even though level 3 is close to the ideal mesh size in terms of the ability of capturing physical mechanisms, it inevitably introduces error into the simulation result. The mean relative error between level 3 and level 4 is 11.37%, whereas it is 17.06% between level 4 and level 5. These numbers are hardly satisfying, and the mesh grids need further refinement to reach convergence, i.e. to have an average relative error below 5%.

Table 4 Number of Elements and Nodes of Each Mesh Level

Mesh Level	1	2	3	4	5
Number of Elements	26,500	212,000	751,500	1,824,000	3,564,625
Number of Nodes	28,768	220,763	770,748	1,858,443	3,618,204

The final mesh contains 770,748 nodes and 751,500 elements. Figure 28 (a) and (b) show the isometric view and a sectioned side view of the mesh grids, respectively.

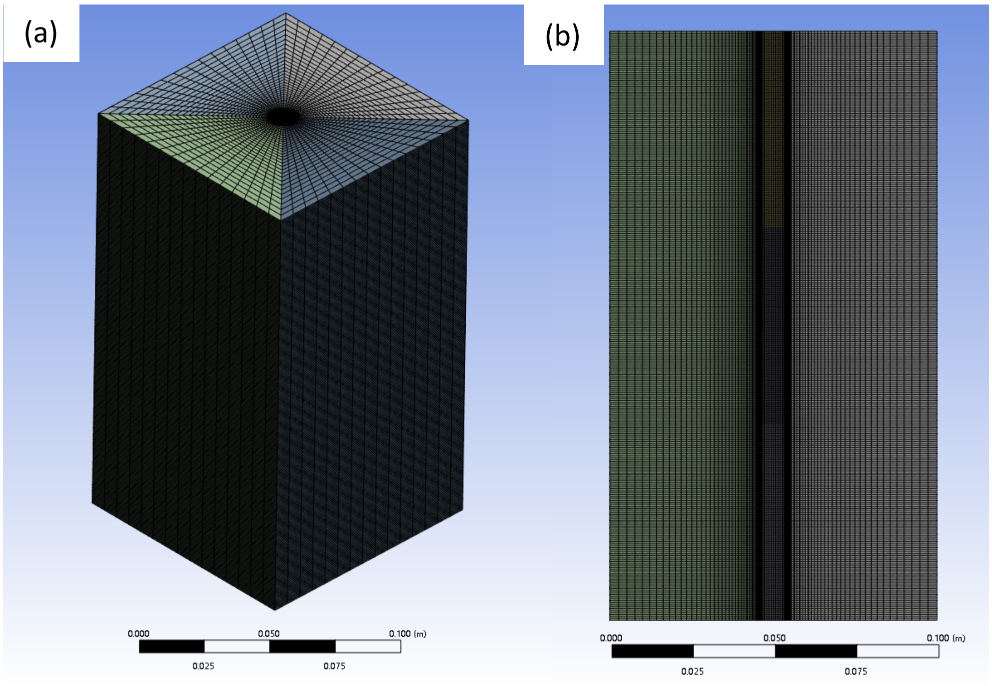

Figure 28 Graphs of Level 3 Mesh (a) Isometric View (b) Sectioned Side View.

4.3 The Influence of Boiling Effects

The influence of boiling effects is studied by comparing the results obtained from a single-phase model and a multiphase model. In the single-phase model, the thermal properties and the flow behaviours of the fluid near the solid wall are only influenced by the heat transfer between the solid sample and the fluid phase, whereas in the multiphase model, these properties are also dependent on the boiling effect. The predicted temperature evolution at the centre of the solid sample of both models are shown in Figure 29 together with the experimentally recorded profile. During the initial stage of the cooling, a small temperature plateau is observed in the predictions of both models. The predicted temperatures are above the experimentally measured values throughout the whole cooling process. Even though the predicted result of the multiphase model is much more reasonable than the results of the single model, significant differences still exist between the temperature curves of the multiphase model and the experimental data.

During the first few seconds of cooling, both models predict the same temperature evolution at the centre of the solid sample. However, after that, the temperature of the single-phase model becomes much higher than the multiphase model. In addition, variations in the cooling trend can be observed in the results of the single-phase model, whereas the temperature curve of the multiphase model is smooth.

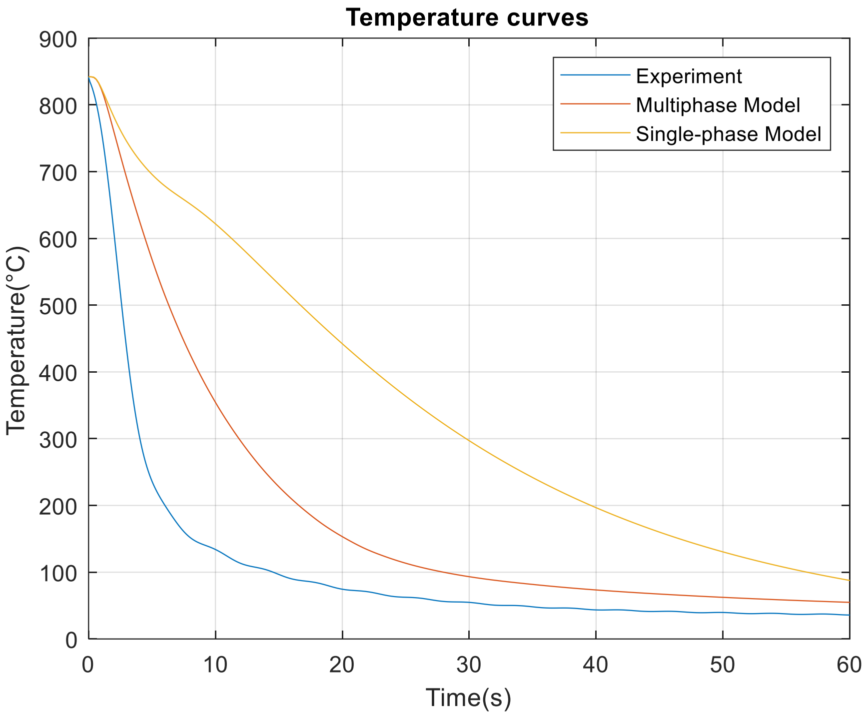

Figure 29 Temperature vs. Time Curves of the Single-phase Model and the Multiphase Model.

To have a better understanding of the overall cooling trend, the cooling rates of these three groups of data are analyzed. Figure 30 (a) and (b) show the cooling rate vs. temperature and cooling rate vs. time curves of these three groups of data, respectively. According to Figure 30 (a), the cooling trend of the multiphase model is very close to the experimental data when the temperature is above 800 ℃, but the subsequent cooling rate increasement is significantly limited for the simulated results. The of the cooling rate curve of the multiphase model is smooth, similar to its temperature curve. In terms of the cooling rate of the single-phase model, after reaching its maximum value, which is significantly smaller than the multiphase model, the cooling rate decreases rapidly to a local minimum value at 660 ℃.

The temperature distribution in the fluid domain is visualized in Figure 31. It is found that the fluid temperature around the solid sample rises very quickly to a very high level which is far beyond the saturation point after the cooling starts, and this state is retained throughout the whole cooling process. This could potentially be the major factor that limits the increasement of the predicted cooling rate. In reality, the heated fluid is supposed to flow upwards away from the solid surface because of a decreased density so the heat would not accumulate in the near-solid fluid region. However, even though gravity is correctly specified in the models, such behaviour is not successfully simulated, and the main reason would be that the density of water is a constant value by default according to the solver.

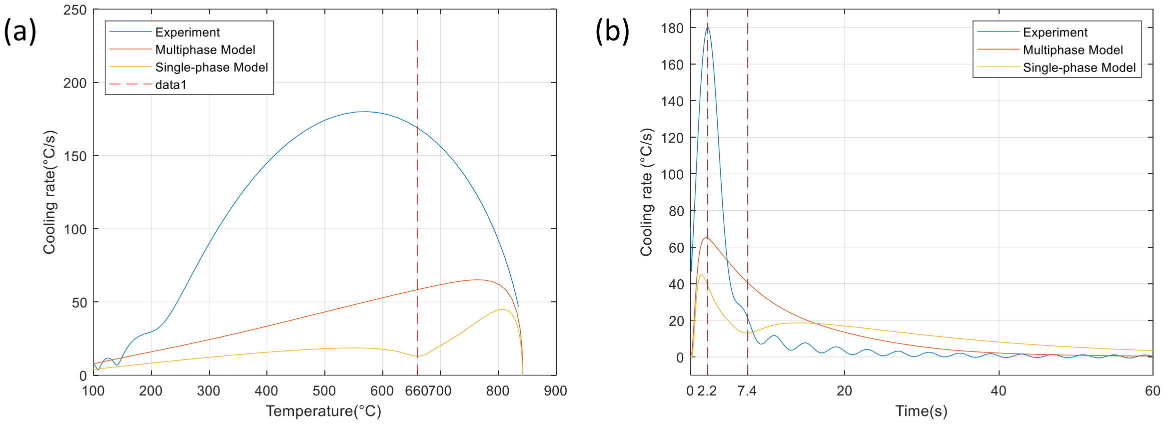

Figure 30 (a) Cooling Rate vs. Temperature, (b) Cooling Rate vs. Time Curves of Single-phase, Multiphase Models and Experimental Data.

In the multiphase model, the fluid temperature around the solid surface is much lower than in the single-phase model. This is because in the multiphase model, the boiling latent heat is extracted from the fluid near the solid surface, and the heat transfer is accelerated. In addition, the movement of the free bubbles creates an upward stream that enhances the convection flows in the near-solid fluid region, which prevents the water from being severely heated. Such movement of the bubbles could be observed in Figure 32.

For a typical quench cooling process, the maximum heat transfer rate often appears at the early stage of nucleate boiling because of a high heat transfer coefficient and a large temperature difference between the solid wall and the fluid phase. However, in this specific quenching process, since the temperature is recorded at the centre of the solid sample, the cooling rate peak is very likely to appear later in time than the maximum heat transfer rate due to the time required for the thermal conduction between the surface and the centre of the sample.

Figure 33 (a) and (b) are two photos taken at different times during the quenching test. In Figure 33 (a), the sample has just been fully immersed in the water, and a big bubble to the right of the sample as well as several small but visible bubbles are formed as a result of the immersion process. At this point, film boiling is ongoing, and the solid surface is covered by a vapour blanket, and bubble departure is hardly noticeable.

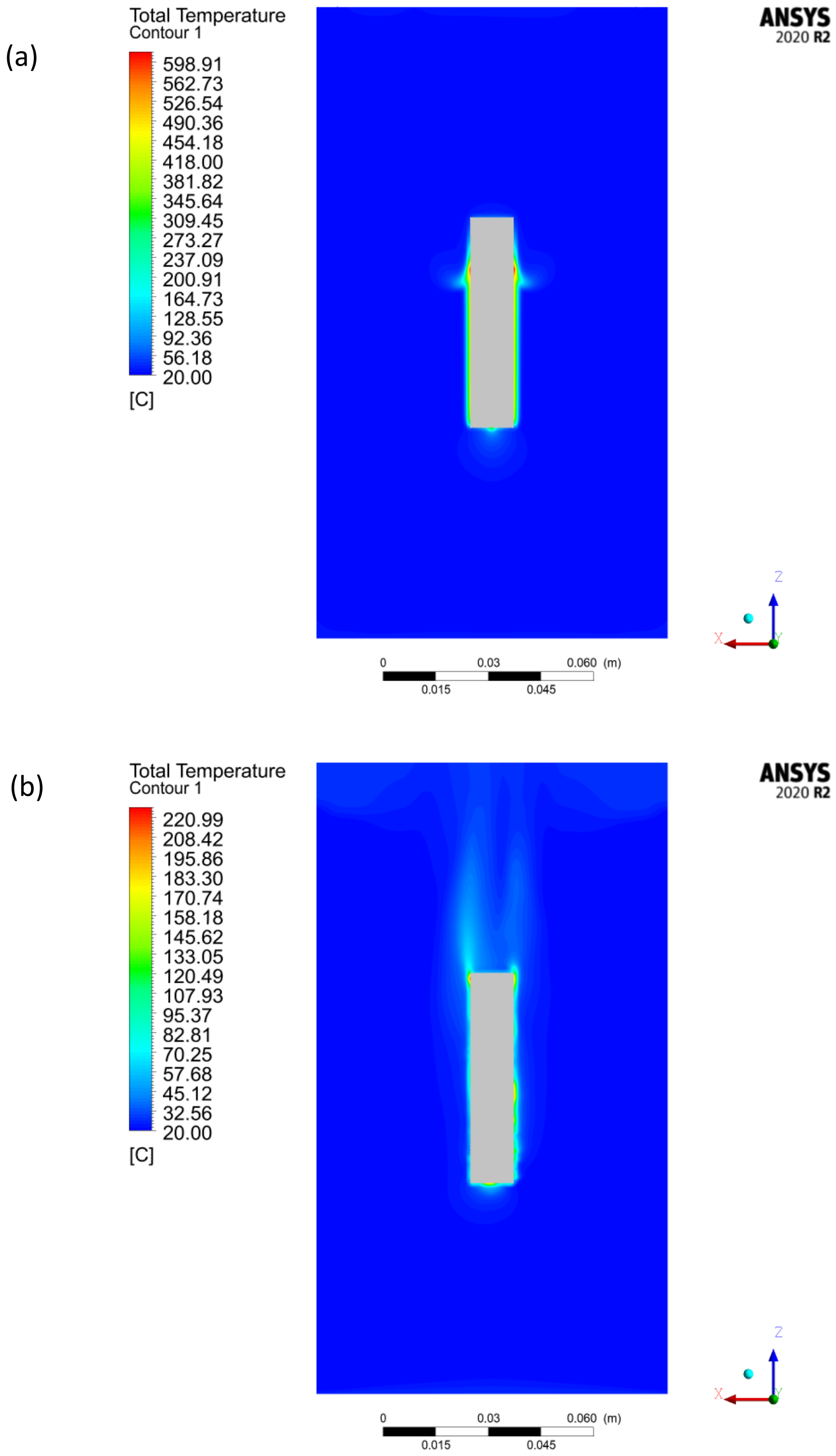

Figure 31 Fluid Temperature Distribution in the Quench Tank at t=2.2 s of (a) Single-phase Model, (b) Multiphase Model.

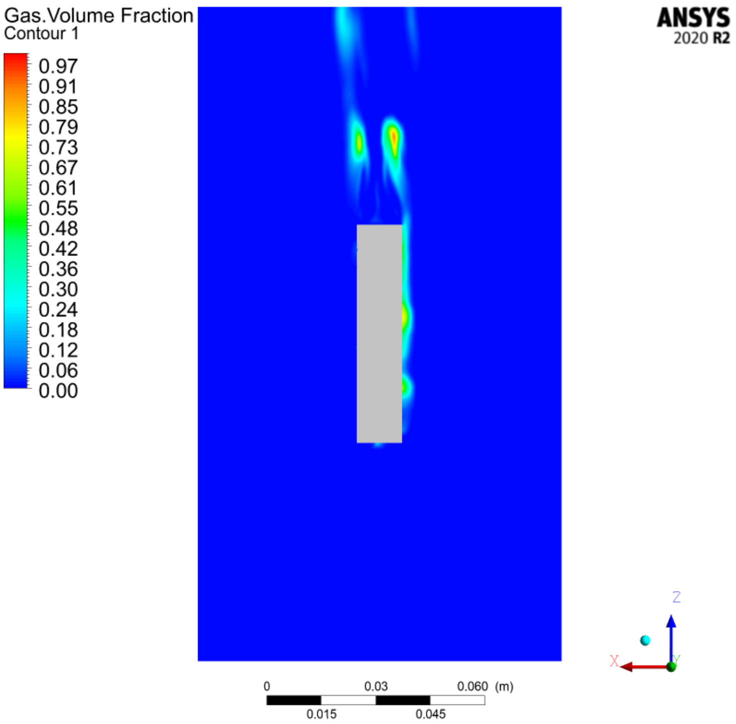

Figure 32 Gas Phase Distribution of the Multiphase Model at t=2.2 s.

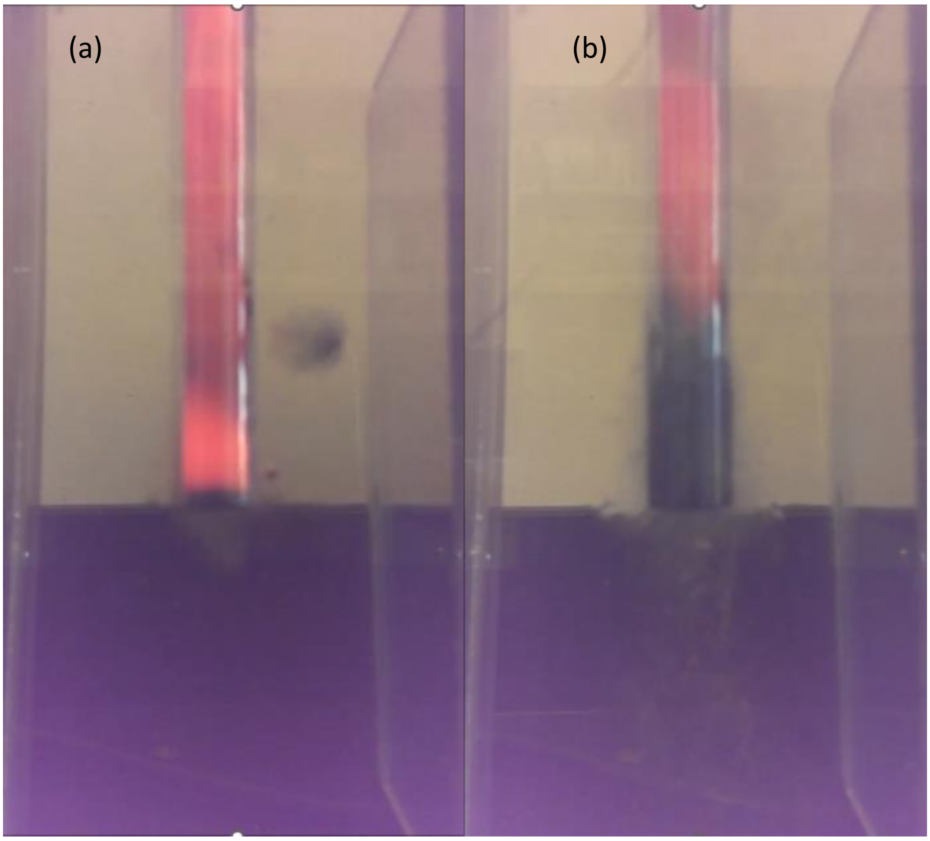

Figure 33 Photos Taken at Different Times During the Quenching Test (a) t=0 s, (b) t=1.4 s.

After approximately 1.4 seconds, the vapour blanket collapses, generating a lot of small bubbles that are not recognizable by the naked eye in the fluid zone near the solid sample. This corresponds to the blurry area around the solid sample in Figure 33 (b). It is therefore conclusive that in the case of this quench cooling experiment, the transition from film boiling to nucleate boiling is completed by the time t=1.4 seconds after fully immersion.

On the other hand, according to the experimentally measured temperature at the centre of the sample, the maximum cooling rate is observed at t=2.2 seconds. This is in good agreement with the statement that the observed cooling rate peak at the centre of the sample is later than the inception of nucleate boiling. According to calculations, the maximum cooling rate of the multiphase model is also at t=2.2 seconds. Even though this time is in perfect agreement with the experimental data, it is improper to conclude that the multiphase model succeeds in mechanically predicting the cooling behaviour during this specific quench cooling case, because of the obvious difference in the maximum cooling rate value and the shape of the cooling rate curve.

4.4 Temperature Dependent Water Density

In this section, the single-phase model and the multiphase model are solved again but the water density is changed to a function of temperature expressed by Equation (131) instead of a constant. The unit of this equation is K and Kg/m^3.

$$\rho_l = 1.625 \times 10^{-5} T^3 - 0.0193 T^2 + 6.947 T + 213.971 \tag{131}$$

The predicted temperature profiles of the single-phase models with a constant water density and a temperature dependent water density are plotted in Figure 34. It could be seen that huge improvement is made by considering the influence of temperature on the water density for the single-phase model. However, there is still significant discrepancy between the result of the single-phase model with a temperature dependent water density and the experimental data.

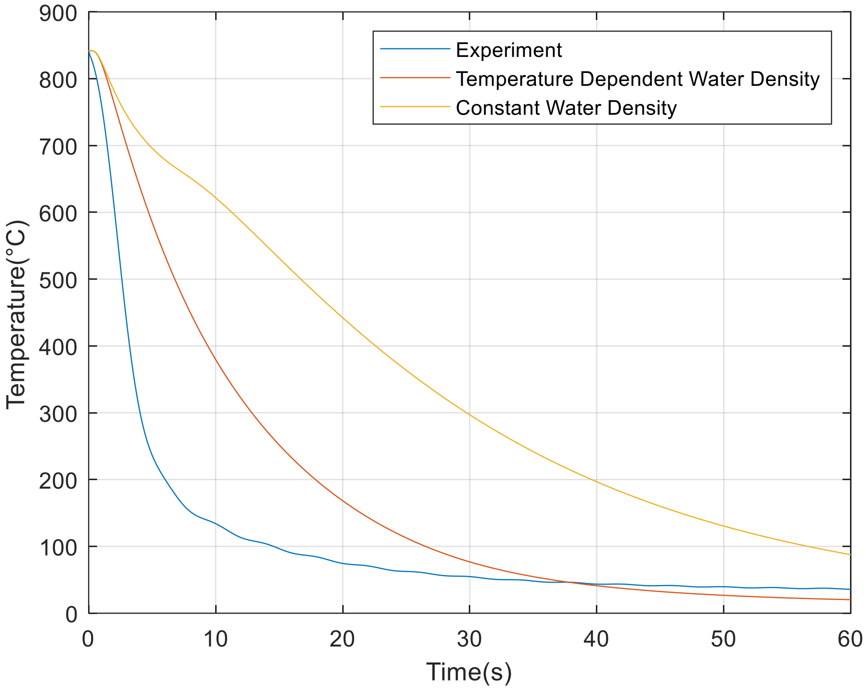

Figure 34 Temperature Curves of Single-phase Models with a Constant and a Temperature Dependent Water Density.

The reason for the improvement in the temperature prediction is confirmed by analyzing the fluid temperature distribution in the quench tank. According to Figure 35 (a), the water around the solid sample is heated up to around 200 ℃ and then rises away from the solid sample under the effect of a decreased density. The water temperature is reduced to approximately 100 ℃ half way to the pressure outlet surface via the convection with the environment. The rising velocity of the heated water is about 0.1 m/s, according to Figure 35 (b). At around t=3 s, the flow pattern of the heated water approaches a semi-steady state and forms a constant rising stream until the solid sample is cooled down to a relatively low temperature.

It can be seen that the fluid temperature around the solid sample of the variable water density model is significantly lower compared to a constant water density according to Figure 31 (a) and Figure 35 (a). This is because the constant rising stream of the variable water density model causes the cool water to flow from the surrounding environment to the near-solid high temperature region, limiting the temperature increasement in the region. As expected, this phenomenon contributes to a largely enhanced cooling rate prediction of the single-phase model.

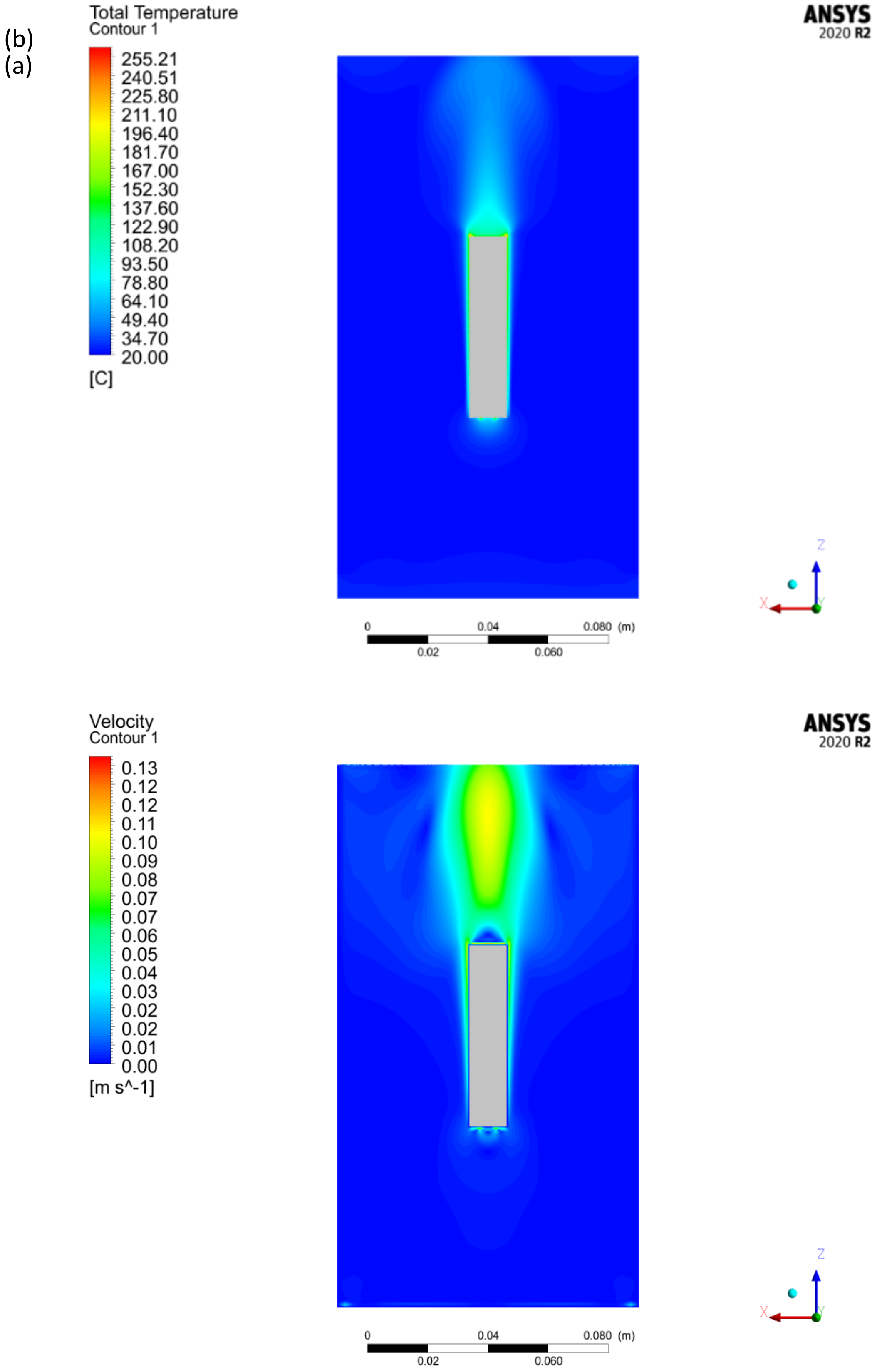

Figure 35 Visualization of Fluid Properties Distribution of the Single-phase Model with a Temperature Dependent Water Density at t=2.2 s (a) Temperature, (b) Velocity.

Unlike the single-phase models, the predicted cooling rate of the multiphase model with a variable water density is almost the same as the previous multiphase model. The temperature and cooling rate curves of these two models are in the Appendices. Interestingly, the prediction of the single-phase model with a variable water density is very close to the results of the multiphase models, as shown in Figure 36.

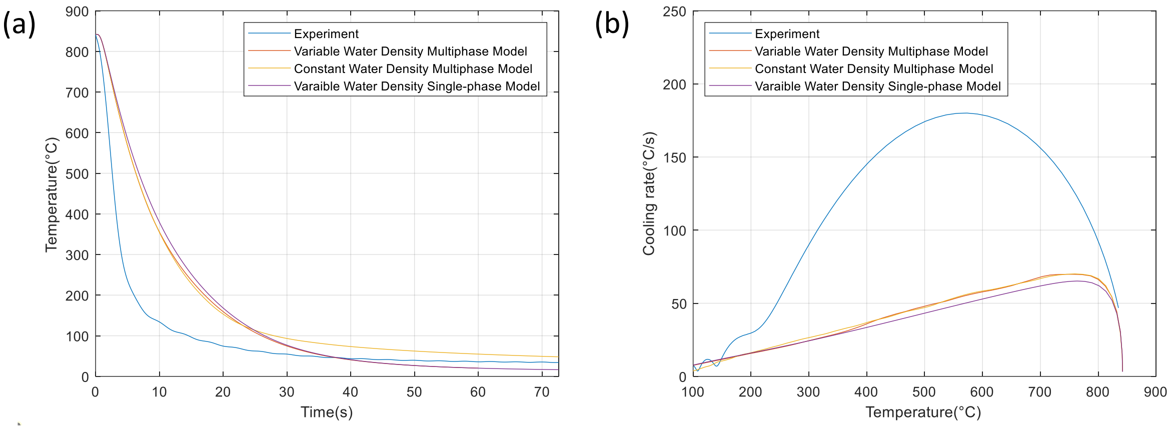

Figure 36 (a) Temperature and (b) Cooling Rate Curves of the Variable Water Density Single-phase Model and the Multiphase Models with Variable and Constant Water Densities.

During the cooling process, the temperature of the single-phase model is slightly higher than the other two models according to Figure 36 (a). This could also be seen from Figure 36 (b), where the cooling rate of the single-phase model is lower than the other two models in a big temperature range from 350 ℃ to the max temperature. However, both the models with the variable water density end up with a temperature lower than the experimental data and model with a constant water density. This is because in the models with the variable water density, the pressure outlet is enabled to avoid the pressure change in the quench tank due to the thermal expansion of water. As the heated water exits the water tank from the pressure outlet, back flow of water at 20 ℃ enters the quench tank to make up the volume loss, and such process yields net energy loss in the quench tank fluid system, so the eventual temperature is very close to the back flow fluid temperature. In the case of the experimental process, the heat loss of the quench tank is carried out via the heat transfer between water and air at the water level surface, which is far slower. As a result, the final temperature of the experimental data is higher than the models with the variable water density. As for the model with a constant water density, all the walls of the quench tank are specified as adiabatic walls, so all the heat is kept in the quench tank, resulting in the highest final temperature among all the data groups.

It can be concluded based on the results of the four models so far that the fluid temperature and flowing behaviour in the near-solid region plays a major role in the cooling of the solid sample. As previously mentioned, heat transfer between the solid sample and the fluid phase at the interface is very likely to be the rate limiting factor of the overall cooling rate of a small-scale solid sample. Particularly, for Inconel 600, the thermal conductivity is higher at high temperature, so the influence of the thermal conduction in the solid domain is further reduced.

In the single-phase model with a constant water density, the water around the solid surface hardly moves, so the heat transferred from the solid sample is accumulated in this region. Due to the high temperature of the surrounding fluid, the temperature difference between the solid wall and the liquid is small, resulting in relatively slow heat transfer rate. Such problem is mitigated by including either a temperature dependent water density or the boiling mass transfer effects. These two modifications enhance the predicted cooling rate in the same manner, which is creating an upward stream from the near-solid fluid region by either the bubble departure and movement or the convection flow due to different densities. Taking the boiling mass transfer effects into account produces slightly better predictions than having a temperature dependent water density, but having these two factors at the same time would not make further improvements. According to Figure 37 and Figure 35 (b), the fluid velocity induced by the boiling effect is higher than that induced by a variable water density.

In conclusion, the fluid temperature in the near-solid region is a key factor of accurately predicting the temperature curve of the solid sample. Meanwhile, the fluid temperature is heavily dependent on the flowing conditions in this region and the factors that may affect the convection heat transfer between the near-solid region and the environment. Therefore, it is optimal for the computational model to incorporate all the factors that could potentially affect the flow conditions in the quench tank.

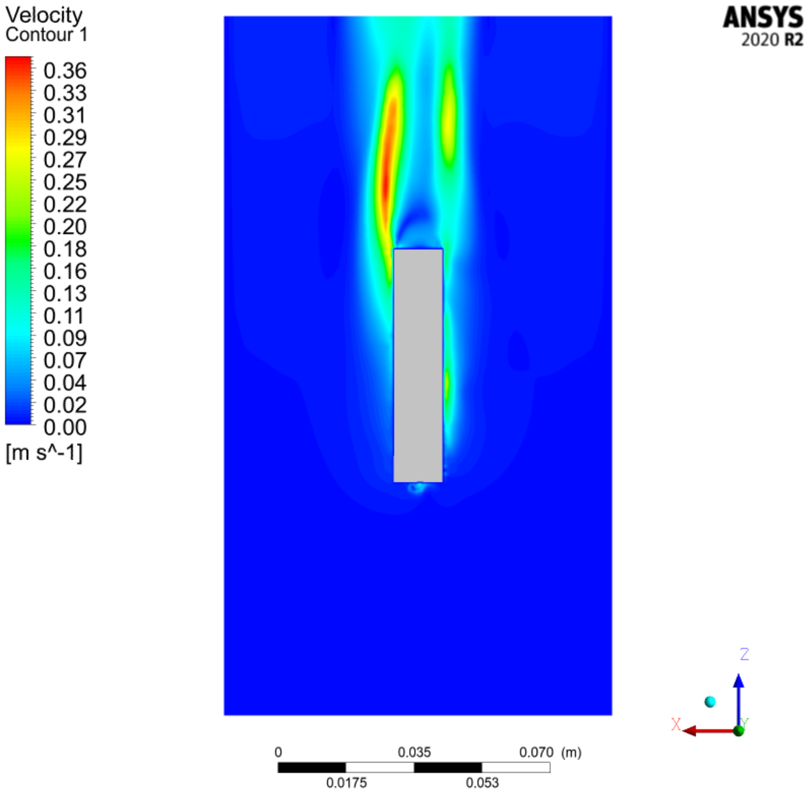

Figure 37 Velocity Distribution in the Quench Tank of The Multiphase Model at t=2.2 s.

4.5 Inlet Flow Enabled (Immersion Process)

Apart from the boiling effects, the immersion process of the solid sample also generates noticeable fluid flow around the solid sample, especially during the initial stage of cooling. As mentioned in §3.11.1 , the immersion process of the solid sample is simulated by setting the gas phase as the initial phase in the quench tank and having a velocity inlet on the bottom surface of the quench tank. The inlet velocity magnitude is described by Equation (132) in the unit of m/s.

$$u_0 = \frac{0.8963}{1 + exp[30(t - 0.2)]} \tag{132}$$

According to Equation (108), the immersion time of this case is 0.4 seconds, and this immersion time is subtracted from the simulation results, i.e., the simulated cooling process is considered to start when the flow time is 0.4 s. This model is a multiphase model with a temperature dependent water density.

The addition of this velocity inlet can potentially cause the instability of the solver, but such problem can be mitigated by reducing the value of C_{u_0} in Equation (107). Other coefficients in the equation must be adjusted accordingly to make sure that the time needed for the immersion process and the total inlet volume are not changed.

If the model is still unstable and C_{u_0} can no longer be reduced, other model parameters are adjusted for a better model stability depending on the cause for the instability. There are two major causes for the instability involved with velocity inlet.

4.5.1 Global Courant Number Exceeds 250.00

Extremely high Global Courant Number can cause huge difficulties to reach convergence, especially for the convergence in the velocity fields. When such problems are encountered, the solution process is interrupted, and the following message is displayed by the solver.

```
Error at Node 0: Global Courant number is greater than 250.00
The velocity field is probably diverging. Please check the solution and reduce
the time-step if necessary.
```

The Global Courant Number (or referred to as Courant-Friedrichs-Lewy, CFL) is a dimensionless value that evaluates the overall flowing rate of the fluid phase. In CFD simulations, the Global Courant Number is closely related to time step size in the ANSYS Fluent solver by the relationship given by Equation (133).

$$CFL_{global} = \Delta t \cdot \max\left(\sum \frac{outgoing\ fluxes}{volume}\right) \tag{133}$$

According to this equation, the Global Courant Number is linearly proportional to the time step size if the flowing conditions are the same. Meanwhile, for a fixed time step size, reducing the overall flowing velocity of the fluid phase can also reduce the Global Courant Number.

In the ANSYS Fluent solver, the CFL is expected to be less than 2 (or 1, depending on the specifications of the solver), so if the fluid flowing behaviours are not changed, the time step size should theoretically be reduced by a factor of 125. This is hardly possible, because the solution time of the model will also increase to an unacceptable level. Instead, a variable time stepping strategy can be applied. In this way, the solver decides the size of every single time step according to Equation (133), as well as a set of user-input values, including initial time step size, number of fixed time steps, time step size growth factor, and the upper limit of the

CFL. The advantage of this strategy is that the time step size is reduced when the flowing condition is rapidly varying, so the stability of the model is ensured, whereas if the overall fluid flow is relatively slow and steady, the solution process is accelerated by gradually switching to larger time step sizes.

4.5.2 Divergence in AMG Solver

When divergence is detected in the AMG solver, abnormally high values of various variables are often obtained, and the following message is returned from the solver.

```
temperature limited to 5.000000e+03 in 466842 cells on zone 6 in domain 1
turbulent viscosity limited to viscosity ratio of 1.000000e+05 in 548811
cells
Stabilizing temperature to enhance linear solver robustness.
Stabilizing temperature using GMRES to enhance linear solver robustness.
Divergence detected in AMG solver: temperature
Stabilizing vof-1 to enhance linear solver robustness.
Stabilizing vof-1 using GMRES to enhance linear solver robustness.
Error at host: floating point exception
Error: floating point exception
Error Object: #f
Warning: An error or interrupt occurred while reading the journal file.
Some commands may not have been completed.

> Halting due to end of file on input.
```

This problem is mainly associated with the selection of solution method and poor mesh quality, more specifically, high skewness and aspect ratio. As mentioned in §4.2 , the regions close to the quench tank wall is inevitably poor, due to the requirement of fine mesh grids in the near-solid area and the need to reduce the solution difficulty. Nevertheless, the impact of poor meshes can be mitigated by changing the discretization scheme from Second Order Upwind to First Order Upwind. For high skewness and aspect ratio elements, the distance between two neighbouring cells can be much higher in a certain direction compared to other directions. Switching the discretization scheme from Second Order Upwind to First Order Upwind can avoid the effects of highly different dimensions of elements in multiple directions.

Another viable method of increasing the stability of the model is to apply Under-Relaxation Factors (URFs) for the diverged variables. A URF is a positive value smaller than 1 which reduces the change of a variable within a single iteration, and consequently improves its convergence [143]. For a certain variable ϕ, the influence of a URF is described by Equation (134).

$$\phi_{n+1} = \phi_n + C_{URF}\Delta\phi \tag{134}$$

However, when the URF is applied, the time required to reach convergence is increased, and the increasement is magnified if the URF is very small.

4.5.3 Results and Discussions

Unfortunately, the addition of velocity inlet to the model does not make a noticeable difference as expected. Even though the temperature curve of the model with the velocity inlet appears to be closer to the experimental data in a very short period after immersion, this does not mean the model predicts the cooling behaviour more accurately. Instead, it is because the exclusion of the immersion time shifts the whole curve to the left direction. In addition, the predicted temperature curve of the model with a velocity inlet shows even larger errors after 5 seconds compared to the multiphase model. In Figure 38, the cooling rate of the model with velocity inlet is slightly below the curve of the multiphase model throughout the whole cooling process, and this is also reflected in the figure of the temperature curves.

To examine whether the velocity inlet functions as expected or not, the vapour phase distribution at t=0.4 s is visualized in Figure 39. As previously mentioned, the velocity inlet is tuned to make sure that the solid sample is immersed into the water and placed at the centre of the quench tank at this time. In this figure, the vapour phase near the bottom surface of the solid sample corresponds to the big bubble generated as a result of the immersion process

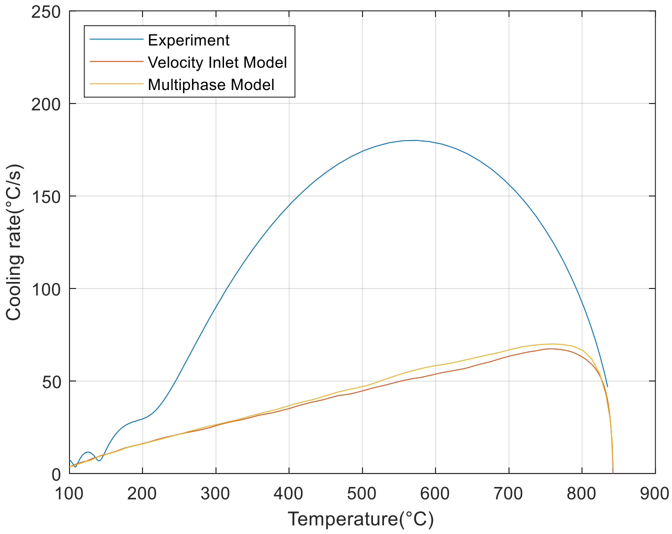

Figure 38 Cooling Rate vs. Temperature Curves of the Model with Velocity Inlet, the Multiphase Model, and the Experimental Data.

in Figure 33 (a). The small bubbles in Figure 33 are also well reflected by the mid-low gas volume fraction region near the solid sample in Figure 39.

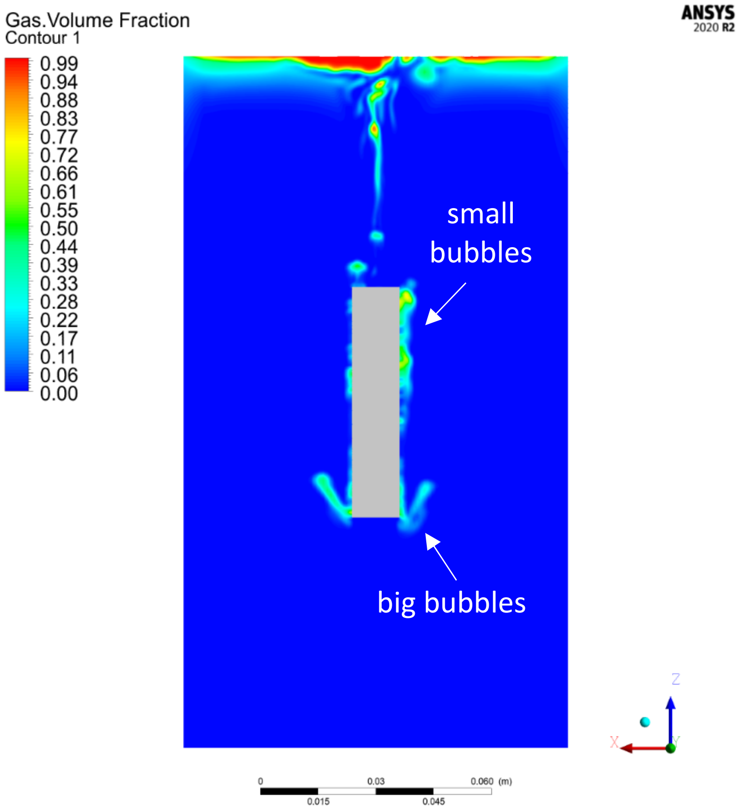

Figure 39 Vapour Phase Distribution in the Water Tank of the Velocity Inlet Model with Velocity Inlet at t=0.4 s.

In addition, a disturbed water surface is successfully predicted by the model as a result of both the immersion movement of the solid sample and the bubbles reaching the water surface. All these phenomena show that the fluid motions induced by the immersion process of the solid sample are successfully reflected in the model.

4.6 Initial Temperature Gradient Inside Solid

In Figure 30, both the simulated temperature curves show a short delay after the cooling is started, whereas the experimentally recorded temperature drops instantly as the cooling is initiated. In Figure 30 (a) and (b), the initial value of the predicted cooling rate is zero, but the experimentally measured cooling rate starts from 47 ℃/s at t=0. In addition, as mentioned before, the experimentally recorded initial temperature is below the expected heating temperature.

These observations indicate that cooling is already ongoing at the solid sample centre when the thermal couple starts recording the temperature. Two possible reasons for this phenomenon are:

a) The quenching system is programmed to start recording the temperature only when a pre-set cooling rate or a certain amount of drop in temperature is reached.
b) The solid sample is pre-cooled in the air while being transferred from the furnace to the quench tank.

Even though the distance between the furnace and the quench tank is quite short according to Figure 25 and the transferring process only takes a short period of time, the spatial difference of temperature is still very likely to form inside the solid sample considering the small dimensions and volume of the sample.

In this case, the initial spatial difference of temperature inside the solid sample has a significant influence on the temperature profile at the centre of the sample, especially during the short period right after the cooling is started. Even if the heat transfer rate at the solid-liquid interface is accurately predicted, noticeable error can be induced if the effect of initial temperature gradient inside the solid sample is not considered. Thus, in this section, an initial temperature gradient in the solid domain is introduced to incorporate the prior cooling effects during the transferring process.

As mentioned in §3.11.3 , the initial solid temperature gradient is assumed to be linearly proportional to the distance to the solid centre, as described by Equation (100).

The predictions of the model with initial temperature gradient and the multiphase model are analysed. The temperature curves of these two models are very close to each other, with the temperature of the initial temperature gradient model being slightly lower. The main difference between these two curves is at the initial stage of the cooling process, as shown in Figure 40. As expected, the initial temperature gradient in the solid sample provides an instant cooling at the sample centre, but this influence diminishes in less than 0.5 s. Such behaviour can be better observed in Figure 41. Even though the model with an initial temperature gradient successfully predicts an initial cooling rate that is very close to the experimental data, the cooling rate rapidly decreases to a level that is equivalent to the multiphase model and no longer has any influence on the subsequent cooling. Therefore, the initial temperature gradient in the model yields an instant temperature drop at the inception of the cooling process but does not have noticeable influence on the subsequent cooling behaviour.

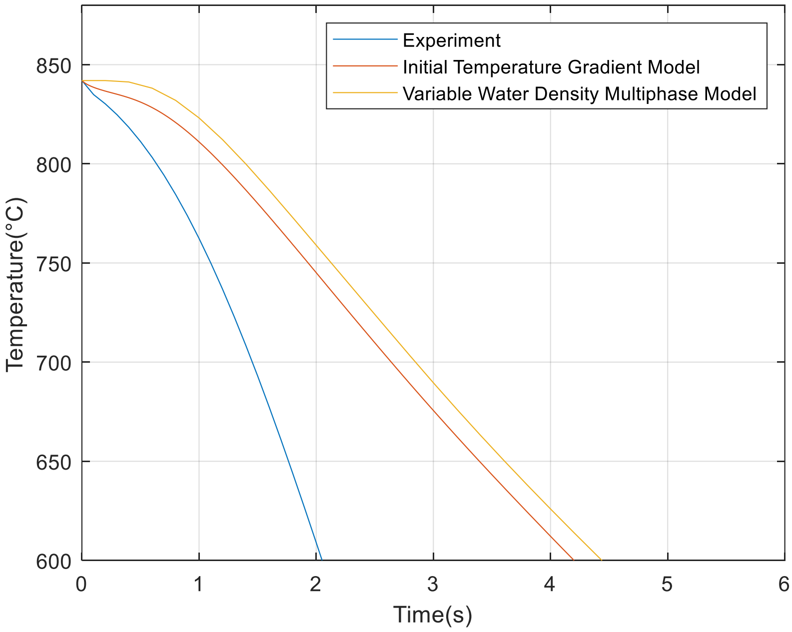

Figure 40 Temperature Curves of the Model with Initial Temperature Gradient and the Multiphase Model in the First Few Seconds of Cooling.

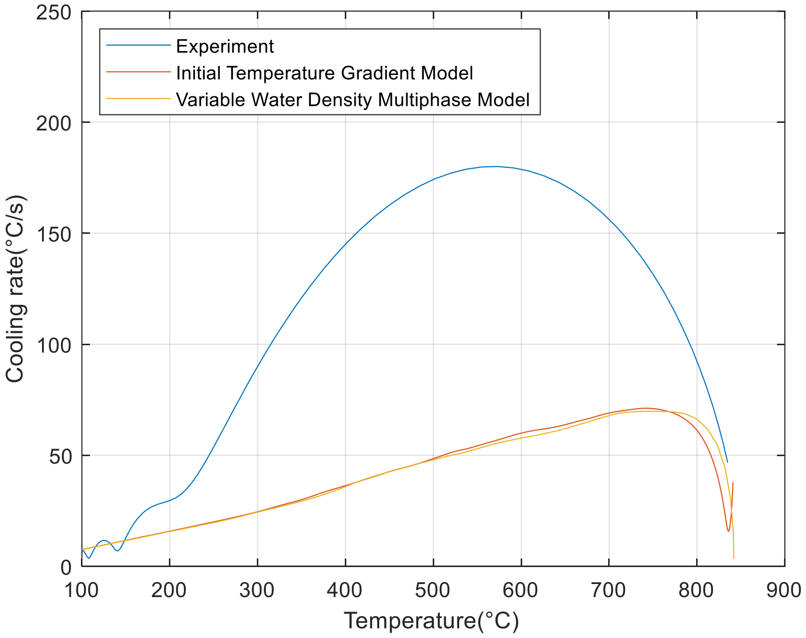

Figure 41 Cooling Rate vs. Temperature Curves of the Model with Initial Temperature Gradient and the Multiphase Model.

Nevertheless, the initial cooling rate of the simulation result illustrates that the effect of the thermal conduction in the solid sample is considered by the model. In addition, the thermal conduction rate induced by the initial temperature gradient is much higher than the heat transfer rate at the solid-liquid interface. This conclusion is drawn from the sharp drop of the cooling rate from the inception of the cooling process.

In the beginning, heat is transferred in the solid sample from the centre to the edge under the effect of a strong heat flux induced by the initial temperature gradient. Since the thermal conduction rate in the solid domain is higher than the heat transfer rate at the solid-liquid interface, the cooling rate of the solid cells that are close to the solid surface is slowed down by the difference between these two heat fluxes. As a result, the temperature gradient in the solid domain is reduced and the cooling rate at the solid centre is decreased. When the local minimum of the cooling rate in Figure 41 is reached, the thermal conduction rate and the heat transfer rate are equal. At the same time, the determining factor of the cooling rate at solid centre is switched from thermal conduction to heat transfer.

In conclusion, for this specific quench cooling case, the cooling rate at the solid centre is determined by the heat transfer rate at the solid-liquid interface. This is because the thermal conduction rate has the potential to reach a higher level than the heat transfer rate, and the temperature evolution at the solid centre is a result of a sequential cooling process which consists of the thermal conduction in the solid domain and the heat transfer at the solid-liquid interface. Meanwhile, in such a small sample, a high temperature gradient can diminish in less than one second, so the temperature at the solid centre is very sensitive to the heat transfer rate at the solid-liquid interface.

4.7 Higher Boiling Intensity

As previously mentioned, the evaporation coefficient of the boiling mass transfer model is subject to adjustment according to the actual boiling intensity. By keeping the condensation coefficient unchanged, a higher evaporation coefficient yields a higher boiling intensity. It is expected that with a higher boiling intensity, the higher bubble generation rate will lead to a stronger rising stream, which can potentially enhance the convection heat transfer in the fluid domain.

The evaporation coefficient is changed from 0.1 to 1 while all other model parameters remain the same, and the results are compared with the reference model, which is the multiphase model.

Figure 42 shows the temperature curves of these two models and the experimental data. Obviously, the increased evaporation coefficient yields slightly faster cooling in the fast-cooling period (also see Figure 92 in Appendices). In addition, the major difference of the cooling rate between the two models are in the time period of 2-30 seconds where the discrepancy between the model results and the experimental data is the most obvious.

As previously discussed, the predominant boiling mechanism in this time period is nucleate boiling. The boiling behaviour predicted by the evaporation condensation boiling mass transfer model is very close to nucleate boiling. Therefore, by increasing the evaporation coefficient, the predicted boiling effect becomes more intense, and closer to the real nucleate boiling effect in the experiment. This exposes a lack of the ability to simulate the real intensity of the nucleate boiling effect.

To characterize the mechanism behind the cooling rate enhancement, the distribution of vapour phase volume fraction and the fluid velocity is visualized for the new model.

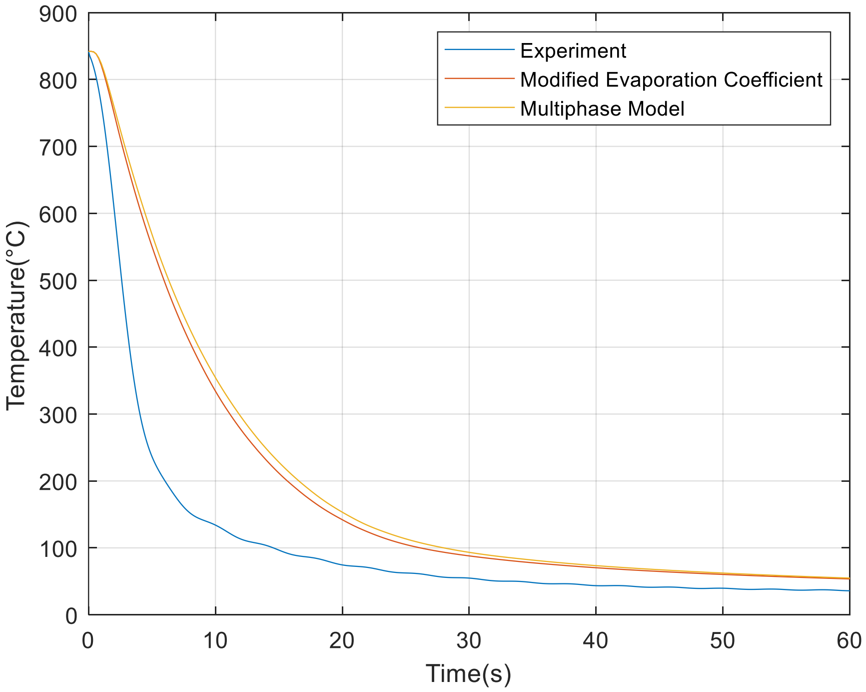

Figure 42 Temperature Curves of the Both Models and the Experimental Data.

Comparing Figure 43 (a) to Figure 32, it can be seen that there is much more vapour phase in the model with an increased boiling evaporation coefficient than in the basic multiphase model. This is an expected result, because a larger evaporation coefficient yields higher vapour generation rate at the same temperature. As a result, the fluid velocity in the near-solid region of this model mostly lies around 0.3 m/s while at some positions it can reach as much as 0.5 m/s, as shown in Figure 43 (b). Compared to the velocity distribution of the multiphase model shown in Figure 37, the much higher velocity field of this model indicates a higher convection heat transfer rate in the fluid domain. However, the fluid temperature in the near-solid region of the new model is significantly higher than that of the multiphase model. This is because in the new model, there is more vapour phase in the near-solid region, so the overall specific heat of the fluid mixture is smaller. In addition, the higher cooling rate at solid centre indicates a higher heat transfer rate at the solid-liquid interface. As a consequence, the transient fluid temperature appears to be higher in the model with an increased evaporation coefficient.

On the other hand, with a higher vapour generation rate, more boiling latent heat is extracted from the liquid phase. This portion of heat is eventually taken away by the vapour bubbles, so the temperature increasement of the liquid phase in the near-solid region is limited.

(a)

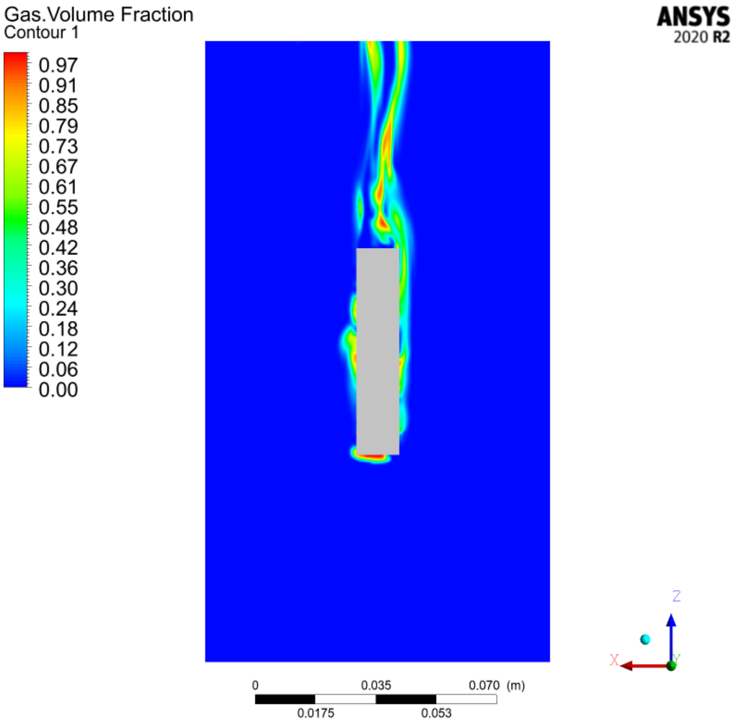

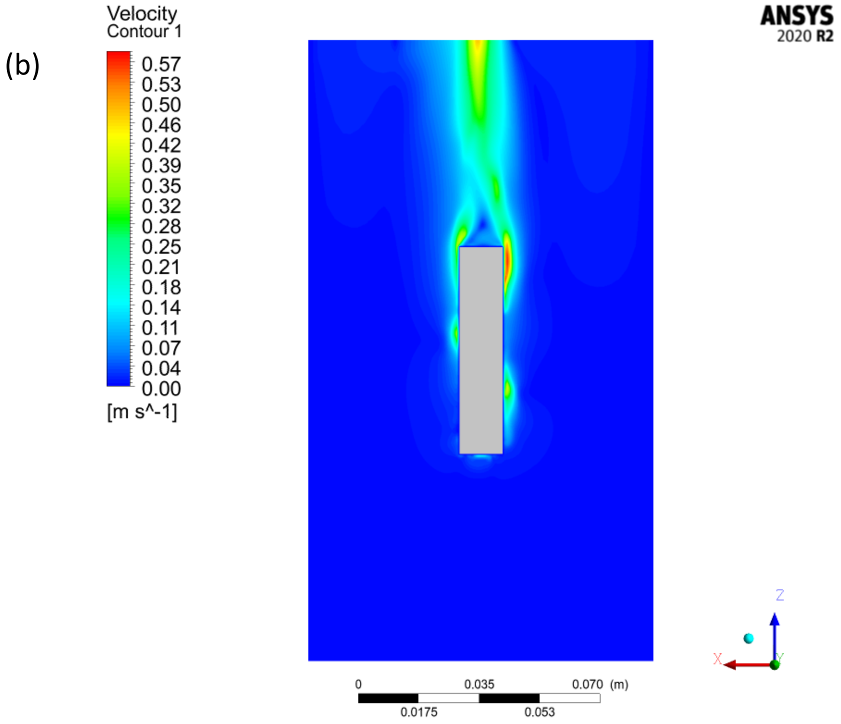

Figure 43 Distribution of Vapour Phase Volume Fraction and Fluid Velocity of the Model with Increased Evaporation Coefficient at t=2.2 s.

4.8 High Intensity Circulating Flow Case

Modifications have been introduced to generate even higher flow intensity around the sample. This is has been achieved by dividing the top surface into two halves, one is a constant velocity inlet where the inlet velocity magnitude increases with increasing distance from the surface centre, the other is pressure outlet. Therefore, a constant circulating flow is generated in the quench tank, which is similar to the effect of agitation. The aim of this simulation is to confirm the influence of a much more intense fluid flow in the fluid domain on the cooling rate of the solid sample.

The results of this model are compared with the reference model (the multiphase model) and shown in Figure 44. It can be seen from the temperature curves that the cooling rate of the new model is significantly increased compared to the multiphase model. However, the cooling trend is not changed, which could be seen from Figure 44 (b). The cooling rate difference between the two models at each temperature is slightly increased from 100 ℃ to 750 ℃, forming a slightly increasing margin between the two cooling rate curves.

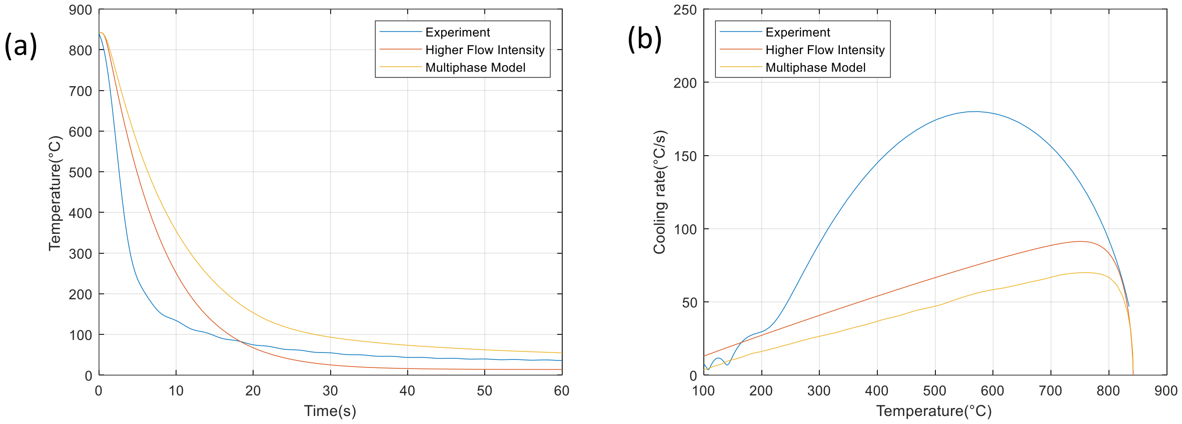

Figure 44 (a) Temperature Curves and (b) Cooling Rate Curves of the Model with Much Higher Flow Intensity.

The flowing behaviour in the quench tank is analysed by visualizing the fluid velocity. In Figure 45, the vectors represent the direction and magnitude of the velocity at different locations. It can be clearly seen that the fluid constantly flows in and out on the top surface because of the boundary conditions. The fluid velocity is relatively low in the bottom half of the quench tank as well as in the near-solid region because of the no-slip conditions of the solid sample and quench tank walls. Nevertheless, the overall fluid flow in the quench tank is rapid enough to significantly enhance the convection heat transfer in the liquid domain.

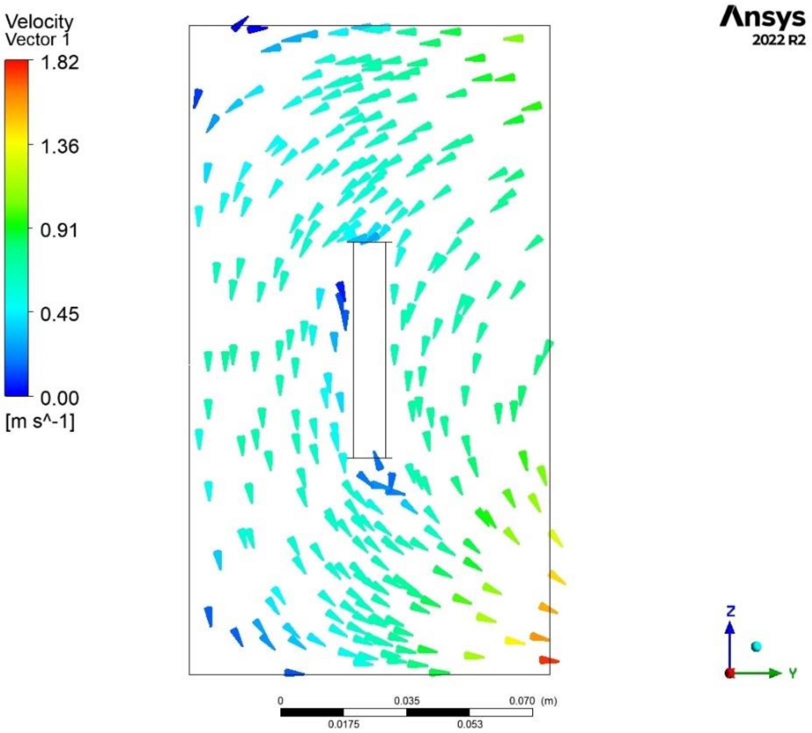

Figure 45 Fluid Velocity Vectors in the Quench Tank at t=1 s.

The temperature conditions of the fluid domain are shown in Figure 46. Under the intense fluid flow in the quench tank, the heated water around the solid sample is transferred away through the pressure outlet, creating a fluid temperature difference in the vertical direction. The intense fluid flow also hinders the formation of bubbles. After being generated at the solid-liquid interface, the vapour phase quickly dissipates into the rapid cool liquid flow, thus no noticeable vapour phase is observed throughout the cooling period. Such flow behaviour increases ensures complete contact between the liquid and the vapour phase, which largely accelerates the condensation process that occurs at the interface.

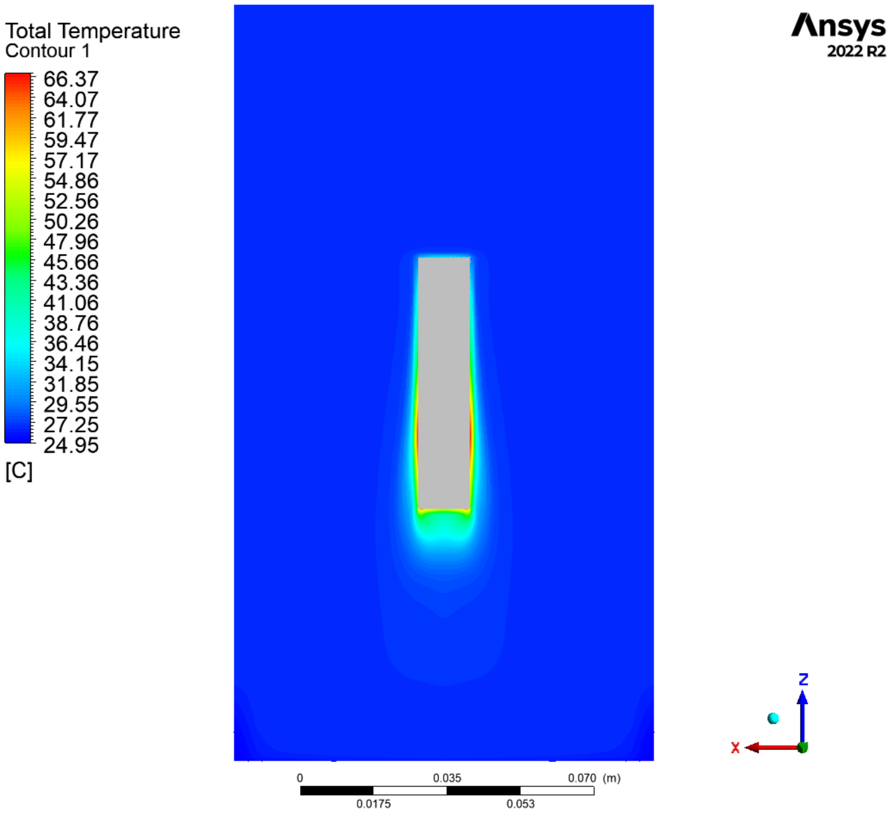

Figure 46 Fluid Temperature Contour in the Quench Tank at t=2.2 s.

4.9 New Mass Transfer Model

The mass transfer model proposed by Sun et al. [93] is applied as a substitution to the evaporation condensation boiling mass transfer model. The new mass transfer model is described by Equation (28). Obviously, this model requires the gradient values of both volume fraction and temperature, so all the three methods of obtaining the gradient value are tested along with this new model.

Since Equation (28) can only predict the generation of vapour phase with a non-zero volume fraction gradient, initial volume of vapour phase is required to make this model work properly. Therefore, the evaporation condensation model is combined with this new model to provide vapour generation in pure liquid cells. If the current composition of a cell is 100% water liquid, then the mass transfer rate is calculated by the evaporation condensation model. If the volume fraction of vapour phase of the current cell is not zero, the mass transfer rate is calculated by Equation (28). The implementation of this combined mass transfer model is accomplished by a mass transfer UDF which can be found in Appendices.

However, this model fails to predict any vapour phase generation during the whole cooling process. This result indicates the mis functioning of the mass transfer model. A possible cause would be that the gradient values are not properly fed to the UDF. If the solver is launched in parallel mode, it always frees up the memory of gradient values. In order to keep the memory of gradient values, the solver has to be running in serial mode. However, the parallel mode involving multiple CPU cores is almost necessary for an acceptable efficiency of the solution process. Therefore, the application of the mass transfer UDF that requires gradient values is not properly carried out due to compatibility issues.

4.10 Heat Flux Boundary Condition

Based on the analysis of previous simulation results, a combination of the coupled thermal boundary condition and the evaporation condensation mass transfer model performs poorly on the simulation of nucleate boiling transfer rate. To justify this judgement, a model with a heat flux boundary condition is tested. The determination of the heat flux value is stated in §3.12.2 .

According to Figure 47, the temperature profiles predicted by different boundary conditions are totally different. This emphasizes the importance of the boundary conditions on the accuracy of the model predictions.

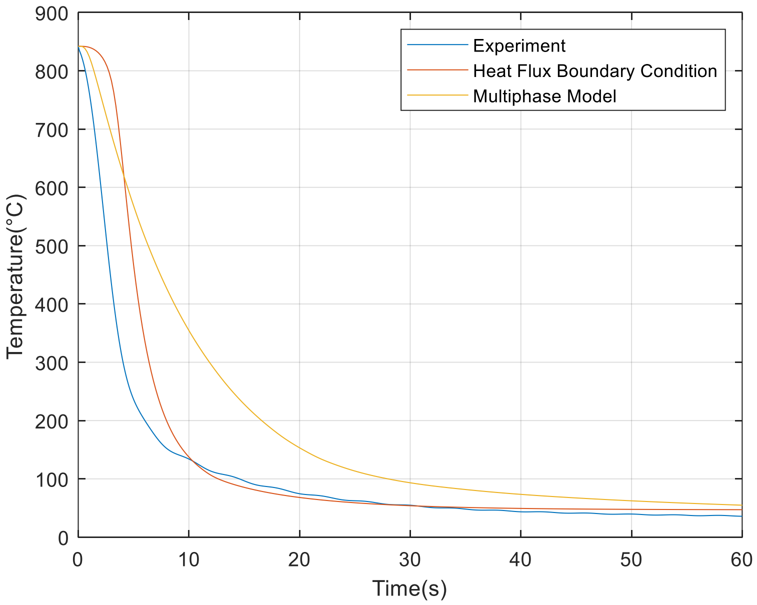

Figure 47 Temperature Curves of the Models and the Experimental Data.

Even though the gap between the experimental data and the result of heat flux boundary condition is big, it mostly looks like a temporal shift rather than error of cooling rate predictions, because the shapes of the two curves are almost the same. In Figure 48, it can be seen that the shapes and the peak values of the two curves are also the same. Hence, it is very likely that the model is successful in simulating the cooling behaviour of the real quench test, but the visualized result is mismatched with the experimental data.

Instead of the simulation data processing method mentioned in §4 , another method is applied to process the simulation result. Due to the fact that the experimentally recorded temperature data starts at a value that is lower than the planned soak temperature and that there is a noticeable immediate cooling rate at the beginning of the experimentally recorded data, it is very likely that the actual cooling is already ongoing when the temperature recording is started.

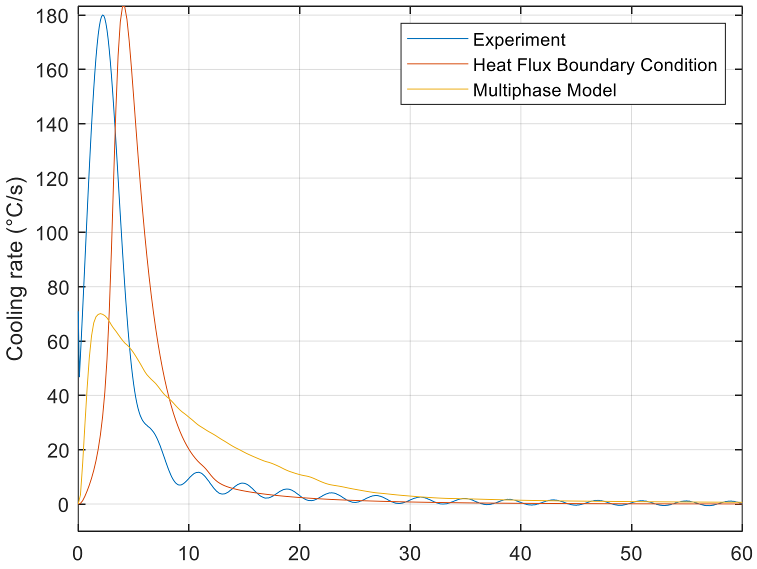

Figure 48 Cooling Rate vs. Time Curves of the Models and the Experimental Data.

According to the experimental data, the temperature at t=0 s is 842 ℃. The closest value in the predicted temperature data is 840.22 ℃ at t=2 s. Thus, the simulated cooling process is assumed to start from 840.22 ℃, and all the time values of the subsequent data points are subtracted by 2 seconds. The data processed by this method is plotted in Figure 49 (a) and (b). With the new simulation data processing method, the temperature and cooling rate curves predicted by the heat flux boundary condition are in perfect match with the experimentally recorded data. The relative average error χ between the simulation result and the experimental data is 27.31% for the entire cooling period (60 s). The error is mostly induced by the low temperature period which is not the major period of concern. Considering only the first 20 seconds of cooling, the relative average error is 2.23%.

However, it must be noted that the application of this empirical heat flux correlation is highly restricted just like most of other empirical methods. Since this method only considers the influence of solid wall temperature on the heat flux at the solid-liquid interface during the cooling process, it cannot incorporate the influence of most local conditions mentioned in §2.4.4 . In addition, this method thoroughly relies on high-order polynomial regression, so the result is very likely to be inaccurate if the initial temperature is extremely low or high. According to the authors, this method is valid only when the initial solid temperature is within the range from 750 ℃ to 950℃ [139].

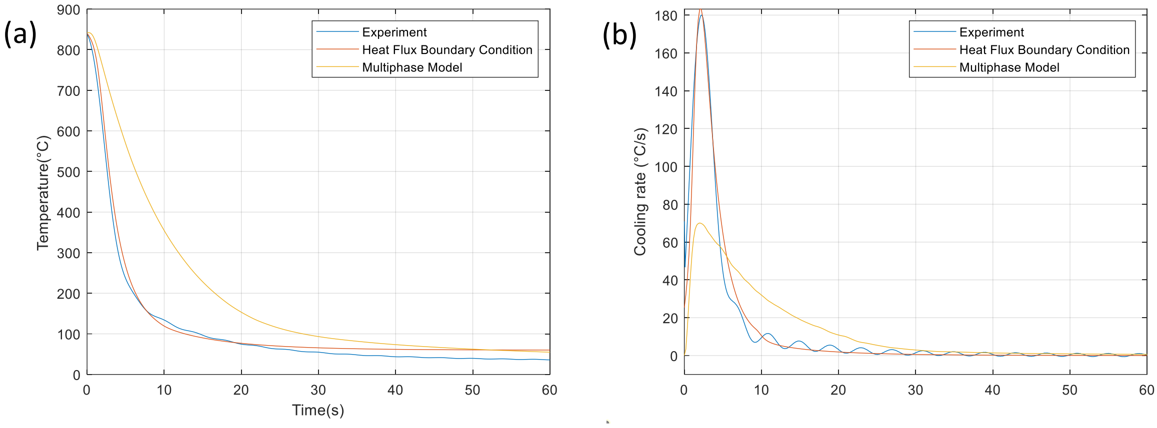

Figure 49 (a) Temperature Curves and (b) Cooling Rate Curves After the New Data Processing Method.

4.11 Parametric Study

In this section, different values of the specific heat and thermal conductivity for both liquid and gas phases are tested in the current model framework. For each property, the tested values are 0.5, 0.75, 1.25, 1.5 times of the actual value. The default thermal conductivity is 0.6 W·m^{-1}·K^{-1} for liquid water and 0.0261 W·m^{-1}·K^{-1} for water vapour. The default specific heat is 4182 J·kg^{-1}·K^{-1} for liquid water, and the value of water vapour is described by Eqn.(135), in the unit of J·kg^{-1}·K^{-1}. The temperature at solid centre is recorded and plotted as shown in Figure 50.

$$Cp = -1.157 \times 10^{-9} * T^4 + 3.216 \times 10^{-6} * T^3 - 2.933 \times 10^{-3} * T^4 \\ + 1.604 * T + 1563.077 \tag{135}$$

The cooling curve of the solid sample does not differ significantly with a varying specific heat, even when the value is halved. On the contrary, the predicted cooling mode can be totally different when the thermal conductivity is changed to 1.5 times. However, this group of data is considered unreliable due to the fact that the cooling rate should increase with a higher fluid thermal conductivity. Throughout the whole simulation process of this case, there is no vapour phase generation, and the temperature of the fluid domain is kept below the saturation point. The model is successful in this part, according to Eqn. (42), that the heat accumulated in the near-solid fluid region dissipates faster with higher thermal conductivity, so the maximum fluid temperature as well as the temperature gradient are lower than the normal case. A possible reason for such unreliability could be that the model fails to capture the correct physical mechanism due to this drastic change in thermal conductivity.

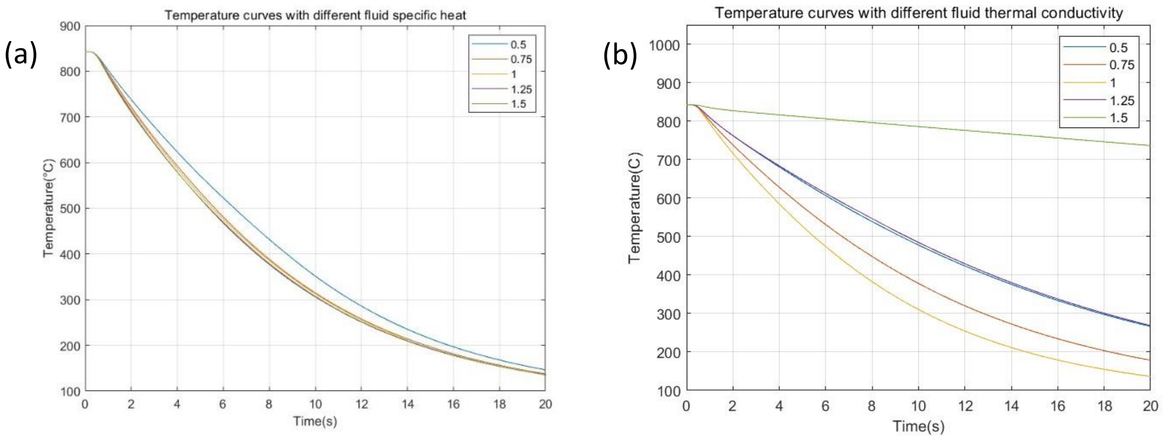

Figure 50 Temperature Curves at Solid Centre for Different (a) Specific Heat, (b) Thermal Conductivity.

Another interesting point is that the 0.5 and 1.25 curves are very close to each other. The mechanism behind this phenomenon is analysed from the perspective of fluid temperature distribution and vapour phase generation. Figure 51 (a) and (b) show the fluid temperature distribution at 2 s of both models, respectively. As can be seen from the figures, the fluid temperature of the 0.5 model is in the range of 70 – 103 ℃, whereas for the 1.25 case, the solid sample is surrounded by fluid over 100 ℃, which indicates that there is more vapour phase for the 1.25 case. This could also be observed from Figure 52. It can be clearly seen that the amount of vapour phase in the 1.25 case is obviously more than in the 0.5 case. Therefore, in both cases, the solid cooling rate is slowed down because of the elevated fluid temperature around the solid sample. In the case of 0.5, such trend is formed by slow thermal conduction in the liquid phase, whereas in the case of 1.25, this is due to a larger amount of vapour phase generated by the boiling effect. However, it is worth noting that the model seems to fail to apply different heat transfer coefficient for liquid and vapour water.

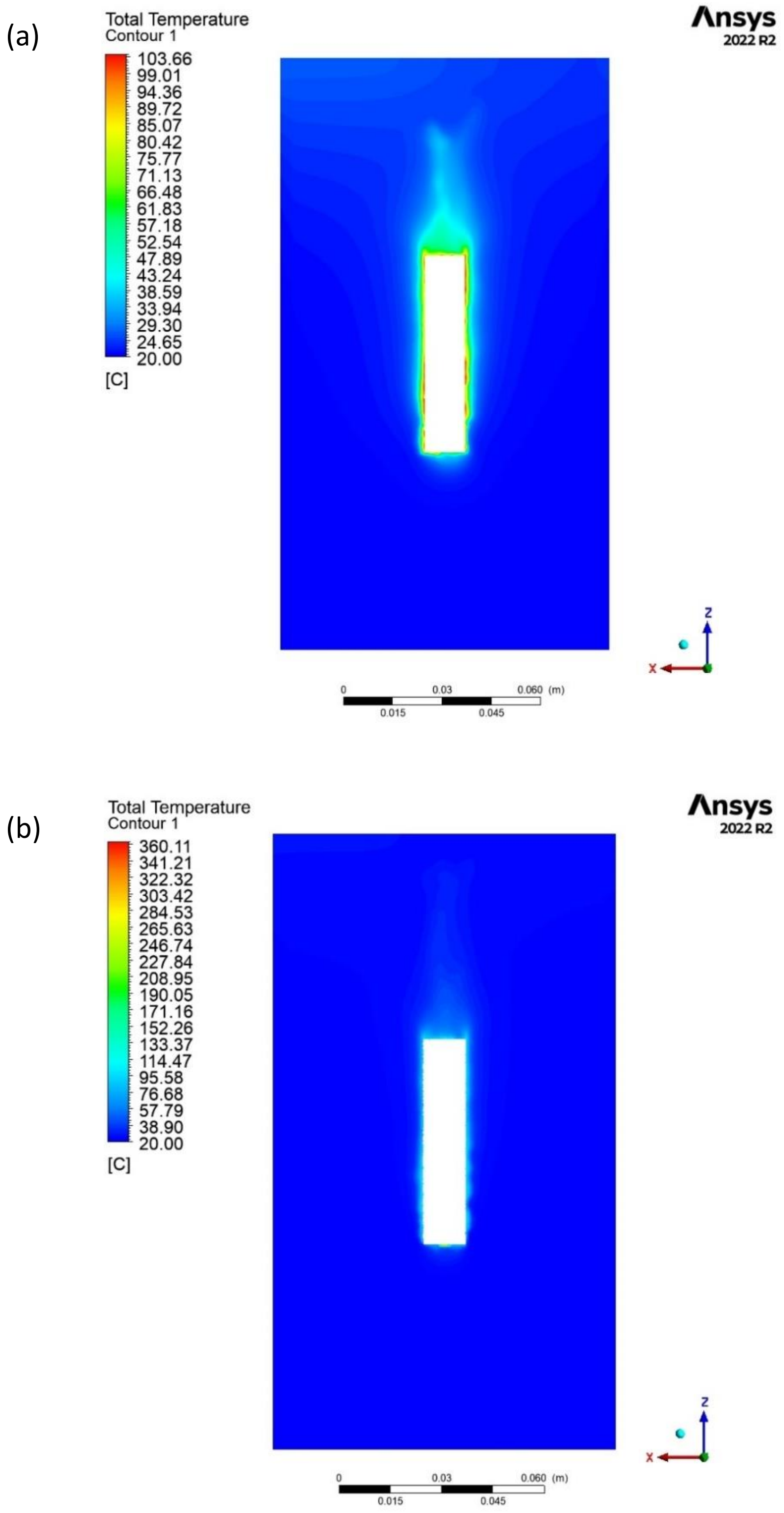

Figure 51 Fluid Temperature Distribution at 2 s of Models (a) 0.5, (b) 1.25.

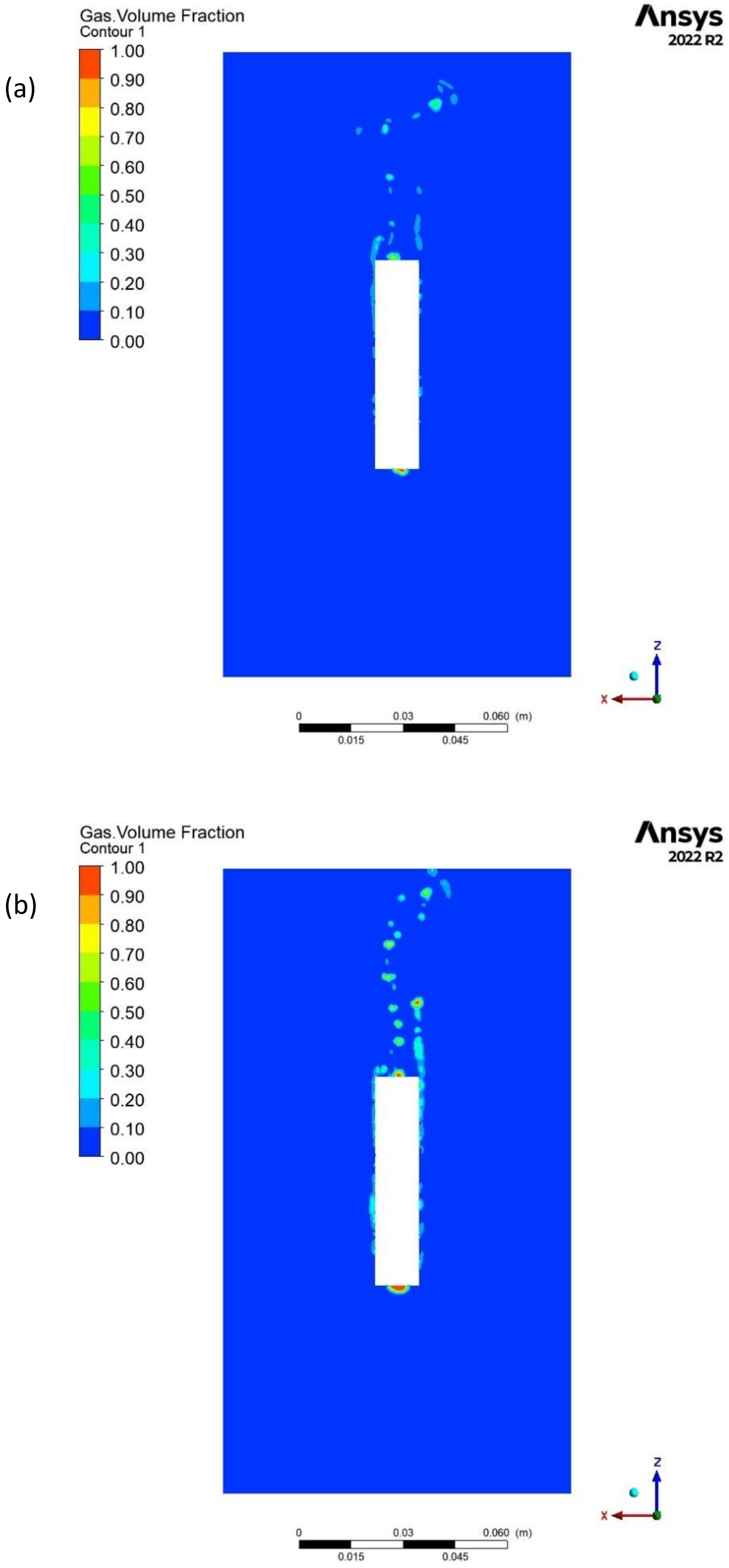

Figure 52 Gas VOF Distribution at 2 s of Models (a) 0.5, (b) 1.25.

4.12 Discussion

In section 4.7 , the evaporation coefficient from Eqn. (24) is shifted from 0.1 to 1. The vapour generating rate is expected to significantly increase as a result because it is directly related to the evaporation coefficient. However, according to Figure 42, the change in the cooling rate at solid centroid is not heavily affected. In addition, even though the amount of vapour phase in Figure 43 (a) is more than that observed in Figure 32, the difference can hardly match how much the evaporation coefficient is changed. Such discovery indicates that despite that the vapour mass generation rate is proportional to the evaporation coefficient, the change in the evaporation coefficient is not directly reflected in the amount of vapour phase predicted by the solver. Due to the inefficiency of documented algorithm and source code of ANSYS Fluent, the reason cannot be clearly stated. This could be involved with the treatment of the interface between liquid and gas phases. As previously mentioned, the framework used in this thesis applies a phenomelogical model on the interface which may fail at capturing the physics by ignoring the velocity divergence. Instead, the surface tension is calculated by the method described by Eqn. (56). Thus, inaccurate characterisation of the physics at liquid vapour interface can lead to errors in predicted vapour pressure so even if the mass of vapour phase generated due to boiling is correct, the observed vapour volume can go wrong. Besides, if the solver fails at predicting the right density for vapour bubbles, the reliability of the results based on Eqn. (53) are also questionable, and the trivial change in the cooling rate in Figure 42 could be attributed to this. As an empirical coefficient, the value of evaporation coefficient can be between 0.1 and 1000 in different scenarios. The results in section 4.7 show that the framework presented in this thesis is not sensitive to the evaporation coefficient.

With varying specific heat of both fluid phases, the cooling rate at solid centroid is hardly changed, as observed from Figure 50 (a). The biggest divergence happens when the specific heat is halved, and the relative divergence between the models with halved Cp and with normal Cp is 9.61%. In other cases, the relative divergence is below 5%. Since the heat transfer rate at the solid-liquid interface is directly related to the temperature difference at both sides, the fluid temperature does not experience significant change either.

It can be seen from Eqn. (53) that the specific heat of fluid phases does not directly affect the total energy solution. However, it appears in Eqn. (43) which determines the temperature of the fluid. The fact that the temperature does not change significantly implies that the kinetic term in Eqn. (43) is the predominant factor of total energy. Therefore, the change in fluid temperature is not great enough to noticeably change the cooling rate of the solid sample. In addition, as previously mentioned, the specific heat is a function of temperature which increases with increasing temperature. This contributes to the result that the temperature of the case with half of the original specific heat value varies the most.

The cooling curves of different thermal conductivity of both fluid phases are investigated as well. As shown in Figure 50 (b), solid cooling curve varies very much with fluid thermal conductivity. As reflected by Eqn. (53), thermal conductivity is the predominant factor of total energy in this specific case. The fluid environment is significantly changed as a result, heavily influencing the cooling rate of the solid sample. This corresponds with the simulation results. It is also worth mentioning that such extend of variation in fluid thermal conductivity can lead to different predominant mechanisms of the whole cooling process.

As previously discussed in § 3.17 , the compressive behaviour of vapour phase at the liquid-vapour interface, which is reflected by the velocity divergence of the interfacial cells, is not taken into account. As a result, the pressure on the bubble surface due to the interfacial compressibility is absence. This hydrostatic force is meant to stabilize the bubble and keep it in its spherical shape. Consequently, in this thesis, bubbles are more likely to break, and the vapour blanket which is supposed to cover the solid surface during film boiling stage can hardly form. Theoretically, this trend increases the contact between the solid surface and liquid and accelerates the overall cooling of the solid sample.

According to Figure 30 (a), the experimentally measured cooling rate reaches its maximum at a much lower solid surface temperature than the simulation results. This is a result of the vapour blanket which forms during film boiling stage. For the simulation results, the maximum cooling rate appears at a much higher temperature, indicating the a much weaker or even absent film boiling effect. Meanwhile, the number of the vapour bubbles predicted by the model is much less than what is seen in the experiment recordings. These two findings prove the bubble instability caused by the lack of hydrostatic pressure on bubble surface.

The overall slower cooling, on the other hand, can hardly be explained by the same mechanism. In all the models except for §4.10 , the predicted solid cooling rate is slower than the experimental data. In §3.17 , it is justified that not taking the velocity divergence at the bubble surface, i.e. the interfacial compressibility, would result in higher liquid temperature, especially in the near-solid fluid zone. This explains the difference between the simulation and experimental results. At the beginning, the film boiling effect slows down the solid cooling rate by creating a vapour layer that disables the solid contact with the liquid phase. In the same time period, film boiling is absent in the simulation so the predicted cooling rate quickly reaches its maximum. Because of the predicted higher liquid temperature, both the average and maximum cooling rates of simulation results are lower than the experiment. Then, the simulated cooling rate keeps reducing as a result of a decreasing temperature difference, whereas in the case of experiment, the cooling rate gradually increases to its maximum.

In summary, based on the observed difference between the simulated and experimentally measured solid temperature profiles, it can be concluded that not taking the compressibility at the bubble surface into account induces significant error to the model framework. The error comes from following aspects:

- Zero velocity divergence leads to higher volume of vapour phase, and the temperature of the liquid mixture in the boiling area would be higher than reality
- Lack of hydrostatic force on the bubble surface makes the bubbles less stable, and film boiling is unlikely to happen

To correctly simulate the effects of boiling mechanisms, it is necessary to incorporate the hydrostatic force (i.e. the interfacial compressibility) on the bubble surface. This can be accomplished by applying von Neumann boundary condition on all the liquid-vapour interfaces. On these boundaries, the divergence of velocity equals the net volumetric mass transfer rate of vapour phase. It’s also worth mentioning that in such case, it is necessary to consider radiation heat transfer, because it plays a vital role during film boiling which is very likely to happen in the simulated.

4.13 Summary

In this chapter, the performances of a group of small-scale models are discussed. The influence of a number of model specifications on the predicted cooling behaviour are investigated. These specifications are boiling effects, the dependence of water density on temperature, velocity inlet (immersion process), initial temperature gradient in the solid domain, greater evaporation coefficient, higher flow intensity, different boiling mass transfer model, and different thermal boundary conditions. The findings can be summarized as follows:

1) Regardless of the accuracy, the model must include either a temperature water density or the boiling effects to deliver results which at least look reasonable.
2) Based on a multiphase model that simulates the boiling mass transfer via the evaporation condensation model, the predicted cooling trend is not changed by the inclusion of a velocity inlet, an initial temperature gradient in the solid domain, and a greater evaporation coefficient. Moreover, these factors only have minor or even negligible influence on the temperature curve of the simulation result. In most cases, such influence yields a small shift in time or temperature of the whole curve.
3) By changing the gravitational direction, high intensity circular flow is formed in the quench tank. Even though this does not change the cooling trend of the sample, it largely enhances the predicted cooling rate and yields much better results.
4) The combination of the coupled thermal boundary condition and the evaporation condensation mass transfer model shows poor performance while predicting the cooling rate during the nucleate boiling stage. All the improvements in the cooling rate prediction that are made based on this specific model parameter combination are direct results of the change in the fluid flow intensity in the near-solid fluid region. The higher the fluid flow intensity is in this region, the faster the predicted cooling rate is.
5) The optimal prediction is obtained by implementing an empirical equation of heat flux as the thermal boundary instead of the coupled interface thermal condition. The overall relative average error is 27.31%, while for the first 20 seconds of cooling, the number is 2.23%.
6) It is very possible that during the experiment process, the data of the initial two seconds of cooling is not recorded.
7) The framework of the small-scale model in this chapter is not sensitive to the evaporation coefficient and the specific heat values of fluid phases, but is highly sensitive to the thermal conduction values of fluid phases. For the best performance of the model, implementing accurate thermal conduction values for all fluid phases is necessary.

5 Small-Scale Probe Shaped Sample

The small-scale probe-shaped sample models are a set of supplementary models based on the small-scale cylindrical sample models. The validation data is originally obtained from a quench test of a probe, as shown in Figure 25 (a). In the small-scale cylindrical sample models, the probe is simplified to a cylinder because the designed effective testing part of the probe is 60 mm from the tip of the probe. However, such simplification is accompanied by the risk of not incorporating the influence of the rest of the probe. In § 4.6 , it is concluded that the thermal conduction has a great influence on the temperature evolution at the solid centre. Therefore, the sample is modelled as an elongated cylinder as opposed to the sample of the previous models to represent a bigger portion of the probe. Most of the model parameters investigated in Chapter 4 are also studied in this chapter, and the material of the solid sample is the same for both models.

All the models in this chapter are multiphase models. The predicted temperature is processed in the same way as stated in §4 . The mesh grids remain the same, but the $\phi 12.5 \times 60$ mm cylindrical cell zone above the sample is changed from fluid to solid. Other model parameters remain the same, including wall treatment, boiling mass transfer model, solution algorithm, spatial and temporal discretization scheme, turbulence model, VOF model, and governing equations.

5.1 Model Geometry and Modification

Figure 53 shows the basic geometry of the models to be discussed in this chapter. Compared to the model discussed in the previous chapter, this model has a quench tank in the exact same dimensions. The sample is elongated from 60 mm to 120 mm while the relative position of the bottom surface of the sample in the quench tank is remained the same. The temperature recording point is located at 30 mm above the bottom surface of the sample and on the axis of symmetry but is no longer the centre of the sample in this case.

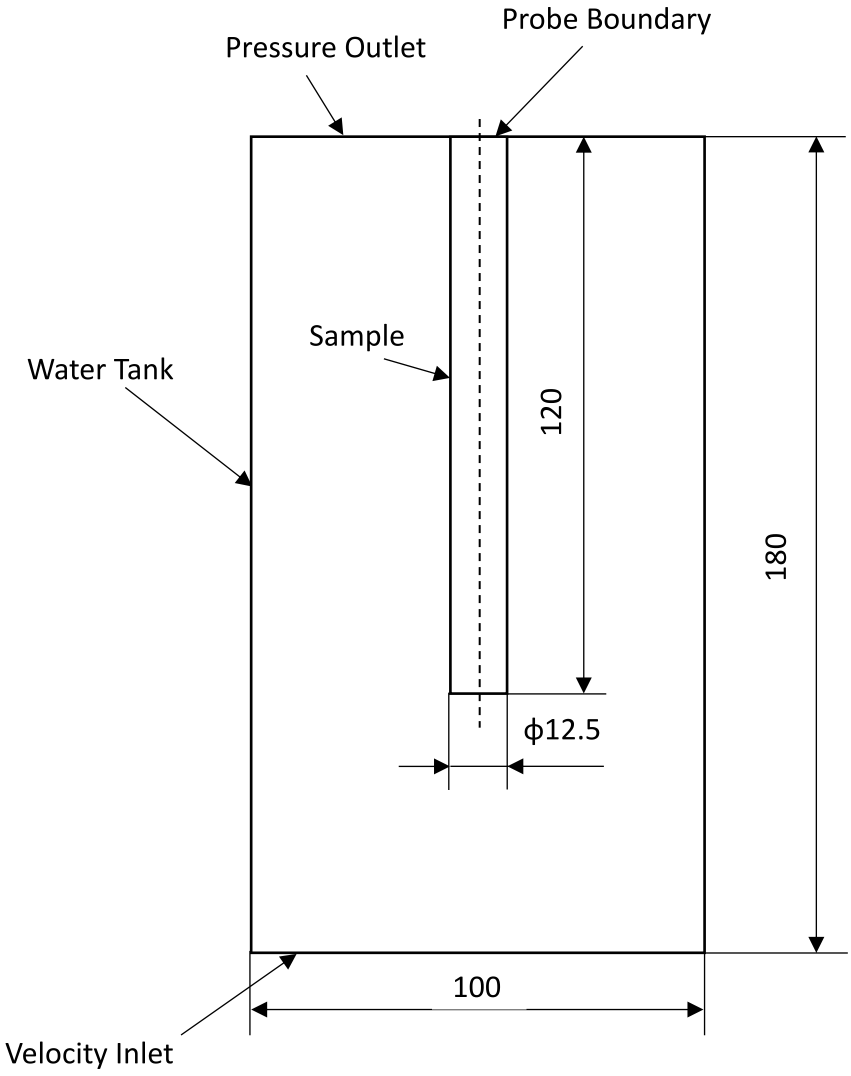

Figure 53 Geometry of a Small-Scale Probe-shaped Sample Model.

5.2 Multiphase Model (Refence Model)

Similar to the models with a cylinder-shaped sample discussed in the previous chapter, the result of a basic multiphase model with a probe-shaped sample is considered as the reference result while analysing the results of other models. The simulated temperature and cooling rate curves are shown in Figure 54 and Figure 55. According to these figures, the cooling is accelerated by including the extra part of the probe. Since the surface to volume ratio of the sample is decreased after the elongation, the portion of the heat transferred to the liquid domain is also reduced. Nevertheless, the thermal conduction effect brought by the extra part of the probe compensates the relative decrease of the cooling caused by the heat exchange with the liquid phase.

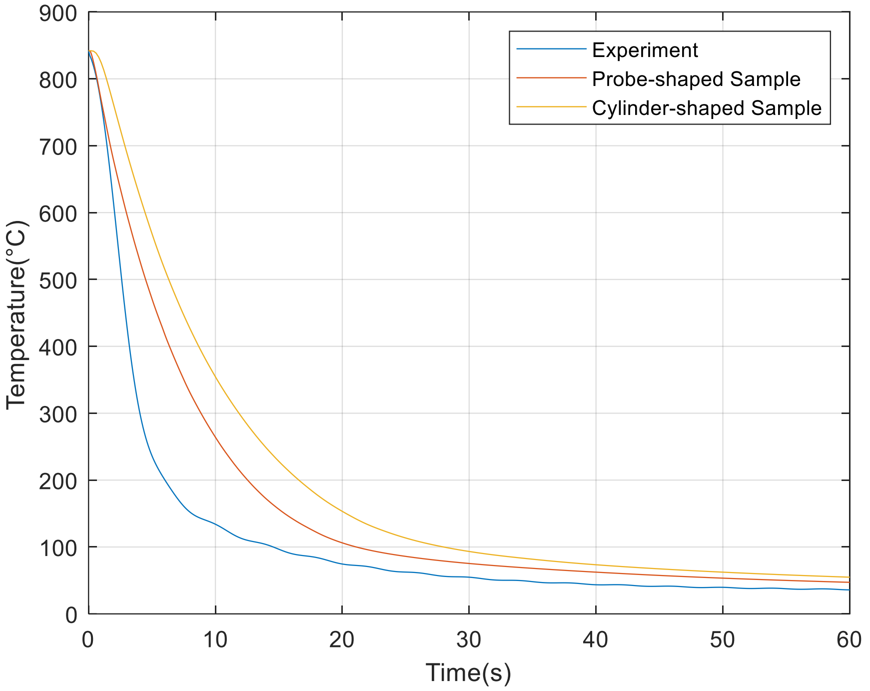

Figure 54 Temperature Curves of the Models with Both Cylinder and Probe Samples and the Experimental Data.

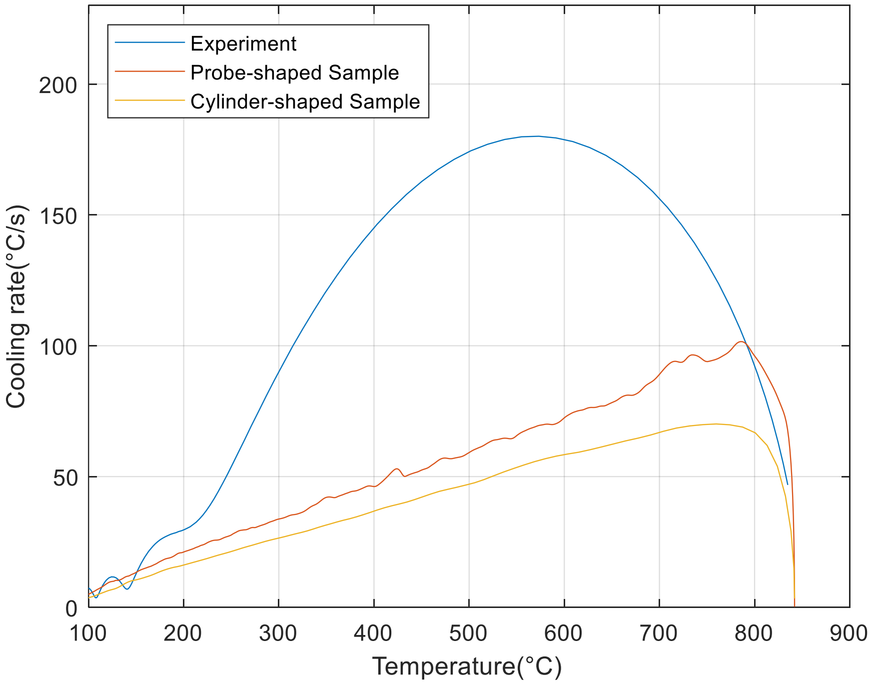

Figure 55 Cooling Rate vs. Temperature Curves of the Models with Both Sample Shapes and the Experimental Data.

The probe-shaped sample model yields the best predictions within one second after the cooling starts. During this period, the cooling rate is almost perfectly simulated (see Figure 55) at the temperature recording point. However, after the one second time point, the subsequent increasement of the cooling rate is absent in the probe-shaped sample model, similarly as in the cylindrical sample models. This means that the inclusion of the rest part of the probe does not change the cooling trend of the sample, and that the limitation of the coupled thermal boundary condition still exists. Nevertheless, the inclusion of more details of the experimental procedure mitigates the error of the model to some extend and yields a slightly more realistic prediction. In addition, it could be seen from Figure 55 that the difference between the cooling rates predicted by both models seems to have a linear relationship with temperature. Since such difference is mostly a result of the thermal conduction effect from the tip of the probe to the unheated part, this phenomenon could be explained by the fact that the thermal conduction rate has a strong dependence on the temperature of the probe tip.

It is also worth noting that noticeable fluctuation in the cooling rate of the model of probe-shaped sample is observed in Figure 55. This phenomenon is undoubtedly a result of the inclusion of the extra part of the probe, but the detailed reason has not been explicitly explained yet. One of the possible reasons would be the more intense interaction with the vapour phase generated. By comparing Figure 56 with Figure 32, it can be clearly seen that there is much more vapour phase in the model with a probe-shaped sample. This can be attributed to the increased solid area in contact with the fluid phase. These vapour phases tend to form larger bubbles than in the cylindrical sample model, so the attachment and detachment of these large bubbles on the solid surface have a more profound influence on the local heat transfer rate of the solid surface. As previously discussed, regardless of the sample shape (probe or cylinder), the radius of the sample is small, so the radial thermal conduction is often completed in a very short period when the heat transfer rate is changed at the solid surface. Thus, the temperature at the centre is really sensitive to the variations of the heat transfer rate at the solid-liquid interface which is induced by the existence of more vapour bubbles, and the temperature curve oscillates as the vapour bubble moves along the solid surface.

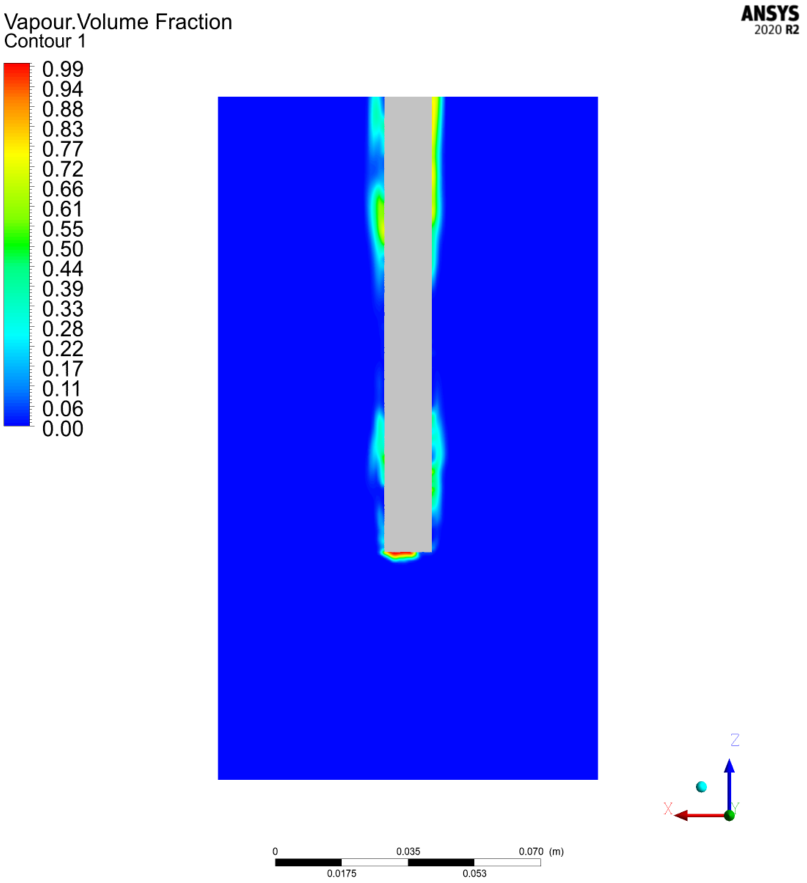

Figure 56 Vapour Phase Distribution Contour of the Model with a Probe-shaped Sample at t=2.2 s.

5.3 Velocity Inlet Model

Similar to the cylinder-shaped sample models, the inclusion of the velocity inlet does not make a significant difference in the overall cooling rate for the probe-shaped sample models. However, in the case of cylinder-shaped sample models, the cooling rate peak of the velocity inlet model is slightly lower than the basic multiphase model (see Figure 38), whereas with the probe-shaped samples, the predicted cooling rate peak with the velocity inlet is higher than the basic multiphase model, as shown in Figure 57.

In this model, the velocity inlet magnitude expression is the same as in the model discussed in §4.5 . Despite the fact that the elongated sample reduces the initially empty volume of the quench tank, the volume of the extra sample part is negligible compared to the volume of the quench tank.

The vapour phase volume fraction contour is generated to analyse the cause of its different

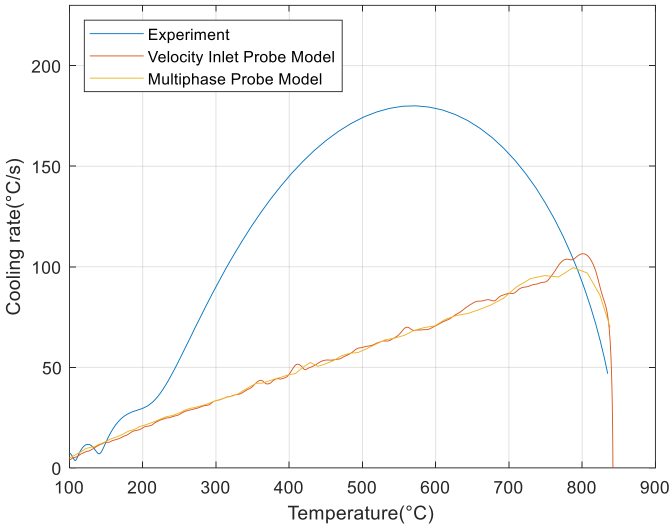

Figure 57 Cooling Rate vs. Temperature Curves of Probe Models with and without Velocity Inlet.

cooling behaviour with the velocity inlet model of cylinder-shaped samples, and the results at t=0.4 s are displayed in Figure 58. Compared to vapour phase distribution which is shown in Figure 39, the result in Figure 58 is far less realistic. Firstly, a vapour volume fraction gradient

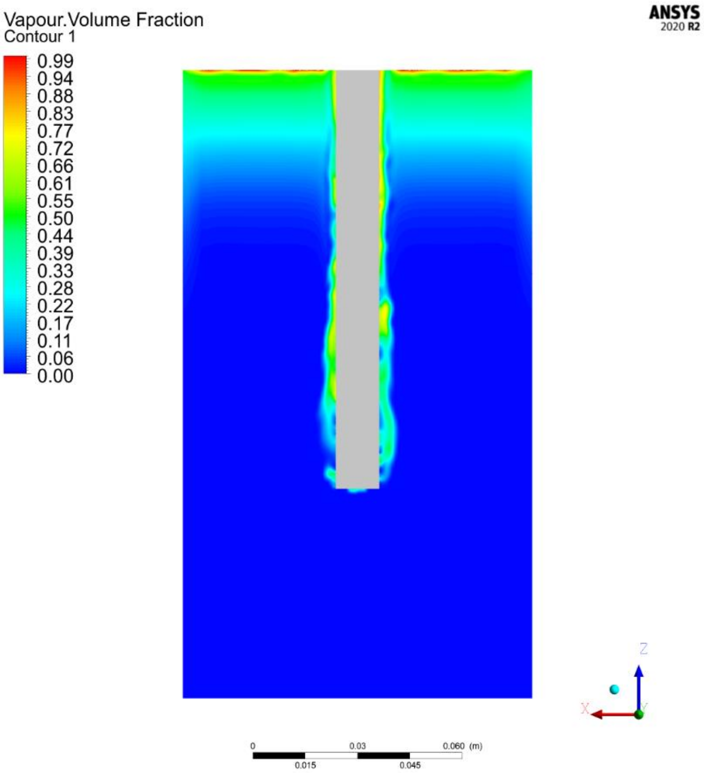

Figure 58 Vapour Phase Volume Fraction Distribution in the Water Tank of the Probe-shaped Sample Model with Velocity Inlet at t=0.4 s.

in z direction is formed near the water level surface. This indicates that the model is encountered with some problems while characterising the phase boundary between the liquid and vapour phases. In Figure 39, even though a vapour phase volume fraction gradient can also be observed in a thin layer beneath the water level, it is caused by the irregular motion and deformation of the water level and is much more realistic than what's shown in Figure 58. Secondly, the big bubbles induced by the immersion process are successfully predicted in Figure 39 but are absent in Figure 58. Therefore, the velocity inlet model with a cylinder-shaped sample delivers a better representation of the physical processes induced by the immersion process than the velocity inlet model with a probe-shaped model.

The thick vapour volume fraction gradient layer in Figure 58 is maintained throughout the whole cooling process. However, the presence of such a coloured layer helps with the observation of the near-solid fluid flow. In Figure 59, it is clearly shown that the region between the two white dashed lines is directly impacted by the rising stream of vapour bubbles caused by the boiling effect. This justifies the statement in §4.7 that a modified or higher boiling intensity can influence the flow conditions in the near-solid fluid region.

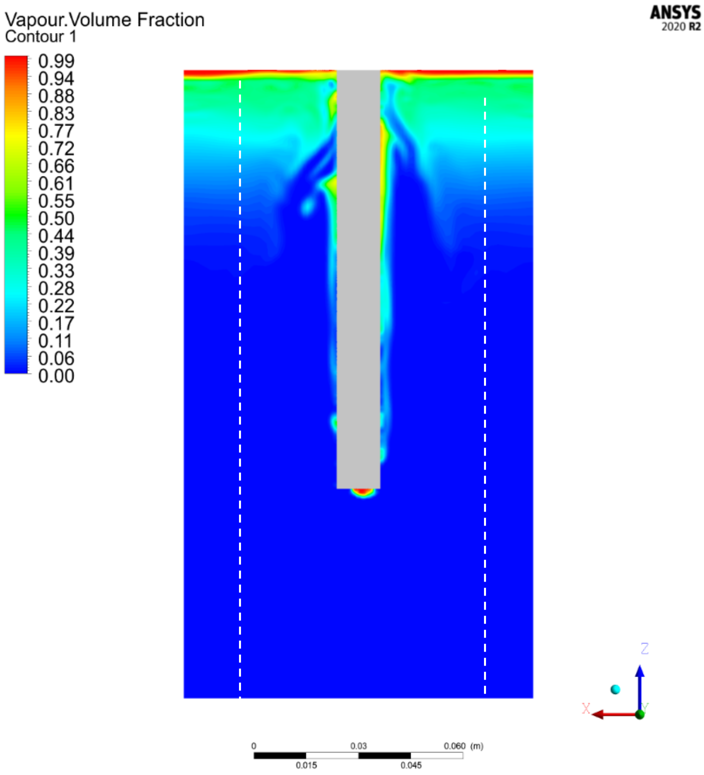

Figure 59 Vapour Phase Volume Fraction Distribution in the Water Tank of the Probe-shaped Sample Model with Velocity Inlet at t=2.2 s.

5.4 Initial Temperature Gradient Inside Solid

With the inclusion of extra solid volume in the model, the effect of the thermal conduction inside the solid domain is expected to be magnified. The solid temperature distribution described by Equation (100) is used in this model. This is a linear relationship between the temperature and the distance from the point where the temperature profile is recorded. After applying this temperature profile, the temperature at the bottom and top surfaces of the probe is 770 ℃ and 600 ℃, respectively.

The prediction of this model is very similar to that of the multiphase model, and the temperature and cooling rate curves of this model are listed in Appendices. As expected, the initial temperature gradient in the solid domain creates immediate cooling rate, and the temperature curve of this model is almost in perfect match with the experimental data. However, this immediate cooling rate also vanishes in no time, and the cooling rate of this model becomes the same with the basic multiphase model with a probe-shaped sample. It is worth noting that due to a larger distance in the longitudinal direction, the immediate cooling rate is much higher than the model with a cylinder-shaped sample.

5.5 Higher Boiling Intensity

As opposed to the basic multiphase model with a probe-shaped sample, the boiling evaporation coefficient is changed from 0.1 to 1. This is expected to increase the generation rate of the vapour phase during the boiling process. The temperature results and comparisons of the model with a modified evaporation coefficient are shown in Figure 60. Noticeable improvement in the cooling rate is made by increasing the evaporation coefficient. Such improvement is almost the same as the cylinder-shaped sample model. In this case, the inclusion of the extra probe volume does not significantly change how the predicted temperature evolution is influenced by the increased evaporation coefficient.

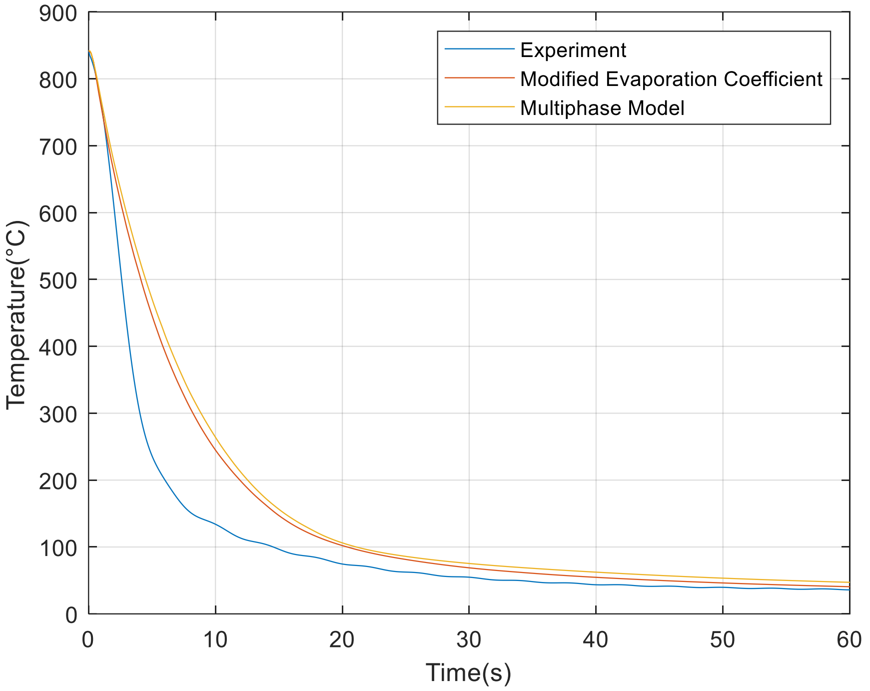

Figure 60 Temperature Curves of the Modified Evaporation Coefficient Model and the Multiphase Model with Probe-shaped Samples.

5.6 High Intensity Circulating Flow Case

In this section, a model with higher flow intensity is generated in the same way as in §4.8 , i.e., the same boundary condition is applied at the side surface. The result of this model is shown and compared with other data in Figure 61. The predicted temperature evolution of this model is very close to the experimentally measured data. In the low temperature range (below 200 ℃), the cooling of the experimental data is significantly slowed down, whereas the temperature of the model with higher flow intensity remains a relatively fast cooling rate and reaches the ambient temperature (20 ℃) rapidly. This is because during the experiment, the average water temperature in the quench tank is increased, especially in the near-solid fluid region. This causes the slow cooling rate in the low temperature range of the experimental data. However, during the simulation, low temperature water flows in and out the quench tank through the pressure outlet, carrying away all the heat transferred from the solid sample. Thus, the temperature in the quench tank is maintained around 20 ℃, and the cooling rate in the low temperature range is not severely influenced.

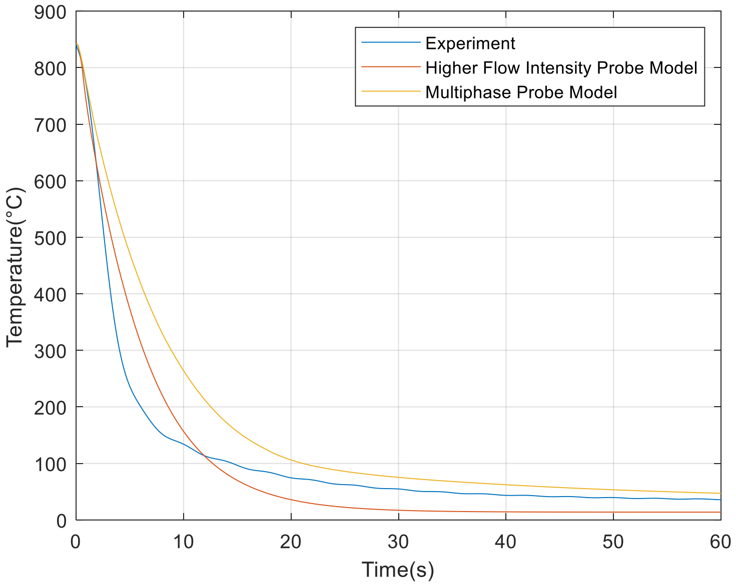

Figure 61 Temperature Curves of the Probe Models with and without a Higher Intensity Flow.

In Figure 62, a sharp peak is observed in the cooling rate curve of the model with higher flow intensity. This is a unique feature that is absent in both the basic multiphase model of a probe-shaped sample (§5.2) and the cylindrical sample model with high flow intensity (§4.8). Such phenomenon can be attributed to the increased contact area between the solid and liquid phases, and the resulted higher heat extraction rate from the solid domain.

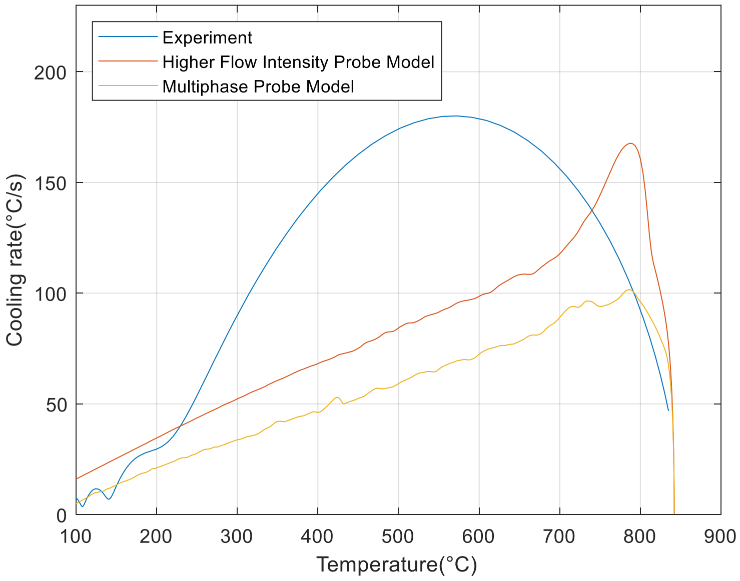

Figure 62 Cooling Rate vs. Temperature Curves of the Probe Models with and without a Higher Intensity Flow.

Similar to Figure 45, the fluid velocity is higher in the area close to the pressure outlet, as shown in Figure 63. However, different from the model in §4.8 , the probe significantly hinders the fluid flow in y direction, thus the mean fluid velocity on the opposite side of the pressure outlet surface is much lower than the other side. Even though the initial temperature is homogeneous in the whole solid domain, the fluid flow behaviour induces a difference in the water temperature surrounding the solid probe in a similar way as in §4.8 .

In addition, this process happens very rapidly. According to Figure 64, the simulated cooling rate peak occurs at t=0.64 s. This is much earlier than the cooling rate peak of the experimental data which is at t=2.2 s.

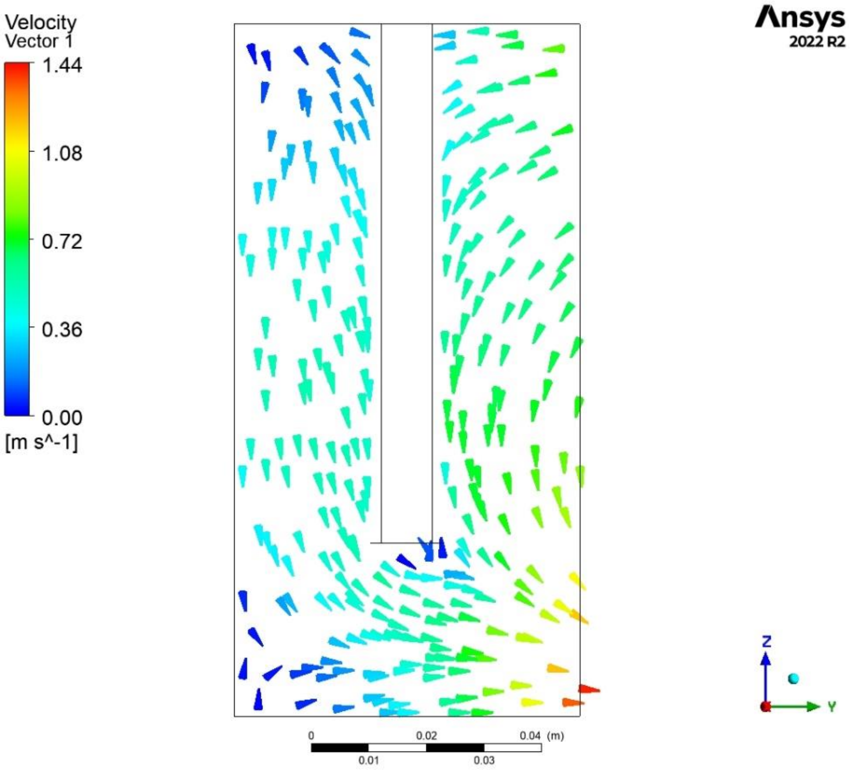

Figure 63 Velocity Vectors in the Quench Tank at t=1 s.

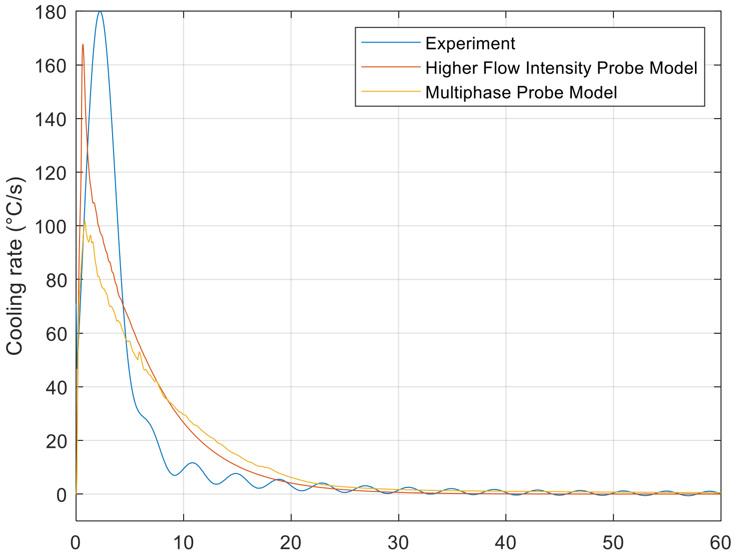

Figure 64 Cooling Rate vs. Time Curves of the Probe Models with and without a Higher Intensity Flow.

5.7 Heat Flux Thermal BC

The same heat flux boundary condition tested in §4.10 is also implemented and tested in this section with the new geometry. This heat flux boundary condition is applied to all solid surfaces except for the top surface, because the top surface is subjected to thermal conduction instead of heat transfer with liquid. The simulation result of the heat flux boundary condition is processed with the same method stated in §4.10 .

The temperature curve of the heat flux boundary condition appears to be steeper than the experimental data, as shown in Figure 65. In the initial cooling stage, the simulated temperature is higher than the experimental data, but after approximately 3.2 seconds, the curve of the simulated temperature falls below the experimental curve.

According to Figure 66, the simulated cooling rate peak is slightly delayed compared to the experimental data but has a much higher peak value. This causes the steeper slope of the simulated temperature curve.

The overall accuracy of this prediction is not as good as the model in §4.10 . A possible reason would be that the expression of the heat flux boundary condition was developed based on the data of fully immersion quenching. However, the model simulates the immersion quenching of a portion of the probe, and the overall cooling is also influenced by the thermal conduction along the longitudinal direction of the probe. In the cylinder-shaped sample model, the effect of the thermal conduction is somehow incorporated by the heat flux boundary condition applied on the top surface.

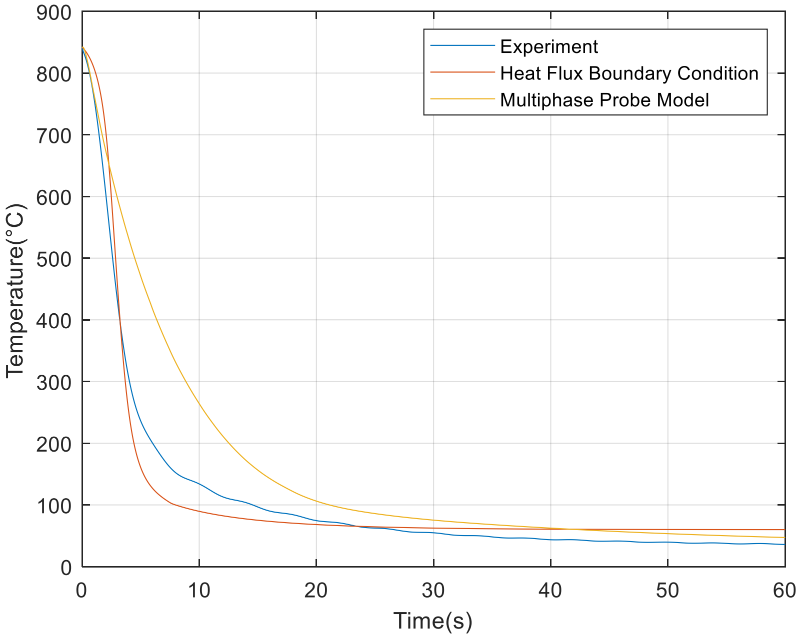

Figure 65 Temperature Curves of the Probe Models with Heat Flux and Coupled Boundary Condition.

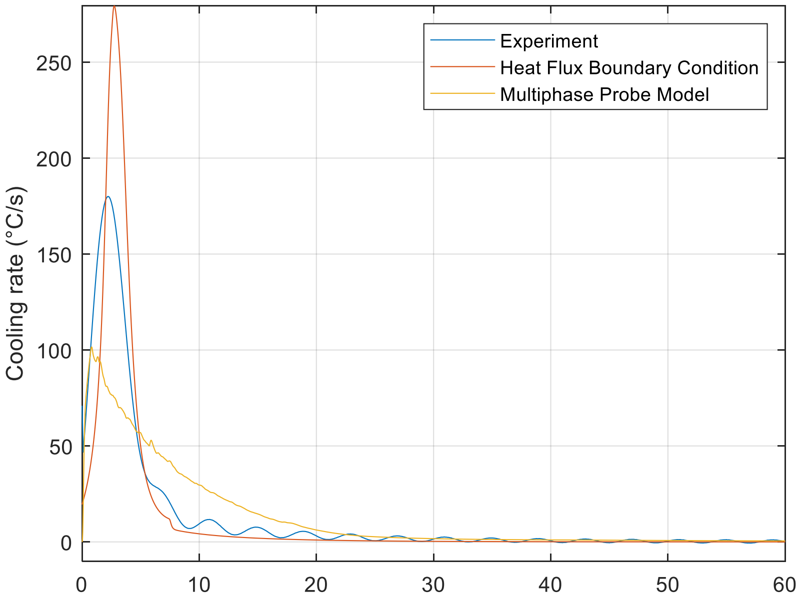

Figure 66 Cooling Rate vs. Time Curves of the Probe Models with Heat Flux and Coupled Boundary Condition.

5.8 Summary

The models with a modified sample shape are investigated in this chapter. The new model geometry includes an extra part of the probe sample to take the potential effects of the longitudinal thermal conduction into account. Most of the model parameters that are studied in Chapter 4 are also investigated in this chapter, and the following conclusions are drawn:

1) After including the extra portion of the probe, the performance of the basic multiphase model is significantly improved. However, the result of the new model geometry still greatly differs from the experimental data.
2) Factors including velocity inlet, initial solid temperature gradient, and higher boiling evaporation coefficient do not have significant influence on the simulated temperature curves of the probe-shaped sample model. The inclusion of a velocity inlet increases the maximum cooling rate at high temperature, whereas for the model with a cylindrical sample, the inclusion of velocity inlet has the opposite influence.
3) By changing the gravitational direction while remaining the same pressure outlet surface, strong circulating fluid flow is formed in the quench tank. This significantly increases the predicted cooling rate. However, this also causes a sharp increase in the cooling rate at high temperature, which is different from the result of the cylinder-shaped sample model with the same fluid condition.
4) With the implementation of the heat flux thermal boundary condition, the model yields a temperature curve which is steeper than the experimentally measured temperature. The predicted cooling rate curve shows a delayed but much higher peak compared to the experimental data. The overall performance of this model is not as good as the cylinder-shaped sample model with the same boundary conditions in terms of temperature prediction accuracy.
5) The inclusion of the extra part of the probe improves the simulation results when the model parameters are conceptually specified based on the physics of the real cooling process but may induce inaccuracy when combined with empirical correlations.

6 Large-scale Sample Simulation Results and Discussion

To extend the applicability of the developed model, the same modelling strategies are used to study a quench cooling process of a much larger sample. This quench cooling case is one of the processing procedures for the material used in the research carried out by Rahimi et al. [144]. Compared to the previously modelled quenching processes, the size of the workpiece in this case is much larger, and the temperature in the bulk material is more sensitive to the distance to the solid surface.

6.1 Experiment and Model Information

The experiment has been carried out by a group of researchers lead by Dr Salaheddin Rahimi in Advanced Forming Research Centre, University of Strathclyde. A cylinder-shaped solid sample made of Inconel 718 is heated up to approximately 980 ℃ in a furnace and then quenched in a cuboid water tank. Both the diameter and height of the sample are 200 mm. The size of the quench tank is 980 × 980 × 1100 mm. Figure 67 (a) and (b) show the photos of the heated sample and the quench tank, respectively.

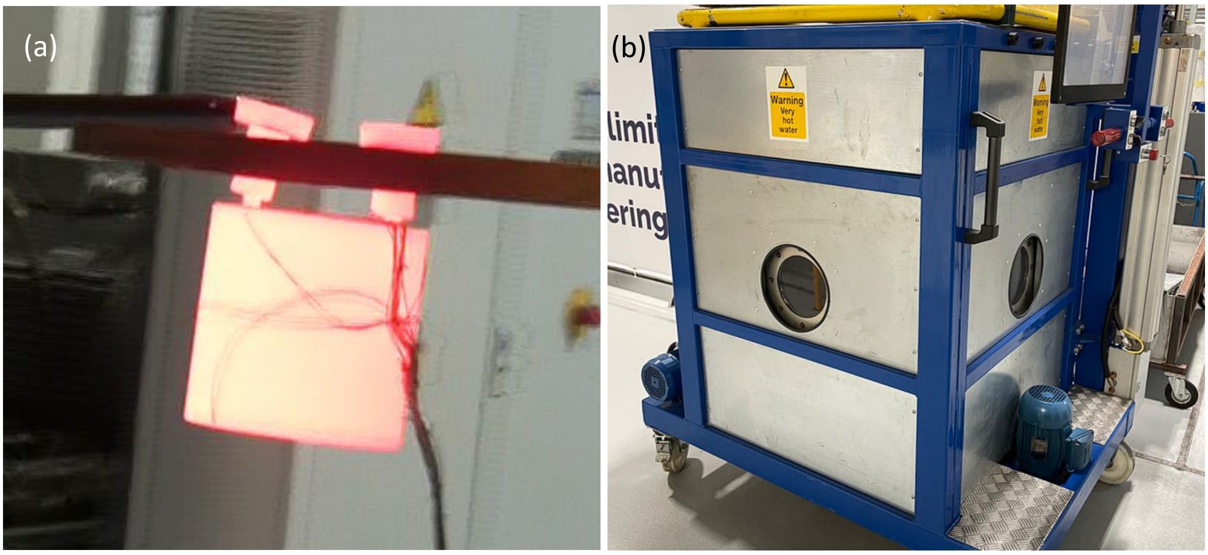

Figure 67 Photographs of (a) The Heated Sample, (b) The Quench Tank.

The detailed chemical composition of the material is not experimentally characterized, so the thermal properties are calculated based on a hypothetical composition that is within the range specified by Table 3. The calculated thermal properties are represented by polynomial functions of temperature, as illustrated in §3.1 .

The model geometry containing both the sample and the quench tank is shown in Figure 68.

The temperature profiles are recorded by thermal couples located at different positions inside the solid, obtaining much more detailed temperature information compared to the quench test of the small-scale sample. This allows the model validation process to provide much more detailed evaluations of the model performance under different geometrical conditions. The locations of the thermal couples are shown in Figure 69. In this figure, thermal couples TC 1-5 are located 3-4 mm beneath the sample surface and are considered to be able to reflect the evolution of superficial temperature. TC 6 and 7 are slightly deeper than the surface group with a depth of approximately 6-7 mm. TC 8 is embedded halfway to the centre in a radial direction, and TC 9 records the temperature of the solid centre.

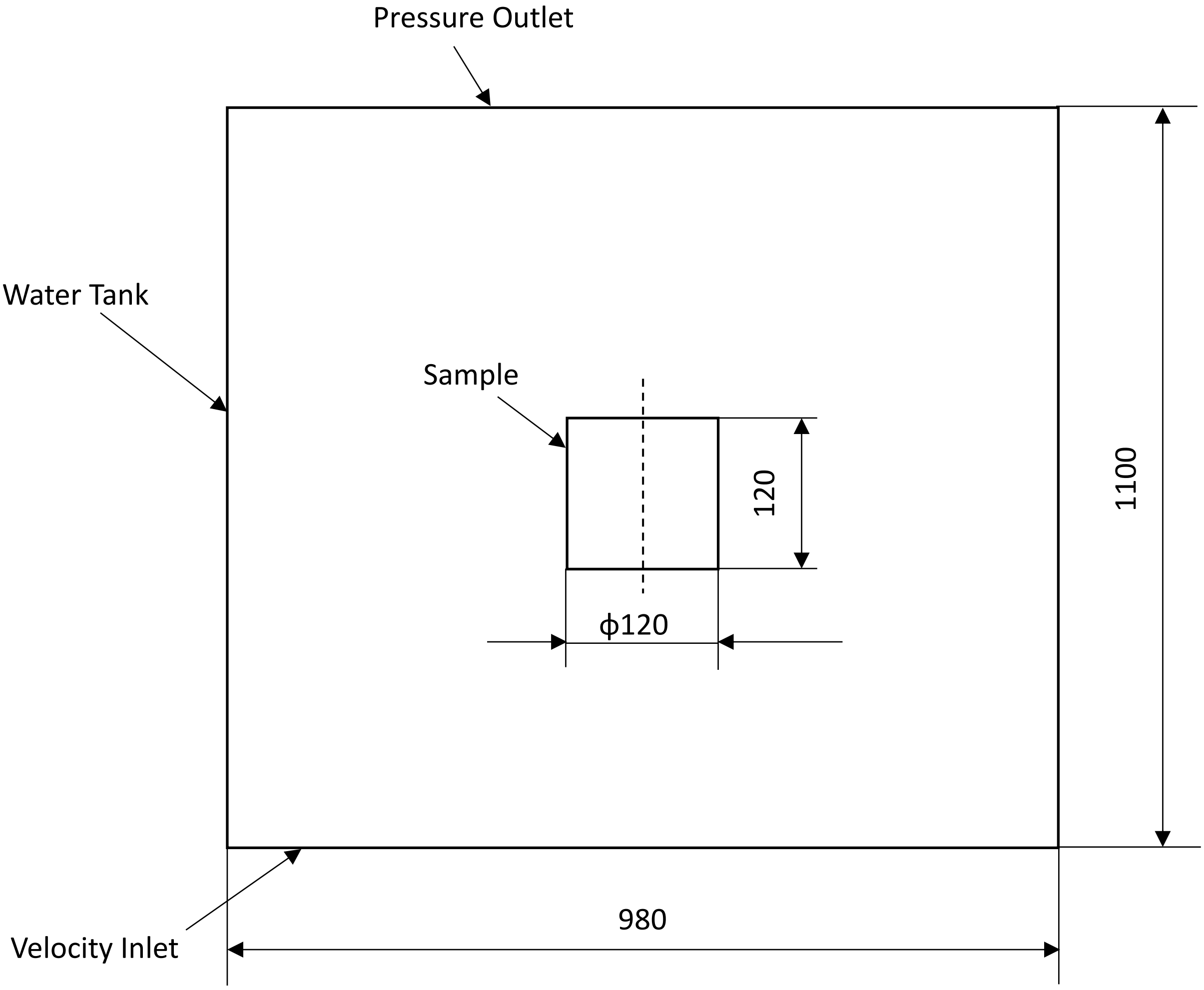

Figure 68 Model Geometry of a Large-Scale Cylindrical Sample Model.

The accuracy of the predicted heat transfer rate at the solid-liquid interface can be evaluated by comparing the experimentally measured and simulated temperature of TC 1- 5. Analysing the results of TC 6 and 7 provides insights of the cooling behaviour of sub-surface positions. In addition, the data of TC 6 can be compared with the data of TC3, TC 8 and TC 9 to analyse the influence of the distance to the solid surface on the cooling trend and help predict the hardenability of the sample. The accuracy of the simulation results of TC 8 and TC 9 reflects the model's capability of dealing with thermal conduction in the solid domain.

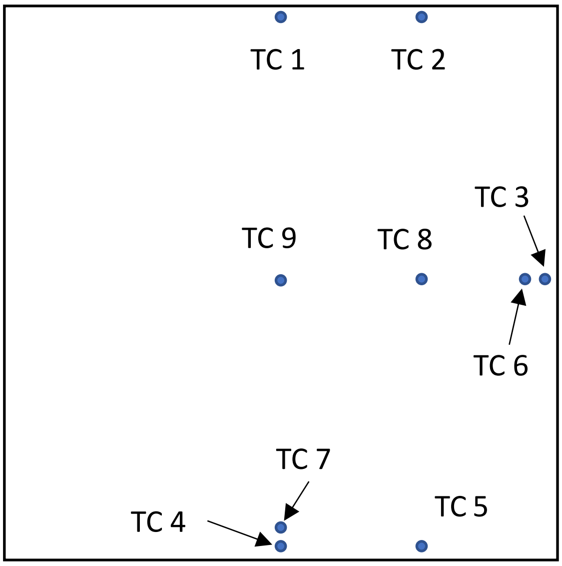

Figure 69 Thermal Couple Positions Inside the Solid Sample.

However, since the solid material has much bigger depth and volume than the small-scale model, the time required to cool down the solid centre is dramatically increased. According to the experimental data, it takes 1500 s (25 min) for the solid centre temperature to be cooled down to 100 ℃, whereas the surface temperature reaches the same level in only 250-350 s (4-6 min). For the small-scale sample, the whole sample is cooled down below 100 ℃ within 30 s. Such huge increasement in the length of the cooling period causes significant increase in the calculation power required to simulate the entire cooling process. In addition, the increased size of the whole model makes the solution process of each single time step much longer as well. If the mesh sizing is kept the same as the small-scale models, the simulation of an entire cooling process of the large-scale model can easily take up to weeks to complete.

Therefore, in order to maintain an acceptable efficiency of the simulation, efforts are made to accelerate the solution process. Structural mesh is also generated for the large-scale model, but the absolute element size is significantly larger than the small-scale models while the total numbers of nodes and elements are comparable. In addition, the variable time stepping strategy is applied. The initial time step size is the same as the previous models, and the size of each subsequent time step is determined based on the growth factor and the Global Courant Number. If the Global Courant Number of the current time step is less than 2, then the size of the next time step is calculated as the product of the current time step size and a growth factor (less than 1.2) determined by the solver. The maximum time step size is specified as 10 times of the initial time step size when the flow time is less than 600 s. After that, the maximum time step size is changed to 100 times of the initial time step size. The reason is that after 600 s, the temperature at near-surface locations does not experience rapid changes anymore, so the model stability would not be severely influenced by having a much larger time step size.

Nevertheless, the solution process of a large-scale model still takes much longer than a small-scale model. Hence, instead of separately investigating the influence of each model parameter on the performance, a couple of models with the specifications that have delivered the optimal results in the previous chapters are simulated and discussed. With the detailed experimentally measured temperature data, the performances of the models are well evaluated, and decent understandings on the key points to the accuracy of a large-scale model are established.

6.2 Mesh Sensitivity Test

The mesh grid is generated in the same way as in §4.2 . The mesh grid is completely structured throughout the whole domain, and mapped conformal mesh is secured at the solid-liquid interface. Similarly, five mesh grids of different refinement levels are generated based on number of divisions on each edge. From level 1 to 5, the mesh refinement level is increased proportionally, and the total number of elements and nodes increase exponentially, as shown in Table 5. In order to test the mesh convergency and reliability, the basic mathematical framework is implemented to the meshes. Due to the high calculation power requirement, the simulated period is relatively short for meshes of high refinement level. The cooling rate at the centre at the bottom surface of the solid sample is recorded, because this is the most concerned property and is also closely related to the accuracy of fluid behaviour which largely depends on the mesh quality.

Table 5 Number of Elements and Nodes of Each Mesh Level.

Mesh Level	1	2	3	4	5
Number of Elements	136,800	461,700	1,094,400	2,137,500	6,566,400
Number of Nodes	141,963	473,208	1,114,763	2,169,228	6,634,363

Figure 70 shows the simulation result of different mesh refinement level. It is observed that the temperature curves of level 1 to 4 exhibit significant temperature fluctuation, especially level 4. Even though the difference between level 3 and 4 is approximately 7% at 200 s, the difference between level 4 and 5 is 9% at 50 s, and tends to further increase with time.

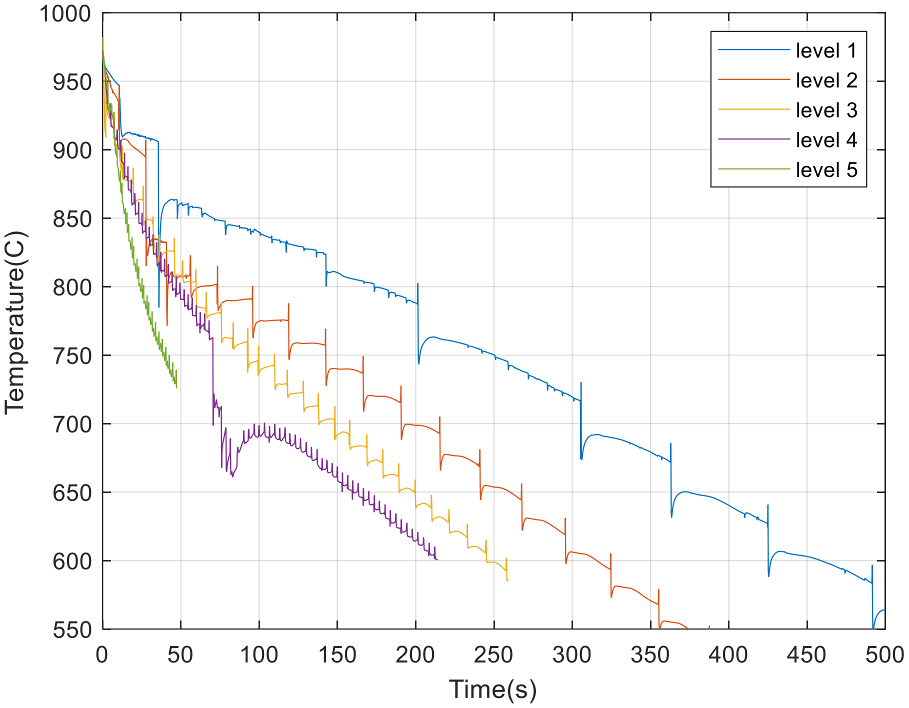

Figure 70 Simulation result of different mesh refinement level.

Nonetheless, the convergency for mesh level 5 cannot be confirmed. Owing to the exponentially increased number of elements and the resulted requirement of memory space and calculation resource, the generation of further refined mesh grid is extremely difficult. Since only one case that involves fluid phase is investigated for large scale model, the mesh sensitivity for this specific case is then tested and displayed in the section §6.3.1 .

6.3 High Intensity Circulating Flow Case

In this section, intensity circulating flow in the quench tank is generated in the same way as in the previous chapters. Thus, the resulting fluid flow pattern is equivalent to the models discussed in §4.8 and §5.6 .

6.3.1 Mesh Sensitivity Test

The mesh performance of this specific case is tested in this section. Mesh level 3 and 5 from §6.2 are selected, and the solid surface temperature profile is recorded as well. In order to increase the calculation efficiency, the mesh grid is modified for level 5 mesh. In the near solid fluid domain, in a layer with a thickness of half of solid thickness is maintained at highly refined level as level 5, and in the rest of the fluid domain, the mesh is coarsened. After such modification, the number of elements is reduced from 6,566,400 to 3,669,120, and the number of nodes is reduced from 6,634,363 to 3,730,047. In Figure 71, the predictions of both mesh levels are displayed in comparison to the experimental data. The biggest relative error between these two meshes appears at 8.8 s which is 13.92%. In addition, the tendency of both curves is in good accordance with the experiment data. Therefore, based on the consideration of the balance between model accuracy and productivity, mesh level 3 is selected as the mesh grid for further model simulation in this chapter.

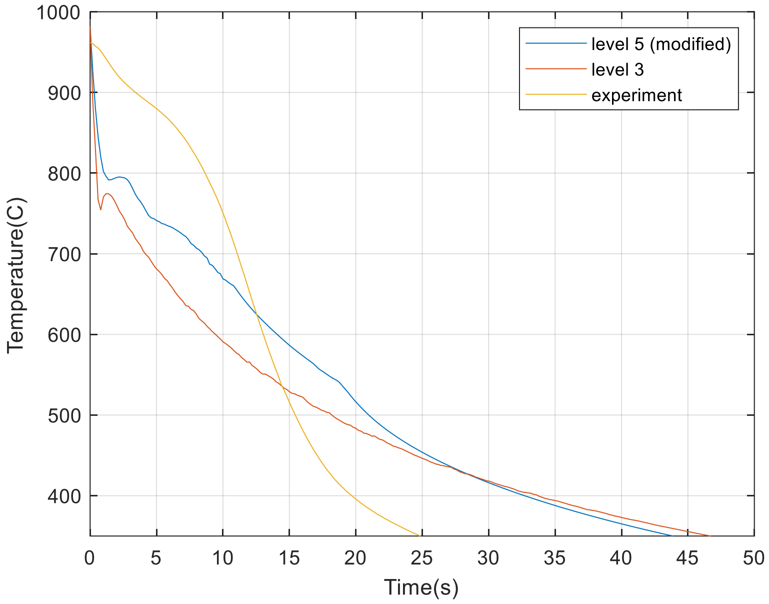

Figure 71 Simulation results for both mesh levels in comparison to the experimental data.

The isometric and sectioned side view of the final mesh is shown by Figure 72 (a) and (b), respectively.

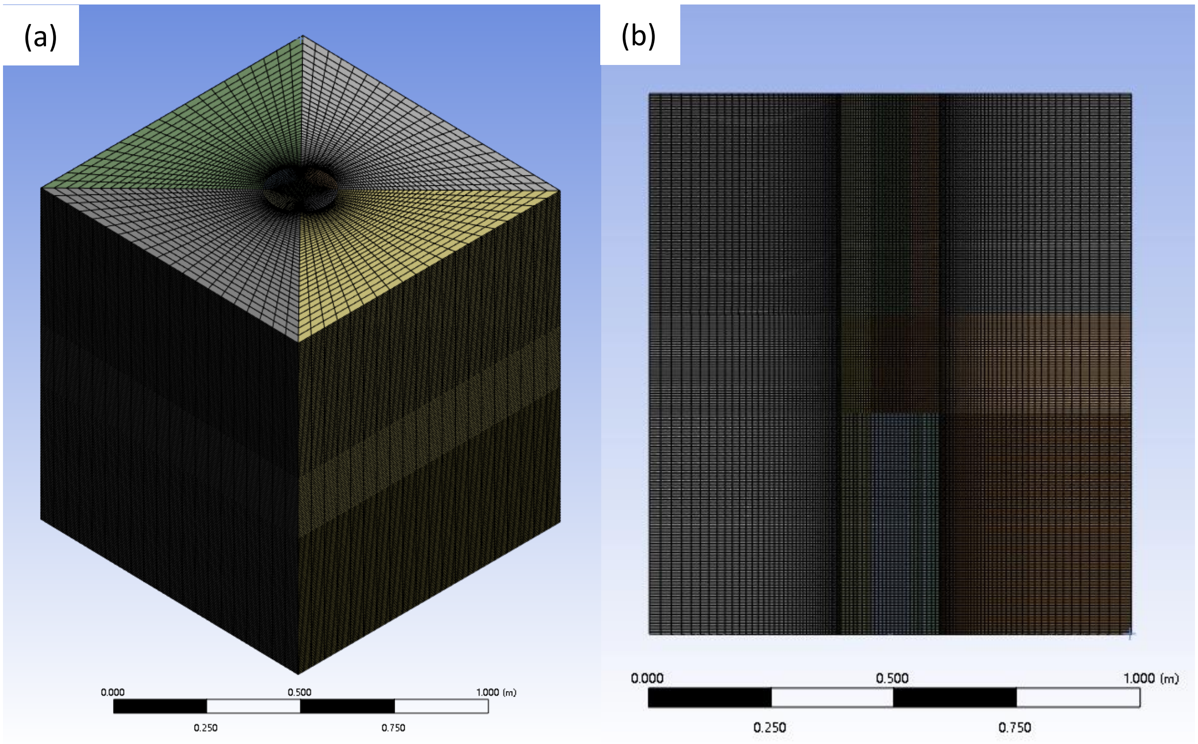

Figure 72 Graphs of Level 3 Mesh (a) Isometric View (b) Sectioned Side View.

6.3.2 Surface Positions

It is observed from Figure 73 that the experimental curves of both TC 1 and TC 4 show a similar but unique shape as opposed to the other curves. These two TCs are located at the centres of the surfaces where the bubble density is the highest. On a large and flat surface, vapour film tends to be generated under high temperature and form a partial sphere surface. The maximum surface height is always located around the face centre, so whenever the vapour film breaks or transforms into bubbles, there is a good chance that the face centre is still in contact with the vapour phase while other parts of the surface are re-wetted by the liquid phase. As a result, the effect of film boiling on the surface HTC is more profound at the face centre than other locations on the surface. Thus, the temperature curves of TC 1 and TC 4 are relatively flat at high temperature.

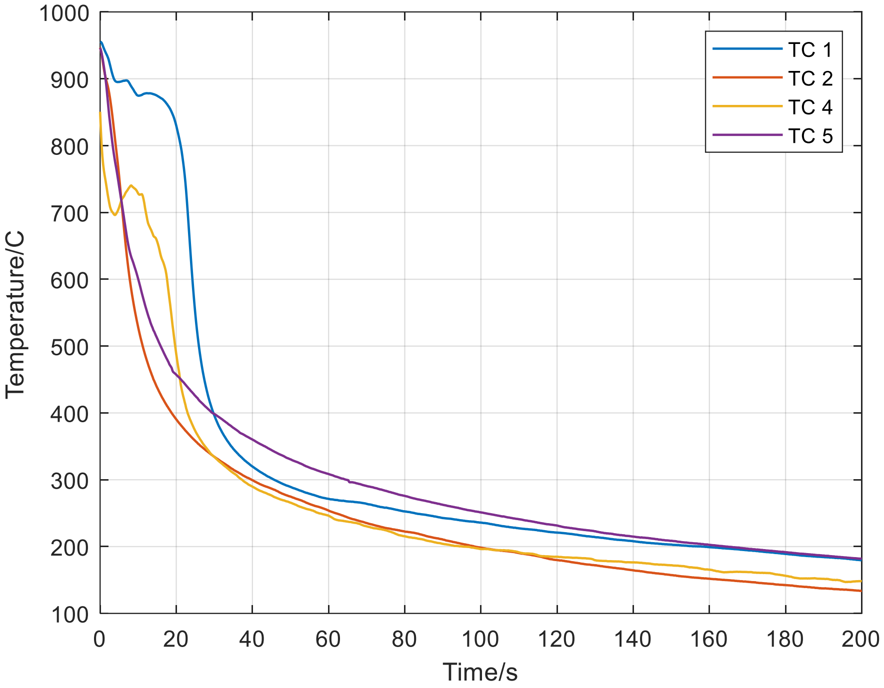

Figure 73 Experimental Temperature Curves at Top and Bottom Surfaces of the Sample.

It is also seen from Figure 73 that the experimentally measured temperature at the top surface centre TC1 is higher than that at the half radius location (TC2). This could be attributed to both the vapour bubble behaviour described above and the different distance to the edge of the sample. However, at the bottom surface, the temperature curves at TC 5 and TC 4 intercept with each other multiple times and the temperature at TC 5 is constantly higher than TC 4 after approximately 21 seconds.

The temperature curves of all the surface thermal couples (TC 1-5) are shown in Figure 74. At the top surface of the sample, the predicted temperature curves at TC 1 and TC 2 show the greatest difference when compared to the corresponding experimental data at the same location among all the five positions analysed. Even though the boiling effect is not incorporated by the model, the model yields a higher cooling rate at TC 2 than TC 1, which is similar to the experimental data. The reason is that TC 2 is located closer to the pressure outlet than TC 1, so the cooling rate is higher as a result of more intense fluid flow. The prediction happens to be in good agreement with the trend of the experimental data in this direction, but such anisotropic nature of this specific model set-up is supposed to show worse performance in other directions at this surface because the cooling rate variation is expected to be isotropic at the top surface.

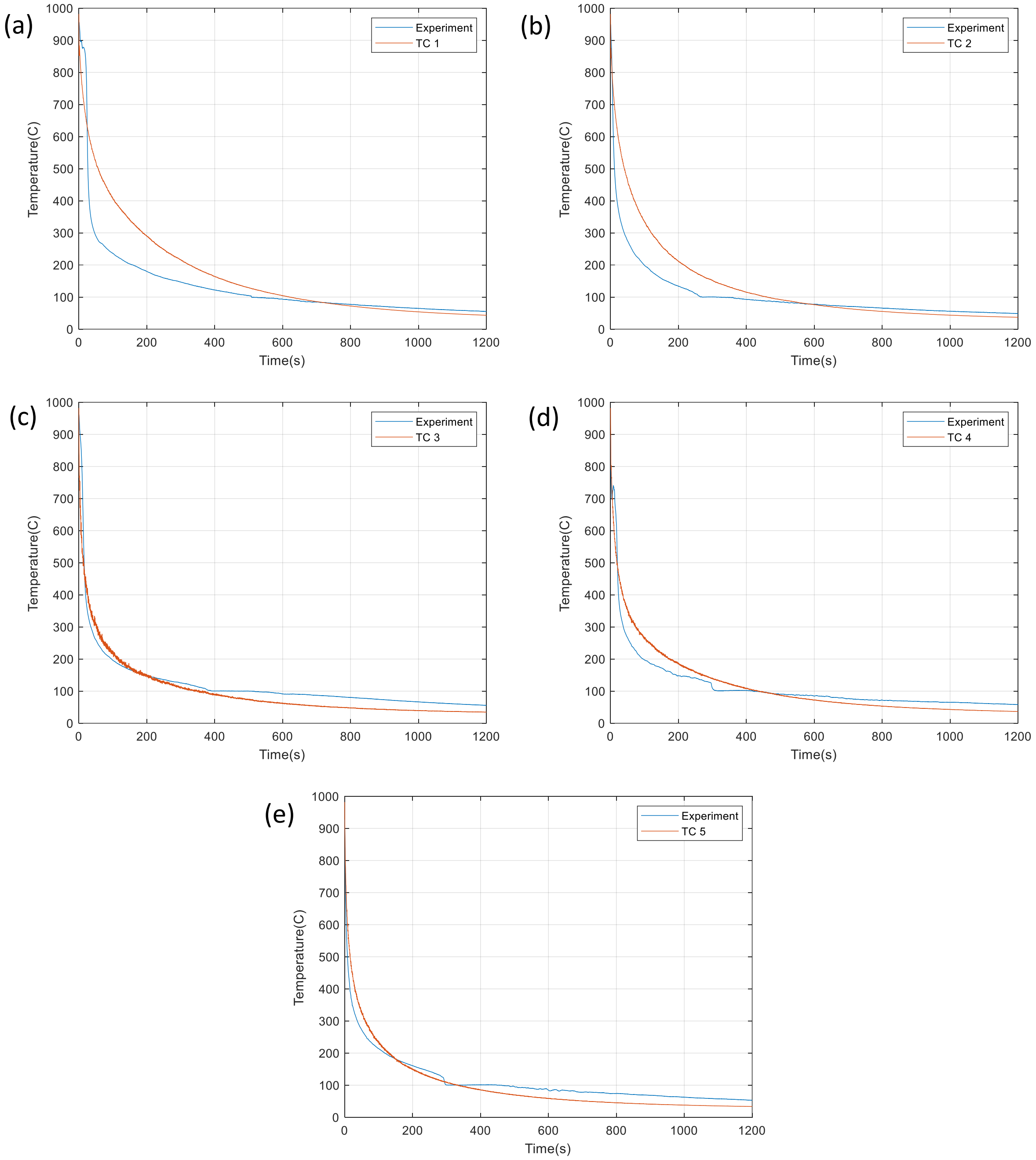

Figure 74 Temperature Curves at (a) TC 1, (b) TC 2, (c) TC 3, (d) TC 4, (e) TC5.

The temperature prediction of TC 3 is in great accordance with the experimental data. Despite the small difference in the initial cooling period and in the low temperature range, the error between the two sets of data is really small throughout the whole cooling process, as shown in Figure 75 (a).

On the bottom surface of the sample, the predictions at TC 4 shows noticeable discrepancy with the experimental data and fails to simulate the effect of film boiling at high temperature. Nevertheless, the simulation result of TC 5 shows decent accuracy that is comparable to TC 3.

To quantify the error between the simulation and the experimental data, the percent error is calculated as the temperature difference between simulation and experimental data divided by the experimental temperature. The percent error at TC 5 is plotted in Figure 75 (b). In the initial stage of cooling, the error is very small, and the prediction shows amazing accuracy, which can also be seen in Figure 74 (e) where the two curves highly converge.

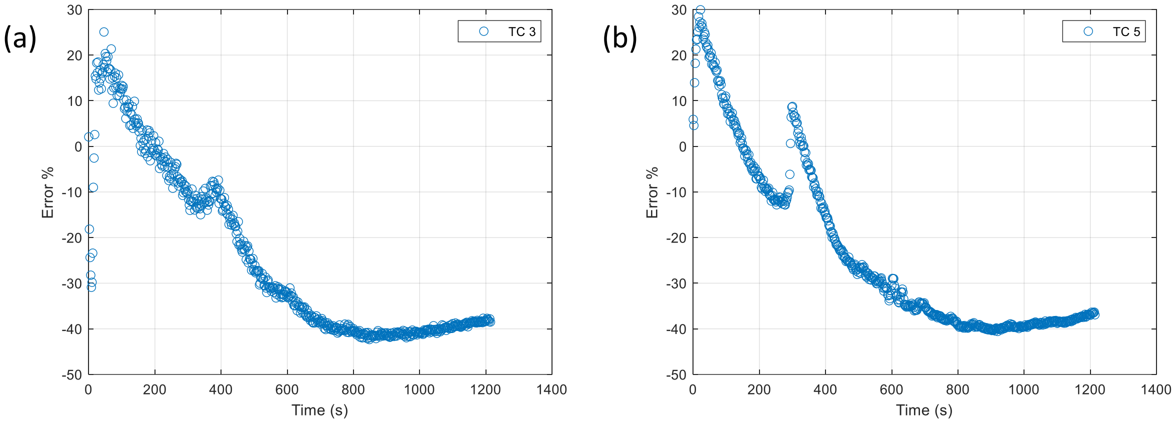

Figure 75 Error Plot of Temperature at (a) TC 3, (b) TC 5.

The absolute values of the percent error significantly increase with time. This is mostly because the absolute experimental temperature value is significantly decreased, so the percent error can reach a relatively high value even with a small absolute temperature error.

In most of the experimentally measured temperature curves displayed in Figure 74, sudden drop to 100 ℃ can be observed. At high surface temperature, the high vapour generation rate provides sufficient vapour flux that fills the thermal couple hole. When the surface temperature is cooled down to a level close to 100 ℃, the boiling intensity is significantly reduced and the amount of vapour can no longer prevent the liquid water from flooding into the thermal couple hole. Hence, the thermal couple is immersed in saturated water, and the recorded temperature becomes 100 ℃.

6.3.3 Sub-surface Positions

The experimental and simulated temperature curves at TC 6 and 7 are shown in Figure 76. TC 6 and 7 are located at sub-surface locations of the side and bottom surfaces of the sample. As can be seen from the figures, the simulated temperature curves at both positions show decent overall accuracy.

For TC 6, the simulation and the experimental data curves highly converge from the beginning of the cooling process up until 100 s. After that, the simulated temperature is lower than the experimentally measured temperature, but the difference is considered to be acceptable. In the case of TC 7, the accuracy of the prediction is slightly worse than TC 6 from 0 to 200 seconds, but the gap between the two curves is smaller afterwards.

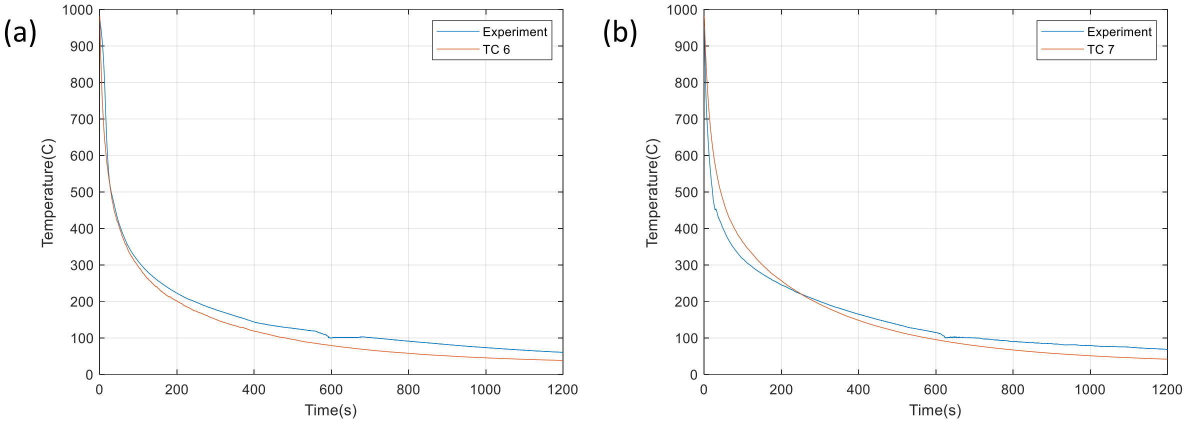

Figure 76 Temperature Curves at (a) TC 6, (b) TC 7.

The difference between the temperature curves of simulation and experimental data at TC 7 is partially inherited from TC 4. TC 7 is located 4.5 mm deeper than TC 4, so the experimental temperature evolution at TC 7 is heavily influenced by the heat transfer conditions at the surface which is reflected by the temperature profile at TC 4. Since the model fails to simulate the cooling trend at TC 4, it is not able to capture the cooling behaviour at TC 7 at a high accuracy either.

The percent error plots of TC 6 and 7 are shown in Figure 77 (a) and (b), respectively. It can be seen that the error at TC 6 is much smaller than at TC 7 at the beginning of the cooling process, but is increased with time in a more rapid rate. In the later stage of the quench cooling process, the errors of both groups of data get close to 40%.

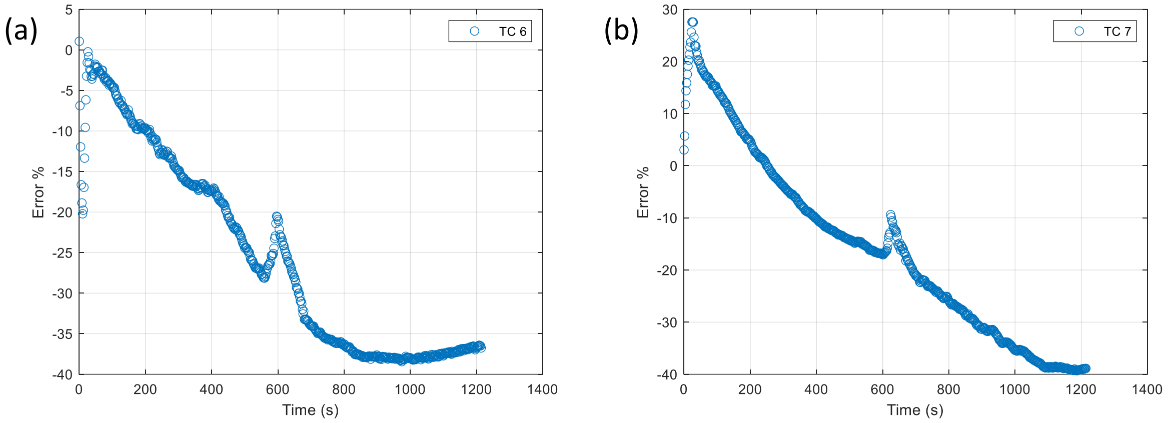

Figure 77 Percent Error Scatter Plots of Temperature Predictions at (a) TC 6, (b) TC 7

6.3.4 Positions in the Bulk Material

The simulation performance at TC 8 and 9 mainly reflects the model's ability to solve for the thermal conduction results in the solid material. This is particularly important in the cases of modelling large components or thick sections. The predicted and experimentally measured temperature curves at both positions are shown in Figure 78 (a) and (b). According to the figures, the model is successful in predicting the temperature inside the solid material. At both positions, the temperature is held at the soak temperature for a while before being cooled down. The temperature is held for about 30 s at TC 8, and about 100 s at TC 9. The distance to the nearest surface from TC 9 is twice as much as TC 8, but the delay in the inception of cooling can be three times as much or even more.

The scatter plots of the percent error of both positions are shown in Figure 78. Like other positions, the percent error is increased in the later phases of cooling. Despite this increasing error, the overall accuracy of the temperature prediction is great. Hence, the calculated solid thermal properties and the calculation of the thermal conduction process in the solid domain are carried out properly. The most likely reason that causes this increasing error is the faster heat transfer rate predicted at the solid-liquid interface. This also explains the consistency in the error scatter plots in Figure 75, Figure 77, and Figure 79.

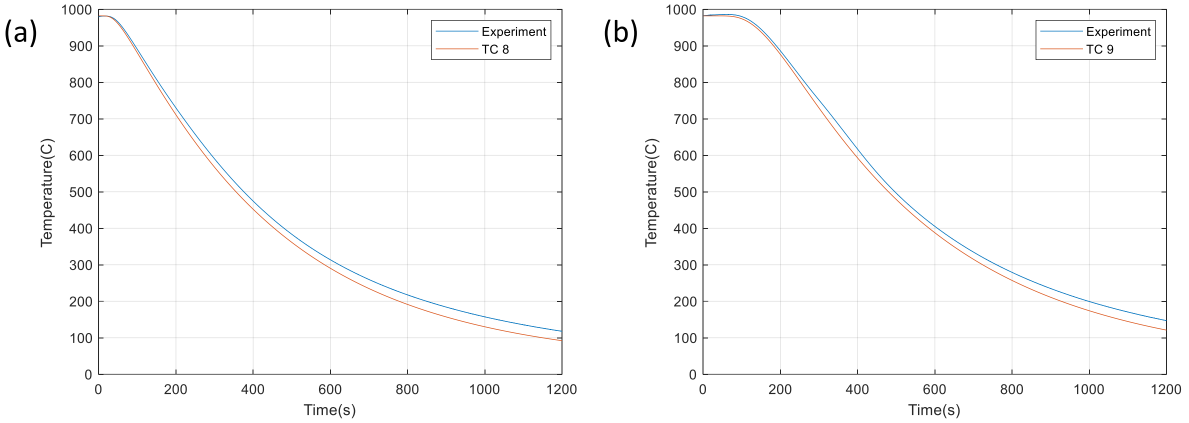

Figure 78 Temperature Curves at (a) TC 8, (b) TC 9.

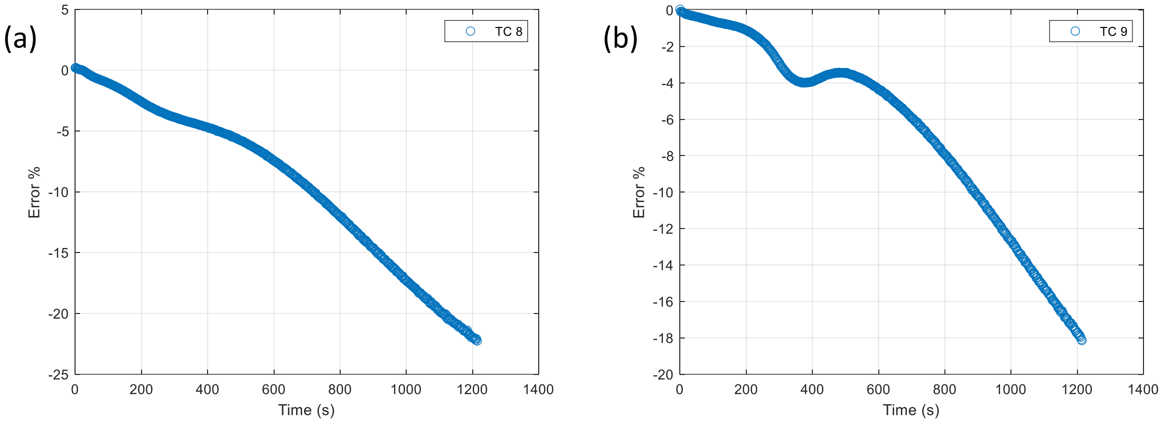

Figure 79 Percent Error Scatter Plots of Temperature Predictions at (a) TC 8, (b) TC 9.

6.3.5 Discussion

From Figure 74 to Figure 77Figure 79, it is observed that for almost all the near-surface sites, the predicted solid cooling rate is slower than the experimental data in the beginning stage. This statement corresponds to the positive relative error displayed in the error plot figures (Figure 75 and Figure 77).

Similarly to the small-scale models, this phenomenon induced by not considering the interfacial compressibility on the bubble surfaces. On the other hand, the error between the simulated result and the experimental data is reduced in the case of large-scale models in comparison to the small-scale ones. This is because in the large-scale case, the water tank is much bigger, so the liquid phase has a higher velocity at the centre area of the fluid domain. As a result, the average fluid temperature around the solid sample is not elevated as much, thus the solid cooling rate is not severely slowed down.

Apart from that, as previously mentioned in §6.2 and §6.3.1 the selection of a balanced mesh grid also introduces error. It can be seen from Figure 70 and Figure 71 that the finer the mesh grids are, the slower cooling is at solid surface positions, and the closer the prediction is to the experimental data. Therefore, the error in the predicted cooling rate is also a result of the selection of a relatively productive mesh refinement level.

It is worth mentioning that the absence of film boiling stage of the simulation results is quite obvious in Figure 71. The relatively slow cooling recorded during the experiment in the first seven or eight seconds of cooling reflects the film boiling stage. The simulated temperature curve does not show a similar trend, indicating the absence of film boiling behaviour of the prediction. Meanwhile, the simulated temperature curves for both mesh refinement levels show abnormally fast cooling rates within a very short period after the cooling begins. After that, the temperature stays the same or even slightly increases a little bit, and then decreases with time at a proper rate. The reason behind this phenomenon is not fully clear. Similar behaviours can also be observed for multiple curves in Figure 70, indicating that it is irrelevant to mesh size.

6.4 Heat Flux Boundary Condition

The heat flux thermal boundary condition tested in § 4.10 and § 5.7 is applied to all the solid-liquid interface in this model instead of the coupled thermal condition. It should be noted that in Babu et al.'s work [139], they stated that the correlation is valid if the soak temperature of the solid is within the range from 750 ℃ to 950 ℃. This is because among all the data they collected via quench cooling tests, the highest soak temperature is 950 ℃. The correlation is established based on the results of these tests, so there is no evidence as to whether the correlation is reliable or not when the soak temperature is above 950 ℃. In this paper, the designed soak temperature of the quench test is 980 ℃, but the process of opening the furnace door and then transferring the sample from the furnace to the quench tank requires 20 seconds or so. As a result, the initial temperature at most surface positions is around 960 ℃.

6.4.1 Surface Positions

The predicted and experimentally measured temperature curves at TC 1-5 are shown in Figure 80. Regardless of the position and the surface orientation, all the simulation results predict much faster cooling rates than the experimental data. This is as expected, because the same heat flux calculation method is applied to all the surfaces without any variation without a guaranteed reliability.

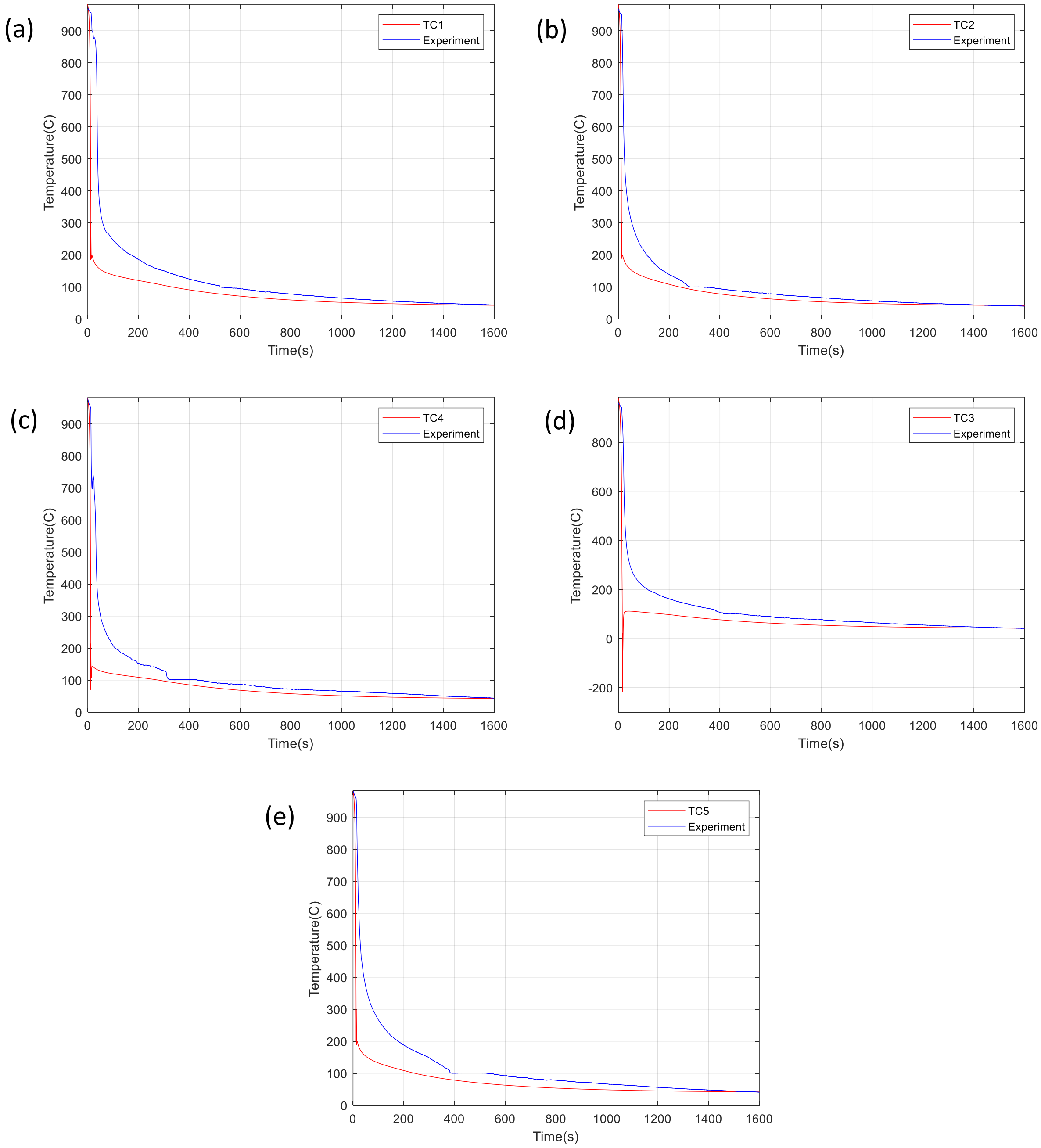

Figure 80 Temperature Curves at (a) TC 1, (b) TC 2, (c) TC 3, (d) TC 4, (e) TC5.

However, at TC 3 and 4, the temperature drops abnormally in very short time. At TC 3, the temperature even becomes negative, which is obviously unrealistic. Such phenomenon is then investigated.

By setting $T_{soak} = 980$ and $T_q = 20$, the normalized heat flux is plotted as a function of solid surface temperature in the range from 20 ℃ to 980 ℃ and shown in Figure 81 (a). In this figure, the location of the peak temperature is marked by the red dashed line. When the surface temperature approaches the peak value from the high temperature end, the normalized heat flux suddenly increases dramatically up to 1.5. However, by definition, this value should not exceed 1.0. This abnormally high heat flux causes the unrealistic temperature evolution at TC 3 and 4.

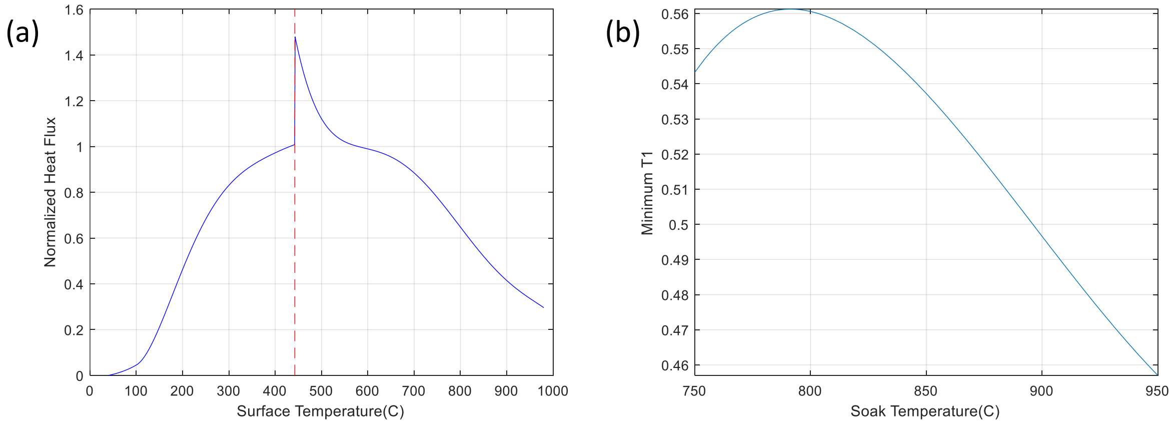

Figure 81 (a) Normalized Heat Flux, (b) Minimum T_1
Plot as a Function of Solid Surface Temperature.

Such abnormal normalized heat flux is closely related to the range of the dimensionless temperature T_1. Calculated by Equation (103), T_1 is ranged from its minimum value to 1.0. The minimum T_1 is related to the soak temperature if the liquid temperature is fixed as 20 ℃. Thus, the relationship between the minimum T_1 value and the soak temperature is plotted in Figure 81 (b). For a valid empirical correlation, the calculated normalized heat flux value must be realistic throughout the entire T_1 range. However, as shown in Figure 82, Equation (104) is a regression result with a T_1 ranged from 0.55 to 1.0. In other words, this equation is not guaranteed to be valid when T_1 becomes smaller than 0.55.

In this case where the soak temperature is 980 ℃, the minimum T_1 value is approximately 0.46 which is much smaller than 0.55, so Equation (104) returns unrealistic results when the surface temperature approaches T_{peak}. Even with a soak temperature of 950 ℃ which is claimed to be a valid input by the authors, the minimum T_1 is still far smaller than 0.55 and the calculated normalized heat flux is unreliable. In fact, the valid soak temperature range for this empirical calculation method is far smaller than that claimed by the authors.

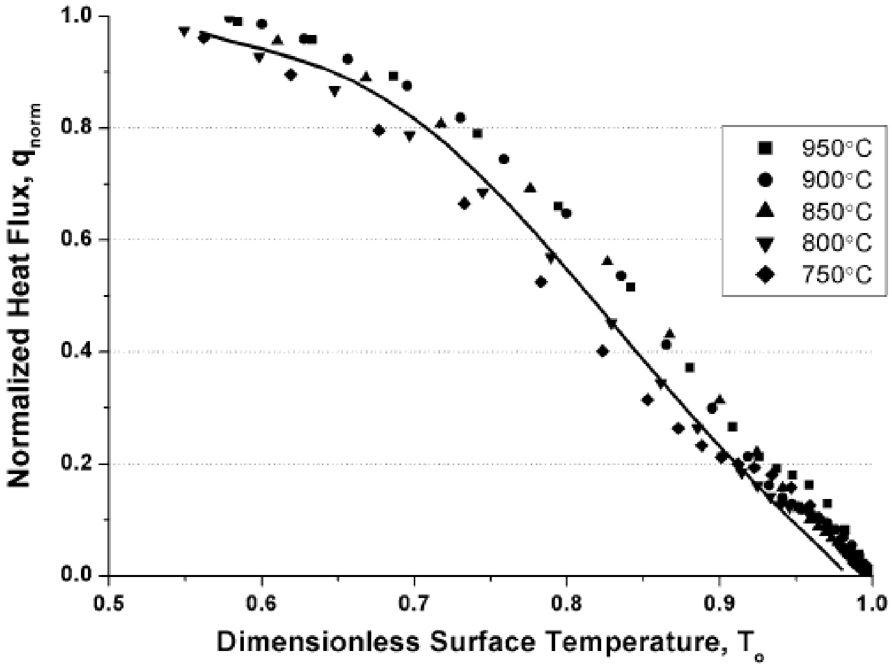

Figure 82 Model for normalized heat flux as a function of dimensionless [139].

6.4.2 Sub-Surface Positions

The predictions at the sub-surface locations (TC 6 and 7) are shown in Figure 83. At these sub-surface positions, the predicted temperature is still much lower than the experimental results at the beginning of the cooling process. These two locations happen to be slightly deeper than TC 3 and 4 where the abnormal temperature profile is generated by the model. However, the corresponding sub-surface thermal couples are not affected by the nearby faulty predictions.

Even though significant gaps exist between the predictions and the experimental data at both locations, the difference is reduced to an acceptable level as the cooling proceeds to low temperature range. Thanks to the very short period when the abnormally high heat flux is applied to the solid surfaces, the predictions at the sub-surface locations are still able to capture the overall cooling rate trend.

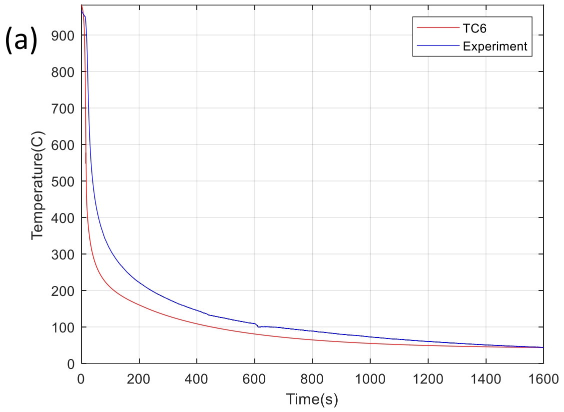

Figure 83 Temperature Curves at (a) TC 6, (b) TC 7.

6.4.3 Positions in the Bulk Material

As can be seen in Figure 84, the model shows decent performance while predicting the temperature inside the solid material. Even though there is still a noticeable gap between the simulation and experimental data curves, the overall temperature evolution trends are in good accordance with each other.

Compared to Figure 78, the gap size between the two curves in Figure 84 are slightly bigger. Since all the model parameters that are directly related to thermal conduction are kept the same for both models, the difference in the gap size is induced by the different predictions at the solid-liquid interface.

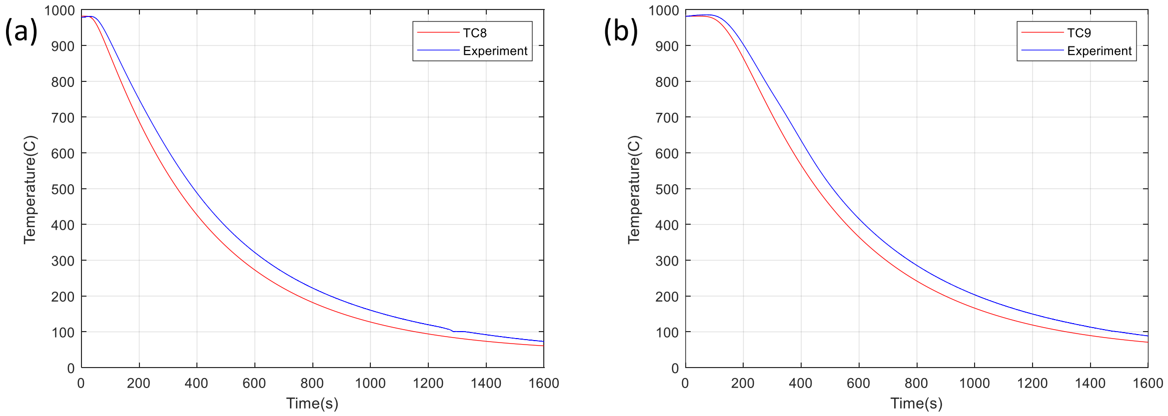

Figure 84 Temperature Curves at (a) TC 8, (b) TC 9.

As a result of the faster cooling predicted by the heat flux thermal boundary condition, the predicted temperature inside the bulk material is also lower than the previous model. As long as the model is implemented with the correct solid thermal properties and the proper mathematical model of solid energy, the temperature evolution trend inside the bulk material can be correctly simulated with minor defects. The cooling rate in the bulk material is not sensitive to the faulty predictions of the heat transfer rate at the solid-liquid interface, but such inaccurate predictions can induce a temperature shift that is maintained throughout the whole cooling process for any location in the bulk material. The magnitude of such temperature shift is determined by the inaccuracy of the heat transfer rate prediction at the solid-liquid interface.

6.5 Summary

In this chapter, the results of two large-scale models are displayed and discussed. In the first model, the thermal boundary condition is remained as coupled, but the pressure outlet surface is changed to a surface that is normal to y axis. This model is referred to as the large-scale coupled model. In the second model, the thermal boundary condition at the solid-liquid interface is changed from coupled to the empirical heat flux equations, and the model is referred to as the large-scale heat flux model.

The large-scale coupled model yields decent simulation results at all the surface positions except for the two positions at the top surface. For the sub-surface and the bulk material locations, the predicted results are considered to be in good accordance with the experimental data. The major concern about this model is that the dissymmetry of the flow conditions in the quench tank may induce anisotropy to the temperature distribution in the solid sample. Nevertheless, this is expected to only affect the superficial cooling behaviour of the solid sample.

The large-scale heat flux model predicts much faster cooling rate in the early stage of the cooling process at all the superficial locations. In some of the locations, severely faulty results are generated because of the highly limited applicability of the applied empirical equations. At sub-surface locations, the simulation result is not influenced by the faulty predictions at the superficial locations. Even though the predicted cooling is still faster than the experimental data, the overall temperature evolution trend is mostly reflected. In the bulk material, the predicted temperature curve is in good accordance with the experimental data, though a small gap exists between the curves.

The findings can be concluded as following:

1) Different from the small-scale models, the high intensity circulating flow yields a much better overall result than the empirical heat flux equation. This is mostly attributed to the limitation of the valid soak temperature range of the empirical equation.
2) The calculated thermal properties of Inconel 718 and the solution of the solid energy equation are successful. As a result, the thermal conduction rate inside the bulk material is properly delt with.
3) The temperature evolution in the bulk material is not sensitive to the heat transfer rate at the solid-liquid interface. If the prediction of the heat transfer rate is inaccurate, it is likely to induce a temperature shift in the bulk material. Such temperature shift is maintained throughout the whole cooling process until the sample is fully cooled down to the ambient temperature.

7 Conclusions and Future Work

The main goal of this project is to develop robust models which are able to predict the temperature evolution of the sample during a quench cooling process without requiring any experimentally acquired data prior to the simulation. The application of these models is focused on not only small-scale components which are often tested in labs, but also on large-scale components or parts with thick sections that are often involved with industrial manufacturing. The models are designed to be based on CFD methods and FEM and are constructed and solved by the ANSYS software packages. The heat transfer and boiling effects are solved by a semi-mechanistic model, but an empirical model is also applied to discuss the difference between the performance of these two methods.

The simulated process of this paper is the immersion quench cooling of cylindrical workpieces of different sizes in liquid water at 20 ℃. According to the sample size, the models are divided into two groups: small-scale models and large-scale models. For the small-scale models, the material of the solid sample is Inconel 600, and the initial solid temperature is 855 ℃. For the large-scale models, the solid sample is made of Inconel 718, and the initial temperature is 980 ℃. The thermal properties of both alloys are calculated as functions of temperature based on the nominal chemical composition and are fed to the solver in the form of polynomial regression.

7.1 Small-scale Models

Two slightly different sample shapes, denoted as cylinder and probe, are modelled in the small-scale models. The influence of various model parameters on the predicted temperature results is analysed. These parameters are mostly reflections of the real physical mechanisms, including velocity inlet (immersion process), initial temperature gradient inside the solid sample, higher overall boiling intensity, circulating fluid flow with higher intensity in the quench tank, empirical heat flux boundary condition. Based on the analysis and discussion of the results of the small-scale models, the following conclusions can be drawn:

1) It is necessary to incorporate the boiling effect into the model for a reasonable prediction. The major improvement of including the boiling effect is that it enables sufficient fluid flow in the near-solid fluid region, which consequently prevents the fluid temperature in

this region from being dramatically increased. Similar effect can also be accomplished by specifying a temperature dependent density for liquid water.

2) By including extra portion of the probe, the solid geometry is better reflected by the probe model. This significantly improves the performance of the model with coupled thermal boundary condition and the evaporation condensation boiling mass transfer model.
3) Model parameters like velocity inlet, initial solid temperature gradient, and higher boiling intensity have the potential to make the model predictions more realistic, but the improvement is very limited. The difference is also made by inducing changes to the fluid flow conditions of the near-solid fluid region. Based on the probe sample geometry, the influence of factors including the velocity inlet, initial solid temperature gradient, and a higher boiling evaporation coefficient may have quite the opposite influence on the predicted cooling rate compared to the cylinder sample geometry.
4) High intensity circulating flow is continuously generated in the quench tank as a result of the specific boundary condition on the surface. Under such circumstance, the predicted cooling rate of the cylinder sample model is significantly enhanced. In the case of the probe sample model, a sharp cooling rate peak is formed because of the thermal conduction in the solid domain and the unevenly distributed fluid velocity.
5) The combination of coupled thermal boundary condition and a semi-mechanistic boiling model (evaporation condensation model) is not able to accurately simulate the high cooling rate during the nucleate boiling phase. Increasing the flow intensity in the near-solid fluid region can increase the cooling rate throughout the whole cooling process but cannot accurately simulate the cooling rate variation trend of the experimental data.
6) The optimal result is obtained by implementing the empirical equation of heat flux as the thermal boundary instead of the coupled interface thermal condition to the cylinder sample model. The overall relative average error is 27.31%, while for the first 20 seconds of cooling, the number is 2.23%. In addition, it is very possible that during the experiment process, the data of the initial two seconds of cooling is not recorded. With proper data processing and selection of this model set-up, the simulation result is in perfect match with the experimental data.

7.2 Large-scale Models

Due to the significantly increased calculation power requirement, the solution process of the large-scale model is far less efficient than the small-scale model. Thus, only two models are eventually solved with the model specifications that have delivered the optimal results in the small-scale models. One has high intensity circulating flow in the quench tank, the other model has normal fluid flow conditions in the quench tank, and the thermal boundary condition is the empirical heat flux equation. The results can be concluded as followings:

1) The optimal prediction is obtained with the combination of a high intensity circulating flow in the quench tank, coupled thermal boundary condition, and the evaporation condensation boiling mass transfer model.
2) Due to the limited applicability of the empirical heat flux equations, the model generates unrealistic temperature profiles at some of the superficial locations. In addition, the cooling rate predicted by this model is much faster than the experimental data in the whole solid domain.
3) The thermal conduction rate in the bulk material is accurately predicted by the model with the implementation of proper solid thermal properties and mathematical model of the energy in the solid domain. In this case, even if the heat transfer rate at the solid surface is not successfully predicted, the temperature prediction inside the bulk material would not be severely affected. In other words, for large-scale workpiece, the accuracy of heat transfer rate at the solid surface is not as important as for small-scale workpieces if the temperature evolution deep inside the bulk material is the only concerned outcome of the model.

7.3 Future Work

The attempt to implement a mass transfer UDF was not achieved in this study. This a result of challenges in the numerical implementation of appropriate interface conditions within the ANSYS software package. Implementation of a boiling mass transfer description that can predict the varying boiling behaviour from film boiling to nucleate boiling and accurately simulate the effects of nucleate boiling is key in reliable fluid flow and energy dissipation predictions when combined with the coupled thermal boundary conditions.

The mathematical framework of the model can be significantly improved via incorporating the interfacial compressibility at the bubble surface. Meanwhile, with the consideration of radiation heat transfer, a real film boiling stage could be reproduced in the simulation result. In this way, the model would be able to represent actual physical mechanisms during a quench cooling process.

In the case with high intensity circulating flow, the relationship between the quench tank geometry and the resulted fluid flow pattern is worth researching. This is also a predominant factor for the cooling rate at the solid surface. It is also possible to adjust the overall flow intensity by adjusting the gravitational acceleration. Such model set-up can potentially be used to simulate the influence of the agitation in the quench tank. In addition, other methods that are able to simulate high intensity fluid flow around the solid surface are also worth researching.

The applicability of the empirical heat flux equation has great potential for improvement. Currently, this regression-based method is only valid when the soak temperature of the solid sample is within the range from 750 ℃ to 850 ℃ according to the testing in this study. By taking a wider range of T_1 into consideration, the method can become truly valid in the range from 750 ℃ to 950 ℃ which is applicable to most quench cooling cases.

Appendices

Journal File for Case Setting

```
;Journal file used for HPC simulation
/file read-case AFRC6

; Turn on energy
/define/model/energy? yes yes yes

; Copy materials from fluent database
/define/materials/copy fluid water-liquid
/define/materials/copy fluid water-vapor
/define/materials/copy solid nickel

; change material properties
/define/materials/change-create/nickel nickel no yes polynomial 3 394.2152
0.1633 8.0519e-6 yes polynomial 3 6.5344 0.0171 -4.2793e-7

; Mesh interface
/define/mesh-interfaces/create conjugate interface-sample () interface-tank
() no no no yes no

; Viscous model and wall function
/define/models/viscous ke-rng yes
/define/models/viscous curvature-correction? yes
/define/models/viscous near-wall-treatment enhanced-wall-treatment? yes
/define/models/viscous near-wall-treatment wf-thermal-effects? yes

; Multiphase
/define/models/multiphase model vof
/define/models/multiphase number-of-phases 2
/define/models/multiphase body-force-formulation yes
/define/models/multiphase vfp implicit 1e-6

; Define phases
/define/phases/phase-domain phase-1 liq yes water-liquid
/define/phases/phase-domain phase-2 gas yes water-vapor
/define/phases/interaction-domain 1 liq gas evaporation-condensation no 0
no yes yes yes yes yes constant 0.072

; Cell zone conditions
/define/boundary-conditions/solid sample mixture yes nickel

; Specify operating conditions
/define/operating-conditions/operating-density/sod 3 1.225
/define/operating-conditions/gravity yes 0 0 -9.81

; Change p-v coupling to coupled
/solve/set/p-v-coupling 24

; Transient formulation changed to unsteady 2nd order
/define/models/u2o y

; Change the discretization scheme
/solve/set/discretization-scheme/mom 0
;/solve/set/discretization-scheme/temperature 0

; Change URF
```

```
;/solve/set/under-relaxation/k 0.6
;/solve/set/under-relaxation/epsilon 0.6
;/solve/set/under-relaxation/temperature 0.8
;/solve/set/under-relaxation/turb-viscosity 0.8

; Define custom field function
;/define/custom-field-functions/define "temp-gradient" " - 3500 *
z_coordinate + 1233.15"
;/define/custom-field-functions/define "radial-temp-gradient-heated" " -
500 * sqrt(x_coordinate ^ 2 + y_coordinate ^ 2 ) + 1128.15"

; Create a Binary transient export
/file/transient-export/cfd binary-export interface-tank interface-sample ()
sample tank () temperature heat-transfer-coef heat-transfer-coef-wall heat-
transfer-coef-wall-adj heat-transfer-coef-yplus heat-flux gas-vof x-
velocity y-velocity z-velocity velocity-magnitude q yes no "binary-export"
"flow-time" 0.2 flow-time 3

; Create autosave
/file/auto-save/sdfe time-step
/file/auto-save/data-frequency 1
/file/auto-save/retain-most-recent-files yes
/file/auto-save/append-file-name-with flow-time 4

; Create cell registers
/solve/cell-registers/add "water" type hexahedron max-point 0.49 0.49 -0.1
min-point -0.49 -0.49 -0.55 q q

; define the bc for velocity inlet
;/define/boundary-conditions/set/velocity-inlet velocity-inlet () mixture
vmag no " 0.6998[m s^-1]/(1+exp(4[s^-1]*(Time - 1.5 [s])))" q

; define phase composition of backflow fluid
;/define/bc/set/pressure-outlet pressure-outlet () gas vf no 1 q

; define the heat flux boundary conditions
;/define/bc/wall conjugate-wall1-1-1-shadow mixture 0 no 0 no yes heat-flux
no "IF(TotalTemperature>715.51[K],-4.8471E6 *(-236.277 [W m^-
2]*((TotalTemperature-293.15[K])/960[K])^5 +939.959 [W m^-
2]*((TotalTemperature-293.15[K])/960[K])^4 - 1468.072[W m^-
2]*((TotalTemperature-293.15[K])/960[K])^3 + 1121.514[W m^-
2]*((TotalTemperature-293.15[K])/960[K])^2 - 419.969 [W m^-
2]*((TotalTemperature-293.15[K])/960[K]) + 62.864 [W m^-2]), -4.8471E6*(-
13.752 [W m^-2]*((TotalTemperature-273.15 [K])/442.3633[K])^5 + 51.469[W
m^-2] * ((TotalTemperature-273.15 [K])/442.3633[K])^4 - 73.201[W m^-
2]*((TotalTemperature-273.15 [K])/442.3633[K])^3 + 47.338[W m^-
2]*((TotalTemperature-273.15 [K])/442.3633[K])^2 - 11.876[W m^-
2]*((TotalTemperature-273.15 [K])/442.3633[K]) + 1.0302 [W m^-2]))" no no
no 90 no 1
/define/bc/wall conjugate-wall1-1-1 mixture 0 no 0 no yes heat-flux no
"IF(TotalTemperature>715.51[K],-4.8471E6 *(-236.277 [W m^-
2]*((TotalTemperature-293.15[K])/960[K])^5 +939.959 [W m^-
2]*((TotalTemperature-293.15[K])/960[K])^4 - 1468.072[W m^-
2]*((TotalTemperature-293.15[K])/960[K])^3 + 1121.514[W m^-
2]*((TotalTemperature-293.15[K])/960[K])^2 - 419.969 [W m^-
2]*((TotalTemperature-293.15[K])/960[K]) + 62.864 [W m^-2]), -4.8471E6*(-
13.752 [W m^-2]*((TotalTemperature-273.15 [K])/442.3633[K])^5 + 51.469[W
m^-2] * ((TotalTemperature-273.15 [K])/442.3633[K])^4 - 73.201[W m^-
2]*((TotalTemperature-273.15 [K])/442.3633[K])^3 + 47.338[W m^-
2]*((TotalTemperature-273.15 [K])/442.3633[K])^2 - 11.876[W m^-
2]*((TotalTemperature-273.15 [K])/442.3633[K]) + 1.0302 [W m^-2]))" no 1
```

```
/solve/initialize/initialize-flow

; Hybrid initialization and patch
/solve/initialize/hyb-initialization yes
;/solve/patch gas tank () () mp 0
;/solve/patch gas () water () mp 0
/solve/patch mixture sample () () temperature 1255.15
/solve/patch mixture tank () () temperature 293.15
;/solve/patch mixture () unheated_probe () temperature yes temp-gradient

; Locations of thermal couples
/surface/point-surface tc-1-1 0 0.096 0.051
/surface/point-surface tc-1-2 0 0.097 0.0053
/surface/point-surface tc-1-3 0 0.094 0.005
/surface/point-surface tc-1-4 0 0.051 0.003
/surface/point-surface tc-1-5 0.051 0 0.002
/surface/point-surface tc-1-6 0.093 0 0.005
/surface/point-surface tc-1-7 0.0965 0 0.005
/surface/point-surface tc-1-8 0.097 0 0.0525
/surface/point-surface tc-1-9 0.051 0 0.097
/surface/point-surface tc-1-10 0.049 0 -0.097

/surface/point-surface tc-2-1 0.001 0 0.097
/surface/point-surface tc-2-2 0.001 0 0.094
/surface/point-surface tc-2-3 0.001 0 0
/surface/point-surface tc-2-4 0.002 0 -0.094
/surface/point-surface tc-2-5 0.002 0 -0.0975
/surface/point-surface tc-2-6 0 0.050 0.097
/surface/point-surface tc-2-7 0 0.050 -0.097
/surface/point-surface tc-2-8 0.0975 0 -0.051
/surface/point-surface tc-2-9 0 0.097 -0.050

; Report definitions of temperature
/solve/report-definitions/add temp-1-1 surface-vertexavg field mixture
temperature surface-names tc-1-1 () q
/solve/report-definitions/add temp-1-2 surface-vertexavg field mixture
temperature surface-names tc-1-2 () q
/solve/report-definitions/add temp-1-3 surface-vertexavg field mixture
temperature surface-names tc-1-3 () q
/solve/report-definitions/add temp-1-4 surface-vertexavg field mixture
temperature surface-names tc-1-4 () q
/solve/report-definitions/add temp-1-5 surface-vertexavg field mixture
temperature surface-names tc-1-5 () q
/solve/report-definitions/add temp-1-6 surface-vertexavg field mixture
temperature surface-names tc-1-6 () q
/solve/report-definitions/add temp-1-7 surface-vertexavg field mixture
temperature surface-names tc-1-7 () q
/solve/report-definitions/add temp-1-8 surface-vertexavg field mixture
temperature surface-names tc-1-8 () q
/solve/report-definitions/add temp-1-9 surface-vertexavg field mixture
temperature surface-names tc-1-9 () q
/solve/report-definitions/add temp-1-10 surface-vertexavg field mixture
temperature surface-names tc-1-10 () q
/solve/report-definitions/add temp-2-1 surface-vertexavg field mixture
temperature surface-names tc-2-1 () q
/solve/report-definitions/add temp-2-2 surface-vertexavg field mixture
temperature surface-names tc-2-2 () q
/solve/report-definitions/add temp-2-3 surface-vertexavg field mixture
temperature surface-names tc-2-3 () q
```

```
/solve/report-definitions/add temp-2-4 surface-vertexavg field mixture
temperature surface-names tc-2-4 () q
/solve/report-definitions/add temp-2-5 surface-vertexavg field mixture
temperature surface-names tc-2-5 () q
/solve/report-definitions/add temp-2-6 surface-vertexavg field mixture
temperature surface-names tc-2-6 () q
/solve/report-definitions/add temp-2-7 surface-vertexavg field mixture
temperature surface-names tc-2-7 () q
/solve/report-definitions/add temp-2-8 surface-vertexavg field mixture
temperature surface-names tc-2-8 () q
/solve/report-definitions/add temp-2-9 surface-vertexavg field mixture
temperature surface-names tc-2-9 () q

; Create min and max ystar
;/solve/report-definitions/add minYstar volume-min field mixture y-star
zone-names tank () q
;/solve/report-definitions/add maxYstar volume-max field mixture y-star
zone-names tank () q

; Set up the min and max ystar plot
;/solve/report-plot/add minYstarplot x-label flow-time y-label minYstar
report-defs minYstar () frequency-of flow-time flow-frequency 0.2 q
;/solve/report-plot/add maxYstarplot x-label flow-time y-label maxYstar
report-defs maxYstar () frequency-of flow-time flow-frequency 0.2 q

; Create report files for temperature curve
/solve/report-files add report-temp-1-1 report-defs temp-1-1 () file-name
"report-temp-1-1.out" frequency-of flow-time flow-frequency 0.02 q
/solve/report-files add report-temp-1-2 report-defs temp-1-2 () file-name
"report-temp-1-2.out" frequency-of flow-time flow-frequency 0.02 q
/solve/report-files add report-temp-1-3 report-defs temp-1-3 () file-name
"report-temp-1-3.out" frequency-of flow-time flow-frequency 0.02 q
/solve/report-files add report-temp-1-4 report-defs temp-1-4 () file-name
"report-temp-1-4.out" frequency-of flow-time flow-frequency 0.02 q
/solve/report-files add report-temp-1-5 report-defs temp-1-5 () file-name
"report-temp-1-5.out" frequency-of flow-time flow-frequency 0.02 q
/solve/report-files add report-temp-1-6 report-defs temp-1-6 () file-name
"report-temp-1-6.out" frequency-of flow-time flow-frequency 0.02 q
/solve/report-files add report-temp-1-7 report-defs temp-1-7 () file-name
"report-temp-1-7.out" frequency-of flow-time flow-frequency 0.02 q
/solve/report-files add report-temp-1-8 report-defs temp-1-8 () file-name
"report-temp-1-8.out" frequency-of flow-time flow-frequency 0.02 q
/solve/report-files add report-temp-1-9 report-defs temp-1-9 () file-name
"report-temp-1-9.out" frequency-of flow-time flow-frequency 0.02 q
/solve/report-files add report-temp-1-10 report-defs temp-1-10 () file-name
"report-temp-1-10.out" frequency-of flow-time flow-frequency 0.02 q
/solve/report-files add report-temp-2-1 report-defs temp-2-1 () file-name
"report-temp-2-1.out" frequency-of flow-time flow-frequency 0.02 q
/solve/report-files add report-temp-2-2 report-defs temp-2-2 () file-name
"report-temp-2-2.out" frequency-of flow-time flow-frequency 0.02 q
/solve/report-files add report-temp-2-3 report-defs temp-2-3 () file-name
"report-temp-2-3.out" frequency-of flow-time flow-frequency 0.02 q
/solve/report-files add report-temp-2-4 report-defs temp-2-4 () file-name
"report-temp-2-4.out" frequency-of flow-time flow-frequency 0.02 q
/solve/report-files add report-temp-2-5 report-defs temp-2-5 () file-name
"report-temp-2-5.out" frequency-of flow-time flow-frequency 0.02 q
/solve/report-files add report-temp-2-6 report-defs temp-2-6 () file-name
"report-temp-2-6.out" frequency-of flow-time flow-frequency 0.02 q
/solve/report-files add report-temp-2-7 report-defs temp-2-7 () file-name
"report-temp-2-7.out" frequency-of flow-time flow-frequency 0.02 q
```

```
/solve/report-files add report-temp-2-8 report-defs temp-2-8 () file-name
"report-temp-2-8.out" frequency-of flow-time flow-frequency 0.02 q
/solve/report-files add report-temp-2-9 report-defs temp-2-9 () file-name
"report-temp-2-9.out" frequency-of flow-time flow-frequency 0.02 q

; Create a zx plane for contours
/surface/plane-surface zx-plane zx-plane 0

; Create temperature contour
/display/objects/create contour temperature field mixture temperature
surfaces-list zx-plane () q
/solve/animate/objects/create temp animate-on temperature view top
frequency-of flow-time flow-time-frequency 0.2 storage-type hsf storage-dir
"" () q

; Create vapour vof contour
/display/objects/create contour vapour-vof field gas vof surfaces-list zx-
plane () q
/solve/animate/objects/create vapour animate-on vapour-vof view top
frequency-of flow-time flow-time-frequency 0.2 storage-type hsf storage-dir
"" () q

; Create velocity contour
/display/objects/create contour velocity field mixture velocity-magnitude
surfaces-list zx-plane () q
/solve/animate/objects/create velocity-magnitude animate-on velocity view
top frequency-of flow-time flow-time-frequency 0.2 storage-type hsf
storage-dir "" () q

; Run calculation
;/solve/set/variable-time-stepping yes no 1 10 1e-5 1e-3 0.8 1.2 1 5e-4
/solve/set/time-step 2e-3
;/solve/set/transientcontrols/multiphase-specific-time-stepping yes 2 1e-4
1 1e-5 0.01 0.8 1.2 1
/solve/dual-time-iterate 40000 100
```

Mass Transfer UDF

```
#include "udf.h"
DEFINE_MASS_TRANSFER(liq_gas,cell,thread,from_index,from_species_index,to_i
ndex,to_species_index)
{
  real m_lg;
  real T_SAT=373.15;
  Thread*liq=THREAD_SUB_THREAD(thread,from_index);
  Thread*gas=THREAD_SUB_THREAD(thread,to_index);

if (C_VOF_G(cell,liq)==0) {

if (C_T(cell, liq) >= T_SAT) {
    m_lg = 0.1*C_VOF(cell,liq)*C_R(cell,liq)*fabs(C_T(cell,liq)-
T_SAT)/T_SAT;
}
else {
    m_lg = -0.1*C_VOF(cell,gas)*C_R(cell,gas)*fabs(T_SAT-
C_T(cell,gas))/T_SAT;
}
}
else {
```

```
        m_lg=2*0.6*NV_DOT(C_T_G(cell,thread),C_VOF_G(cell,liq))/2266667;
}
  return (m_lg);
}
```

Solution Logs Files of a Running Simulation

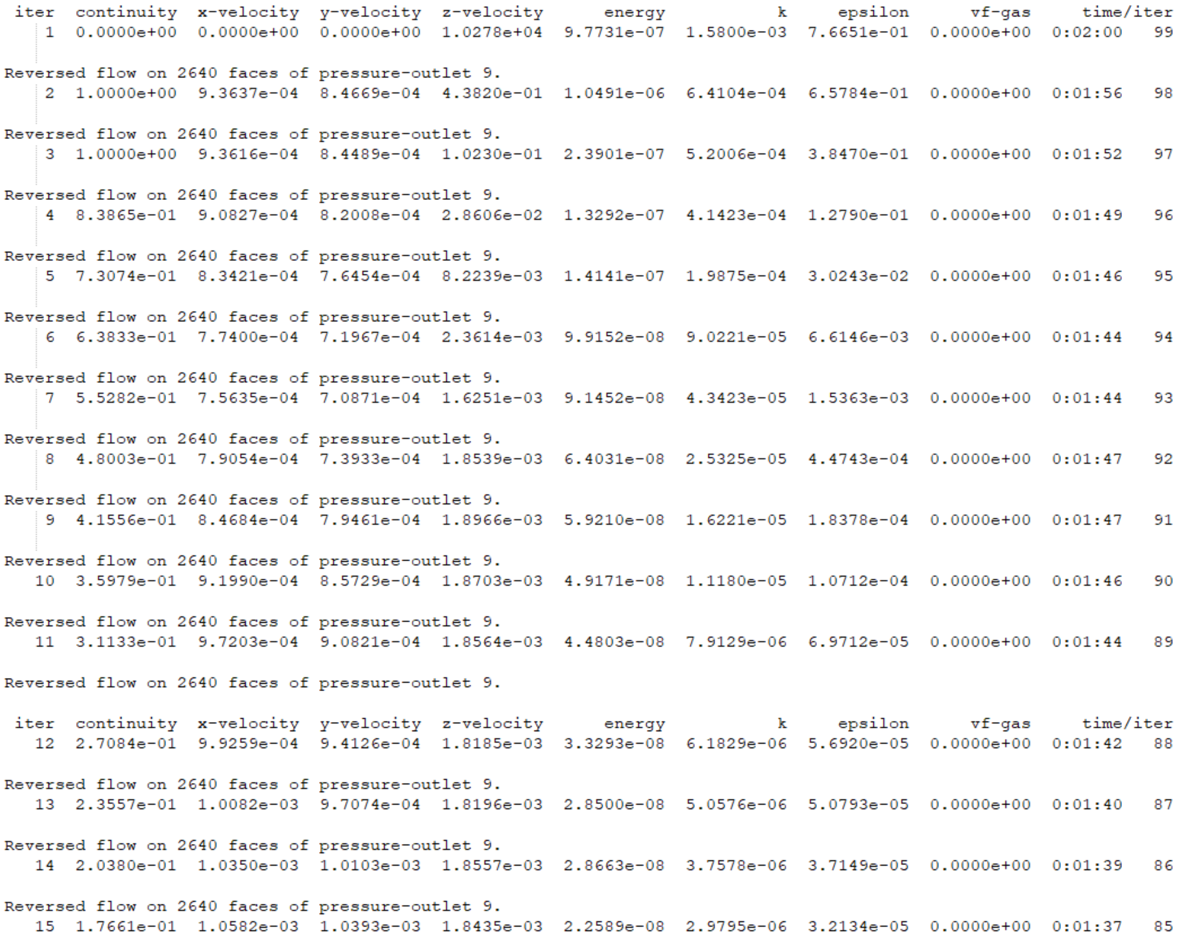

```
  iter  continuity  x-velocity  y-velocity  z-velocity      energy           k     epsilon      vf-gas     time/iter
     1  0.0000e+00  0.0000e+00  0.0000e+00  1.0278e+04  9.7731e-07  1.5800e-03  7.6651e-01  0.0000e+00  0:02:00   99

 Reversed flow on 2640 faces of pressure-outlet 9.
     2  1.0000e+00  9.3637e-04  8.4669e-04  4.3820e-01  1.0491e-06  6.4104e-04  6.5784e-01  0.0000e+00  0:01:56   98

 Reversed flow on 2640 faces of pressure-outlet 9.
     3  1.0000e+00  9.3616e-04  8.4489e-04  1.0230e-01  2.3901e-07  5.2006e-04  3.8470e-01  0.0000e+00  0:01:52   97

 Reversed flow on 2640 faces of pressure-outlet 9.
     4  8.3865e-01  9.0827e-04  8.2008e-04  2.8606e-02  1.3292e-07  4.1423e-04  1.2790e-01  0.0000e+00  0:01:49   96

 Reversed flow on 2640 faces of pressure-outlet 9.
     5  7.3074e-01  8.3421e-04  7.6454e-04  8.2239e-03  1.4141e-07  1.9875e-04  3.0243e-02  0.0000e+00  0:01:46   95

 Reversed flow on 2640 faces of pressure-outlet 9.
     6  6.3833e-01  7.7400e-04  7.1967e-04  2.3614e-03  9.9152e-08  9.0221e-05  6.6146e-03  0.0000e+00  0:01:44   94

 Reversed flow on 2640 faces of pressure-outlet 9.
     7  5.5282e-01  7.5635e-04  7.0871e-04  1.6251e-03  9.1452e-08  4.3423e-05  1.5363e-03  0.0000e+00  0:01:44   93

 Reversed flow on 2640 faces of pressure-outlet 9.
     8  4.8003e-01  7.9054e-04  7.3933e-04  1.8539e-03  6.4031e-08  2.5325e-05  4.4743e-04  0.0000e+00  0:01:47   92

 Reversed flow on 2640 faces of pressure-outlet 9.
     9  4.1556e-01  8.4684e-04  7.9461e-04  1.8966e-03  5.9210e-08  1.6221e-05  1.8378e-04  0.0000e+00  0:01:47   91

 Reversed flow on 2640 faces of pressure-outlet 9.
    10  3.5979e-01  9.1990e-04  8.5729e-04  1.8703e-03  4.9171e-08  1.1180e-05  1.0712e-04  0.0000e+00  0:01:46   90

 Reversed flow on 2640 faces of pressure-outlet 9.
    11  3.1133e-01  9.7203e-04  9.0821e-04  1.8564e-03  4.4803e-08  7.9129e-06  6.9712e-05  0.0000e+00  0:01:44   89

 Reversed flow on 2640 faces of pressure-outlet 9.

  iter  continuity  x-velocity  y-velocity  z-velocity      energy           k     epsilon      vf-gas     time/iter
    12  2.7084e-01  9.9259e-04  9.4126e-04  1.8185e-03  3.3293e-08  6.1829e-06  5.6920e-05  0.0000e+00  0:01:42   88

 Reversed flow on 2640 faces of pressure-outlet 9.
    13  2.3557e-01  1.0082e-03  9.7074e-04  1.8196e-03  2.8500e-08  5.0576e-06  5.0793e-05  0.0000e+00  0:01:40   87

 Reversed flow on 2640 faces of pressure-outlet 9.
    14  2.0380e-01  1.0350e-03  1.0103e-03  1.8557e-03  2.8663e-08  3.7578e-06  3.7149e-05  0.0000e+00  0:01:39   86

 Reversed flow on 2640 faces of pressure-outlet 9.
    15  1.7661e-01  1.0582e-03  1.0393e-03  1.8435e-03  2.2589e-08  2.9795e-06  3.2134e-05  0.0000e+00  0:01:37   85
```

Supplementary Figures

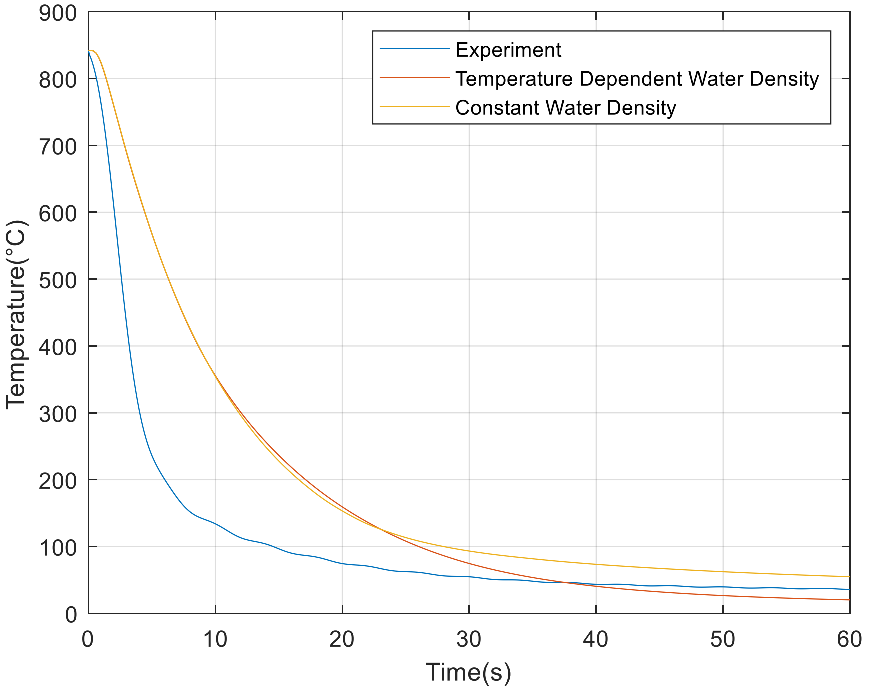

Figure 85 Temperature vs. Time Curves of The Multiphase Models with Water Densities That Are Dependent and Independent of Temperature.

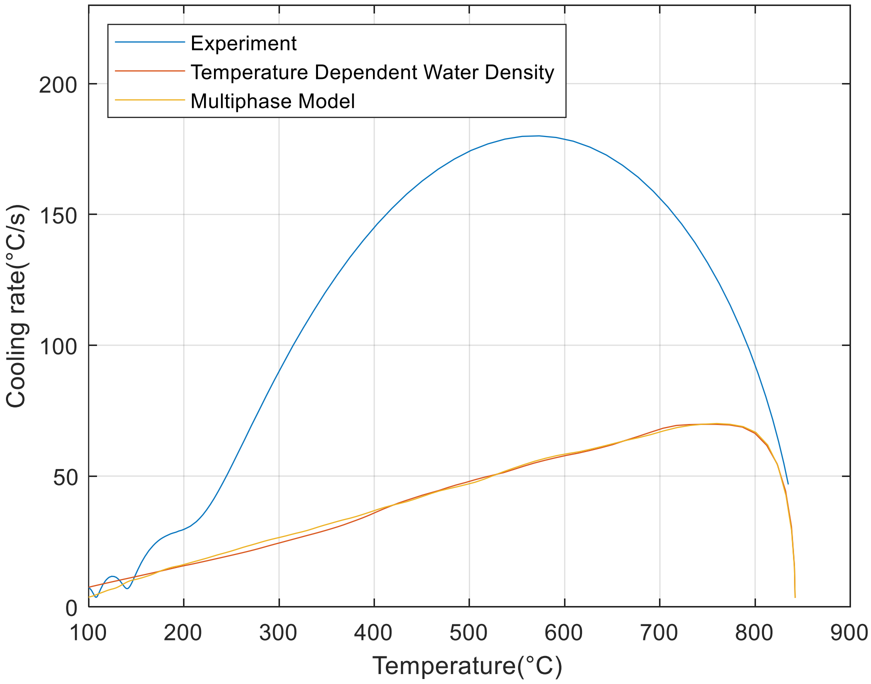

Figure 86 Cooling Rate vs. Temperature Curves of The Multiphase Models with Water Densities That Are Dependent and Independent of Temperature.

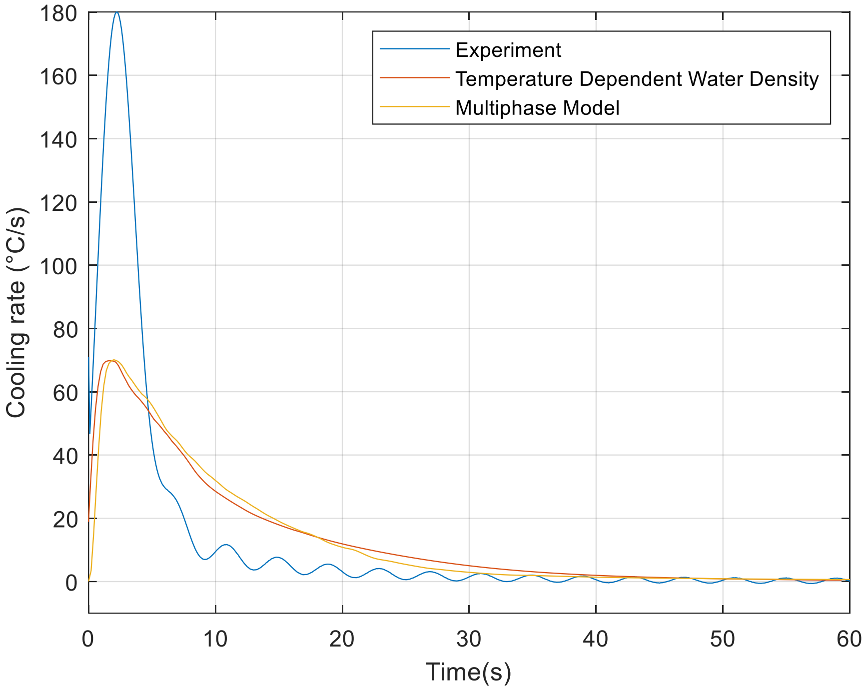

Figure 87 Cooling Rate vs. Time Curves of The Multiphase Models with Water Densities That Are Dependent and Independent of Temperature.

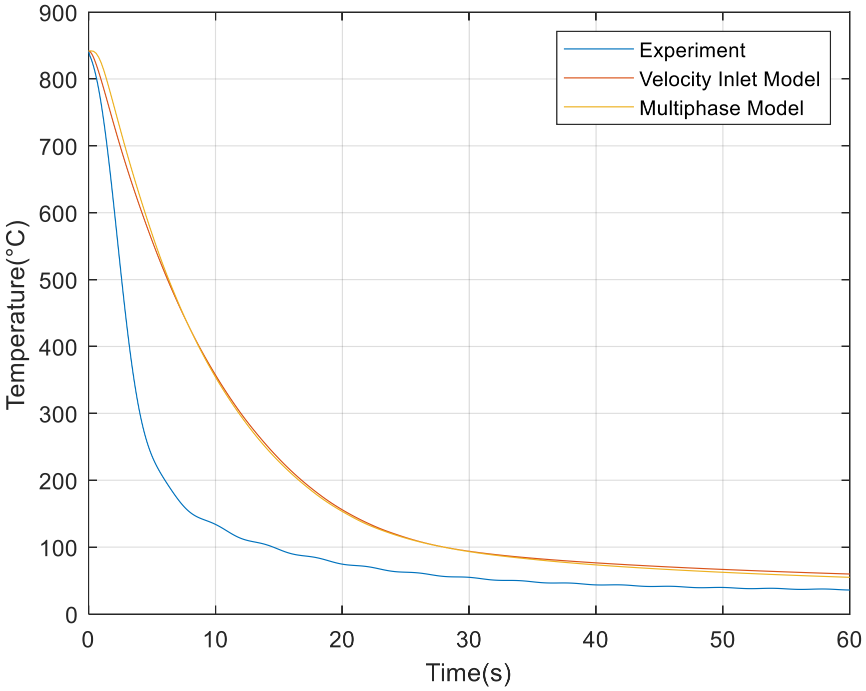

Figure 88 Temperature Curves of the Model with Velocity Inlet, the Multiphase Model, and the Experimental Data.

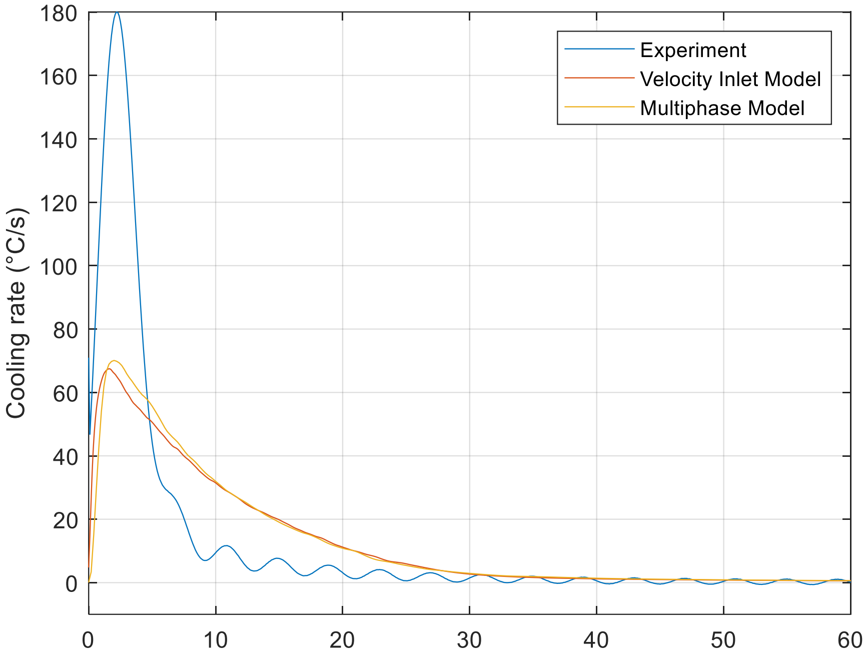

Figure 89 Cooling Rate vs. Time Curves of the Model with Velocity Inlet, the Multiphase Model, and the Experimental Data.

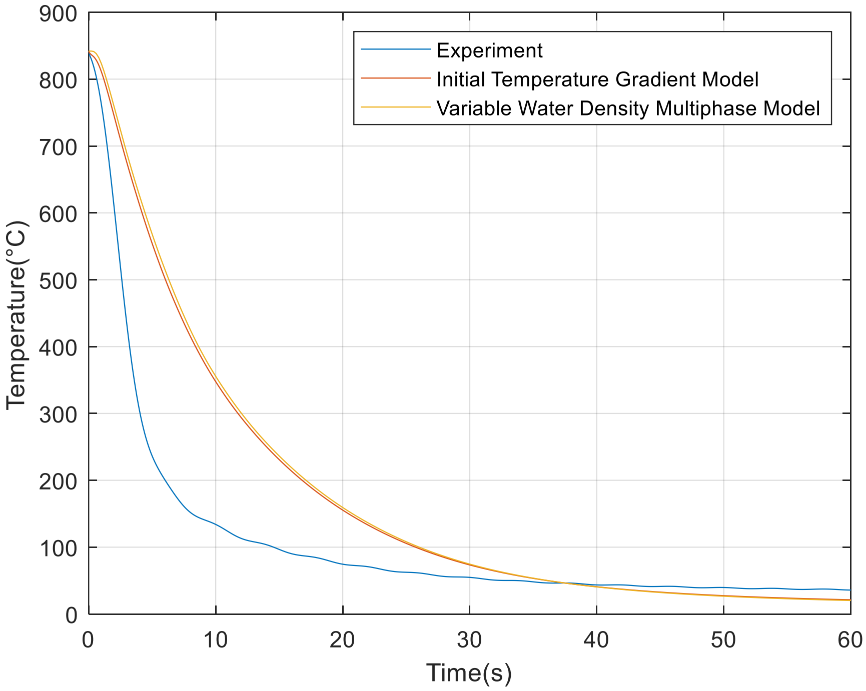

Figure 90 Temperature vs. Time Curves of the Model with Initial Temperature Gradient and the Variable Water Density Multiphase Model.

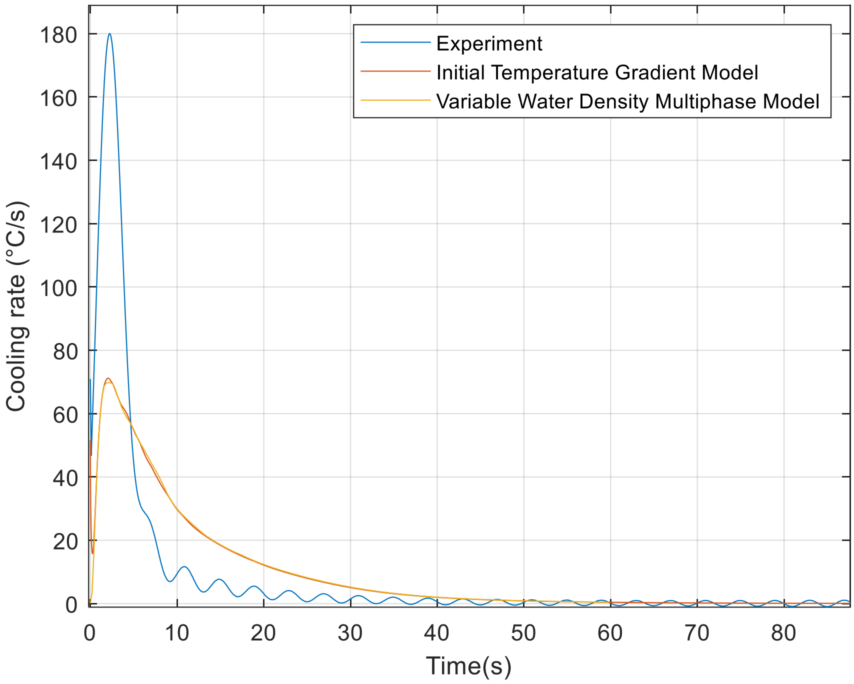

Figure 91 Cooling Rate vs. Time Curves of the Model with Initial Temperature Gradient and the Variable Water Density Multiphase Model.

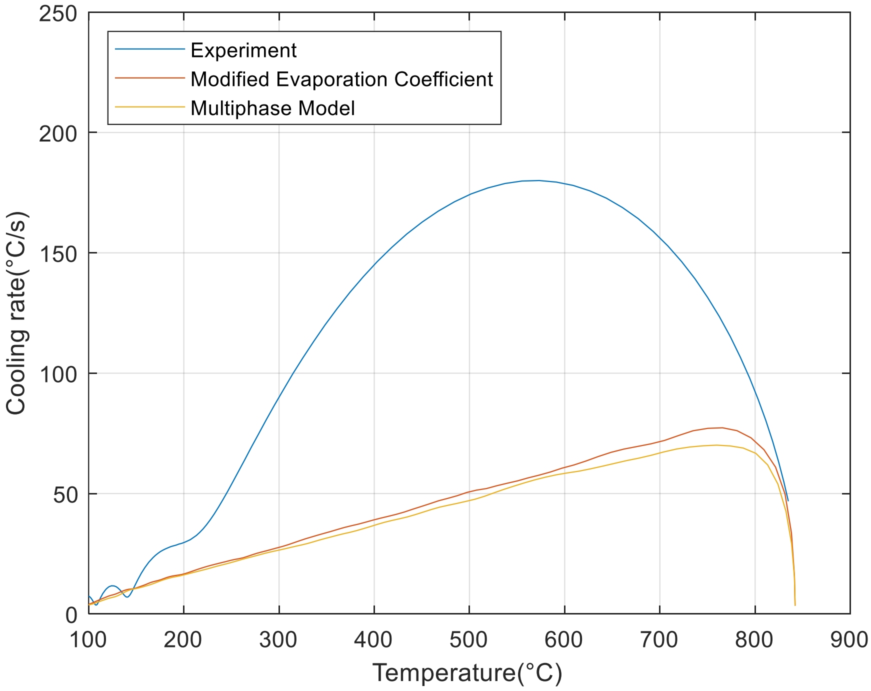

Figure 92 Cooling Rate vs. Temperature Curves of the Models with and without a Modified Evaporation Coefficient and the Experimental Data.

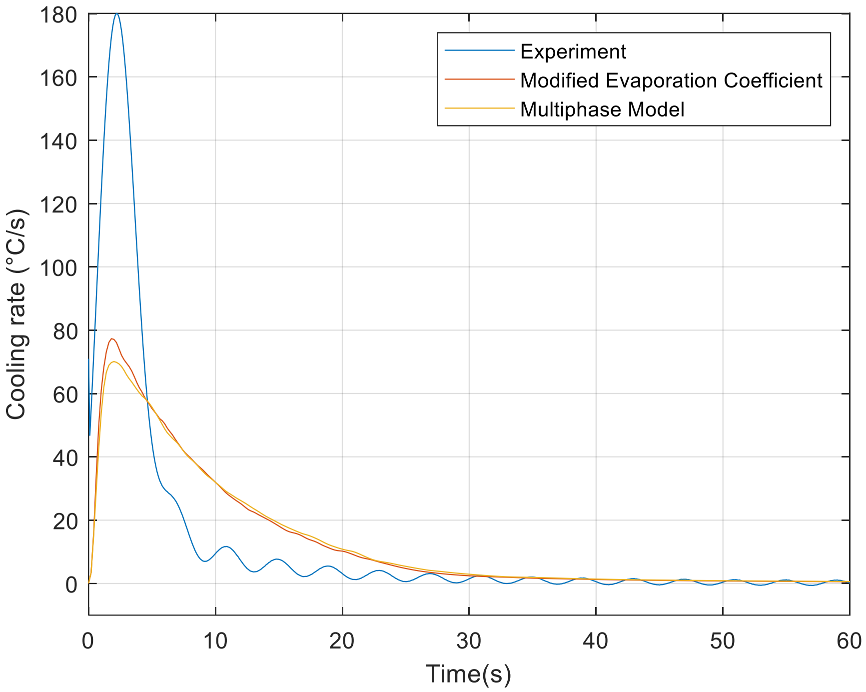

Figure 93 Cooling Rate vs. Time Curves of the Models with and without a Modified Evaporation Coefficient and the Experimental Data.

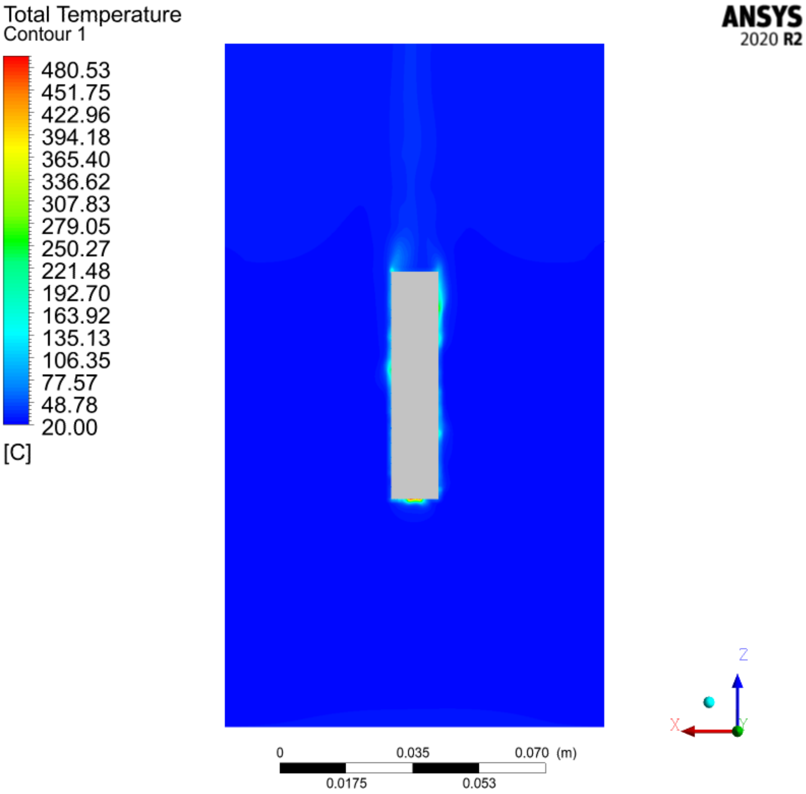

Figure 94 Temperature Distribution of the Model with an Increased Evaporation Coefficient at t=2.2 s.

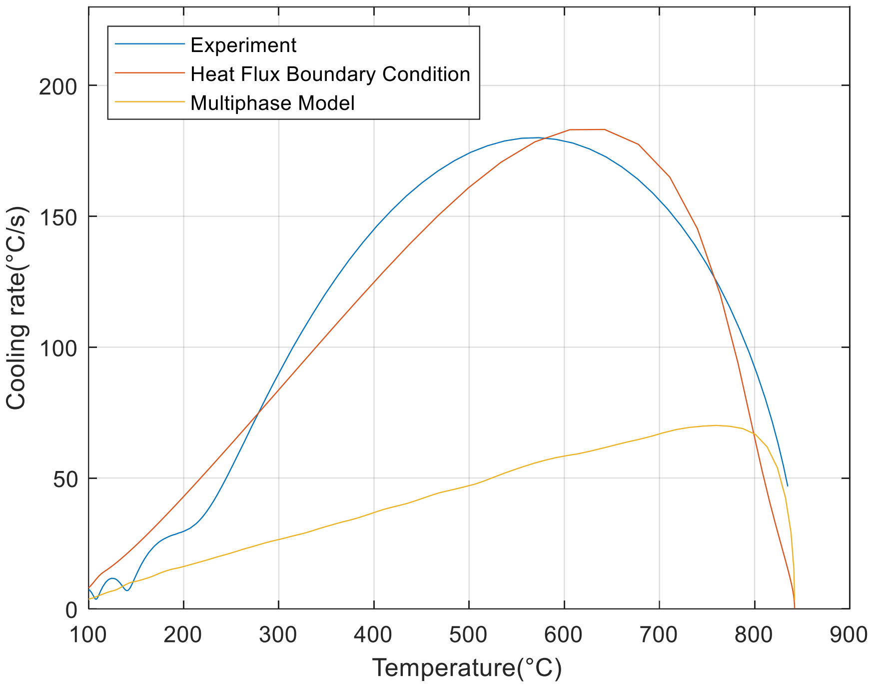

Figure 95 Cooling Rate vs. Temperature Curves of the Models with Heat Flux and Coupled Boundary Conditions.

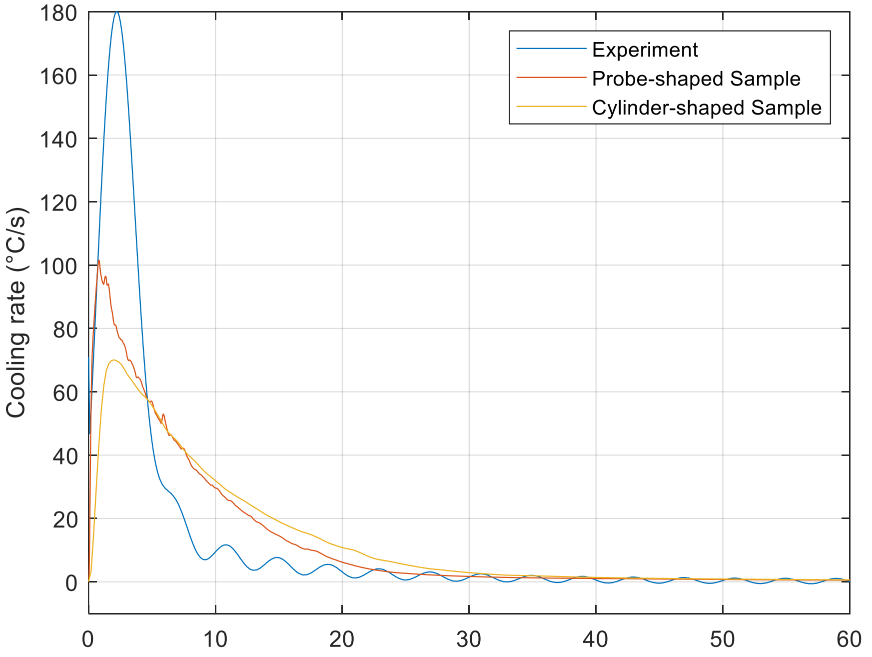

Figure 96 Cooling Rate vs. Time Curves of the Models with Both Sample Shapes and the Experimental Data.

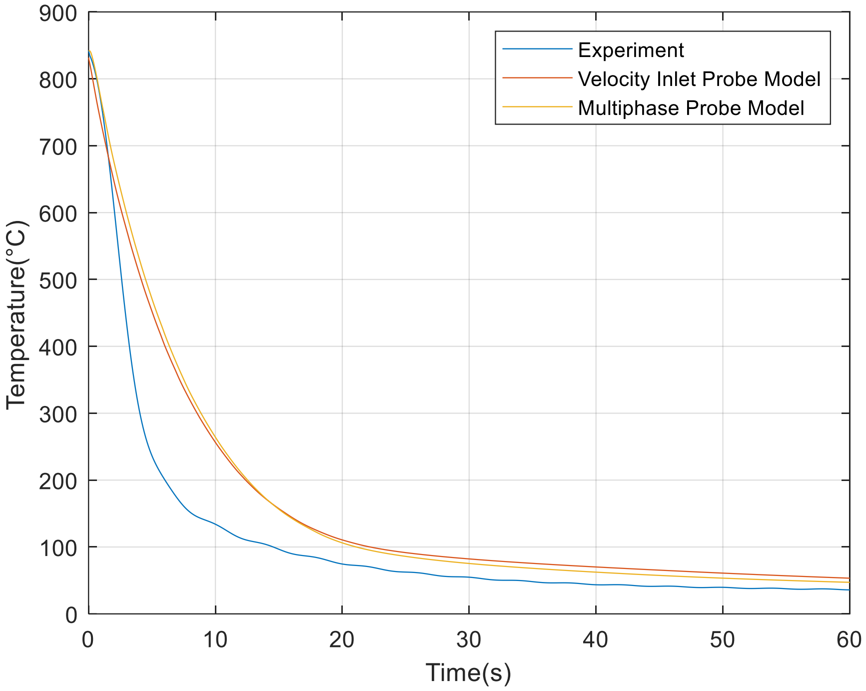

Figure 97 Temperature Curves of Probe Models with and without Velocity Inlet.

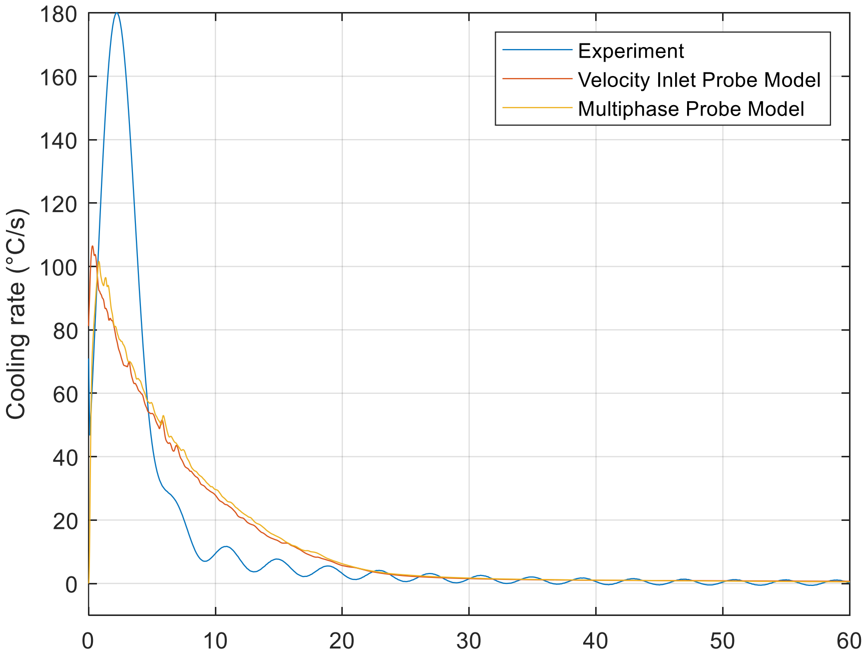

Figure 98 Cooling Rate vs. Time Curves of Probe Models with and without Velocity Inlet.

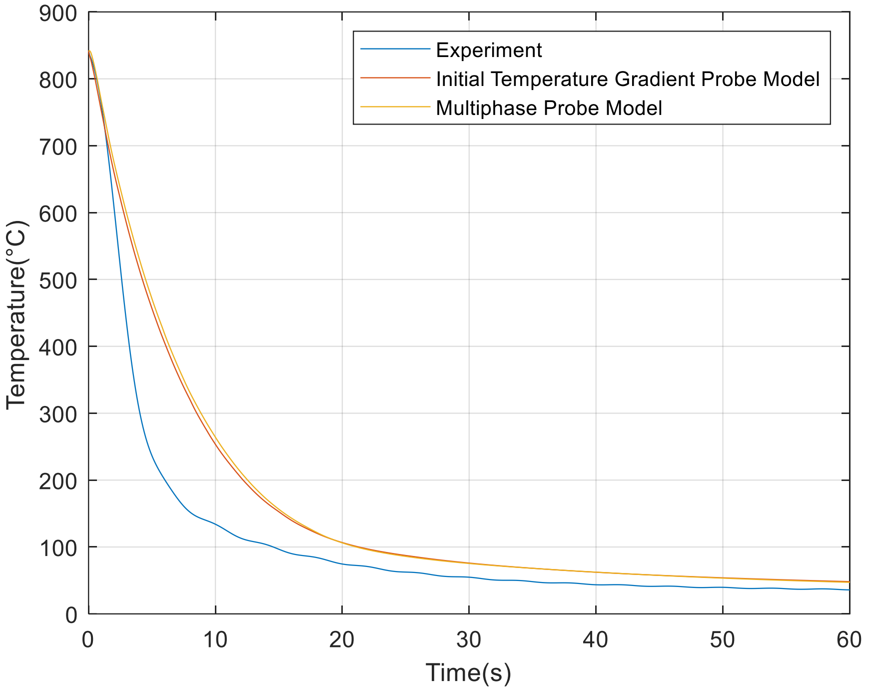

Figure 99 Temperature Curves of the Probe-shaped Sample Models with and without Initial Temperature Gradient.

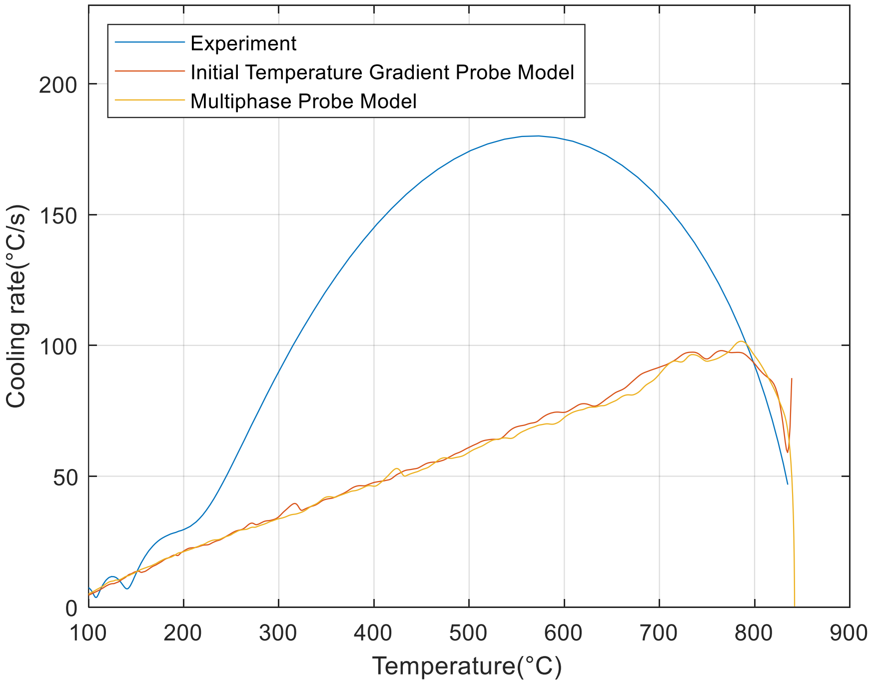

Figure 100 Cooling Rate vs. Temperature Curves of the Probe-shaped Sample Models with and without Initial Temperature Gradient.

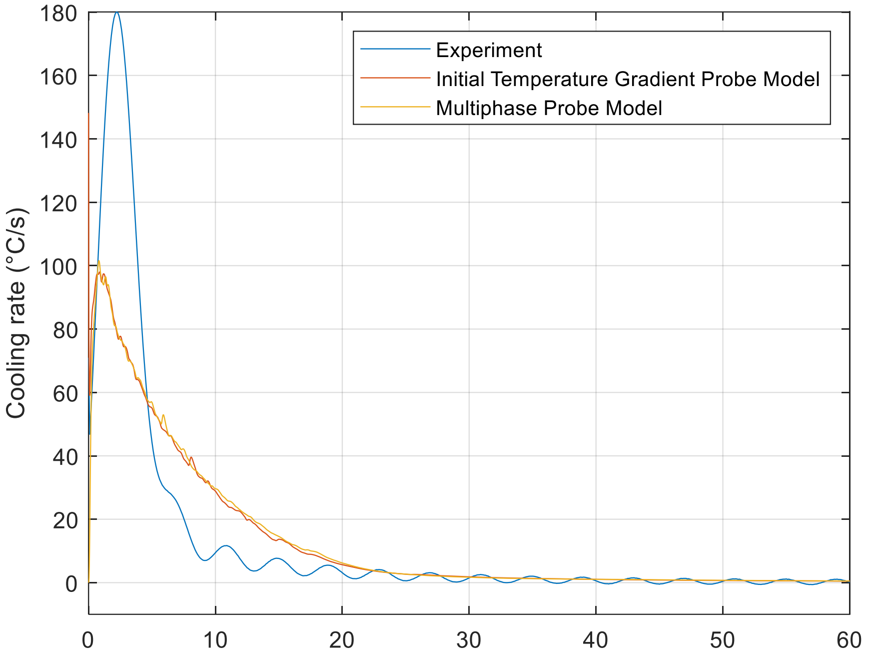

Figure 101 Cooling Rate vs. Time Curves of the Probe-shaped Sample Models with and without Initial Temperature Gradient.

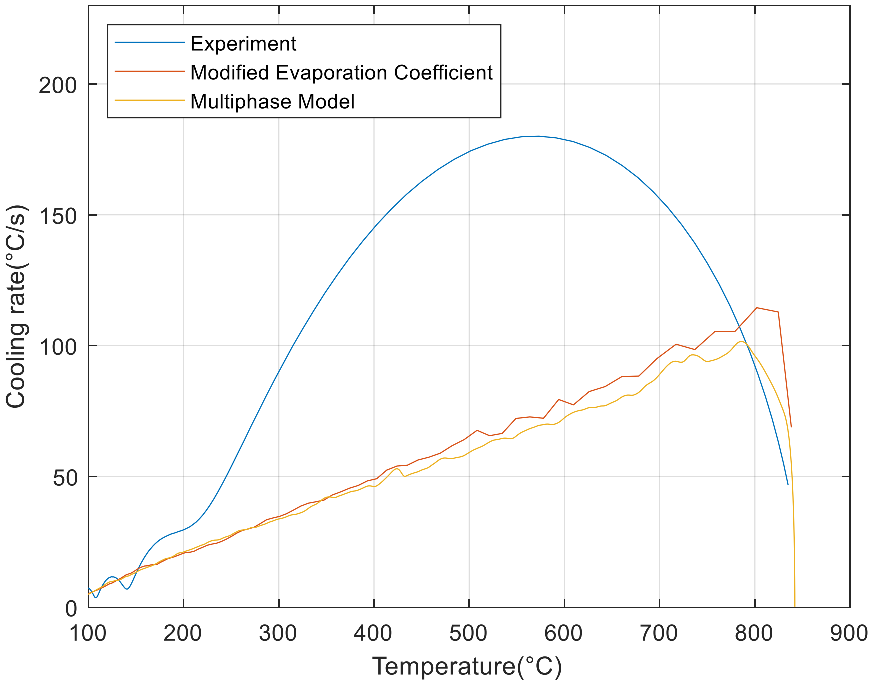

Figure 102 Cooling Rate vs. Temperature Curves of the Modified Evaporation Coefficient Model and the Multiphase Model with Probe-shaped Samples.

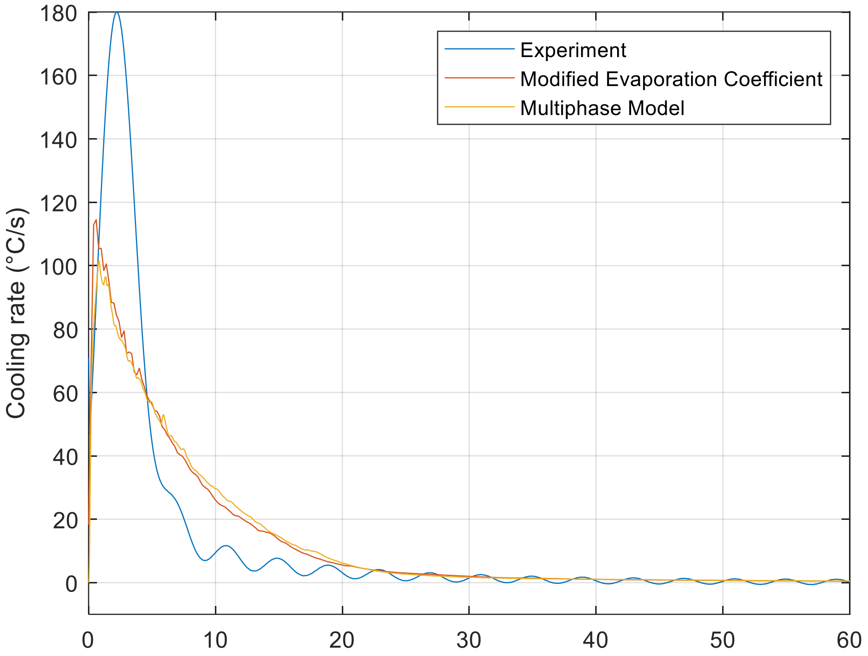

Figure 103 Cooling Rate vs. Time Curves of the Modified Evaporation Coefficient Model and the Multiphase Model with Probe-shaped Samples.

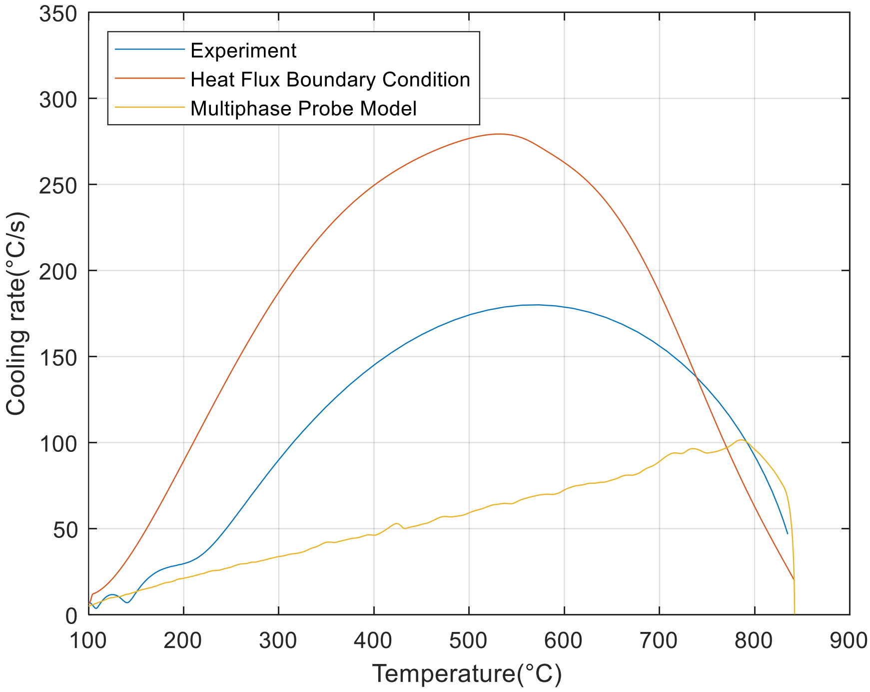

Figure 104 Cooling Rate vs. Temperature Curves of the Probe Models with Heat Flux and Coupled Boundary Conditions.

Acknowledgements

First of all, I would like to thank my supervisors Eric J. Palmiere and Bradley P. Wynne for their great help throughout the entire project. They always provide me with really helpful suggestions and feedbacks when I am encountered with any difficulty related to my research.

I would also like to thank Michael P. Howson and Salaheddin Rahimi for sharing their valuable data with me. Their data are of vital importance for the validation of my models.

Special thanks to my parents. They have unconditionally supported me since the beginning of the project. I am always inspired and encouraged whenever I get to meet them, especially during the pandemic.

I also want to thank all my colleges of Advanced Metallic System CDT Sheffield 2018 Cohort. We have worked through several projects, and I appreciate all the support from them and the communication with them.

Finally, I would like to thank all my friends from Chinese Students and Scholars Association Sheffield. We had a great time enjoying casual activities on holidays. Last but not least, special thanks to April who has accompanied me through my hardest time.

References

1. GÜR, C. and C. Şimşir, Simulation of quenching: A Review. Materials Performance and Characterization, 2012. 1(1).

2. Fernandes, F.M.B., S. Denis, and A. Simon, Mathematical-Model Coupling Phase-Transformation and Temperature Evolution during Quenching of Steels. Materials Science and Technology, 1985. 1(10): p. 838-844.

3. de Oliveira, W.P., et al., Thermomechanical analysis of steel cylinders quenching using a constitutive model with diffusional and non-diffusional phase transformations. Mechanics of Materials, 2010. 42(1): p. 31-43.

4. Burtchen, M., et al., Simulation of Quenching Treatments on Bearing Components. Strojniski Vestnik-Journal of Mechanical Engineering, 2009. 55(3): p. 155-159.

5. Leidenfrost, J.G., A tract about some qualities of common water. 1964: Carolyn SE Wares.

6. Jan, J., et al., Development and Validation of Cfd Methodology to Simulate Water Quenching Process. Proceedings of the Asme 9th International Manufacturing Science and Engineering Conference, 2014, Vol 2, 2014.

7. Krause, F., S. Schuttenberg, and U. Fritsching, Modelling and simulation of flow boiling heat transfer. International Journal of Numerical Methods for Heat & Fluid Flow, 2010. 20(3-4): p. 312-331.

8. Prakash, M., et al., A new approach to boiling simulation using a discrete particle based method. Computers & Graphics, 2015. 53: p. 118-126.

9. Crespo, A.J., et al., DualSPHysics: Open-source parallel CFD solver based on Smoothed Particle Hydrodynamics (SPH). Computer Physics Communications, 2015. 187: p. 204-216.

10. Xiong, H.-b., C.-y. Zhang, and Z.-s. Yu, Multiphase SPH modeling of water boiling on hydrophilic and hydrophobic surfaces. International Journal of Heat and Mass Transfer, 2019. 130: p. 680-692.

11. Shadloo, M.S., G. Oger, and D. Le Touzé, Smoothed particle hydrodynamics method for fluid flows, towards industrial applications: Motivations, current state, and challenges. Computers & Fluids, 2016. 136: p. 11-34.

12. Cleary, P.W., et al., Smooth particle hydrodynamics: status and future potential. Progress in Computational Fluid Dynamics, an International Journal, 2007. 7(2-4): p. 70-90.

13. Monaghan, J.J., Smoothed particle hydrodynamics. In: Annual review of astronomy and astrophysics. Vol. 30 (A93-25826 09-90), p. 543-574., 1992. 30: p. 543-574.

14. Monaghan, J. and J. Lattanzio, Further studies of a fragmentation problem. Astronomy and Astrophysics (ISSN 0004-6361), vol. 158, no. 1-2, April 1986, p. 207-211., 1986. 158: p. 207-211.

15. Sigalotti, L.D.G., et al., Smoothed particle hydrodynamics simulations of evaporation and explosive boiling of liquid drops in microgravity. Physical Review E, 2015. 92(1): p. 013021.

16. Fernandez, J., et al., Using SPH one-way coupled to DEM to model wet industrial banana screens. Minerals Engineering, 2011. 24(8): p. 741-753.

17. Potapov, A.V., M.L. Hunt, and C.S. Campbell, Liquid–solid flows using smoothed particle hydrodynamics and the discrete element method. Powder Technology, 2001. 116(2-3): p. 204-213.

18. Barcarolo, D.A., et al. Voronoi-SPH: on the analysis of a hybrid finite volumes-smoothed particle hydrodynamics method. in 9th Int. SPHERIC workshop. 2014.

19. Bao, Y.B. and J. Meskas, Lattice Boltzmann method for fluid simulations. Department of Mathematics, Courant Institute of Mathematical Sciences, New York University, 2011. 44.

20. He, X. and L.-S. Luo, Theory of the lattice Boltzmann method: From the Boltzmann equation to the lattice Boltzmann equation. Physical review E, 1997. 56(6): p. 6811.

21. Körner, C., et al., Parallel lattice Boltzmann methods for CFD applications, in Numerical solution of partial differential equations on parallel computers. 2006, Springer. p. 439-466.

22. Khazaeli, R., M.R. Nazari, and A. Zadehgol, Introducing a modified exact difference method for incorporating unsteady and non-uniform force terms in lattice kinetic models.

Computers & Mathematics with Applications, 2019. 78(3): p. 723-740.

23. Lallemand, P. and L.S. Luo, Theory of the lattice boltzmann method: dispersion, dissipation, isotropy, galilean invariance, and stability. Phys Rev E Stat Phys Plasmas Fluids Relat Interdiscip Topics, 2000. 61(6 Pt A): p. 6546-62.

24. Zhang, L., et al., A study of boiling on surfaces with temperature-dependent wettability by lattice Boltzmann method. International Journal of Heat and Mass Transfer, 2018. 122: p. 775-784.

25. Li, Q., et al., Lattice Boltzmann modeling of boiling heat transfer: The boiling curve and the effects of wettability. International Journal of Heat and Mass Transfer, 2015. 85: p. 787-796.

26. Gong, S. and P. Cheng, A lattice Boltzmann method for simulation of liquid–vapor phase-change heat transfer. International Journal of Heat and Mass Transfer, 2012. 55(17-18): p. 4923-4927.

27. Gong, S. and P. Cheng, Lattice Boltzmann simulation of periodic bubble nucleation, growth and departure from a heated surface in pool boiling. International Journal of Heat and Mass Transfer, 2013. 64: p. 122-132.

28. Sun, T., W. Li, and S. Yang, Numerical simulation of bubble growth and departure during flow boiling period by lattice Boltzmann method. International Journal of Heat and Fluid Flow, 2013. 44: p. 120-129.

29. Toro, L., et al., The Finite Element Method (Fem): An Application to Fluid Mechanics and Heat Transfer. Fine chemical technologies, 2018. 13(4): p. 17-25.

30. Jeong, W. and J. Seong, Comparison of effects on technical variances of computational fluid dynamics (CFD) software based on finite element and finite volume methods. International Journal of Mechanical Sciences, 2014. 78: p. 19-26.

31. Gohil, T., et al., Simulation of oscillatory flow in an aortic bifurcation using FVM and FEM: a comparative study of implementation strategies. International Journal for Numerical Methods in Fluids, 2011. 66(8): p. 1037-1067.

32. Ahmad, N., et al., Numerical simulation of macrosegregation: a comparison between finite volume method and finite element method predictions and a confrontation with experiments. Metallurgical and Materials Transactions A, 1998. 29: p. 617-630.

33. Idelsohn, S.R., E. Oñate, and F.D. Pin, The particle finite element method: a powerful tool to solve incompressible flows with free‐surfaces and breaking waves. International journal for numerical methods in engineering, 2004. 61(7): p. 964-989.

34. Oñate, E., et al., The particle finite element method—an overview. International Journal of Computational Methods, 2004. 1(02): p. 267-307.

35. Cremonesi, M., et al., A state of the art review of the particle finite element method (PFEM). Archives of Computational Methods in Engineering, 2020. 27(5): p. 1709-1735.

36. Aubry, R., S. Idelsohn, and E. Onate, Particle finite element method in fluid-mechanics including thermal convection-diffusion. Computers & structures, 2005. 83(17-18): p. 1459-1475.

37. Bravo, R., et al., Sediment transport problems by the particle finite element method (PFEM). Computational Particle Mechanics, 2020. 7(1): p. 139-149.

38. Sun, Z., et al., Investigation of non-linear ship hydroelasticity by CFD-FEM coupling method. Journal of Marine Science and Engineering, 2021. 9(5): p. 511.

39. Ye, Z. and S.-C. Hsu, Predicting real-time deformation of structure in fire using machine learning with CFD and FEM. Automation in Construction, 2022. 143: p. 104574.

40. Kim, K.-H., et al., Fully coupled BEM-FEM analysis for ship hydroelasticity in waves. Marine Structures, 2013. 33: p. 71-99.

41. Lin, Q., et al., A CFD-FEM numerical study on shot peening. International Journal of Mechanical Sciences, 2022. 223: p. 107259.

42. Oberkampf, W.L., et al., Error and uncertainty in modeling and simulation. Reliability Engineering & System Safety, 2002. 75(3): p. 333-357.

43. Helton, J.C., et al., Representation of analysis results involving aleatory and epistemic

uncertainty. International Journal of General Systems, 2010. 39(6): p. 605-646.

44. Evcil, G.E., O. Mustak, and C. Simsir, Simulation of through-hardening of SAE 52100 steel bearings - Part II: Validation at industrial scale. Materialwissenschaft Und Werkstofftechnik, 2016. 47(8): p. 746-754.

45. Deng, X.H. and D.Y. Ju, Modeling and Simulation of Quenching and Tempering Process in steels. International Federation for Heat Treatment and Surface Engineering (20th Congress), 2013. 50: p. 368-374.

46. La Vecchia, G.M., A. Pola, and F. Zola, Computer simulation of the heat treatment process applied to a forged shaft. Metallurgia Italiana, 2010(5): p. 5-11.

47. Barrena-Rodriguez, M.D., et al., An Efficient Fluid-Dynamic Analysis to Improve Industrial Quenching Systems. Metals, 2017. 7(6).

48. Jiang, Y., et al., Superposition method for the simulation of heat transfer. International Journal of Heat and Mass Transfer, 2018. 120: p. 914-922.

49. Stephan, P. and J. Kern, Evaluation of heat and mass transfer phenomena in nucleate boiling. International Journal of Heat and Fluid Flow, 2004. 25(2): p. 140-148.

50. Paul, S., M. Fernandino, and C.A. Dorao, On the scaling of convective boiling heat transfer coefficient. International Journal of Heat and Mass Transfer, 2021. 164.

51. Denis, S., D. Farias, and A. Simon, Mathematical-Model Coupling Phase-Transformations and Temperature Evolutions in Steels. Isij International, 1992. 32(3): p. 316-325.

52. John, B., P. Senthilkumar, and S. Sadasivan, Applied and Theoretical Aspects of Conjugate Heat Transfer Analysis: A Review. Archives of Computational Methods in Engineering, 2019. 26(2): p. 475-489.

53. Chen, X. and P. Han, A note on the solution of conjugate heat transfer problems using SIMPLE-like algorithms. International Journal of Heat and Fluid Flow, 2000. 21(4): p. 463-467.

54. Errera, M.P., et al., A numerical predictive model for conjugate heat transfer with radiation. International Journal of Heat and Mass Transfer, 2020. 160.

55. Dhir, V.K., Boiling heat transfer. Annual Review of Fluid Mechanics, 1998. 30: p. 365-401.

56. Guo, D.Z., et al., Phase Change Heat Transfer Simulation for Boiling Bubbles Arising from a Vapor Film by the Voset Method. Numerical Heat Transfer Part a-Applications, 2011. 59(11): p. 857-881.

57. Fujita, Y., et al., Nucleate Boiling Heat-Transfer and Critical Heat-Flux in Narrow Space between Rectangular Surfaces. International Journal of Heat and Mass Transfer, 1988. 31(2): p. 229-239.

58. Hsu, S.H., et al., On the formation of vapor film during quenching in de-ionized water and elimination of film boiling during quenching in natural sea water. International Journal of Heat and Mass Transfer, 2015. 86: p. 65-71.

59. Barnea, Y., E. Elias, and I. Shai, Flow and Heat-Transfer Regimes during Quenching of Hot Surfaces. International Journal of Heat and Mass Transfer, 1994. 37(10): p. 1441-1453.

60. Srinivasan, V., et al., Numerical Simulation of Immersion Quench Cooling Process: Part I. Imece 2008: Heat Transfer, Fluid Flows, and Thermal Systems, Vol 10, Pts a-C, 2009: p. 1941-1954.

61. Chen, Y.Z., Heat Transfer in Film Boiling of Flowing Water. Heat Transfer - Theoretical Analysis, Experimental Investigations and Industrial Systems, 2011: p. 235-260.

62. Stephan, P. and J. Hammer, A New Model for Nucleate Boiling Heat-Transfer. Warme Und Stoffubertragung-Thermo and Fluid Dynamics, 1994. 30(2): p. 119-125.

63. Snyder, N.W. and T.T. Robin, Mass-Transfer Model in Subcooled Nucleate Boiling. Journal of Heat Transfer, 1969. 91(3): p. 404-&.

64. Firouzi, M., T. Howes, and A.V. Nguyen, A quantitative review of the transition salt concentration for inhibiting bubble coalescence. Advances in Colloid and Interface Science, 2015. 222: p. 305-318.

65. Abdalrahman, K.H.M., Sabariman, and E. Specht, Influence of salt mixture on the heat transfer during spray cooling of hot metals. International Journal of Heat and Mass Transfer,

2014. 78: p. 76-83.

66. Vakarelski, I.U., et al., Stabilization of Leidenfrost vapour layer by textured superhydrophobic surfaces. Nature, 2012. 489(7415): p. 274-277.

67. Sartori, E., A critical review on equations employed for the calculation of the evaporation rate from free water surfaces. Solar Energy, 2000. 68(1): p. 77-89.

68. Chen, J.C., Correlation for Boiling Heat Transfer to Saturated Fluids in Convective Flow. Industrial & Engineering Chemistry Process Design and Development, 1966. 5(3): p. 322-&.

69. Kiyomura, I.S., et al., A predictive model for confined and unconfined nucleate boiling heat transfer coefficient. Applied Thermal Engineering, 2017. 127: p. 1274-1284.

70. Stephan, K. and M. Abdelsalam, Heat-transfer correlations for natural convection boiling. International Journal of Heat and Mass Transfer, 1980. 23(1): p. 73-87.

71. Bromley, L.A., Heat transfer in stable film boiling. Vol. 2295. 1949: US Atomic Energy Commission, Technical Information Division.

72. Srinivasan, V., et al., Numerical simulation of immersion quench cooling process using an Eulerian multi-fluid approach. Applied Thermal Engineering, 2010. 30(5): p. 499-509.

73. Zuber, N., Nucleate boiling. The region of isolated bubbles and the similarity with natural convection. International Journal of Heat and Mass Transfer, 1963. 6(1): p. 53-78.

74. Hua, T.C. and J.J. Xu, Quenching boiling in subcooled liquid nitrogen for solidification of aqueous materials. Materials Science and Engineering a-Structural Materials Properties Microstructure and Processing, 2000. 292(2): p. 169-172.

75. Srinivasan, V., et al., Numerical simulation of immersion quenching process of an engine cylinder head. Applied Mathematical Modelling, 2010. 34(8): p. 2111-2128.

76. Jeschar, R., E. Specht, and C. Köhler, Heat transfer during cooling of heated metallic objects with evaporating liquids. Theory and technology of quenching: a handbook, 1992: p. 73-92.

77. Ribatski, G. and J.M.S. Jabardo, Experimental study of nucleate boiling of halocarbon

refrigerants on cylindrical surfaces. International journal of heat and mass transfer, 2003. 46(23): p. 4439-4451.

78. Chu, H.Q. and B.M. Yu, A new comprehensive model for nucleate pool boiling heat transfer of pure liquid at low to high heat fluxes including CHF. International Journal of Heat and Mass Transfer, 2009. 52(19-20): p. 4203-4210.

79. Chen, S.G., C.I. Weng, and J.M. Lin, Inverse estimation of transient temperature distribution in the end quenching test. Journal of Materials Processing Technology, 1999. 86(1-3): p. 257-263.

80. Archambault, P. and A. Azim, Inverse resolution of the heat-transfer equation: application to steel and aluminum alloy quenching. Journal of materials engineering and performance, 1995. 4: p. 730-736.

81. Archambault, P., S. Denis, and A. Azim, Inverse resolution of the heat-transfer equation with internal heat source: Application to the quenching of steels with phase transformations. Journal of Materials Engineering and Performance, 1997. 6(2): p. 240-246.

82. Kim, H.K. and S.I. Oh, Evaluation of heat transfer coefficient during heat treatment by inverse analysis. Journal of Materials Processing Technology, 2001. 112(2-3): p. 157-165.

83. Li, H.P., et al., Inverse heat conduction analysis of quenching process using finite-element and optimization method. Finite Elements in Analysis and Design, 2006. 42(12): p. 1087-1096.

84. Hobold, G.M. and A.K. da Silva, Visualization-based nucleate boiling heat flux quantification using machine learning. International Journal of Heat and Mass Transfer, 2019. 134: p. 511-520.

85. Bouissa, Y., et al., Prediction of heat transfer coefficient during quenching of large size forged blocks using modeling and experimental validation. Case Studies in Thermal Engineering, 2019. 13.

86. de Kock, D.J., K.J. Craig, and J.A. Snyman, Using mathematical optimization in the CFD analysis of a continuous quenching process. International Journal for Numerical Methods in

Engineering, 2000. 47(5): p. 985-999.

87. Lee, W.H., Pressure iteration scheme for two-phase flow modeling. IN" MULTIPHASE TRANSPORT: FUNDAMENTALS, REACTOR SAFETY, APPLICATIONS". 1980: p. 407-432.

88. Alizadehdakhel, A., M. Rahimi, and A.A. Alsairafi, CFD modeling of flow and heat transfer in a thermosyphon. International Communications in Heat and Mass Transfer, 2010. 37(3): p. 312-318.

89. De Schepper, S.C.K., G.J. Heynderickx, and G.B. Marin, Modeling the evaporation of a hydrocarbon feedstock in the convection section of a steam cracker. Computers & Chemical Engineering, 2009. 33(1): p. 122-132.

90. Wu, H.L., et al., Simulation of refrigerant flow boiling in serpentine tubes. International Journal of Heat and Mass Transfer, 2007. 50(5-6): p. 1186-1195.

91. Sun, D.L., J.L. Xu, and Q.C. Chen, Modeling of the Evaporation and Condensation Phase-Change Problems with Fluent. Numerical Heat Transfer Part B-Fundamentals, 2014. 66(4): p. 326-342.

92. Ganapathy, H., et al., Volume of fluid-based numerical modeling of condensation heat transfer and fluid flow characteristics in microchannels. International Journal of Heat and Mass Transfer, 2013. 65: p. 62-72.

93. Sun, D.L., J.L. Xu, and L. Wang, Development of a vapor-liquid phase change model for volume-of-fluid method in FLUENT. International Communications in Heat and Mass Transfer, 2012. 39(8): p. 1101-1106.

94. Wang, D.M., et al. Numerical modeling of quench cooling using Eulerian two-fluid method. in ASME International Mechanical Engineering Congress and Exposition. 2002.

95. Tanguy, S., et al., Benchmarks and numerical methods for the simulation of boiling flows. Journal of Computational Physics, 2014. 264: p. 1-22.

96. Sahut, G., et al., Numerical simulation of boiling on unstructured grids. Journal of Computational Physics, 2021. 432.

97. Das, S. and H. Punekar, On development of a semimechanistic wall boiling model.

Journal of Heat Transfer, 2016. 138(6).

98. Kobasko, N., P. Krukovskyi, and D. Yurchenko, Initial and critical heat flux densities evaluated on the basis of CFD modeling and experiments during intensive quenching. Hte'07: Proceedings of the 5th Iasme / Wseas International Conference on Heat Transfer, Thermal Engineering and Environment, 2007: p. 294-+.

99. Guan, C.-K., J.F. Klausner, and R. Mei, A new mechanistic model for pool boiling CHF on horizontal surfaces. International Journal of Heat and Mass Transfer, 2011. 54(17-18): p. 3960-3969.

100. Tentner, A., H.D. Chen, and R.Y. Zhang, Simulation of two-phase flow and heat transfer phenomena in a boiling water reactor using the lattice Boltzmann method. Physica a-Statistical Mechanics and Its Applications, 2006. 362(1): p. 98-104.

101. Chien, L.H. and R.L. Webb, A nucleate boiling model for structured enhanced surfaces. International Journal of Heat and Mass Transfer, 1998. 41(14): p. 2183-2195.

102. Colombo, M., et al., Assessment of semi-mechanistic bubble departure diameter modelling for the CFD simulation of boiling flows. Nuclear Engineering and Design, 2019. 344: p. 15-27.

103. Marto, P. and W. Rohsenow, THE EFFECT OF SURFACE CONDITIONS ON NUCLEATE POOL BOILING HEAT TRANSFER TO SODIUM. Technical Report No. 5219-33. 1965, Massachusetts Inst. of Tech., Cambridge. Dept. of Mechanical Engineering.

104. Tachibana, F., M. Akiyama, and H. Kawamura, Non-hydrodynamic aspects of pool boiling burnout. Journal of Nuclear Science and Technology, 1967. 4(3): p. 121-130.

105. Guglielmini, G. and E. Nanei, Effect of heating wall thickness on pool boiling burnout. Int. J. Heat Mass Transfer;(United Kingdom), 1976. 19(9).

106. Paz, M.C., et al., On the effect of surface roughness and material on the subcooled flow boiling of water: Experimental study and global correlation. Experimental Thermal and Fluid Science, 2015. 64: p. 114-124.

107. Kern, J. and P. Stephan, Theoretical model for nucleate boiling heat and mass transfer

of binary mixtures. Journal of Heat Transfer-Transactions of the Asme, 2003. 125(6): p. 1106-1115.

108. Kamatchi, R. and S. Venkatachalapathy, Parametric study of pool boiling heat transfer with nanofluids for the enhancement of critical heat flux: A review. International Journal of Thermal Sciences, 2015. 87: p. 228-240.

109. Ciloglu, D. and A. Bolukbasi, The quenching behavior of aqueous nanofluids around rods with high temperature. Nuclear Engineering and Design, 2011. 241(7): p. 2519-2527.

110. Kim, H., et al., On the quenching of steel and zircaloy spheres in water-based nanofluids with alumina, silica and diamond nanoparticles. International Journal of Multiphase Flow, 2009. 35(5): p. 427-438.

111. Kim, S.J., et al., Surface wettability change during pool boiling of nanofluids and its effect on critical heat flux. International Journal of Heat and Mass Transfer, 2007. 50(19-20): p. 4105-4116.

112. Lee, C.Y., T.H. Chun, and W.K. In, Effect of change in surface condition induced by oxidation on transient pool boiling heat transfer of vertical stainless steel and copper rodlets. International Journal of Heat and Mass Transfer, 2014. 79: p. 397-407.

113. Kim, S.H., et al., Boiling heat transfer and critical heat flux evaluation of the pool boiling on micro structured surface. International Journal of Heat and Mass Transfer, 2015. 91: p. 1140-1147.

114. Hu, H., et al., Boiling and quenching heat transfer advancement by nanoscale surface modification. Scientific Reports, 2017. 7.

115. Kruse, C., et al., Extraordinary Shifts of the Leidenfrost Temperature from Multiscale Micro/Nanostructured Surfaces. Langmuir, 2013. 29(31): p. 9798-9806.

116. Fernandes, P. and K.N. Prabhu, Comparative study of heat transfer and wetting behaviour of conventional and bioquenchants for industrial heat treatment. International Journal of Heat and Mass Transfer, 2008. 51(3-4): p. 526-538.

117. Bertsch, S.S., E.A. Groll, and S.V. Garimella, Effects of heat flux, mass flux, vapor quality,

and saturation temperature on flow boiling heat transfer in microchannels. International Journal of Multiphase Flow, 2009. 35(2): p. 142-154.

118. Nishikawa, K., et al., Effect of Surface Configuration on Nucleate Boiling Heat-Transfer. International Journal of Heat and Mass Transfer, 1984. 27(9): p. 1559-1571.

119. Zhu, K., et al., Finite element simulation on residual stress during immersion quenching and pre-stretching of Al7055 thick plates. Materials Research Express, 2022. 9(2).

120. Buczek, A. and T. Telejko, Investigation of heat transfer coefficient during quenching in various cooling agents. International Journal of Heat and Fluid Flow, 2013. 44: p. 358-364.

121. Leblond, J.-B., et al., Mathematical models of anisothermal phase transformations in steels, and predicted plastic behaviour. Materials science and technology, 1985. 1(10): p. 815-822.

122. Chen, L.Q. and W. Yang, Computer-Simulation of the Domain Dynamics of a Quenched System with a Large Number of Nonconserved Order Parameters - the Grain-Growth Kinetics. Physical Review B, 1994. 50(21): p. 15752-15756.

123. Carlone, P., G.S. Palazzo, and R. Pasquino, Finite element analysis of the steel quenching process: Temperature field and solid-solid phase change. Computers & Mathematics with Applications, 2010. 59(1): p. 585-594.

124. Starink, M., Kinetic equations for diffusion-controlled precipitation reactions. Journal of materials science, 1997. 32: p. 4061-4070.

125. DP, K. and M. RE, A general equation prescribing the extent of the austenite-martensite transformation in pure iron-carbon alloys and plain carbon steels. Acta Metallurgica, 1959. 7(1): p. 59-60.

126. Corrotherm International®. March 3rd, 2020]; Available from: https://www.corrotherm.co.uk/grades/inconel-600.

127. AZO Materials. June 1st, 2021]; Available from: https://www.azom.com/article.aspx?ArticleID=4459.

128. Brackbill, J.U., D.B. Kothe, and C. Zemach, A continuum method for modeling surface

tension. Journal of computational physics, 1992. 100(2): p. 335-354.

129. Urone, P.P. and R. Hinrichs, College Physics (OpenStax). 2012, OpenStax.

130. Lee, W., A Pressure Iteration Scheme for Two-Phase Modeling. Technical Report LA-UR 79-975. Los Alamos, New Mexico, 1979.

131. Orszag, S., et al., Renormalization group modeling and turbulence simulations, International conference on near-wall turbulent flows, Tempe, Arizona. 1993.

132. Kim, J.-Y., et al., Comparison of near-wall treatment methods for high Reynolds number backward-facing step flow. International Journal of Computational Fluid Dynamics, 2005. 19(7): p. 493-500.

133. Launder, B.E. and D.B. Spalding, The numerical computation of turbulent flows, in Numerical prediction of flow, heat transfer, turbulence and combustion. 1983, Elsevier. p. 96-116.

134. Jayatilleke, C., The influence of Prandtl number and surface roughness on the resistance of the laminar sub- layer to momentum and heat transfer(Laminar sublayer resistance to momentum and heat transfer, noting effects of Prandtl number and surface roughness using mathematical model and experiments). 1969.

135. Barth, T. and D. Jespersen. The design and application of upwind schemes on unstructured meshes. in 27th Aerospace sciences meeting. 1989.

136. Holmes, D. and S. Connell. Solution of the 2D Navier-Stokes equations on unstructured adaptive grids. in 9th computational fluid dynamics conference. 1989.

137. Rausch, R.D., J.T. Batina, and H.T. Yang. Spatial adaption procedures on unstructured meshes for accurate unsteady aerodynamic flow computation. in AIAA/ASME/ASCE/AHS/ASC 32nd Structures, Structural Dynamics and Materials Conference. 1991.

138. Anderson, W.K. and D.L. Bonhaus, An implicit upwind algorithm for computing turbulent flows on unstructured grids. Computers & Fluids, 1994. 23(1): p. 1-21.

139. Babu, K. and T. Prasanna Kumar, Mathematical modeling of surface heat flux during quenching. Metallurgical and Materials Transactions B, 2010. 41: p. 214-224.

140. Rhie, C.M. and W.-L. Chow, Numerical study of the turbulent flow past an airfoil with trailing edge separation. AIAA journal, 1983. 21(11): p. 1525-1532.

141. Flint, T.F., et al., A thermal fluid dynamics framework applied to multi-component substrates experiencing fusion and vaporisation state transitions. Communications Physics, 2020. 3(1): p. 196.

142. Howson, M., et al., An analysis of the quenching performance of a copper nanofluid prepared using laser ablation. Journal of Thermal Science and Engineering Applications, 2016. 8(4): p. 044501.

143. Barron, R. and A.A. Salehi Neyshabouri, Effects of under‐relaxation factors on turbulent flow simulations. International journal for numerical methods in fluids, 2003. 42(8): p. 923-928.

144. Rahimi, S., M. King, and C. Dumont, Stress relaxation behaviour in IN718 nickel based superalloy during ageing heat treatments. Materials Science and Engineering a-Structural Materials Properties Microstructure and Processing, 2017. 708: p. 563-573.